Imperial College London
Department of Electrical and Electronic Engineering

MEMS MICRO-CONTACT PRINTING ENGINES

by
Choonee, Kaushal R V

MEng, Electrical and Electronic Engineering
Imperial College London, 2007

Prof. R.R.A. Syms
Supervisor

Prof. A.S. Holmes
Internal Examiner

Prof. J. Cooper
External Examiner

A dissertation submitted to Imperial College London for the degree of
Doctor of Philosophy
November 2010

Abstract

This thesis investigates micro-contact printing (μCP) engines using micro-electro-mechanical systems (MEMS). Such engines are self-contained and do not require further optical alignment and precision manipulation equipment. Hence they provide a low-cost and accessible method of multilevel surface patterning with sub-micron resolution. Applications include the field of biotechnology where the placement of biological ligands at well controlled locations on substrates is often required for biological assays, cell studies and manipulation, or for the fabrication of biosensors.

A miniaturised silicon μCP engine is designed and fabricated using a wafer-scale MEMS fabrication process and single level and bi-level μCP are successfully demonstrated. The performance of the engine is fully characterised and two actuation modes, mechanical and electrostatic, are investigated. In addition, a novel method of integrating the stamp material into the MEMS process flow by spray coating is reported.

A second μCP engine formed by wafer-scale replica moulding of a polymer is developed to further drive down cost and complexity. This system carries six complementary patterns and allows six-level μCP with a layer-to-layer accuracy of 10 μm over a 5 mm x 5 mm area without the use of external aligning equipment. This is the first such report of aligned multilevel μCP.

Lastly, the integration of the replica moulded engine with a hydraulic drive for controlled actuation is investigated. This approach is promising and proof of concept has been provided for single-level patterning.

Declaration

The work presented in Chapter 3 was carried out in collaboration with Dr H. Zou (Dalian University of Technology), who developed the process flow and fabricated the silicon engines while the author focussed on design, characterisation and experimentation. The simulation of the structure in Section 3.2.3 was carried out by Dr T. Besant and Dr D. Barnes (Hiflux Ltd., UK).

All other results reported in this thesis are primarily due to the author except for background results which are clearly referenced. The findings of Chapter 2, 3, 4 and 5 have been published and are listed in Section 7.3.

Acknowledgements

Firstly, I would like to thank my supervisor, Richard Syms for his help and guidance throughout this work. Not only is he an outstanding researcher but he has been a great supervisor and it has been a pleasure to work with him.

I would also like to thank Imad Jaimoukha who always had his door open since I first joined Imperial in 2003. Over these years, I benefited from his help, advice and support time and time again.

I was lucky to work in a research group with many excellent colleagues. Thank you to everyone from OSD for the fun times and the many interesting discussions. In particular, I am grateful to Munir Ahmad for patiently teaching me the delicate art of microfabrication, and Helin Zou for fabricating the first MEMS engine. I am also thankful to the night-shift cleanroom users for the camaraderie and for watching out for each other.

My friends provided the chats, the laughter, the coffee breaks and the pub nights required to sustain this work. Big thanks to my EEE/ISE classmates of 2007 (especially Fabrice, Ketan, Kunal, Munga, Soha, Siavash), and my housemates from Walham House for making it all easier. Thanks also to my friends outside Imperial for reminding me about the world out there.

Most of all, I would like to thank my parents for their continued support and for providing me with such amazing opportunities, and my sister, Preeyah, for her constant encouragement. Thank you for your faith in me. Finally, my very special thanks go to Evi for her love, understanding and unwavering support in this endeavour.

To my parents,

Table of Contents

Abstract 2

Declaration 3

Acknowledgements 4

List of Figures 12

List of Tables 21

Abbreviations 22

1 Introduction 23

1.1 Micro-contact printing (μCP) 26

1.1.1 PDMS Stamp 26

1.1.2 Ink and Substrates: SAM of alkanethiols on gold 28

1.2 μCP in microfabrication 30

1.2.1 Patterning of silicon by μCP of etch masks 31

1.2.2 Micro and nano-structuring by selective deposition on contact printed templates 32

1.2.3 μCP of non-planar substrates 33

1.2.4 Large area μCP for electronics 34

1.3 μCP in biology and biochemistry 36

1.3.1 Patterning proteins and cells 36

1.3.2 μCP for *in vitro* studies of neurons 39

1.4 Limitations of μCP 41

1.4.1 Distortion of the stamp due to shrinkage on curing 41

1.4.2 Conformal contact and long range pattern accuracy 42

1.4.3 Tools and techniques for large area alignment and printing 43

1.4.4 Mechanical stability of the relief features....45
1.5 Alternative methods of patterning SAMs....48
1.6 Research objectives....50
1.6.1 MEMS and its suitability for μCP....51
1.6.2 Thesis structure....54
1.7 References....56
2 Micro-structuring of PDMS for μCP stamps and other applications....63
2.1 Properties of PDMS....64
2.2 PDMS casting and moulding....66
2.3 Subtractive structuring of PDMS: Laser ablation and wet etching....68
2.3.1 Laser ablation....68
2.3.2 Etching of PDMS....68
2.4 Embossing....70
2.5 Spray Coating of PDMS....72
2.5.1 Motivation....72
2.5.2 PDMS spray deposition: Background....73
2.5.3 PDMS Spray deposition: Experimental methods....76
2.5.4 PDMS Spray deposition: Results....80
2.5.5 PDMS spray deposition on microstructured surfaces....84
2.5.6 Applications of PDMS spray coating....89
2.5.7 Summary: Spray deposition of PDMS....92
2.6 Conclusion....93
2.7 References....94

3 Silicon μCP engine 98

3.1 Introduction - MEMS 98

3.1.1 Silicon springs 98

3.1.2 Actuation 99

3.1.3 Alignment 100

3.1.4 Outline of this chapter 102

3.2 Concept and Design 102

3.2.1 Concept 102

3.2.2 Self-alignment 103

3.2.3 Flexure – Elastic Suspension 104

3.2.4 Print head 107

3.2.5 PDMS Stamp 109

3.2.6 Actuation 109

3.2.7 Prototype layout and operation 110

3.3 Fabrication 112

3.3.1 Process Flow 112

3.3.2 Prototype Devices 115

3.4 Mechanical characterisation 116

3.4.1 Measurement of stiffness 116

3.4.2 Manually actuated μCP 117

3.5 Discussion 119

3.6 References 121

4 Electrostatically driven μCP 123

4.1 Silicon μCP engine as a parallel plate electrostatic actuator 123
4.1.1 Model 123
4.1.2 Pull-in in a simple parallel plate actuator 124
4.2 Electrostatic actuation 126
4.2.1 Characterisation 126
4.2.2 Electrostatically driven μCP 128
4.2.3 Discussion: Electrostatic μCP 131
4.3 Overcoming electrical discharge 132
4.3.1 Electrical discharge 132
4.3.2 Reducing voltages across the air gap 133
4.3.3 Design rules to avoid dielectric breakdown 139
4.4 Experimental verification of electrostatic μCP with built in dielectric 141
4.4.1 Experimental setup 141
4.4.2 μCP Results 144
4.5 Conclusion 145
4.6 References 147
5 Replica moulded μCP engine 148
5.1 Concept and design 148
5.1.1 Self-alignment 149
5.1.2 Elastic backing 150
5.1.3 Pattern Stability 151
5.1.4 Simulation 152
5.1.5 Stamps and patterns for multilevel characterisation 154

5.2 Fabrication 156
5.2.1 Master and Target 156
5.2.2 PDMS Stamp Casting 160
5.3 Experimental methods 163
5.3.1 μCP protocol 163
5.3.2 Absolute distortion and layer-to-layer alignment 163
5.4 Results and Discussion 165
5.4.1 6-level μCP 165
5.4.2 Absolute distortion 166
5.4.3 Layer-to-layer accuracy 167
5.4.4 Comparison with previous work 169
5.4.5 μCP with different inks 170
5.5 Conclusion 172
5.6 References 173
6 Hydraulically actuated μCP engine 175
6.1 Hydraulic and pneumatic actuation in microsystems 175
6.2 Design and Concept 176
6.2.1 Hydraulic actuation 176
6.2.2 Replica moulded μCP stamp 177
6.2.3 Modelling of Membrane 178
6.2.4 Simulation 181
6.3 Fabrication 184
6.3.1 Si master fabrication 184

6.3.2 PDMS stamp casting and assembly 187
6.3.3 Bonding onto hydraulic chuck 190
6.3.4 Modified assembly process 191
6.4 Experimental results and discussion 193
6.4.1 Free deformation 193
6.4.2 Contact and μCP with a hydraulic drive 197
6.5 Conclusions 199
6.6 References 200
7 Conclusions 201
7.1 Summary 201
7.2 Conclusions and Future work 203
7.3 List of Publications 206
Appendix A: Inks and Etchants for μCP 207
A1 Inks 207
A2 Substrates 208
A3 Stamps and inking 208
A4 Printing 208
A5 Etchants 208
A6 References 209

List of Figures

Figure 1-1 μCP of an alkanethiol ink on Au. A PDMS stamp is inked and brought into contact with an Au coated substrate. SAMs are formed in the contacted region. 26

Figure 1-2 Distortion in PDMS stamps, a) pairing of slender features, b) sagging of the stamp with sparse features. 28

Figure 1-3 Representation of alkanethiol SAM on Au (111) 29

Figure 1-4 Si patterning by μCP of a metal masking layer. The metal layer is first contact printed and the unprotected area is etched off. The remaining metal is then used as a mask for KOH etching or RIE of the underlying Si. 31

Figure 1-5 a) μCP to pattern templates for electroless deposition. After placement of the monolayer, the substrate is immersed in a copper containing solution. b) SEM of the deposited copper (from [1.43]). 32

Figure 1-6 Templates with two SAMs for controlled deposition. First, a hydrophobic SAM is patterned by μCP (left). The unfilled area is covered with a hydrophilic SAM (middle) and finally, the targeted material is deposited (right) adsorbs onto the hydrophilic regions only. 33

Figure 1-7 a) Micro-coil on glass capillary formed by μCP. b) Free-standing micro-spring. After electroplating, the cylindrical glass substrate is etched away to release the springs.....33

Figure 1-8 a) μCP on micro-structured Si. b) CVD resulting in Cu deposition on SAM-free region (trough and sidewalls)[1.41]. c) Catayltic growth resulting in suspended NT between Si posts [1.52]. 34

Figure 1-9 a) μCP on a thin plastic substrate. b) Completed circuit showing an array of TFT formed by μCP [1.60] 35

Figure 1-11 a) Micro-fluidic networks to ink a flat PDMS stamp for μCP. b) Microfabricated silicon inking chip for parallel inking. 39

Figure 1-12 a) Alignment stage from [1.82]. b) Localised growth of hippocampal neurons on electrodes[1.83].....40
Figure 1-13 a) Trilayer stamp from [1.16]. b) Stamp with flexible glass backing [1.16].....43
Figure 1-14 a) Flexible stamp by IBM [1.56]. In the image, the stamp (highlighted by a red line) is in a bent position and is not touching the stamp. b) Philips Wavemaker [1.57]. Valves sequentially switched on to cause contact of the stamp to substrate. 44
Figure 1-15 GeSiM μ-CP 2.1. PDMS diaphragm is attached to a stamp holder connected to an *x*-*y* stage. A linear *z* actuator brings the stamp close to the substrate. Pressure is applied to achieve contact with the substrate.....45
Figure 1-16 Generic PDMS stamp indicating relief feature dimensions. σ denotes the applied pressure. 46
Figure 1-17 a) Writing patterns of SAM by dip-pen nanolithography (DPN). It is generally accepted that a water meniscus at the tip-substrate interface transports the molecules. b) Illustration of an 2d array of cantilevers for parallel DPN [1.102].....48
Figure 1-18 SEM of inverted pyramids (V-grooves) formed in Si(100) by anisotropic etching. The largest feature is 400 μm long. 51
Figure 1-19 SEM of trenches in Si formed by DRIE. the inset highlights the scalloping sidewalls. (from [1.111]).....52
Figure 1-20 SEM of a) single axis accelerometer with capacitive sensing, b) vibrating ring gyroscope formed by deep etching of polysilicon. Images are from [1.118]. 53
Figure 1-21 SEM of a) micro-mirror array from Texas Instruments, b) an ink jet nozzle array from [1.122] 54
Figure 2-1 a) Structure of linear PDMS consisting of a siloxane backbone (-Si-O-). b) Cross-link reaction (hydrosilylation) between methyl hydrogen siloxane units in the curing agent and dimethyl vinyl units in the base. 65

Figure 2-2 a) Casting of PDMS on a Si master. b) SEM of V-shaped bars formed by moulding against a KOH-etched Si master. c) SEM of dense high aspect ratio structures cast against a Si master formed by DRIE. 67
Figure 2-3 a) Sub-surface drilling of a micro-capillary by laser ablation[2.33]. b) Dry etching of PDMS with RIE. Inset is an SEM image highlighting the roughness. (adapted from [2.34]) 69
Figure 2-4 a) Illustration of embossing. b) SEM of an embossed PDMS part showing a void due to trapped air 71
Figure 2-5 Illustration of Instability leading to droplet formation 74
Figure 2-6 Illustration of a Venturi nozzle 76
Figure 2-7 a) Modeller's airbrush used for spray coating. b) Rotating spray deposition system showing rotating chuck, screens, and spray gun. 78
Figure 2-8 a) Variation of fluid 20cSt diluted, spray coated PDMS fim thickness with time, for different rotation rates. Points are data, straight lines are best fits. b) Variation of radial roughness with thickness, for different rotation rates. Injection pressure: 40psi; separation 30mm. 81
Figure 2-9 a) Variation of fluid 20cSt diluted, spray coated PDMS tangential roughness with thickness, for different injection pressures. Rotation rate: 135 rpm; separation 30 mm. b) Variation of film thickness with time for optimised parameters. c) Variation of uniformity with film thickness. Points are data, straight lines are best fits. 82
Figure 2-10 a) Variation of hexane-diluted spray PDMS film thickness with time, for optimised parameters. b) Variation of uniformity with thickness. Points are data, straight lines are best fits. 83
Figure 2-11 3D Maps of coated surfaces. a) Optimised conditions. b) Low Pressure Conditions 84

Figure 2-12 SEM views of Fluid 20cSt diluted PDMS. a) 5 μm wide bars and 40 μm period. b) 5 μm wide bars and 10 μm period. 85
Figure 2-13 Hexane-diluted PDMS spray coated silicon microstructure with 5 μm width and 10 μm period. 86
Figure 2-14 SEM view of Fluid 20 cSt diluted PDMS spray coated silicon V-groove structure a) with chuck temperature = 20 C; b) with chuck temperature = 150 C 87
Figure 2-15 a) Key dimensions used in definition of conformality. b) Variation of conformality with temperature. c) Variation of surface roughness (Ra) with temperature. Material used is Fluid 20 cSt diluted PDMS. 88
Figure 2-16. SEMs of plasma activated bonding of Fluid 20 cSt PDMS covered structures: a) and b) 2μm deep rectangular channels formed by DRIE. For high channel width to height ratios such as in b) the run off significantly alters the shape of the channel. c) and d) 300 μm deep channels formed by KOH etching of Si (100). 91
Figure 2-17 SEM views of Au patterns (bright) on Si (dark) made by μCP using a spray coated stamp: a) 10 μm bars, b) varying bar widths showing defects. 92
Figure 3-1 a) Leaf spring formed by through-wafer DRIE and bonding onto a substrate with pre-etched pits to enable movement [3.7]. The springs joins the proof mass of an accelerometer to its frame. b) Through wafer etched suspended springs [3.8]. c) Thin cantilever spring formed by undercutting [3.9]. 99
Figure 3-2 MEMS actuators (from [3.18]); a) electrostatic comb drive, b) thermal 'hot'-arm actuator. 100
Figure 3-3 a) Illustration of crystal-plane orientation. b) Etched Si V-grooves combined with silicon nitride mechanical springs for aligning and fixing optical fibres [3.20]. c) Spacer chip formed by a matching teeth and grooves in single crystal silicon[3.22]. 101
Figure 3-4 Self Alignment: a) U-grooves and fibre. b) V-grooves and rail 103

Figure 3-5 Elastic Suspension: a) Overall chip. b) Individual Springs.....104
Figure 3-6 Variation of system stiffness with displacement.....107
Figure 3-7 Variation of a) static sag, b) resonant frequency, with spring dimensions. 108
Figure 3-8 Print head deflection and retraction 109
Figure 3-9 a) Plan and b) section view of a silicon μCP engine, showing alignment and deflection.....111
Figure 3-10 Process flow for μCP engine. Main steps are: elastic suspension patterning, stamper features formation, alignment groove and snap out tab etching, die release, and PDMS coating.....113
Figure 3-11 Optical image of finished device (single crystal Si)) a) in a whole wafer, b) after detaching and aligning on machined target substrate. SEM images of c) bottom view, d) top of device.....115
Figure 3-12 Load deflection characteristic for BSOI devices 116
Figure 3-13 Stamp pattern with SU-8 photoresist and Si after PDMS spray coating.....117
Figure 3-14 SEM of patterned 5μm and 10μm Au lines on Si (dark: Si, pale: Au).....119
Figure 3-15 SEM images of Au (bright) patterns on Si (dark) formed aligned μCP and etching showing a) intersections of 10μm and 2μm lines b) intersections of 10μm and 10μm lines c) intersecting decreasing line widths from 10μm to 2μm. d) large area > 3mm ×3mm patterning. 120
Figure 3-16 Alignment accuracy of overlaid patterns (dark: Si, pale: Au). A first print is made, the stamp shifted laterally by a few mm, and a second print made. The combined print is revealed by etching away the uncovered Au. The left side of the image shows the region printed twice whilst the right side shows the region printed only once.....120
Figure 4-1 a) Electrostatic operation of Si μCP engine, b) Equivalent electro-mechanical model.....124

Figure 4-2 Variation or normalised separation σ with normalised electrostatic force η 126
Figure 4-3 Electrical characterisation of μCP engine using PI spacers 127
Figure 4-4 Experimental voltage-deflection characteristics of different devices 128
Figure 4-5 Optical image showing damage to substrate due to discharge.....128
Figure 4-6 Electrostatically actuated contact, showing discharge damage and faint pattern transfer 129
Figure 4-7 SEM images of electrostatically actuated μCP showing a) ink transfer in non relief regions, b) dentritic features emanating from each side of the lines (image rotated compared to (a)).....130
Figure 4-8 Modified Paschen curve combining avalanche ionisation with vapour arc [4.3] at atmospheric pressure.....133
Figure 4-9 Electro-mechanical model with series C1 134
Figure 4-10 Introduction of C_1 implies that parasitic capacitance, C_2, between the frame of the actuator and the substrate, starts to influence the operation. 136
Figure 4-11 a) Parallel plate capacitor with built-in series capacitor, b) electrical equivalent circuit 138
Figure 4-12 Voltage across dielectrics in varactor 139
Figure 4-13 Voltage-gap characteristic for the air gap at different spring stiffness's. Breakdown voltage is overlaid for comparison. 140
Figure 4-14 a) Experimental arrangement used to test electrostatic μCP. Conductive surfaces are painted black. b) SEM of thick PDMS stamp.....141
Figure 4-15 Membrane cross-section during imaging. The inclined segments are not reliably captured. Surfaces AA represent the flat spacer surface which is the reference plane.....143
Figure 4-16 Deflection profile of membrane at different applied voltages. The two datasets are displaced with respect to each other for clarity.....144

Figure 5-1 Self-aligned μCP system. The upper image shows the plan view of the steel elastic backing while the lower image shows the cross-sectional view of the device showing self-alignment. 149

Figure 5-2 Layout of supporting bar. The 3 × 3 array can now carry any features without any risk of roof collapse between the cells. 151

Figure 5-3 Images of the model used for FEA of the membrane stamp. a) Deflection profile of the stamp under load of 20 MPa. b) Contact pressure (pale) on the underside of the stamp for the same load. 152

Figure 5-4 a) Normalised contact area variation with applied load. b) Displacement of the print head with applied force. 153

Figure 5-5 a) multiple stamps on a single silicon wafer. b) schematic of a single die showing 3×3 cells containing print pattern and supporting bar (Mask #1) and alignment groove (Mask #2). c) Close up of the pattern. Variants carry the same periodic bar pattern but shifted laterally, e.g. variant #1 carries the leftmost group, variant #2 the second group from the left, and so on. Variant "all" carries all six groups. 155

Figure 5-6 High resolution pattern carrying 10μm, 5μm and 2.5μm wide bars with mark to space ratios of unity. The pattern is rotated compared to Figure 5-5c. 156

Figure 5-7 Process flow for a) Master and b) target wafers. 157

Figure 5-8 SEMs of a) the cross-section of the 10 μm periodic bar patterns formed by RIE, b) the V-grooves at the convex corners formed by KOH etching. 158

Figure 5-9 Stamp replication process. PDMS is first cast, then the steel elastic backing attached, followed by a encapsulating PDMS layer. The completed stamp is cured and then peeled off from the master. 160

Figure 5-10 SEM of one of the patterns of PDMS stamp cast on high resolution master. For reliable imaging, the polymer was coated with a ~ 10 nm layer of Au prior to SEM. 161

Figure 5-11 a) Optical image of a completed stamp. b) SEM of finished die highlighting successful moulding. 162
Figure 5-12 Optical image showing an array of 4 stamps aligned onto a target substrate 162
Figure 5-13 Experimental results of μCP showing a) 6-level μCP, b) close up of adjacent prints showing small misalignment. The SEM images show Au patterns (bright) on Si formed by contact printing (6 times) and etching (see Section5.3.1) 165
Figure 5-14 SEM of Au (pale) on Si (dark) showing 500nm features 166
Figure 5-16 Distribution of layer-to-layer misalignment based on 50 prints 168
Figure 5-18 Condensation figure revealing the patterns of SAMs with different monolayers. The different droplet distributions on the hydrophilic (-COOH) and hydrophobic (-CH3) provide sufficient contrast for imaging by optical microscopy. 171
Figure 6-1 Outline of hydraulic system consisting of inlet/outlet, hydraulic cavity, and a deformable membrane 177
Figure 6-2 Cross-section view of μCP engine with PI elastic backing 178
Figure 6-3 Schematic of the cross-section of the stamp fixed at the edges. In contact, the deformed stamp can be approximated by a pyramidal shape (marked by dotted lines) and the volume enclosed by deformed membrane is given in Equation 6.2. 180
Figure 6-4 Model used for simulation. Relevant surfaces/parts are labelled. 182
Figure 6-5 Upper row: deformation of membrane without any contact surface. Lower row: deformation of membrane with a contact surface 190 μm from the initial surface. Deformation in bottom row is exaggerated for clarity. Z-scale is different in each row. 183
Figure 6-6 Simulation results showing variation of support contact area as the load is applied. For the range of loads displayed, the roof does not make contact at all. 183
Figure 6-7 Process flow for Si master for a) Part A, b) Part B 184
Figure 6-8 SEMS of completed a) Part A master, b) part B master 185

Figure 6-9 Moulding and stacking of PDMS parts with PI elastic backing. At all times, the PDMS parts are held by a rigid surface (either the Si master or the PI film). 188
Figure 6-10 Optical images of finished stamp showing a) 4× 2 array peeled off from master, b) single die 190
Figure 6-11 a) Optical micrograph of Perspex hydraulic chuck, b) schematic of PDMS membrane bonded onto chuck 191
Figure 6-12 Modified assembly of PDMS onto hydraulic chuck: a) schematic, b) photograph with the contact surface removed 192
Figure 6-14 Optical micrograph of Au-coated stamps used for imaging. The cracks are due to the metal coating process. 194
Figure 6-15 White light interferometer contour plots of membrane with a) 0.0 mL, b) 0.10 mL deformation 195
Figure 6-16 Maximum deflection at the centre of membrane as a function of injected volume 196
Figure 6-17 Comparison of free deformation results from experimental set up with FEA ... 196
Figure 6-18 Optical micrographs showing Au patterns (dark) on glass (pale/transparent). The Au patterns are formed by μCP with different volumes and etching (as per Appendix A) ... 197
Figure 6-19 Normalised contact area as a function of injected volume 198
Figure 7-1 a) Illustration of monolithic PDMS stamp, b) Simulation data showing operating pressure required to induce contact with different device size 205

List of Tables

Table 3-1 Process parameters for Si μCP engine 114

Table 5-1 Process parameters for master substrate 159

Table 5-2 Process parameters for target substrate 159

Table 6-1 Thickness weighted average values of elastic constants for multilayer structure . 179

Table 6-2 Process parameters for Part A master 186

Table 6-3 Process parameters for Part B master 187

Table 6-4 Process parameters for moulding and bonding parts A and B 189

Table 7-1 Performance of replica-moulded multi-level μCP engines 203

Table A-1 Alkanethiols for μCP on Au 207

Abbreviations

μCP	Micro-contact printing
μTAS	Micro-total-analysis systems
AFM	Atomic force microscope
BSOI	Bonded-silicon-on-insulator
DI	Deionised
DRIE	Deep reactive ion etching
FEA	Finite element analysis
HDT	Hexadecanethiol
IPA	Isopropyl alcohol
MEMS	Micro-electro-mechanical systems
PDMS	Poly(dimethyl)siloxane
PI	Polyimide
RIE	Reactive ion etching
SAM	Self-assembled monolayer
SEM	Scanning electron microscope

1 Introduction

Miniaturisation is central to advances in modern science and technology as products of micro- and nanotechnology typically provide lower power consumption, higher efficiency, improved speed, and lower cost relative to conventional macroscopic systems. In addition, as sizes scale down, surface-to-volume ratio increases and different physicochemical mechanisms come into play thus allowing the development of new devices and the observation of interesting physical phenomena.

Top-down micro- and nanofabrication methods, which shape structures from bulk material into smaller structures, have been developed by the microelectronics industry to fabricate integrated circuits. The batch fabrication process revolves around optical lithography and associated techniques, and has been adapted to silicon micromachining to realise micro-electro-mechanical systems (MEMS). MEMS devices have had commercial success as automotive sensors (accelerometers, pressure sensors), actuators for digital light processing (micro-mirrors), ink-jet printer heads, and more recently in consumer electronics (mobile phones, game consoles).

MEMS technology can also be used in the area of biochemical and biomedical technology. Such devices are termed bio-MEMS and applications include targeted drug delivery, in vivo and in vitro diagnostics, implants, drug discovery, gene expression profiling, and many others. With the healthcare systems already being stretched in many countries, there is a shift towards decentralisation and MEMS can provide miniaturised lab-on-chips (LOC), also termed micro-total-analysis systems (μTAS), that enable point of care testing of patients. In the area of biological implants, opto-electromechanical parts that restore some functionality

to damaged organs (e.g. retinal implants that restore some vision to the blind) or micro-devices that can navigate through the body and deliver drugs at specific locations are all conceivable for the near future. Another important and perhaps more realistic application of bio-MEMS lies in the formation of structures that enable fundamental studies of cells and other biological entities. MEMS are especially important here as their sizes are comparable to these biological bodies, e.g. cells measure from 1μm – 100μm.

In the above biomedical and biochemical applications, there is usually a need to locally sensitize substrates or surfaces so that they exhibit specific biochemical properties. The main patterning process available in MEMS is photolithography but this remains an obstacle as it provides limited control over surface properties and is often incompatible with biochemical components. Moreover, in research in life sciences where MEMS structures are used to study biological/biochemical components, such tools are too expensive and inaccessible.

A simple but powerful technique, termed micro-contact printing (μCP), was pioneered by the Whitesides group in 1993 and aimed to address this issue. μCP enabled rapid and cheap nanofabrication without the need for a cleanroom environment, whilst adding control of the surface properties.

This dissertation will concern the general area of bio-MEMS and will focus on μCP as a means of functionalising structures. This research culminates in MEMS μCP engines that enable multilevel patterning of biochemical compounds, without requiring conventional cleanroom equipment, thus making the process accessible to non-silicon end users. Over the next sections, the field of μCP is introduced, the achievements and limitations are presented,

and applications are discussed. Research objectives are then formulated and the suitability of MEMS in meeting them is highlighted.

1.1 Micro-contact printing (μCP)

μCP is essentially a miniaturised form of flexography where a flexible stamp carrying relief features is coated with an ink and brought into contact with a substrate. It was first introduced by Kumar and Whitesides in 1993 [1.1] who used a poly(dimethyl)siloxane (PDMS) polymer as stamp, an alkanethiol as ink, and a gold coated substrate . The ink forms a *self-assembled monolayer* (SAM) on the contacted regions as illustrated in Figure 1-1. Feature sizes ranging from 100 nm to a few cm can routinely be patterned. Since the initial discovery, tremendous advances have been made to the stamp, ink and substrate.

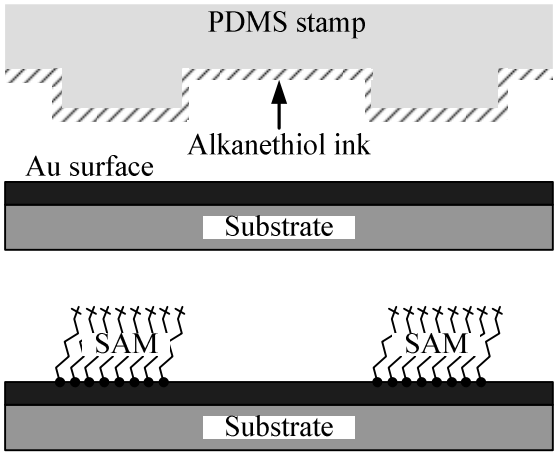


Figure 1-1 μCP of an alkanethiol ink on Au. A PDMS stamp is inked and brought into contact with an Au coated substrate. SAMs are formed in the contacted region.

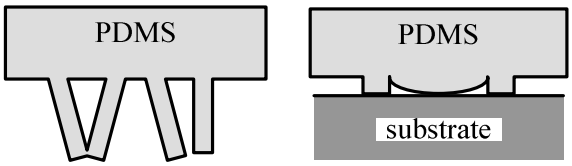
1.1.1 PDMS Stamp

The starting point in μCP is the stamp which is made from elastomeric PDMS. Generally, a 2-part heat curable mixture, which consists of a (viscous) liquid base and a curing agent, is used. On heating the polymer crosslinks and solidifies. Thus, this material is particularly suitable for processes like spin coating or replica moulding against a silicon (or other

material) master fabricated by conventional microfabrication techniques. The most popular commercial form of PDMS reported in literature is Sylgard 184 from Dow Corning [1.2].

Several properties of PDMS are instrumental to the formation of high quality patterns. Firstly, because of its elastomeric nature, it conforms to the surface over a relatively large area. With its 2-part thermal curing formulation, it can easily be cast or moulded against microfabricated masters. It is homogeneous, isotropic and optically transparent to about 300 nm, provides a surface which has a low interfacial free energy and is chemically inert. It can thus be easily released from fragile microfabricated structures [1.3]. Also with some modification, it can be made UV photocurable as in [1.4]. It is also porous and has a tendency to adsorb certain molecules [1.5] which is advantageous in μCP [1.1, 6]. Furthermore, its surface properties can be tailored by exposing it to oxygen plasma (see e.g. [1.7-9]). The plasma treatment can similarly be used to irreversibly bind PDMS surfaces to glass or to each other [1.10-13] and hence enables the construction of complex 3D geometries.

The softness and flexibility of PDMS (Young's modulus, E ≈ 1-2MPa), while allowing conformal contact over large areas, is also a limitation as the features on the stamp tend to get distorted. For Sylgard 184, Delamarche *et al*.[1.14] found that the height to width ratio of the relief structures on the stamp had to be within 0.2 to 2 to generate defect free patterns. Structures above that range tend to collapse under their own weight or to pair up (Figure 1-2) while those below that range are unable to resist the pressure during printing and lead to sagging [1.3] (see Figure 1-2).



a) b)

Figure 1-2 Distortion in PDMS stamps, a) pairing of slender features, b) sagging of the stamp with sparse features.

To solve the problems associated to the soft material, a number of solutions have been proposed. A tougher version of PDMS, with a compression modulus ~5 times that of Sylgard, was synthesised in [1.15]. This was mechanically stable and could support relief features of height to width ratios ranging from 0.02 to 5. However, such stamps lacked the ability to conform to uneven surfaces.

To meet the diverging demands of pattern stability and conformal contact, composite stamps [1.15, 16] involving a cushion of soft PDMS (such as Sylgard 184) and a layer of harder PDMS were developed, enabling the generation of $\approx$ 50 nm features. Other solutions have been proposed and these are discussed in greater detail in Section 1.4.

1.1.2 Ink and Substrates: SAM of alkanethiols on gold

The other components required for μCP is an ink and a suitable substrate. This is significantly different from conventional macroscopic stamping since only a single molecular layer is transferred and this monolayer self-assembles to form a densely packed overlayer.

Self-assembly is the spontaneous organisation of molecules or objects into stable states. The final self-assembled structure is close to or at thermodynamic equilibrium and therefore tends to form spontaneously and reject defects. Self-assembly is ubiquitous in nature and processes

such as the folding of proteins or formation of DNA illustrate its purpose [1.3]. SAMs are the most widely studied and best developed examples of nonbiological, self-assembled systems. They form spontaneously by chemisorption[1] and self-organisation of functionalised, long-chain organic molecules onto the surfaces of appropriate substrates. SAMs are usually prepared by exposing the substrate to the vapour or by immersion in solution of the reactive species.

The best characterised systems of SAMs are alkanethiols on gold [1.17-23]. Alkanethiols have the general formula $CH_3(CH_2)_nSH$ and it is generally accepted that the sulphur atoms form a $(\sqrt{3}\times\sqrt{3})R30^0$ overlayer on Au(111). The sulphur tail of the molecule is bound to the Au substrate, the alkyl $(CH_2)_n$ chain is oriented at $\approx 30^o$ to the normal, and the head group, **X**, points outwards and dictates the surface properties of the monolayer (see Figure 1-3). The structure is 2-3 nm tall when n = 15. In the case of an alkanethiol, X = CH_3, a methyl group, but thiols with other head groups, e.g. X = COOH, can also be used. The reaction is of the form $X(CH_2)_nSH + Au^0 \rightarrow X(CH_2)_nS^-Au^I + 1/2H_2$.

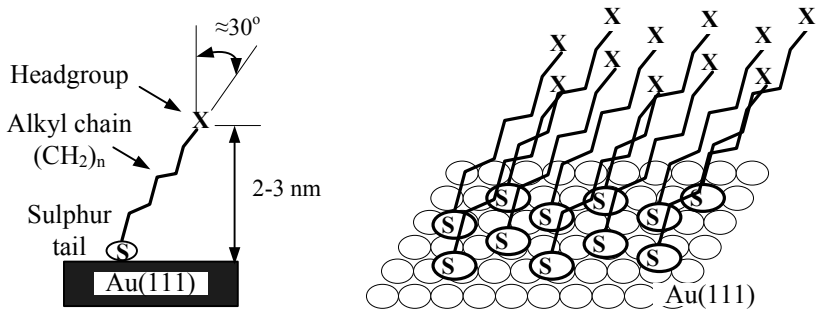


Figure 1-3 Representation of alkanethiol SAM on Au (111)

[1] Chemisorption is a type of adsorption whereby a molecule adheres to a surface through the formation of a chemical bond, as opposed to the Van der Waals forces which cause physisorption

A key feature of μCP is that forming SAMs using that route takes a few seconds, but forming them from solution takes minutes to hours. For a highly ordered quasi-crystalline organic monolayer, the length of the alkyl chain needs to be long enough, that is, n > 11. Commonly used alkanethiols that meet this condition are hexadecanethiol (HDT) with n = 15, octadecanethiol (OCT) n = 17, and eicosanethiol (ECT) n = 19. From [1.24, 25], it is known that the lighter HDT is more diffusive but protects better than ECT when the SAM is used as a mask in cyanide-based etch solutions. OCT is shown to be a good compromise.

Substrates other than Au can also be patterned as long as an appropriate ink that can form a sufficiently ordered monolayer and withstand subsequent processing is available. Alkanethiols can be used to pattern Ag[1.26], Cu[1.27], and Pd[1.28]. Alkanephosphonic acids have been used to form monolayers on Al[1.29] and indium tin oxide [1.30], and methods have been developed for patterning Si directly by the formation of siloxane SAMs on Si-OH surfaces [1.31] or alkoxyl SAMs on Si-Cl surfaces [1.32]. Siloxane SAMs have been used to pattern metal oxides such as Al_2O_3 and TiO_2 [1.33]. Reviews of ink/substrate combinations can be found in [1.34, 35]. There is now some interest in inks that are less specific to particular substrates [1.36].

1.2 μCP in microfabrication

μCP was initially intended as an alternative to photolithography in patterning sub-micrometer features [1.3]. In photolithography, the resolution is in practice approximately equal to the wavelength (λ) whilst, in μCP, the minimum feature size is ultimately limited by van der Waals contact, which is a sub-angstrom phenomenon [1.37]. In addition, μCP is compatible

with non planar surfaces and provides control over the chemistry of the patterned surfaces. In this section, μCP as a method of generating structures is examined.

1.2.1 Patterning of silicon by μCP of etch masks

Soon after the first demonstration of μCP [1.1], the metal layer patterned by μCP was transferred to the underlying Si substrate by wet etching [1.6, 38] and reactive ion etching (RIE) [1.39]. First, the metal layer is patterned by etching in a cyanide-based solution which attacks the exposed metal but not the SAM covered region. A detailed protocol is provided in Appendix A. The patterned metal is then used as a mask to pattern the underlying substrate. Either Au or Ag could be used as the metal masking layer with a KOH etchant for the wet process. With RIE, a Au/Ni masking layer was used and resolutions of 0.3μm have been achieved although the edge quality was poor. This two-step patterning is illustrated in Figure 1-4. Finnie *et al.* later demonstrated μCP of docosyltrichlorosilane on silicon and directly used the SAM as a mask for wet etching of Si(100) [1.40].

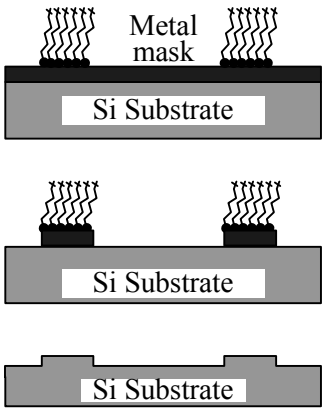


Figure 1-4 Si patterning by μCP of a metal masking layer. The metal layer is first contact printed and the unprotected area is etched off. The remaining metal is then used as a mask for KOH etching or RIE of the underlying Si.

1.2.2 Micro and nano-structuring by selective deposition on contact printed templates

μCP has also been used to pattern templates for additive structuring. One approach is to use the patterned monolayer as an inhibitor that prevents nucleation during chemical vapour deposition (CVD) [1.41] of Cu at 150 ^{o}C to 200 ^{o}C or atomic layer deposition [1.42]. Alternatively, the patterned monolayer can be used as a receptor; in [1.43], μCP with Pd(II) on a TiO_x layer is carried out and the Pd(II) catalyst is used for electroless deposition of copper. This is illustrated in Figure 1-5a, which describes the patterning by μCP followed by deposition, and Figure 1-5b, which shows an SEM of the deposited metal.

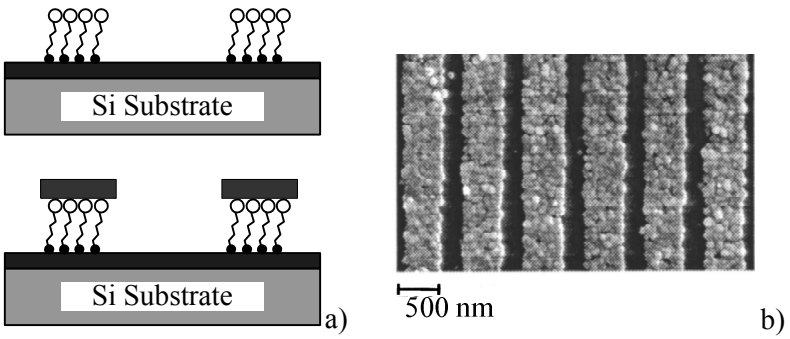


Figure 1-5 a) μCP to pattern templates for electroless deposition. After placement of the monolayer, the substrate is immersed in a copper containing solution. b) SEM of the deposited copper (from [1.43]).

Others have contact printed substrates with hydrophobic SAM and filled the empty area with hydrophilic SAM from solution. These substrates with well defined regions can then be used to guide the deposition of a magnetite suspension as in [1.44], and to control crystallisation [1.38], wetting [1.45], or condensation [1.46]. This approach is illustrated in Figure 1-6, highlighting the μCP, backfilling and selective deposition steps. Using this approach μCP can be used to pattern precursor layers for the growth of aligned carbon nanotubes, e.g. [1.47, 48].

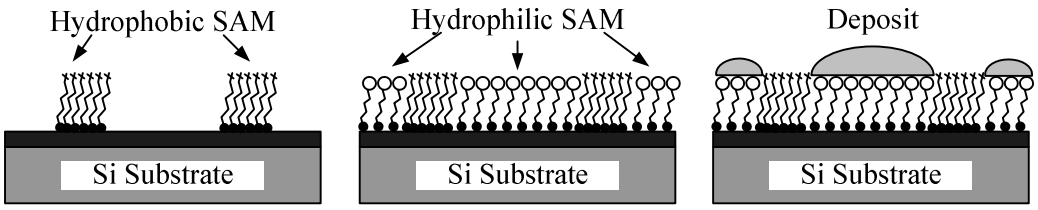


Figure 1-6 Templates with two SAMs for controlled deposition. First, a hydrophobic SAM is patterned by µCP (left). The unfilled area is covered with a hydrophilic SAM (middle) and finally, the targeted material is deposited (right) adsorbs onto the hydrophilic regions only.

1.2.3 µCP of non-planar substrates

Patterning of non-planar substrates is one of the strengths of µCP as it involves conformal contact of a soft compliant stamp. Photolithography, on the other hand, is limited by depth of focus and requires a constant separation across the entire area. In MEMS especially, patterning inside etched microstructures or slanted edges would be useful as demonstrated in [1.49]. Other 3D structures such as micro-coils [1.50] and free-standing micro-springs [1.51] have been made by µCP on an Au coated glass capillary. This was carried out by rolling the capillary on an inked PDMS stamp carrying parallel bar patterns. The capillary was etched to remove unprotected Au and then electroplated. The resulting devices are shown in Figure 1-7a and b.

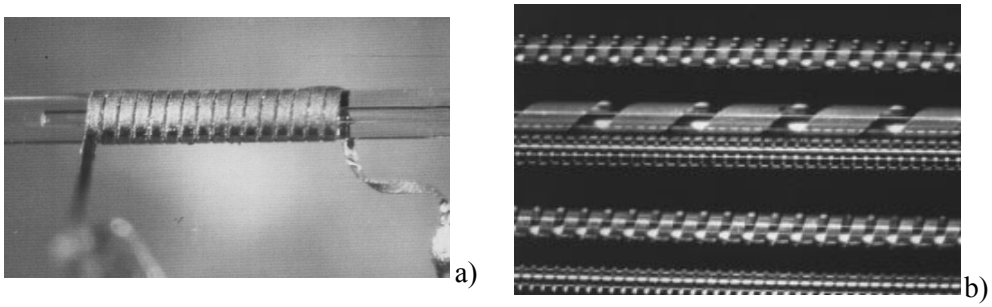


Figure 1-7 a) Micro-coil on glass capillary formed by µCP. b) Free-standing micro-spring. After electroplating, the cylindrical glass substrate is etched away to release the springs.

The ability to pattern micro-structured substrates also enables the fabrication of interesting devices. In [1.41], silicon posts are contact printed with a flat stamp (as shown in Figure 1-8a) and the deposited layer acts as a passivator in a subsequent CVD step. The vapour deposited Cu is thus only deposited on the sidewall and at the bottom of the channel as illustrated in Figure 1-8b. Alternatively, in [1.52], Si posts are coated with a precursor catalyst material that directs the growth of single walled nanotubes (SWNT) towards adjacent posts. This results in suspended SWNT held by Si posts that lie in a plane parallel to the substrate. Figure 1-8c shows the four patterned Si posts with suspended nanowires between them.

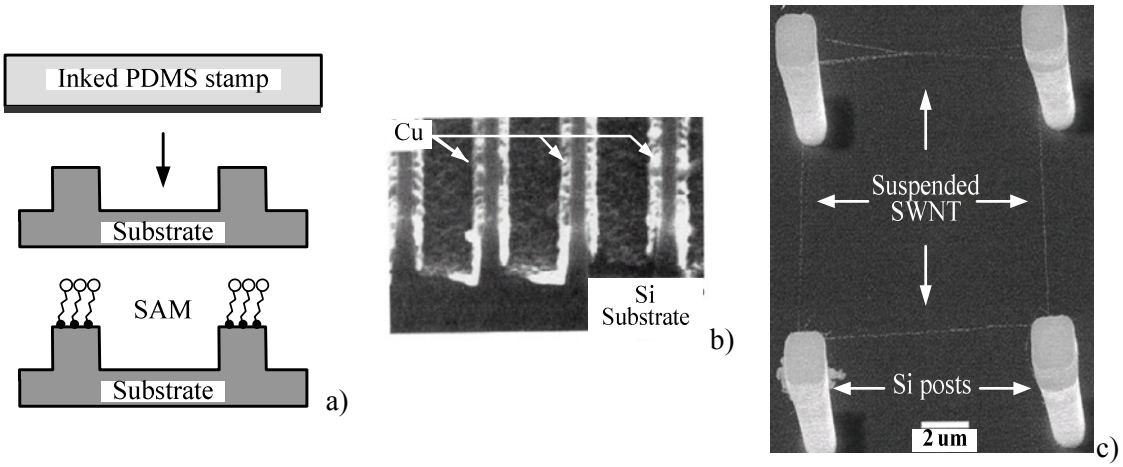


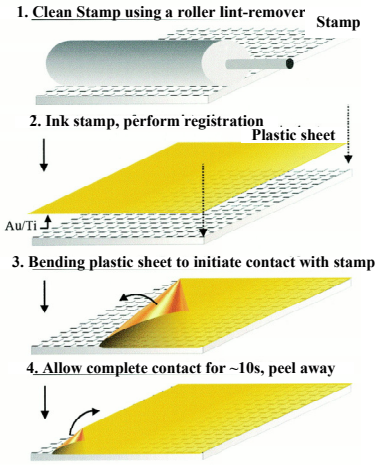
Figure 1-8 a) µCP on micro-structured Si. b) CVD resulting in Cu deposition on SAM-free region (trough and sidewalls)[1.41]. c) Catayltic growth resulting in suspended NT between Si posts [1.52].

1.2.4 Large area µCP for electronics

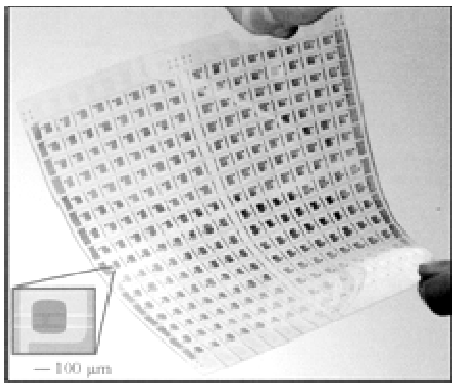
µCP was initially viewed as a potential replacement for conventional lithography and some, such as the IBM Zurich group [1.53], have made significant contributions to making µCP a truly high resolution commercial patterning method. Some of the proposed tools include modified bond aligners and rotary presses that allow µCP of 100 mm × 100 mm substrates. The former is hampered by an uncontrolled contact front and trapped air pockets, whilst the

latter exhibits higher pattern distortion due to the curvature. Burgin *et al.* [1.54] revisit the platen press approach and introduce an inflatable bladder that initiates contact whilst the printing is carried out in an evacuated chamber to solve the problem of trapped air pockets. Such approaches yield accuracies of > 12ppm [1.53], which is far from the challenging 1ppm accuracy required for microelectronics.

The focus of μCP has since shifted to defining circuit metallisation for flexible electronics (including organic) [1.55]. μCP is particularly suitable since it offers micrometer resolutions, large area patterning, resilience to defects, and compatibility to various materials as well as flexible substrates. The main challenge for commercializing μCP for large area electronics involves achieving reliable registration and control of the stamping process. A number of groups have already reached impressive milestones e.g. IBM [1.56], Philips [1.57, 58], or Lucent [1.59-61]. The tooling and stamps used in these cases is examined thoroughly in Section 1.4. A schematic depicting μCP on a flexible substrate is illustrated in Figure 1-9a and the completed electronic display formed from this method is shown in Figure 1-9b.



a)



b)

Figure 1-9 a) μCP on a thin plastic substrate. b) Completed circuit showing an array of TFT formed by μCP [1.60]

1.3 μCP in biology and biochemistry

Microbiological systems, with feature sizes > 50 μm, are well matched to the patterning possibilities offered by microfabrication [1.62-64]. downscaling down of sizes lead to improved heat and mass transfer, faster reactions, better resolutions, and smaller volumes of reagents. In addition, surface properties become increasingly important in determining the performance, especially for biological systems. SAMs have become indispensable for modelling and controlling biologically relevant surfaces, whilst μCP is suited to patterning with micrometer accuracy over large areas. In this section, some key applications and examples of biomolecular patterning with μCP are presented. Many other publications covering this interesting area are covered in the following reviews [1.63-66].

1.3.1 Patterning proteins and cells

Generating patterns of proteins and cells is important for biosensor technologies [1.67], tissue engineering, and fundamental studies of cell biology [1.66]. Protein microarrays allow analysis and screening of a large number of biomolecules [1.68, 69]. For these applications, controlled placement of biological ligands at well defined locations is required. Patterning methods include inkjet printing and μCP amongst others. Inkjet printing is a serial process and provides resolutions of ≈ 100 μm at best [1.70, 71]. μCP, on the other hand, is a parallel process allowing resolutions of ≈ 1 μm that enable, e.g., the study of single cells as opposed to populations of cells.

μCP of SAMs of alkanethiolates on Au or Ag provides model substrates for cell adhesion studies [1.72]. A typical method of generating such substrates is described next. μCP is first used to pattern a $–CH_3$ terminated monolayer. The underivatized substrate area is then covered with a different thiol terminated in ethylene glycol (EG), e.g.

$HS(CH_2)_{11}(OCH_2CH_2)_nOH(EG)_n$, with n = 2-7, by immersion in solution. The EG terminated regions prevent adhesion of proteins whilst the $–CH_3$ areas act as adhesive island. After monolayer patterning, fibronectin (FN) is incubated on the hydrophobic regions and the FN provides the extra cellular matrix (ECM) that supports the growth of bovine endothelial cells. The process is illustrated in Figure 1-10a. Figure 1-10b shows a population of bovine endothelial cells growing on patterned substrate. Such a method of directing cell adhesion and growth has been used to investigate cell motility [1.73]. Here, single fibroblast cells are grown on 900 μm^2 ECM scaffolds of different shapes and aspect ratios (see Figure 1-10c), and these experiments reveal that cells preferentially grow lamellipodia from their corners. In [1.74], patterned ECM were used to investigate the orientation and division axis of cells. Using the same scaffolding approach but with different SAMs, Yeo *et al*. [1.75] designed dynamic substrates that could sequentially release and attach cells in response to an applied electric potential. The SAM in this case contained an electroactive moiety, o-silyl hydroquinone, that releases attached cells when a voltage is applied.

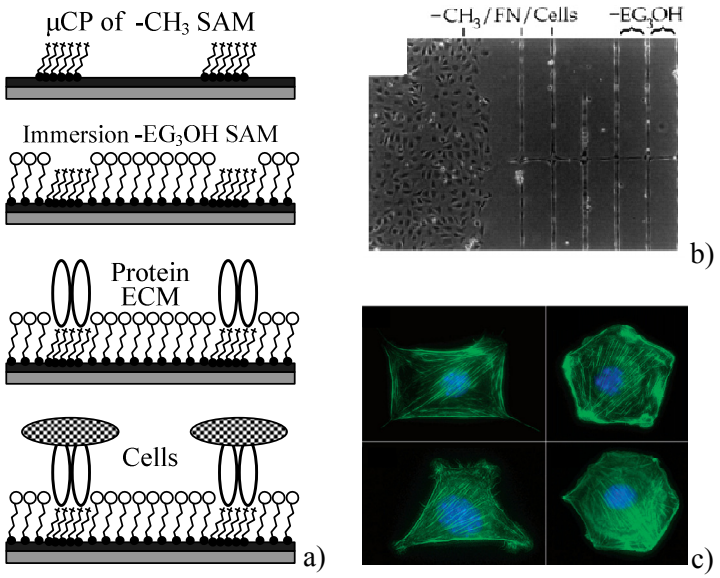


Figure 1-10 a) Scheme for localised cell binding via μCP of substrate. b) Bovine endothelial cells bound on $-CH_3$ features only. Fine lines are 10 μm wide [1.72]. c) Fluorescent images of fibroblast cells on ECM scaffolds of different shapes but same area (900 μm^2). Cells preferentially extend lamellipodia from corners [1.73].

In the method above, a SAM is first patterned and acts as a template for subsequent growth of cells. Direct patterning of proteins, where the protein solution itself is an ink, can also be achieved [1.76]. Poly(lysine) ink has been patterned on glass with millimetre resolutions. The PDMS stamp first had to be oxidised to adsorb the protein solution. Resolution was driven down to 1 μm [1.77]. Here, it was found that a solution of immunoglobulin (IgG) readily adsorbed to modified hydrophobic PDMS, and the IgG fully transferred onto glass, polysterene, or hydrophobic silicon. Features sizes of 100 nm have been obtained with conventional PDMS stamps by "subtractive" printing [1.53]. In this approach, a structured PDMS stamp is contacted to a flat substrate, which is homogeneously covered with a protein, and removed. The protein from the contacted areas is lifted off and remains on the relief features of the structured stamp, leading to a patterned substrate. These lifted molecules can be further used by printing onto another substrate.

Protein patterning is more useful in the form of arrays for screening multiple molecules in an analyte. In [1.78], printing of arrays of different proteins is achieved by using a microfluidic network to deliver inks to different areas of a flat stamp. The stamp is then brought into contact with the substrate and a single print produces a multi-ink pattern. This approach works for slow-diffusing protein solutions, unlike thiols or metallic ions, since they remain accurately positioned on the PDMS stamp. This is illustrated in Figure 1-11a. A similar approach where a silicon micro-fluidic chip with ink reservoirs and ink "wells" is used to deliver to a mating stamp is demonstrated in [1.79]. This approach is shown to pattern 36 spots of 100 μm diameter and is illustrated in Figure 1-11b. This method can be scaled to accommodate more inks and dots.

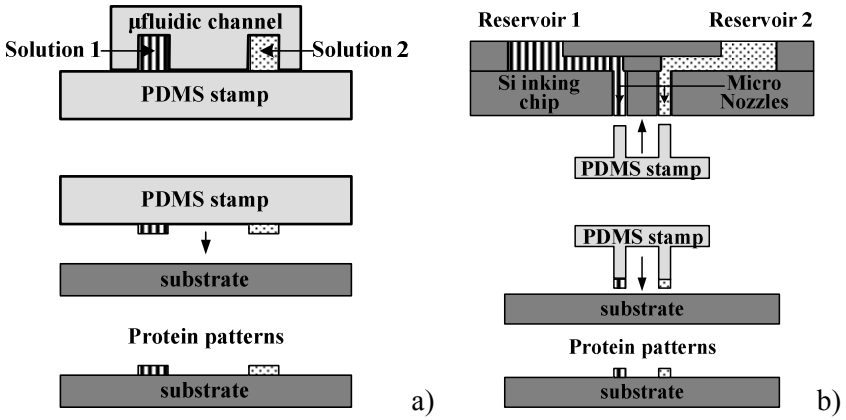


Figure 1-11 a) Micro-fluidic networks to ink a flat PDMS stamp for µCP. b) Microfabricated silicon inking chip for parallel inking.

1.3.2 µCP for *in vitro* studies of neurons

There is also significant interest in *in vitro* studies of neurons [1.80, 81] where SAMs are used to place neurons over the electrodes for reliable recording. The surface functionalization is carried out using µCP as above but with alignment to the readout electrodes. Currently, alignment is carried out using customized systems that combine 3-axis alignment stages with an optical microscope [1.82, 83] and localized binding to the electrodes can be achieved. A similar tool with load adjustment is presented in [1.84]. However, such setups are slow and cumbersome especially for multilevel printing. Also, alignment is only possible with transparent substrates. The alignment stage is illustrated in Figure 1-12a and an illustration of localised neuron binding on a patterned micro electrode array is shown in Figure 1-12b, where the dark features are the metallic electrodes.

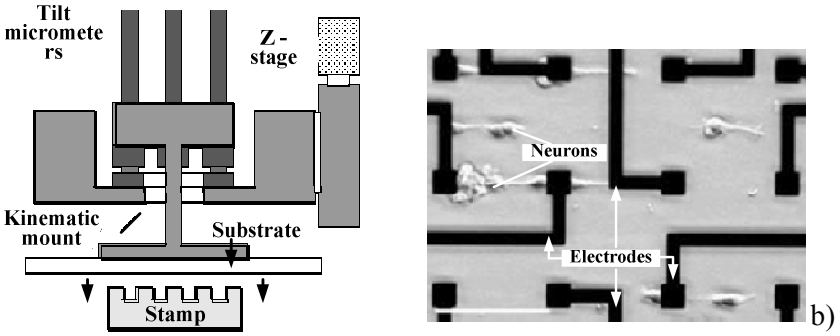


Figure 1-12 a) Alignment stage from [1.82]. b) Localised growth of hippocampal neurons on electrodes[1.83].

1.4 Limitations of μCP

Since the initial demonstration, μCP has remained conceptually the same although a wider range of inks and substrates can now be accommodated. Some additional variations to the original techniques, such as printing under water, are reviewed in [1.85]. The focus has also shifted from high resolution patterning for microfabrication to surface engineering templates for biochemical applications. A major hurdle, however, remains the mechanical stability of the soft elastomeric stamp, which makes registration and alignment difficult. The problem is compounded by the fact that the end-users are biochemists and biologists who have limited access to the expensive equipment available to the microfabrication community. In this section, the sources of deformation in PDMS and the problem of registration are examined. Techniques used by other groups to solve these problems are also presented.

1.4.1 Distortion of the stamp due to shrinkage on curing

PDMS stamps are typically thermally cured against silicon master. Severe distortions occur because PDMS and Si have significantly different coefficients of thermal expansion (C_{PDMS} = $3.1\times10^{-4}K^{-1}$ for PDMS and $C_{Si} = 2.6\times10^{-6}K^{-1}$ for Si, in a 1-dimensional case), and hence, during the casting step, the Si master expands much less than the polymer. Since the Si is much stiffer than PDMS, the polymer retains the dimensions of the Si and is effectively strained by $\varepsilon = C_{PDMS}(T_{CURING} - T_{ROOM})$ [1.86]. As soon as it is released, the stamp contracts by about 1.5% to a relaxed state (for a curing temperature of ≈100 ^{o}C). Whilst, lower temperature curing can used to minimize this, curing times then become prohibitively long, for example, with Sylgard 184, curing time at 25 ^{o}C is of the order of days [1.2]. Alternatively, the mask can be offset to compensate for the eventual contraction but this is restrictive as only a specific curing temperature and PDMS thickness are catered for. A solution would be to bond the PDMS device to a stiff support such as glass prior to releasing

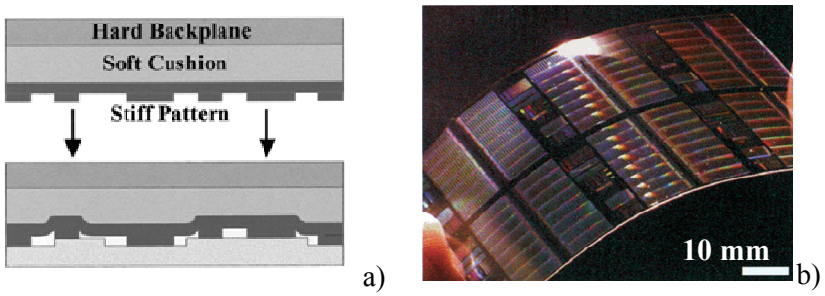
from the master. Demoulding then becomes problematic as the separation forces required may cause the substrate to break, especially if large areas are concerned. The use of a flexible but stiff backing layer such as an overhead transparency is shown to be a good solution [1.87].

1.4.2 Conformal contact and long range pattern accuracy.

With a Young's modulus of 1-2 MPa, PDMS stamps are almost always combined with a stiffer backing layer to facilitate handling and registration. As mentioned earlier, rigid layers are hard to separate, but in addition, as described in [1.88], the pressure (σ) required to bring two surfaces in contact is proportional to sum of the bulk modulus of the two layers and is given by $\sigma = \pi E^* \Delta/\lambda$, where λ is wavelength of sinusoidal roughness, Δ is the amplitude, and E^* is the bulk modulus and is given by $E^* = E_1/(1-\nu_1^2) + E_2/(1-\nu_2^2)$, where E is the Young's modulus and ν is the Poisson ratio, with the subscripts denoting the respective surfaces. Hence, with rigid surfaces, large controlled pressures may be required, which may cause the fine relief features to collapse. Moreover, whilst the combination of rigid layers with thin PDMS guarantees long range order and reduces thermal shrinkage [1.15, 89, 90], conformability to the substrate will be poor as the PDMS has less "margin" to adapt to the surface.

A solution in the form of tri-layer stamps is presented in [1.15]. These consist of a rigid backing like glass, a soft cushioning layer of Sylgard 184, and a hard layer of a stiffer (by a factor of 5-10) PDMS formulation (denoted h-PDMS) that carries the pattern (see Figure 1-13a). The soft PDMS allows the stamp to bend and conform to some extent, whilst the hard layer is able to carry and replicate fine 50 nm features [1.16]. This approach combines both the lateral stiffness required for stamp stability whilst preserving the ability to bend out of

plane and conform to the substrate. An improved version involves a thin bendable glass back plane (100 µm) with 75 µm thick Sylgard 184 or 30 µm h-PDMS stamp layer (see Figure 1-13b). Here, separation can be achieved more easily by peeling off.



a) b)

Figure 1-13 a) Trilayer stamp from [1.16]. b) Stamp with flexible glass backing [1.16].

1.4.3 Tools and techniques for large area alignment and printing

To increase the yield and repeatability of µCP, a number of groups have devised contact aligner type tools to provide improved mechanical control. In [1.54], a stamp aligner with alignment optics that carefully brings a glass backed stamp on contact with a substrate is demonstrated. For 3 inch substrates, a runout (feature to feature misalignment between the template and the stamp pattern) of 1 µm was obtained under optimum conditions and minimum feature size demonstrated was 500 nm.

In [1.56], IBM presents a different approach. Instead of a rigid back plane, a thin Invar sheet is used to provide the lateral stiffness whilst maintaining flexibility. Figure 1-14a shows the arrangement with the stamp initially held in a bent position just above the substrate by two motorised stages which are then carefully moved to unbend the stamp and make contact. Substrates of up to 15 square inches could be patterned with maximum distortions of ~3µm and average distortions of ~1µm.

Another ingenuous method has been developed by Philips and is briefly introduced in [1.57, 58]. It consists of a ~800 µm thick PDMS stamp mounted on a flexible 100 µm glass support. The latter provides in plane stability/rigidity whilst preserving the out of plane bendability. The PDMS-glass layer is held by vacuum to an array of grooves and each groove could be independently switched between vacuum and a mild pressure of 2 kPa, which would cause the stamp to deflect downwards by up to 150 µm. The stamp-air actuator array assembly would be brought in close proximity, 100 ±10 µm, to the substrate using a precision stage with alignment optics. The assembly is illustrated in Figure 1-14b. By serially switching on and off adjacent groups of grooves, localised regions are deflected and hence printed, and these local deflections are observed to travel like a wave across the entire stamp. 150 mm ×150 mm substrates have been patterned in this way with average distortions of 0.7 µm. Large open areas, usually prone to sagging, are successfully patterned due to the low contact pressure.

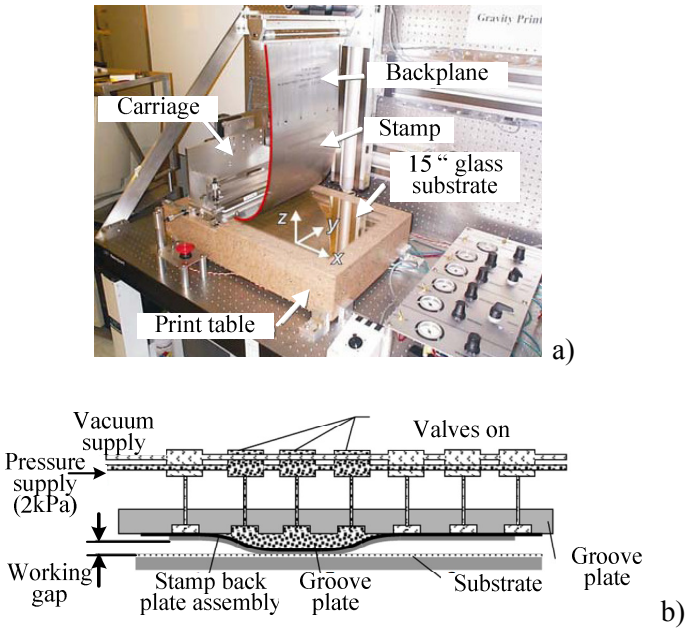


Figure 1-14 a) Flexible stamp by IBM [1.56]. In the image, the stamp (highlighted by a red line) is in a bent position and is not touching the stamp. b) Philips Wavemaker [1.57]. Valves sequentially switched on to cause contact of the stamp to substrate.

A commercial solution, the μ-CP 2.1 [1.91], has also recently been proposed by Gesim (Grosserkmannsdorf, Germany) and targets the biochemistry community . The latter combines a motorised *x-y* stage, alignment optics, and a PDMS stamp in the form of a diaphragm. This is illustrated in Figure 1-15. Contact is achieved by a combination of motorised vertical displacement and pneumatic actuation. The former brings the stamp holder close to the substrate while the latter ensures controlled contact to the substrate. The printable area is 10 mm × 10 mm, and stamps are injection moulded with a special mould that contains features that lock into the stamp holder tool. Positioning accuracy of 5μm is achievable with transparent substrates.

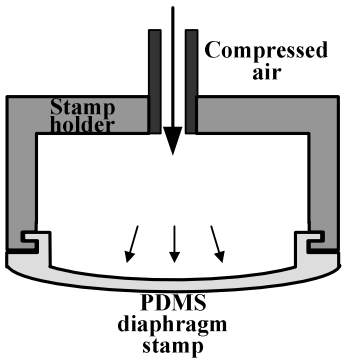


Figure 1-15 GeSiM μ-CP 2.1. PDMS diaphragm is attached to a stamp holder connected to an *x-y* stage. A linear *z* actuator brings the stamp close to the substrate. Pressure is applied to achieve contact with the substrate.

1.4.4 Mechanical stability of the relief features

The low modulus of PDMS also imposes certain restrictions on the feature resolution as well as aspect ratio. In terms of resolution, the commonly used Sylgard 184 formulation can only replicate features down to 500 nm in the best cases. A ten-fold improvement in resolution can

be obtained by using stiffer PDMS [1.15, 16], but there are still constraints in terms of aspect ratios.

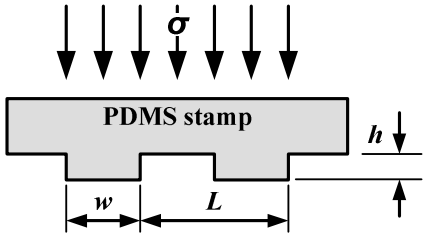


Figure 1-16 Generic PDMS stamp indicating relief feature dimensions. σ denotes the applied pressure.

In [1.92], Delamarche *et al.* conducted a limited experimental study of μCP with stamps having the same material properties, and feature width, *w*, but varying height, *h*. The stamp feature dimensions are illustrated in Figure 1-16. Too large *h/w* would lead to the post buckling/ falling under its own weight, and too low *h/w* would usually lead to the recessed regions sagging and making unwanted contact. This led to the design guideline of keeping *h/w* between 0.2 and 2 [1.3]. Also, too dense patterns (large *w/L*) combined with large *h/w* are prone to pairing up.

The issue of stamp deformation remained under scrutiny and in 2002, [1.93] Hui *et al.* provided a thorough theoretical framework for the dimensional stability of stamps in soft lithography. Their work was based on structures consisting of periodic bars of height *h*, width *w*, and separation between bars *L*. For μCP, the three main failure modes are: (i) buckling, which occurs when the bars are slender, i.e., $h>>w$, (ii) lateral collapse, which occurs when closely spaced slender bars stick together due to the high surface energy of PDMS relative to its stiffness, and (iii) roof collapse, $h<<w$, $w<<L$, which occurs when recessed regions come into contact with the substrate.

The first two failure modes, i.e. buckling and lateral collapse, are relatively easily avoided by choosing bars of suitable aspect ratios. Roof collapse, however, remains the most limiting failure mode [1.94]. For some skewed geometries where the bar height, h, is small, even without any loading, or even self weight, the roof regions may still contact the substrate due to the adhesion energy of the PDMS/substrate interface [1.95, 96].

For stamps with shallow posts and open areas, that is, $w<<L$, and $h<<w$, the maximum loading pressure sustainable before roof collapse is induced is given by [1.93], $\sigma_\infty < \pi E^* h/2L\cosh^{-1}(1/\sin(\pi w/2L))$, where $E^* = E/(1-\nu^2)$ is the bulk modulus, E is the Young's modulus, and ν is the Poisson ratio. In [1.97], this expression is verified experimentally for w/L=0.5 and varying h/L. In [1.94], various w/L ratios as well as different geometries, e.g. arrays of posts and comb structures, are considered and it is reported that for L/w<4, that expression overestimates the collapse pressures.

One way of circumventing these aspect ratio issues has been demonstrated by the Philips Wavemaker [1.57, 58] which minimises the contact pressures, but this solution is complicated albeit elegant. Another way seems to be the use of flexible backing polymers as demonstrated in [1.98]. The authors fabricate a multilayer stacked stamp consisting of 25 μm PDMS with the relief features, a 25 μm polyimide (PI) backing layer, followed by a further two layers of PDMS (60 μm) and PI (25 μm). The robustness is illustrated with patterns of 60μm wide bars with 60μm spacing, and a height of 500nm; a single layer PDMS stamp undergoes roof collapse whereas the stacked stamp replicates the features accurately.

1.5 Alternative methods of patterning SAMs

In addition to μCP, other methods of patterning SAMs have been investigated. Inkjet printing [1.70, 71] has been shown to generate high quality patterns for features above 100 μm. Subtractive patterning by "writing" on thiol coated Au substrate with a laser beam can generate features with similar dimensions [1.99]. Electron beams have been used in a similar manner to generate patterns 25 nm wide [1.100]. Another method which has had more success is dip-pen nanolithography (DPN), which is an AFM based technique where the tip is coated with an ink and brought close to the substrate [1.101]. Condensation of water at the tip-substrate interface then channels the molecules to the substrate. The width of the dot can be varied through the contact time with the substrate. In the case of a line, the rastering speed determines the line width. This is illustrated in Figure 1-17a. Resolutions down to 15 nm have been achieved and a variety of substrates can be patterned with different inks. In addition to writing, the AFM tip can be used to chemically, electrically or mechanically induce desorption of a SAM with similar resolutions.

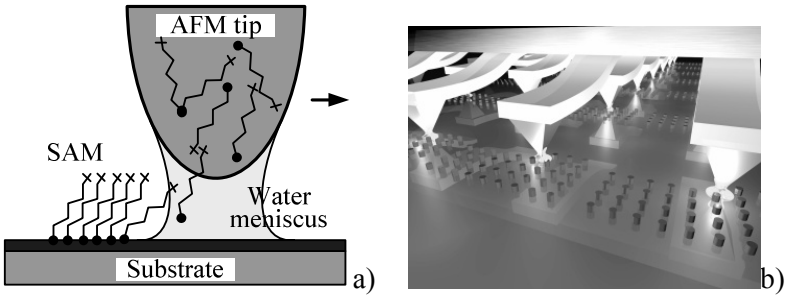


Figure 1-17 a) Writing patterns of SAM by dip-pen nanolithography (DPN). It is generally accepted that a water meniscus at the tip-substrate interface transports the molecules. b) Illustration of an 2d array of cantilevers for parallel DPN [1.102].

Unlike μCP, the above methods are serial processes and are therefore inherently slow. Inkjet printing, however, is relatively cheap although the resolution is poor. Laser patterning comes

with a large overhead cost, while DPN is limited to small areas due to the short travel range of the positioning actuators (typically ≈ 100 μm). Yet, DPN is the SAM patterning method that has had the most success and it is being commercialised by NanoInk (IL, USA) [1.103]. One reason for its success is that the underlying technology (cantilever fabrication, *x-y-z* piezo-actuators for positioning of the tip, tip deflection sensing and control, etc.) is already well understood from the development of the AFM [1.104]. The main limitation of DPN is its speed and small area, but this issue is being addressed with parallel DPN arrays which carry multiple tips (Figure 1-17b). Such a method is reported in [1.102] where a 1 cm^2 area is patterned with 80nm dots using a parallel system with 55000 cantilever tips.

A parallel large area alternative to μCP is photochemistry using deep-UV (see e.g. [1.105]). Here a photosensitive SAM is exposed through a mask. The irradiated regions then become amenable to subsequent remodification. This approach is like conventional lithography except that a SAM is used instead of thicker photoresist thus alleviating issues such as depth of focus or standing wave formation. However, this method involves significant overhead and high cost of ownership especially for biologists.

Reliable methods of patterning SAM have been presented above but none combine simplicity with functionality as elegantly as μCP. Yet, inkjet and DPN have proven to be more accessible as ancillary tools are already available. Analogous systems for μCP have been developed but remain problematic, expensive, or complicated. There is therefore a clear need for simple low cost stand-alone tools for μCP.

1.6 Research objectives

In sections 1.2-1.5, the area of μCP has been reviewed. The applications are far-ranging and include fabrication of exotic devices, sensitisation of sensors, and the generation of templates for probing bio-molecules in novel ways. Yet there is still a need for tools that enable reliable aligning, handling and actuation of the stamp. Solutions have been proposed (see Section 1.4.3) but most would be deemed too expensive and inaccessible by the biochemistry community. Based on the above review, the following design aims for a μCP engine can be formulated.

- The device should require minimal overhead equipment (e.g. optical alignment tools) to operate.
- Compatibility with common "inks" such as alkanethiol is needed. Hence, the stamp needs to be made of the well established PDMS.
- Multilevel printing with different inks without cross-contamination is required. Therefore, a reliable inking and aligning system is needed.
- Stamps can be re-used, but cannot be completely cleaned of ink, so a single ink per stamp approach is favoured. Hence, the solution must be low cost.
- The device should have a high in-plane modulus to ensure accurate registration, but still allow conformal contact to the substrate.
- The ability of μCP to quickly pattern large areas should be preserved. However, contact and separation forces scale with area and this criterion will be challenging to meet.
- A controlled actuation mechanism that enables contact and separation of the stamp to and from the substrate is required.

1.6.1 MEMS and its suitability for µCP

MEMS technology has the potential to meet most of the objectives specified. Already, PDMS stamps are made by casting against masters fabricated by MEMS microfabrication techniques, and methods of further exploiting microsystems technology need to be explored.

MEMS microfabrication technology has evolved considerably since Petersen published his seminal paper [1.106] which first introduced silicon as a mechanical material and a comprehensive review is presented by Madou in [1.107]. A key early development was the discovery of anisotropic etching down (111) planes of crystalline silicon [1.108], and such a machined structure is shown in Figure 1-18. The latter shows inverted pyramids with a sidewall angle of 54.7^{o}. Further details regarding the anisotropic etch and possible applications for the slanted structure are provided in Chapter 3.

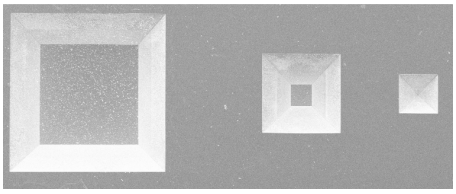


Figure 1-18 SEM of inverted pyramids (V-grooves) formed in Si(100) by anisotropic etching. The largest feature is 400 µm long.

New techniques such as deep reactive ion etching (DRIE) [1.109], have vastly increased capabilities, allowing robust high-aspect ratio (HAR) features to be formed in multi-layers without restrictions from crystal orientation. An example of such structures is illustrated in Figure 1-19 which shows 5 µm-wide and 25 µm-deep trenches formed in Si. The inset highlights the sidewall roughness which is due to the cyclic etching and passivation steps of the DRIE process [1.110, 111]. DRIE can also be combined with bonded-silicon-on-insulator

(BSOI) wafers to form suspended HAR structures. BSOI is a multilayer material obtained by fusing a thermally oxidised silicon wafer to another silicon wafer, which is subsequently polished back to the desired thickness [1.112]. The mechanical structures are formed in the Si layer by DRIE and are released by etching the buried oxide layer (see e.g. [1.113, 114]).

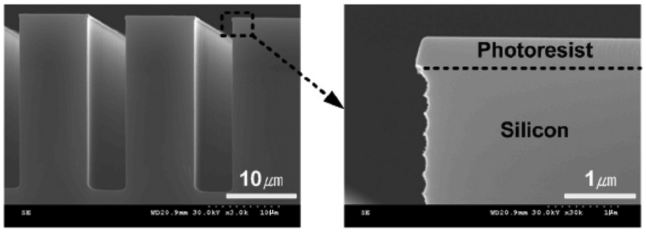


Figure 1-19 SEM of trenches in Si formed by DRIE. the inset highlights the scalloping sidewalls. (from [1.111])

A wide range of micro-actuators has also been developed (see e.g. [1.115]); these typically combine an elastic suspension with an electrostatic, electrothermal, electromagnetic or piezoelectric drive. These actuation mechanisms and their compatibility with a μCP engine will be discussed further in Chapter 3.

Early examples of commercially successful MEMS systems include integrated inertial sensors by Analog Devices. These was initially designed for the automotive industry [1.116] but the technology used to fabricated shock sensors has been adapted to make miniaturised gyroscopes [1.117, 118], which find applications in a number of popular consumer products such as games consoles and mobile phones. In fact, a recent report by iSuppli Corp predicts that the MEMS market will grow to $8.8 billion in 2012 and this growth will be driven by the increased demand for inertial sensors in mobile phones [1.119]. Examples of an accelerometer and a vibrating ring gyroscope are shown in Figure 1-20. The former is z-oriented and employs capacitive sensing, whilst the latter is operated in vibrational mode with

driving and sensing electrodes. A review of micro-gyroscope architectures and their performances is provided in [1.117].

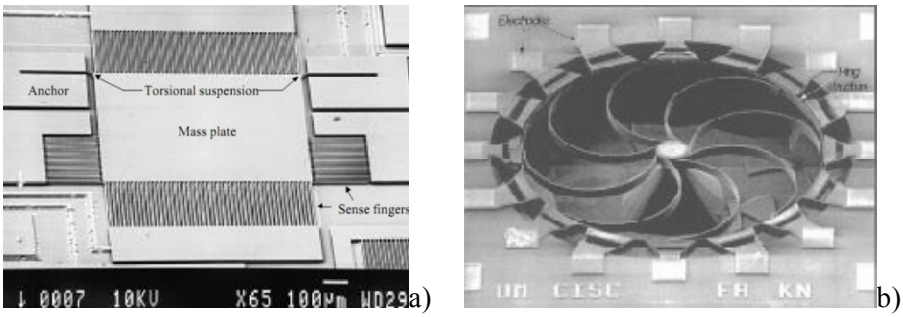
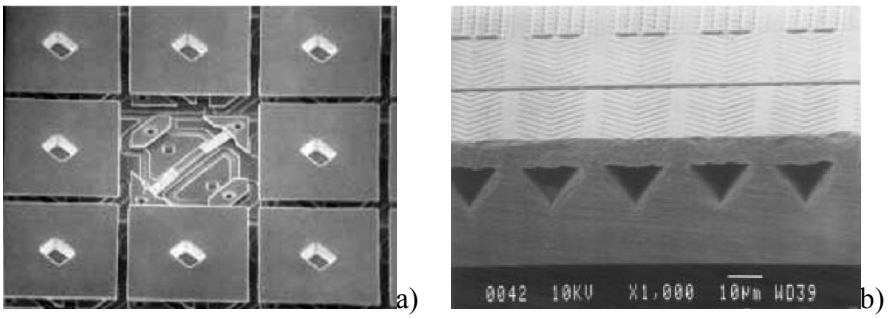


Figure 1-20 SEM of a) single axis accelerometer with capacitive sensing, b) vibrating ring gyroscope formed by deep etching of polysilicon. Images are from [1.118].

Another example of commercially successful MEMS is the Digital Light Processor (DLP) of Texas Instruments [1.120, 121] which is used in projection displays. The latter consists of an array of individually addressable $10 \times 10\ \mu m^2$ micro-mirrors which can be actuated to the correct angle to form an image on a projection screen. Figure 1-21a shows an array of micro-mirrors used in the DLP. The mirror in the central cell is removed to reveal the hinges that allow the micro-mirror to tilt. Silicon microtechnology is also widely available commercially in the form of micromachined ink-jet printer nozzles, which can be packed densely enough to allow high resolution printing. MEMS actuation principles such as piezoelectric, thermal [1.122], or electrostatic [1.123] can be used to eject tiny droplets. Figure 1-21b shows an array of such nozzles fabricated by bulk etching and driven with integrated polysilicon heaters.

Apart from the above examples, other MEMS devices exist and can be categorised as optical, radio frequency (RF), and bio-MEMS amongst others. Optical MEMS typically aims to monolithically integrate optics, electronics and mechanics, or to provide tuneable optical

components with improved efficiency (see e.g. [1.124]). RF MEMS concerns the development of circuit components for high frequency operation with enhanced performance and tuneability (see e.g. [1.125]). The final category, bio-MEMS, is closely related to μTAS and encompasses the use of MEMS for biochemical analysis and detection, clinical intervention, or fundamental biological studies. An introduction to the field is given by Wang and Soper in [1.126].



a) b)

Figure 1-21 SEM of a) micro-mirror array from Texas Instruments, b) an ink jet nozzle array from [1.122]

This dissertation lies within the category of bio-MEMS and aims to enable multi-level μCP using an accessible and low-cost solution. MEMS technology will be used to integrate mechanical features, such as a flexure suspension, an actuation mechanism and alignment features, together with a soft PDMS stamp to form complete miniature μCP engines. Although one of the strengths of μCP is large area patterning, the contact area will initially be restricted to a few mm^2 due to unfavourable scaling of contact and separation forces.

1.6.2 Thesis structure

In this chapter, the subject of μCP was reviewed, its technological importance demonstrated, and unsolved problems in the area identified. This background study enabled the formulation of research objectives and design aims. In Chapter 2, the fabrication of a PDMS stamp is

investigated and its integration into a MEMS process flow is considered. A novel solution, whose applications include, but are not limited to, stamps for μCP, is presented. In Chapter 3, the design, fabrication and characterisation a silicon μCP engine is presented. In Chapter 4, the feasibility of electrostatic actuation of the silicon μCP engine is analysed and results are presented. Electrostatically-driven μCP in general is discussed. Chapter 5 presents a low cost disposable replica-moulded miniature polymer μCP engine. Multilevel printing is demonstrated and alignment data is presented. In Chapter 6, the approach of Chapter 5 is combined with a hydraulic actuation mechanism. Finally, conclusions are presented in Chapter 7.

1.7 References

[1.1] A. Kumar and G. M. Whitesides, "Features of gold having micrometer to centimeter dimensions can be formed through a combination of stamping with an elastomeric stamp and an alkanethiol ``ink" followed by chemical etching," *Appl. Phys. Lett.,* vol. 63, pp. 2002-2004, 1993.

[1.2] DowCorningCorporation, "Product Information: Sylgard 184 Silicone elastomer." vol. Form 10-898F-01.

[1.3] Y. Xia and G. M. Whitesides, "Soft Lithography," *Angew. Chem. Int. Ed.,* vol. 37, pp. 550-575, 1998.

[1.4] K. M. Choi and J. A. Rogers, "A Photocurable Poly(dimethylsiloxane) Chemistry Designed for Soft Lithographic Molding and Printing in the Nanometer Regime," *J. Am. Chem. Soc.,* vol. 125, pp. 4060-4061, 2003.

[1.5] J. N. Lee, C. Park, and G. M. Whitesides, "Solvent Compatibility of Poly(dimethylsiloxane)-Based Microfluidic Devices," *Anal. Chem.,* vol. 75, pp. 6544-6554, 2003.

[1.6] Y. Xia, X.-M. Zhao, and G. M. Whitesides, "Pattern transfer: self-assembled monolayers as ultrathin resists," *Microelectron. Eng.,* vol. 32, pp. 255-268, 1996.

[1.7] E. Delamarche, C. Donzel, F. S. Kamounah, H. Wolf, M. Geissler, R. Stutz, P. Schmidt-Winkel, B. Michel, H. J. Mathieu, and K. Schaumburg, "Microcontact Printing Using Poly(dimethylsiloxane) Stamps Hydrophilized by Poly(ethylene oxide) Silanes," *Langmuir,* vol. 19, pp. 8749-8758, 2003.

[1.8] R. B. A. Sharpe, D. Burdinski, J. Huskens, H. J. W. Zandvliet, D. N. Reinhoudt, and B. Poelsema, "Chemically Patterned Flat Stamps for Microcontact Printing," *J. Am. Chem. Soc.,* vol. 127, pp. 10344-10349, 2005.

[1.9] H. Makamba, J. H. Kim, K. Lim, N. Park, and J. H. Hahn, "Surface modification of poly(dimethylsiloxane) microchannels," *Electrophoresis,* vol. 24, pp. 3607-3619, 2003.

[1.10] M. J. Owen and P. J. Smith, "Plasma treatment of polydimethylsiloxane," *J. Adhes. Sci. Tech.,* vol. 8, pp. 1063-1075, 1994.

[1.11] S. Bhattacharya, A. Datta, J. M. Berg, and S. Gangopadhyay, "Studies on surface wettability of poly(dimethyl) siloxane (PDMS) and glass under oxygen-plasma treatment and correlation with bond strength," *J. Microelectromech. Syst.,* vol. 14, pp. 590-597, 2005.

[1.12] B. H. Jo, L. M. Van Lerberghe, K. M. Motsegood, and D. J. Beebe, "Three-dimensional micro-channel fabrication in polydimethylsiloxane (PDMS) elastomer," *J. Microelectromech. Syst.,* vol. 9, pp. 76-81, 2000.

[1.13] J. C. McDonald, D. C. Duffy, J. R. Anderson, D. T. Chiu, H. Wu, O. J. A. Schueller, and G. M. Whitesides, "Fabrication of microfluidic systems in poly(dimethylsiloxane)," *Electrophoresis,* vol. 21, pp. 27-40, 2000.

[1.14] E. Delamarche, H. Schmid, B. Michel, and H. Biebuyck, "Stability of molded polydimethylsiloxane microstructures," *Adv. Mater.,* vol. 9, pp. 741-746, 1997.

[1.15] H. Schmid and B. Michel, "Siloxane Polymers for High-Resolution, High-Accuracy Soft Lithography," *Macromolecules,* vol. 33, pp. 3042-3049, 2000.

[1.16] T. W. Odom, J. C. Love, D. B. Wolfe, K. E. Paul, and G. M. Whitesides, "Improved Pattern Transfer in Soft Lithography Using Composite Stamps," *Langmuir,* vol. 18, pp. 5314-5320, 2002.

[1.17] C. D. Bain, E. B. Troughton, Y. T. Tao, J. Evall, G. M. Whitesides, and R. G. Nuzzo, "Formation of monolayer films by the spontaneous assembly of organic thiols from solution onto gold," *J. Am. Chem. Soc.,* vol. 111, pp. 321-335, 1989.
[1.18] E. B. Troughton, C. D. Bain, G. M. Whitesides, R. G. Nuzzo, D. L. Allara, and M. D. Porter, "Monolayer films prepared by the spontaneous self-assembly of symmetrical and unsymmetrical dialkyl sulfides from solution onto gold substrates: structure, properties, and reactivity of constituent functional groups," *Langmuir,* vol. 4, pp. 365-385, 1988.
[1.19] M. D. Porter, T. B. Bright, D. L. Allara, and C. E. D. Chidsey, "Spontaneously organized molecular assemblies. 4. Structural characterization of n-alkyl thiol monolayers on gold by optical ellipsometry, infrared spectroscopy, and electrochemistry," *J. Am. Chem. Soc.,* vol. 109, pp. 3559-3568, 1987.
[1.20] G. E. Poirier and E. D. Pylant, "The Self-Assembly Mechanism of Alkanethiols on Au(111)," *Science,* vol. 272, pp. 1145-1148, May 24, 1996 1996.
[1.21] G. E. Poirier, "Mechanism of Formation of Au Vacancy Islands in Alkanethiol Monolayers on Au(111)," *Langmuir,* vol. 13, pp. 2019-2026, 1997.
[1.22] D. K. Schwartz, "Mechanisms and kinetics of self-assembled monolayer formation," *Annu. Rev. Phys. Chem.,* vol. 52, pp. 107-137, 2001.
[1.23] N. B. Larsen, H. Biebuyck, E. Delamarche, and B. Michel, "Order in Microcontact Printed Self-Assembled Monolayers," *J. Am. Chem. Soc.,* vol. 119, pp. 3017-3026, 1997.
[1.24] T. E. Balmer, H. Schmid, R. Stutz, E. Delamarche, B. Michel, N. D. Spencer, and H. Wolf, "Diffusion of Alkanethiols in PDMS and Its Implications on Microcontact Printing," *Langmuir,* vol. 21, pp. 622-632, 2005.
[1.25] R. B. Bass and A. W. Lichtenberger, "Microcontact printing with octadecanethiol," *Appl. Surf. Sci.,* vol. 226, pp. 335-340, 2004.
[1.26] Y. Xia, E. Kim, and G. M. Whitesides, "Microcontact Printing of Alkanethiols on Silver and Its Application in Microfabrication," *J. Electrochem. Soc.,* vol. 143, pp. 1070-1079, 1996.
[1.27] Y. Xia, E. Kim, M. Mrksich, and G. M. Whitesides, "Microcontact Printing of Alkanethiols on Copper and Its Application in Microfabrication," *Chem. Mat.,* vol. 8, pp. 601-603, 1996.
[1.28] J. C. Love, D. B. Wolfe, R. Haasch, M. L. Chabinyc, K. E. Paul, G. M. Whitesides, and R. G. Nuzzo, "Formation and Structure of Self-Assembled Monolayers of Alkanethiolates on Palladium," *J. Am. Chem. Soc.,* vol. 125, pp. 2597-2609, 2003.
[1.29] L. B. Goetting, T. Deng, and G. M. Whitesides, "Microcontact Printing of Alkanephosphonic Acids on Aluminum & Pattern Transfer by Wet Chemical Etching," *Langmuir,* vol. 15, pp. 1182-1191, 1999.
[1.30] T. L. Breen, P. M. Fryer, R. W. Nunes, and M. E. Rothwell, "Patterning Indium Tin Oxide and Indium Zinc Oxide Using Microcontact Printing and Wet Etching," *Langmuir,* vol. 18, pp. 194-197, 2002.
[1.31] D. Wang, S. G. Thomas, K. L. Wang, Y. Xia, and G. M. Whitesides, "Nanometer scale patterning and pattern transfer on amorphous Si, crystalline Si, and SiO surfaces using self-assembled monolayers," *Appl. Phys. Lett.,* vol. 70, pp. 1593-1595, 1997.
[1.32] Y. Jun, D. Le, and X. Y. Zhu, "Microcontact Printing Directly on the Silicon Surface," *Langmuir,* vol. 18, pp. 3415-3417, 2002.
[1.33] P. M. St John and H. G. Craighead, "Microcontact printing and pattern transfer using trichlorosilanes on oxide substrates," *Appl. Phys. Lett.,* vol. 68, pp. 1022-1024, 1996.

[1.34] J. C. Love, L. A. Estroff, J. K. Kriebel, R. G. Nuzzo, and G. M. Whitesides, "Self-Assembled Monolayers of Thiolates on Metals as a Form of Nanotechnology," *ChemInform,* vol. 36, 2005.
[1.35] R. K. Smith, P. A. Lewis, and P. S. Weiss, "Patterning self-assembled monolayers," *Progr. Surf. Sci.,* vol. 75, pp. 1-68, 2004.
[1.36] D. Burdinski, M. Saalmink, J. P. W. G. v. d. Berg, and C. v. d. Marel, "Universal Ink for Microcontact Printing," *Angew. Chem. Int. Ed.,* vol. 45, pp. 4355-4358, 2006.
[1.37] P. S. Weiss, "A Conversation with Prof. George Whitesides: Pioneer in Soft Nanolithography," *ACS Nano,* vol. 1, pp. 73-78, 2007.
[1.38] A. Kumar, H. A. Biebuyck, and G. M. Whitesides, "Patterning Self-Assembled Monolayers: Applications in Materials Science," *Langmuir,* vol. 10, pp. 1498-1511, 1994.
[1.39] T. K. Whidden, D. K. Ferry, M. N. Kozicki, E. Kim, A. Kumar, J. Wilbur, and G. M. Whitesides, "Pattern transfer to silicon by microcontact printing and RIE," *Nanotechnology,* p. 447, 1996.
[1.40] K. R. Finnie, R. Haasch, and R. G. Nuzzo, "Formation and Patterning of Self-Assembled Monolayers Derived from Long-Chain Organosilicon Amphiphiles and Their Use as Templates in Materials Microfabrication," *Langmuir,* vol. 16, pp. 6968-6976, 2000.
[1.41] N. L. Jeon, R. G. Nuzzo, Y. Xia, M. Mrksich, and G. M. Whitesides, "Patterned self-assembled monolayers formed by microcontact printing direct selective metalization by chemical vapor deposition on planar and nonplanar substrates," *Langmuir,* vol. 11, pp. 3024-3026, 1995.
[1.42] M. H. Park, Y. J. Jang, H. M. Sung-Suh, and M. M. Sung, "Selective Atomic Layer Deposition of Titanium Oxide on Patterned Self-Assembled Monolayers Formed by Microcontact Printing," *Langmuir,* vol. 20, pp. 2257-2260, 2004.
[1.43] H. Kind, M. Geissler, H. Schmid, B. Michel, K. Kern, and E. Delamarche, "Patterned Electroless Deposition of Copper by Microcontact Printing Palladium(II) Complexes on Titanium-Covered Surfaces," *Langmuir,* vol. 16, pp. 6367-6373, 2000.
[1.44] S. Palacin, P. C. Hidber, J.-P. Bourgoin, C. Miramond, C. Fermon, and G. M. Whitesides, "Patterning with Magnetic Materials at the Micron Scale," *Chem. Mat.,* vol. 8, pp. 1316-1325, 1996.
[1.45] H. A. Biebuyck and G. M. Whitesides, "Self-Organization of Organic Liquids on Patterned Self-Assembled Monolayers of Alkanethiolates on Gold," *Langmuir,* vol. 10, pp. 2790-2793, 1994.
[1.46] G. P. Lopez, H. A. Biebuyck, C. D. Frisbie, and G. M. Whitesides, "Imaging of features on surfaces by condensation figures," *Science,* vol. 260, pp. 647-649, April 30, 1993 1993.
[1.47] H. Kind, J.-M. Bonard, L. s. ForrÃ³, K. Kern, K. Hernadi, L.-O. Nilsson, and L. Schlapbach, "Printing Gel-like Catalysts for the Directed Growth of Multiwall Carbon Nanotubes," *Langmuir,* vol. 16, pp. 6877-6883, 2000.
[1.48] S. Huang and A. W. H. Mau, "Selective Growth of Aligned Carbon Nanotubes on a Silver-Patterned Substrate by the Silver Mirror Reaction," *J. Phys. Chem. B,* vol. 107, pp. 3455-3458, 2003.
[1.49] A. Folch and M. A. Schmidt, "Wafer-level in-registry microstamping," *J. Microelectromech. Syst.,* vol. 8, pp. 85-89, 1999.
[1.50] J. A. Rogers, R. J. Jackman, and G. M. Whitesides, "Constructing single- and multiple-helical microcoils and characterizing their performance as components of microinductors and microelectromagnets," *J. Microelectromech. Syst.,* vol. 6, pp. 184-192, 1997.

[1.51] J. A. Rogers, R. J. Jackman, and G. M. Whitesides, "Microcontact printing and electroplating on curved substrates: Production of free-standing three-dimensional metallic microstructures," *Adv. Mater.,* vol. 9, pp. 475-477, 1997.
[1.52] A. M. Cassell, N. R. Franklin, T. W. Tombler, E. M. Chan, J. Han, and H. Dai, "Directed Growth of Free-StandingSingle-Walled Carbon Nanotubes," *J. Am. Chem. Soc.,* vol. 121, pp. 7975-7976, 1999.
[1.53] B. Michel, A. Bernard, A. Bietsch, E. Delamarche, M. Geissler, D. Juncker, H. Kind, J.-P. Renault, H. Rothuizen, H. Schmid, P. Schmidt-Winkel, R. Stutz, and H. Wolf, "Printing meets lithography: Soft approaches to high-resolution patterning," *IBM J. Res. Dev.,* vol. 45, 2001.
[1.54] T. Burgin, V. E. Choong, and G. Maracas, "Large Area Submicrometer Contact Printing Using a Contact Aligner," *Langmuir,* vol. 16, pp. 5371-5375, 2000.
[1.55] J. A. Rogers and R. G. Nuzzo, "Recent progress in soft lithography," *Materials Today,* vol. 8, pp. 50-56, 2005.
[1.56] E. Delamarche, J. Vichiconti, S. A. Hall, M. Geissler, W. Graham, B. Michel, and R. Nunes, "Electroless Deposition of Cu on Glass and Patterning with Microcontact Printing," *Langmuir,* vol. 19, pp. 6567-6569, 2003.
[1.57] M. M. J. Decre, R. M. Schneider, D. Burdinski, J. Schellekens, M. Saalmink, and R. Dona, "Wave Printing (I) : Towards Large-Area, Multilayer Microcontact Printing," *Mater. Res. Soc. Symp. Proc. Vol. EXS-2,* vol. M4, p. 9, 2004.
[1.58] J. Schellekens, D. Burdinski, M. Saalmink, M. Beenhakkers, G. Gelinck, and M. M. J. Decre, "Wave Printing (II): Polymer MISFETs Using Microcontact Printing," *Mater. Res. Soc. Symp. Proc. Vol. EXS-2,* vol. M2, p. 9, 2004.
[1.59] J. A. Rogers, "Toward Paperlike Displays," *Science,* vol. 291, pp. 1502-1503, 2001.
[1.60] J. A. Rogers, Z. Bao, K. Baldwin, A. Dodabalapur, B. Crone, V. R. Raju, V. Kuck, H. Katz, K. Amundson, J. Ewing, and P. Drzaic, "Paper-like electronic displays: Large-area rubber-stamped plastic sheets of electronics and microencapsulated electrophoretic inks," *Proc. Natl. Acad. Sci.,* vol. 98, pp. 4835-4840, 2001.
[1.61] J. A. Rogers, Z. Bao, A. Makhija, and P. Braun, "Printing Process Suitable for Reel-to-Reel Production of High-Performance Organic Transistors and Circuits," *Adv. Mater.,* vol. 11, pp. 741-745, 1999.
[1.62] D. J. Harrison, K. Fluri, K. Seiler, Z. Fan, C. S. Effenhauser, and A. Manz, "Micromachining a Miniaturized Capillary Electrophoresis-Based Chemical Analysis System on a Chip," *Science,* vol. 261, pp. 895-897, 1993.
[1.63] D. B. Weibel, W. R. DiLuzio, and G. M. Whitesides, "Microfabrication meets microbiology," *Nat Rev Micro,* vol. 5, pp. 209-218, 2007.
[1.64] G. M. Whitesides, E. Ostuni, S. Takayama, X. Jiang, and D. E. Ingber, "Soft Lithography In Biology And Biochemistry," *Ann. Biomed. Eng.,* vol. 3, pp. 335-373, 2001.
[1.65] J. C. Love, L. A. Estroff, J. K. Kriebel, R. G. Nuzzo, and G. M. Whitesides, "Self-Assembled Monolayers of Thiolates on Metals as a Form of Nanotechnology," *Chemical Reviews,* vol. 105, pp. 1103-1170, 2005.
[1.66] R. S. Kane, S. Takayama, E. Ostuni, D. E. Ingber, and G. M. Whitesides, "Patterning proteins and cells using soft lithography," *Biomaterials,* vol. 20, pp. 2363-2376, 1999.
[1.67] M. Mrksich and G. M. Whitesides, "Patterning self-assembled monolayers using microcontact printing: A new technology for biosensors?," *Trends Biotechnol.,* vol. 13, pp. 228-235, 1995.
[1.68] P. Bertone and M. Snyder, "Advances in functional protein microarray technology," *FEBS Journal,* vol. 272, pp. 5400-5411, 2005.

[1.69] G. MacBeath and S. L. Schreiber, "Printing Proteins as Microarrays for High-Throughput Function Determination," *Science,* vol. 289, pp. 1760-1763, 2000.
[1.70] L. Pardo, W. C. Wilson, and T. Boland, "Characterization of Patterned Self-Assembled Monolayers and Protein Arrays Generated by the Ink-Jet Method " *Langmuir,* vol. 19, pp. 1462-1466, 2002.
[1.71] A. Bietsch, M. Hegner, H. P. Lang, and C. Gerber, "Inkjet Deposition of Alkanethiolate Monolayers and DNA Oligonucleotides on Gold: Evaluation of Spot Uniformity by Wet Etching," *Langmuir,* vol. 20, pp. 5119-5122, 2004.
[1.72] M. Mrksich, L. E. Dike, J. Tien, D. E. Ingber, and G. M. Whitesides, "Using Microcontact Printing to Pattern the Attachment of Mammalian Cells to Self-Assembled Monolayers of Alkanethiolates on Transparent Films of Gold and Silver," *Exp. Cell. Res.,* vol. 235, pp. 305-313, 1997.
[1.73] A. Brock, E. Chang, C.-C. Ho, P. LeDuc, X. Jiang, G. M. Whitesides, and D. E. Ingber, "Geometric Determinants of Directional Cell Motility Revealed Using Microcontact Printing," *Langmuir,* vol. 19, pp. 1611-1617, 2003.
[1.74] M. Thery, V. Racine, A. Pepin, M. Piel, Y. Chen, J.-B. Sibarita, and M. Bornens, "The extracellular matrix guides the orientation of the cell division axis," *Nat Cell Biol,* vol. 7, pp. 947-953, 2005.
[1.75] W.-S. Yeo, M. N. Yousaf, and M. Mrksich, "Dynamic Interfaces between Cells and Surfaces:â€‰ Electroactive Substrates that Sequentially Release and Attach Cells," *J. Am. Chem. Soc.,* vol. 125, pp. 14994-14995, 2003.
[1.76] C. D. James, R. C. Davis, L. Kam, H. G. Craighead, M. Isaacson, J. N. Turner, and W. Shain, "Patterned Protein Layers on Solid Substrates by Thin Stamp Microcontact Printing," *Langmuir,* vol. 14, pp. 741-744, 1998.
[1.77] A. Bernard, E. Delamarche, H. Schmid, B. Michel, H. R. Bosshard, and H. Biebuyck, "Printing Patterns of Proteins," *Langmuir,* vol. 14, pp. 2225-2229, 1998.
[1.78] A. Bernard, J. P. Renault, B. Michel, H. R. Bosshard, and E. Delamarche, "Microcontact Printing of Proteins," *Adv. Mater.,* vol. 12, pp. 1067-1070, 2000.
[1.79] C.-E. Ho, C.-C. Chieng, M.-H. Chen, and F.-G. Tseng, "Rapid Microarray System For Passive Batch-Filling and In-Parallel-Printing Protein Solutions," *J. Microelectromech. Syst.,* vol. 17, pp. 309-317, 2008.
[1.80] P. M. St. John, L. Kam, S. W. Turner, H. G. Craighead, M. Issacson, J. N. Turner, and W. Shain, "Preferential glial cell attachment to microcontact printed surfaces," *J. Neurosci. Methods,* vol. 75, pp. 171-177, 1997.
[1.81] M. Scholl, C. Sprössler, M. Denyer, M. Krause, K. Nakajima, A. Maelicke, W. Knoll, and A. Offenhäusser, "Ordered networks of rat hippocampal neurons attached to silicon oxide surfaces," *J. Neurosci. Methods,* vol. 104, pp. 65-75, 2000.
[1.82] C. D. James, R. Davis, M. Meyer, A. Turner, S. Turner, G. Withers, L. Kam, G. Banker, H. Craighead, M. Issacson, J. Turner, and W. Shain, "Aligned microcontact printing of micrometer-scale poly-L-Lysine structures for controlled growth of cultured neurons on planar microelectrode arrays," *IEEE Trans. Biomed Engng.,* vol. 47, pp. 17-21, 2000.
[1.83] L. Lauer, S. Ingebrandt, K. Scholl, and A. Offenhauer, "Aligned microcontact printing of biomolecules on microelectronic device surfaces," *IEEE Trans. Biomed. Eng.,* vol. 48, pp. 838-842, 2001.
[1.84] E. B. Chakra, B. Hannes, G. Dilosquer, C. D. Mansfield, and M. Cabrera, "A new instrument for automated microcontact printing with stamp load adjustment," *Rev. Sci. Instrum.,* vol. 79, pp. 064102-9, 2008.
[1.85] A. Perl, D. Reinhoudt, N., and J. Huskens, "Microcontact Printing: Limitations and Achievements," *Adv. Mater.,* vol. 21, pp. 2257-2268, 2009.

[1.86] A. Govindaraju, A. Chakraborty, and C. Luo, "Reinforcement of PDMS masters using SU-8 truss structures," *J. Micromech. Microeng.,* vol. 15, pp. 1303-1309, 2005.
[1.87] C. Moraes, Y. Sun, and C. A. Simmons, "Solving the shrinkage-induced PDMS alignment registration issue in multilayer soft lithography," *J. Micromech. Microeng.,* vol. 19, p. 065015, 2009.
[1.88] A. Bietsch and B. Michel, "Conformal contact and pattern stability of stamps used for soft lithography," *J. Appl. Phys.,* vol. 88, pp. 4310-4318, 2000.
[1.89] J. A. Rogers, K. E. Paul, and G. M. Whitesides, "Quantifying distortions in soft lithography," *J. Vac. Sci. Technol. B,* vol. 16, pp. 88-97, 1998.
[1.90] M. Tormen, T. Borzenko, B. Steffen, G. Schmidt, and L. W. Molenkamp, "Using ultrathin elastomeric stamps to reduce pattern distortion in microcontact printing," *Appl. Phys. Lett.,* vol. 81, pp. 2094-2096, 2002.
[1.91] GeSIM, Micro-Contact Printing Instruments, http://www.gesim.de.
[1.92] E. Delamarche, H. Schmid, B. Michel, and H. Biebuyck, *Adv. Mater.,* vol. 9, p. 741, 1997.
[1.93] C. Y. Hui, A. Jagota, Y. Y. Lin, and E. J. Kramer, "Constraints on Microcontact Printing Imposed by Stamp Deformation," *Langmuir,* vol. 18, pp. 1394-1407, 2002.
[1.94] M. M. J. Decre, P. H. M. Timmermans, O. van der Sluis, and R. Schroeders, "Numerical and Experimental Study of Critical Roof Collapse Conditions in Soft Lithography," *Langmuir,* vol. 21, pp. 7971-7978, 2005.
[1.95] Y. Y. Huang, W. Zhou, K. J. Hsia, E. Menard, J.-U. Park, J. A. Rogers, and A. G. Alleyne, "Stamp Collapse in Soft Lithography," *Langmuir,* vol. 21, pp. 8058-8068, 2005.
[1.96] K. J. Hsia, Y. Huang, E. Menard, J. U. Park, W. Zhou, J. Rogers, and J. M. Fulton, "Collapse of stamps for soft lithography due to interfacial adhesion," *Appl. Phys. Lett.,* vol. 86, pp. 154106-3, 2005.
[1.97] K. G. Sharp, G. S. Blackman, N. J. Glassmaker, A. Jagota, and C.-Y. Hui, "Effect of Stamp Deformation on the Quality of Microcontact Printing: Theory and Experiment," *Langmuir,* vol. 20, pp. 6430-6438, 2004.
[1.98] E. Menard, L. Bilhaut, J. Zaumseil, and J. A. Rogers, "Improved Surface Chemistries, Thin Film Deposition Techniques, and Stamp Designs for Nanotransfer Printing," *Langmuir,* vol. 20, pp. 6871-6878, 2004.
[1.99] M. R. Shadnam, S. E. Kirkwood, R. Fedosejevs, and A. Amirfazli, "Direct Patterning of Self-Assembled Monolayers on Gold Using a Laser Beam," *Langmuir,* vol. 20, pp. 2667-2676, 2004.
[1.100] D. W. Carr, M. J. Lercel, C. S. Whelan, H. G. Craighead, K. Seshadri, and D. L. Allara, "High-selectivity pattern transfer processes for self-assembled monolayer electron beam resists," *J. Vac. Sci. Technol. A,* vol. 15, pp. 1446-1450, 1997.
[1.101] D. S. Ginger, H. Zhang, and C. A. Mirkin, "The Evolution of Dip-Pen Nanolithography," *Angew. Chem. Int. Ed.,* vol. 43, pp. 30-45, 2004.
[1.102] K. Salaita, Y. Wang, J. Fragala, R. A. Vega, C. Liu, and C. A. Mirkin, "Massively Parallel Dip-Pen Nanolithography with 55 000-Pen Two-Dimensional Arrays13," *Angew. Chem. Int. Ed.,* vol. 45, pp. 7220-7223, 2006.
[1.103] NanoInk, Dip Pen Nanolithography, http://www.nanoink.net.
[1.104] F. J. Giessibl, "Advances in atomic force microscopy," *Rev. Mod. Phys.,* vol. 75, p. 949, 2003.
[1.105] C. S. Dulcey, J. H. Georger, M.-S. Chen, S. W. McElvany, C. E. O'Ferrall, V. I. Benezra, and J. M. Calvert, "Photochemistry and Patterning of Self-Assembled Monolayer Films Containing Aromatic Hydrocarbon Functional Groups," *Langmuir,* vol. 12, pp. 1638-1650, 1996.

[1.106] K. E. Petersen, "Silicon as a mechanical material," *Proc. IEEE,* vol. 70, pp. 420-457, 1982.
[1.107] M. Madou, *Fundamentals of Microfabrication*: CRC Press, 1997.
[1.108] K. E. Bean, "Anisotropic etching of silicon," *IEEE Trans. Electron Devices,* vol. 25, pp. 1185-1193, 1978.
[1.109] E. H. Klaassen, K. Petersen, J. M. Noworolski, J. Logan, N. I. Maluf, J. Brown, C. Storment, W. McCulley, and G. T. A. Kovacs, "Silicon fusion bonding and deep reactive ion etching: a new technology for microstructures," *Sensors and Actuators A,* vol. 52, pp. 132-139, 1996.
[1.110] A. M. Hynes, H. Ashraf, J. K. Bhardwaj, J. Hopkins, I. Johnston, and J. N. Shepherd, "Recent advances in silicon etching for MEMS using the ASE(TM) process," *Sensors and Actuators A,* vol. 74, pp. 13-17, 1999.
[1.111] B. Wu, A. Kumar, and S. Pamarthy, "High aspect ratio silicon etch: A review," *J. Appl. Phys.,* vol. 108, pp. 051101-20, 2010.
[1.112] A. Benitez, J. Esteve, and J. Bausells, "Bulk silicon microelectromechanical devices fabricated from commercial bonded and etched-back silicon-on-insulator substrates," *Sensors and Actuators A,* vol. 50, pp. 99-103, 1995.
[1.113] R. R. A. Syms, "BSOI MOEMS," in *MOEMS and Miniaturized Systems V*, San Jose, CA, USA, 2005, pp. 83-94.
[1.114] C. Gui, M. de Boer, J. G. E. Gardeniers, H. Jansen, J. W. Berenschot, and M. Elwenspoek, "Fabrication of multi-layer substrates for high aspect ratio single crystalline microstructures," *Sensors and Actuators A,* vol. 70, pp. 61-66, 1998.
[1.115] H. Fujita, "Microactuators and micromachines," *Proc. IEEE,* vol. 86, pp. 1721-1732, 1998.
[1.116] D. S. Eddy and S. D.R., "Application of MEMS technology in automotive sensors and actuators," *Proc. IEEE,* vol. 86, p. 1747, 2002.
[1.117] K. Liu and et al., "The development of micro-gyroscope technology," *J. Micromech. Microeng.,* vol. 19, p. 113001, 2009.
[1.118] N. Yazdi, F. Ayazi, and K. Najafi, "Micromachined inertial sensors," *Proc. IEEE,* vol. 86, pp. 1640-1659, 1998.
[1.119] S. Deffree, "Sensors to drive global MEMS market to $8.8 billion in 2012," *EDN,* vol. 53, p. 68, 2008.
[1.120] P. F. Van Kessel, L. J. Hornbeck, R. E. Meier, and M. R. Douglass, "A MEMS-based projection display," *Proc. IEEE,* vol. 86, pp. 1687-1704, 1998.
[1.121] J. M. Younse, "Mirrors on a chip," *Spectrum, IEEE,* vol. 30, pp. 27-31, 1993.
[1.122] C. Jingkuang and K. D. Wise, "A high-resolution silicon monolithic nozzle array for inkjet printing," *IEEE Trans. Electron Devices,* vol. 44, pp. 1401-1409, 1997.
[1.123] S. Kamisuki, T. Hagata, C. Tezuka, Y. Nose, M. Fujii, and M. Atobe, "A low power, small, electrostatically-driven commercial inkjet head," in *Proc. 11th Int. Workshop on MicroElectroMechanical Systems, Heidelberg*, 1998, pp. 63-68.
[1.124] M. C. Wu, O. Solgaard, and J. E. Ford, "Optical MEMS for lightwave communication," *Journal of lightwave technology,* vol. 24, p. 4433, 2007.
[1.125] G. M. Rebeiz, *RF MEMS: theory, design, and technology*: John Wiley & Sons, Inc., 2003.
[1.126] W. Wang and S. A. Soper, *Bio-MEMS: Technologies and Applications*: CRC Press, 2007.

2 Micro-structuring of PDMS for μCP stamps and other applications

The elastomeric PDMS stamp with relief features is a key element of μCP. Some of its main assets are 1) its ability to conform to a substrate over large areas, 2) its propensity to adsorb hydrophobic molecules and hydrocarbons such as alkanethiols solutions, and act as an ink reservoir, and, 3) its user friendliness, low cost, and ease of fabrication [2.1]. The convenience of PDMS led to applications beyond μCP and gave rise to a set of patterning techniques termed *soft lithography*, after the elastomeric nature of PDMS.

Soft lithographic techniques include μCP, replica moulding and other variants. Feature sizes ranging from 100 nm to mm can easily be replicated and soft lithography has become an important tool for rapid prototyping of microchips for microfluidics and micro-total-analysis systems (μTAS). Polymers and plastics such as poly-carbonate (PC) or polymethyl-methacrylate (PMMA) were already being used to make microfluidic devices [2.2] in the early 1990s. However, PDMS, with its ease and low cost of fabrication being highlighted by μCP, became the material of choice by the end of that decade [2.3]. Even now, although it is well known that PDMS is far from perfect, it remains, according to pioneers in the field of μTAS, a key material [2.4].

Applications of soft lithography in biology and biochemistry are reviewed in [2.5]. PDMS components range from fluid channels [2.3, 6], to seals [2.7], valves [2.8] and pumps [2.9], mixers [2.10], cyclers for polymerase chain reaction [2.11], capillary electrophoresis separators [2.12, 13], and electrospray nozzles [2.14]. In the related area of nanoimprint lithography (NIL), which allows the generation of ~25 nm structures by embossing a heated

thermoplastic [2.15], PDMS has been used both as a soft master [2.16] and as a thermocurable resist [2.17]. Exploiting its flexibility, PDMS has been used to form varifocal lenses[2.18], tuneable diffraction gratings [2.19], and as a curved substrate for an optical sensor emulating the human eye [2.20]. Lastly, the non-toxicity and biocompatibility of PDMS have led it to being used in pharmaceutical applications such as porous membranes to control the release of drugs in dermal patches [2.21] and tablet coatings [2.22].

In this chapter, the properties of PDMS and its micro-structuring methods are examined. The established fabrication route, replica moulding, is reviewed. Subtractive methods such as etching and laser ablation are then presented. Embossing, also termed nanoimprint lithography (NIL), and its application to PDMS is discussed, and some initial experimental results are presented. Lastly, spray coating of PDMS is developed, characterised, and its merits presented.

2.1 Properties of PDMS

PDMS is a polymer belonging to the category of silicones. As a linear unbranched polymer, it has the monomer formula $–((CH_3)_2Si\text{-}O\text{-})_n$ and its structure is illustrated in Figure 2-1 [2.23]. The methyl terminations ($-CH_3$) impart the hydrophobic property whilst the siloxane backbone (-Si-O-) provide flexibility. With a melting point of c.a. -55 ^oC, it exists as a liquid at low molecular weights (low *n*), while at higher molecular weights (high *n*), polymer chain entanglement occurs and the polymer takes the form of a solid gum [2.23, 24]. In this fluid form, it finds applications as lubricating oil, foam control, personal care and cosmetics amongst others.

Elastomeric forms of PDMS are obtained by cross linking. The commercial formulation commonly used in the community, Sylgard 184 (Dow Corning Corp) [2.25], is a 2-part, heat curable mixture consisting of a base and a curing agent. After mixing, the blend crosslinks and solidifies. Curing times vary from 24 hours at 23 ^{o}C to 15 minutes at 150 ^{o}C. In this formulation of PDMS, some of the methyl groups in the polymer chain of Figure 2-1a are replaced by vinyl groups (-CH=CH_2). Similarly, the some of the methyl groups in the curing agent are replaced by hydrogen (-H). The curing agent also contains silica fillers (for hardness) and a platinum catalyst which induces a hydrosilylation reaction which joins the hydrogen groups in the curing agent to the vinyl groups in the base and leads to a solid crosslinked polymer. The reaction is illustrated in Figure 2-1b. Hard PDMS (h-PDMS), introduced by [2.26], is made using a similar approach but with a base of different molecular weight and cross-link density.

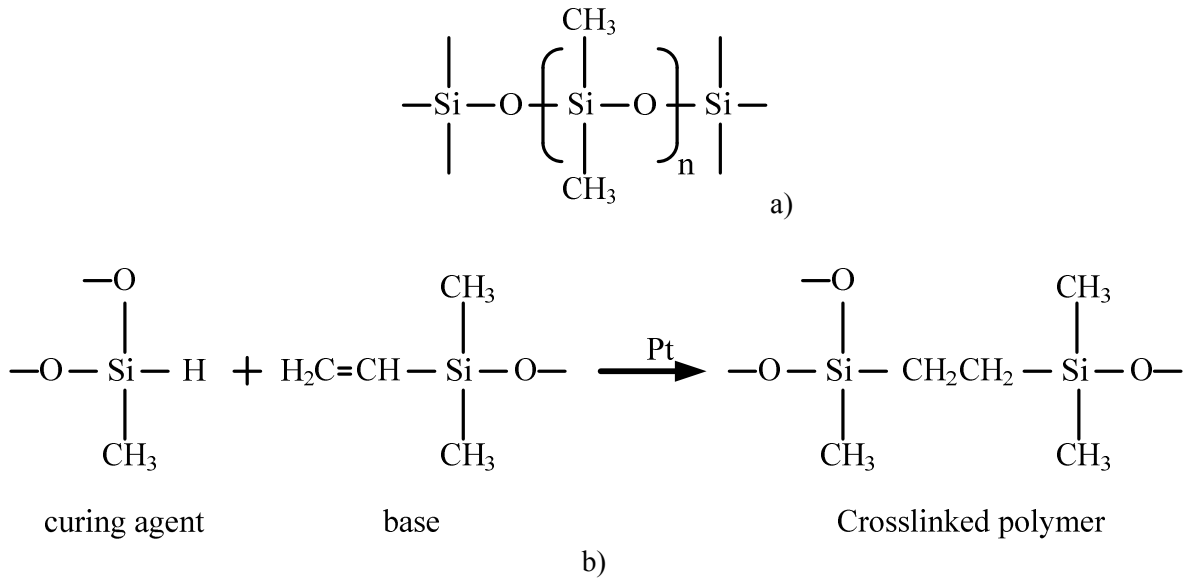


Figure 2-1 a) Structure of linear PDMS consisting of a siloxane backbone (-Si-O-). b) Cross-link reaction (hydrosilylation) between methyl hydrogen siloxane units in the curing agent and dimethyl vinyl units in the base.

2.2 PDMS casting and moulding

Casting is a cheap and experimentally simple method of generating structures. PDMS (Sylgard 184) is especially suitable because of its 2-part curing method and reasonable cure times. Masters are typically made using MEMS microfabrication technology. Typically, a Si or SiO_2 substrate is coated with thick photoresist and the latter is patterned by optical lithography [2.1]. The availability of SU-8, a photosensitive epoxy capable of forming high aspect ratio structures for MEMS [2.27], has increased possibilities as masters with deep features can easily be made [2.28, 29]. Alternatively, a micromachined silicon substrate formed by conventional photolithography and DRIE or KOH crystalline etch can be used. Non-photolithographic methods of generating masters are also available and are described in [2.30].

A typical process flow, starting with a structured master is illustrated in Figure 2-2a. Masters can be formed in any suitable method, but a key requirement is that they are treated with a release agent to facilitate the peeling off of the polymer after curing. Figure 2-2a illustrates a structure made by patterning thick resist on Si. A common antistiction treatment is to expose the masters to a vapour of 1,1,2,2-tetrahydroperfluorodecytrichlorosilane (FDTS) [2.31] and this treatment is often termed silanisation. Another method, which is adopted here, is the deposition of a conformal teflon-like layer, CF_x, using the passivation cycle of a DRIE [2.28, 32].

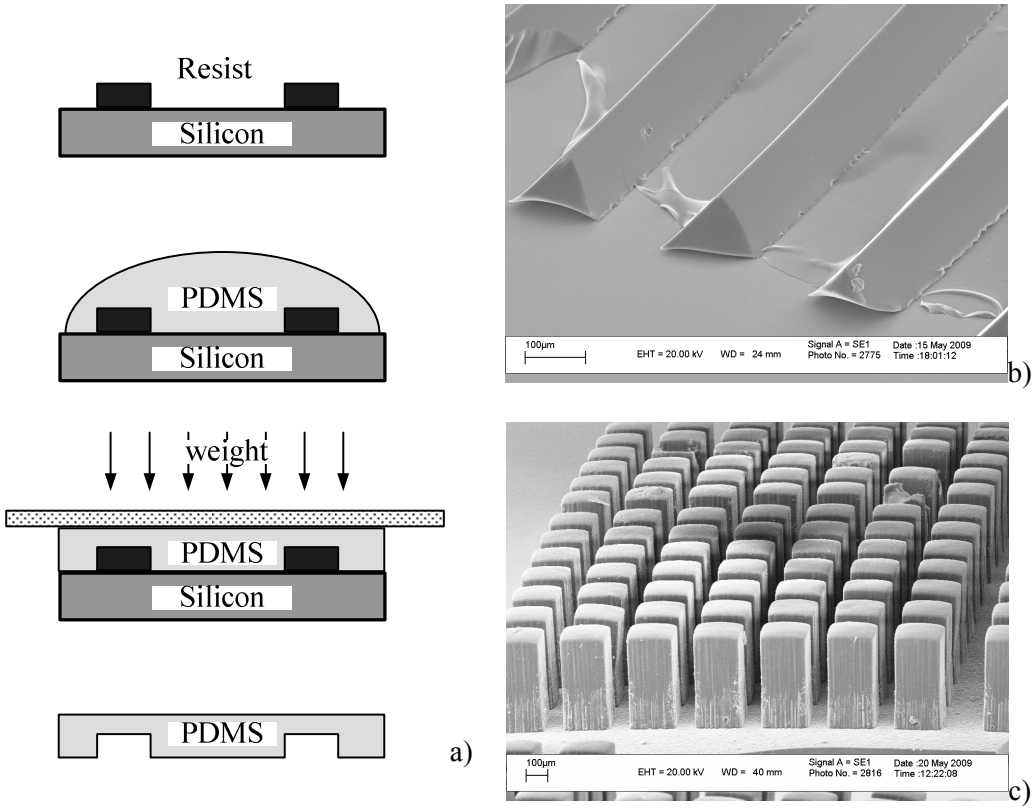


Figure 2-2 a) Casting of PDMS on a Si master. b) SEM of V-shaped bars formed by moulding against a KOH-etched Si master. c) SEM of dense high aspect ratio structures cast against a Si master formed by DRIE.

The thoroughly mixed and degassed PDMS precursor is then poured onto the suitably treated master and allowed to flow into the channels. Initial experiments show that, especially for high aspect ratio masters, degassing in a desiccator ensures complete filling of the trenches. After filling, the thickness of the elastomer is fixed either by spin coating or by placing a weight on top. Finally, the assembly is cured and the polymer is peeled off. Examples of PDMS structures formed using the above methods are shown in Figure 2-2b and c. Note that the polymers were coated with a thin layer of Au to enable reliable SEM imaging.

2.3 Subtractive structuring of PDMS: Laser ablation and wet etching

2.3.1 Laser ablation

Patterning of PDMS for microfluidics by laser ablation has been demonstrated in e.g. [2.12]. In this work, 110 μm wide channels with depths of 33 μm were rapidly generated using a relatively cheap CO_2 laser. Being a direct write process, laser ablation is maskless and designs can quickly be modified. However, the fabrication time per prototype is high given the serial nature of the process. Moreover, whilst good for writing lines, laser ablation is presumably very slow at removing large open areas, and the surface roughness may be an issue in some applications. Lastly, laser ablation causes localised heating of the polymer, which, although not reported in this paper, may modify its surface properties.

Laser ablation is perhaps best used to complement replica moulding, as demonstrated by Kim *et al.* [2.33]. Here the tight focus of a 800 nm femtosecond pulsed laser beam is used to drill capillaries as small as 0.5 μm wide 35 μm below the surface. Such features cannot be formed by replica moulding. An illustration of a device is shown in Figure 2-3a. The large channels are formed in PDMS by conventional casting, whilst laser ablation is used for the micro-capillary connecting the two.

2.3.2 Etching of PDMS

RIE based dry etching of PDMS has been demonstrated by Garra *et al.* [2.34]. An O_2/ CF_4 gas mixture is used and maximum etch rates of 20 μm/hour have been obtained. The masking material used is Al and it is defined by conventional photolithography. The main benefit of

this form of patterning is that the PDMS is already crosslinked and no further shrinkage is induced. Moreover, it preserves the batch, wafer-scale nature of replica moulding. However, the etched surfaces (and sidewalls) are very rough and can be observed qualitatively in Figure 2-3b. Also, the changes to the surface properties of the PDMS after ion bombardment are unknown.

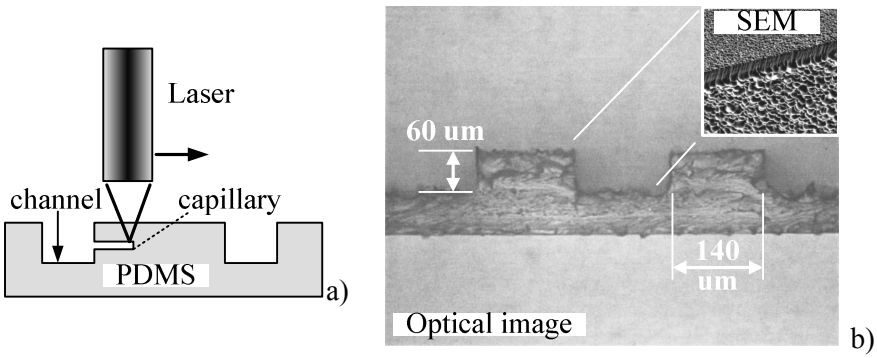


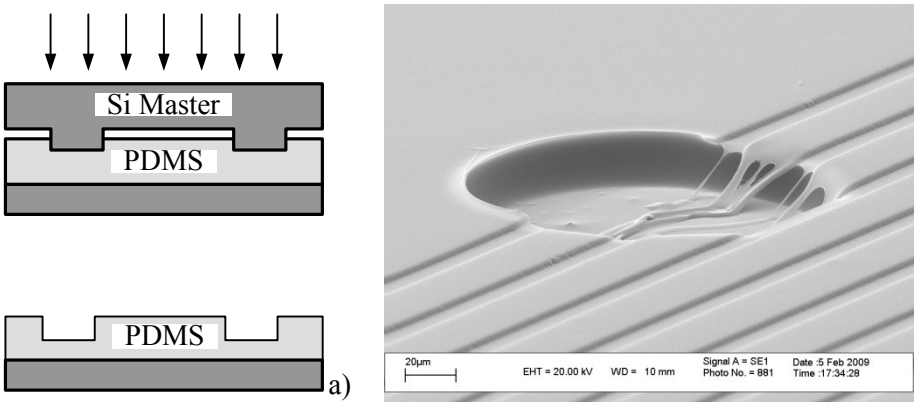
Figure 2-3 a) Sub-surface drilling of a micro-capillary by laser ablation[2.33]. b) Dry etching of PDMS with RIE. Inset is an SEM image highlighting the roughness. (adapted from [2.34])

2.4 Embossing

Hot embossing of polymers for the fabrication of miniature chips is well established as described in e.g. [2.35]. Chou *et al.* [2.15] have demonstrated the fabrication of 25 nm features in PMMA and the term nanoimprint lithography (NIL) was coined. Limitations of the techniques were the high temperature (> T_g; for PMMA, $T_g \approx 110\ ^{o}C$) and pressures (>10 MPa) required to achieve uniform patterning. Step and flash imprint lithography (SFIL), was developed as an alternative to circumvent these issues [2.36]. SFIL uses a low viscosity photocurable prepolymer and the casting process is chemical (rather than physical) in nature and requires low pressures. A transparent master is however required. Pedersen *et al*. have devised a compact low cost imprinter for thermal NIL using a flexible master which is pneumatically actuated to emboss PMMA [2.37] using pressures of ≈ 500 kPa. Separation is similarly achieved by mild suction (≈ 70 kPa).

PDMS has been used as a master for embossing PMMA both in SFIL [2.16] and NIL [2.37]. Here, pre-formed PDMS is used as a master to emboss PMMA. However, few have reported on embossing using PDMS as the thermocurable resist, which is surprising given the technological relevance of the latter. Tormen *et al.* [2.39] and later Malanquin *et al.* [2.17] highlight the low pressure and temperature required and present some initial results but do not provide a detailed analysis of the pattern fidelity. Recently, Hoh *et al.* have reported nanoembossing of 1 μm wide and 200 nm deep trenches in PDMS (Sylgard 184) using a Si master [2.40]. The imprint area was limited to 10 μm × 10μm and the applied load was 1 kPa. In this case, a flat slab of the polymer is allowed to crosslink at room temperature for 24 hours, so that it is firm enough to handle but still tacky. The master is contacted and a load is maintained to form a shallow imprint.

Prior to the publication of [2.40], the author and others in the group had attempted similar experiments using partially cured Sylgard 184. The polymer was spun onto a Si substrate and partially cured, and a microfabricated Si master was pressed into the polymer (see Figure 2-4a). Qualitatively, it was found that the more crosslinked the polymer was, the better the pattern fidelity, but the shallower the imprint. In addition, for imprints greater than a few micrometers, when the PDMS was mildly crosslinked and still soft (5 minutes baking at 60 ^{o}C prior to embossing), large voids due to trapped air were observed in the polymer film (see Figure 2-4b). Imprinting in vacuum was shown to solve this problem [2.41]. In addition, separation after embossing was very problematic and was found to depend on the features and the imprint depths. For example, for shallow features (< 5 μm) exhibiting a total contact area of 1.7 cm^2 separation forces of 20 N (i.e. pressure of ≈ 120 kPa) were required, whereas for deeper features (10 – 20 μm), separation failed.



a) b)

Figure 2-4 a) Illustration of embossing. b) SEM of an embossed PDMS part showing a void due to trapped air

Given the problematic nature of embossing PDMS, an alternative method of structuring was sought and is presented in the next section.

2.5 Spray Coating of PDMS

2.5.1 Motivation

The methods of structuring PDMS discussed above have their limitations. Embossing is marred by high separation forces between master and substrate. RIE provides a rough surface with chemically altered surface properties. Replica moulding works well for thick layers (>50 μm) which are strong enough to be peeled off. Thinner layers tend to tear up upon release. In addition, none of the above enables conformal coating of a predefined surface. Furthermore, as indicated in Chapter 1, Section 1.6, a MEMS based solution to the μCP alignment problem may require deposition of PDMS on a fragile Si structures. None of the above deposition steps are gentle enough. Lastly, MEMS fabrication can involve high temperatures (above the operating range of Sylgard 184, which is 200 ^{o}C) or harsh chemicals and a PDMS deposition method that can be applied post-microfabrication is required.

Spray coating meets the above conditions; the process is low impact and can be carried out after the Si device is released. Spray coating has been extensively investigated for deposition of photoresist onto three-dimensional microstructures [2.42-45] using, for example, the EV101 spray-coater (EV Group, Innsbruck, Germany) [2.46]. Diluted, low viscosity resist [2.45] and a high carrier gas flow [2.44] are required to obtain small droplet sizes, and hence low surface roughness. Ultrasonic atomisation may also be used [2.43]. A rapidly evaporating solvent or a heated sample is also required for uniform coverage of raised features. Spray coating has also been used for deposition of sol-gel materials [2.47], and the related method of electrospray has been investigated [2.48]. Spray coating of PDMS has, however, so far received very limited attention [2.49, 50].

In this section a PDMS spray-coating jig using a modeller's airbrush is designed and characterised. Film quality is analysed and conformal coating of structures is demonstrated. Functionality of the polymer for μCP and plasma activated bonding is verified.

2.5.2 PDMS spray deposition: Background

The overall aim in spray coating is to obtain small droplets from an atomized spray, to minimise surface roughness while still achieving a uniform, pinhole-free film. Background literature on atomization is reviewed and materials and experimental set up are described. The key process parameters are shown to be the spray injection pressure and the PDMS viscosity.

Atomization

Spray coating is carried out by a process akin to coaxial atomization, in which a high-speed coaxial gas stream is used to break up a liquid jet and disperse it into droplets much smaller than the jet diameter. A similar mechanism is used in cryogenic rocket engines, in which a liquid oxygen jet is atomised by a high-speed annular flux of hydrogen [2.51]. Despite considerable recent efforts, recently reviewed in [2.52], coaxial atomization is still relatively poorly understood. The physical processes are different to those occurring when the liquid jet discharges into stagnant gas [2.53]. For this case, Rayleigh investigated the mechanism for break-up in 1879, and proposed a hydrodynamic instability due to surface tension. In 1931, Weber showed in turn that viscosity has a stabilising effect. For coaxial atomisation, additional processes can occur by a transfer of kinetic energy from the gas to the liquid, and Varga et al. [2.54] have shown a series of instabilities is involved. A Kelvin-Helmholtz

instability first develops in the annular shear layer at the liquid discharge nozzle, creating surface ripples in the liquid that subsequently grow into tongues and vortex sheets. Rayleigh-Taylor instabilities then develop at the crests of the tongues due to the action of the light gas pushing against the heavier fluid. These instabilities strip the fluid from the tongues as a series of fine ligaments and droplets (see Figure 2-5).

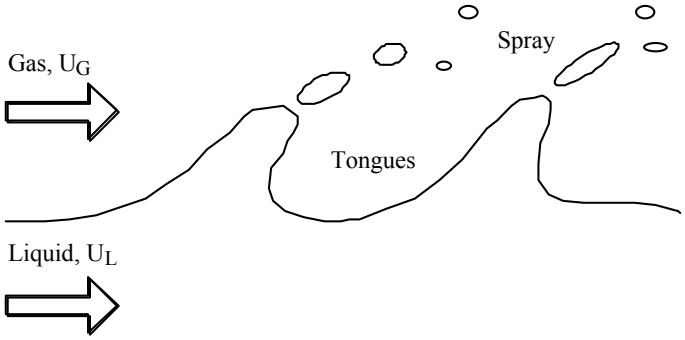


Figure 2-5 Illustration of Instability leading to droplet formation

The exact details of spray formation are complicated, and even more so for non-Newtonian fluids [2.55] such as PDMS polymer. For Newtonian fluids, spray formation depends on a set of dimensionless parameters including the gas and liquid Reynolds numbers $Re_G = U_G\rho_G(D_G - D_L)/\mu_G$ and $Re_L = U_L\rho_L D_L/\mu_L$, which define the ratio of inertial to viscous forces, the gas Weber number $We_G = \rho_G(U_G - U_L)^2 D_L/\sigma$, which defines the ratio between the pressure force of the gas on the liquid and the confining force of surface tension, and the Ohnesorge number $Oh = \mu_L/(\rho_L D_L \sigma)^{1/2}$, which defines the ratio between viscous and surface tension forces. Here ρ is density, μ is dynamic viscosity, σ is surface tension, U is velocity, D is the diameter of the flow, and the subscripts L and G denote liquid and gas respectively. The momentum flux ratio $M = \rho_G U_G^2/\rho_L U_L^2$ and the mass flux ratio $m = \rho_L U_L A_L/\rho_G U_G A_G$ are also important, where A is cross-sectional area of the flow. It is generally accepted that the droplet size

reduces with a decrease in liquid viscosity and also with an increase in gas velocity and in the gas/liquid mass-flow ratio.

Further complications arise from the use (as here) of a Venturi nozzle, whose operation has been investigated as part of Venturi Scrubbers. Venturi scrubbers use a liquid spray to remove particles entrained in the gas, and have been studied extensively. Different arrangements exist; in ejector scrubbers, the liquid is introduced axially into a gas flow upstream of the throat of a convergent/divergent nozzle [2.56], while in Pease-Anthony scrubbers, it is introduced transversely through one or more nozzles at the throat (Figure 2-6) [2.57]. In the latter case, the cylindrical symmetry associated with co-axial atomization may be lost. Although the atomization mechanism must be similar, theoretical models have been less detailed because of these distinctions and spray size distributions tend to be empirical. A widely-accepted expression for the Sauter mean diameter D_{32} of the drops originally proposed by Nukiyama has the form [2.58, 59]:

$$D_{32} = \left(\frac{0.585}{U_G - U_L}\right)\sqrt{\frac{\sigma}{\rho_L}} + 1.683 \times 10^{-3}\left(\frac{\mu_L}{\sqrt{\rho_L \sigma}}\right)^{0.45}\left(1000\frac{Q_L}{Q_G}\right)^{1.5} \qquad (2.1)$$

Here Q_L and Q_G are volumetric flow rates, the various constants are in SI units and D_{32} is in metres. Other empirical expressions exist [2.60], but these and Equation 2.1 again point to a need for a low liquid viscosity, a high gas velocity and a high gas/liquid mass flow ratio.

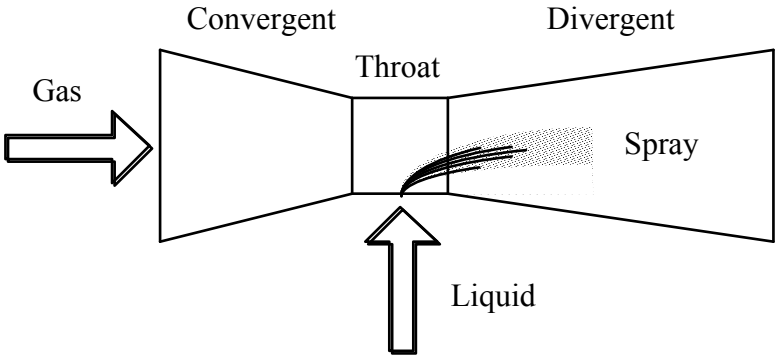


Figure 2-6 Illustration of a Venturi nozzle

2.5.3 PDMS Spray deposition: Experimental methods

Materials

Experiments were performed with Dow Corning Sylgard 184 [2.25]. This material has a dynamic viscosity of μ = 3900 mPa.s, or a kinematic viscosity of $\nu = \mu/\rho = 3.8 \times 10^3$ cSt at a density of $\rho = 1.03 \times 10^3$ kg/m^3. Since it is so viscous it cannot be used in an airbrush directly. To reduce its viscosity it was therefore mixed with a silicone fluid with a shorter chain length as reported in [2.50]. Dow Corning 200 Fluid 20 cSt [2.61], another PDMS composition with μ = 19 mPa.s, ν = 20 cSt and $\rho = 0.95 \times 10^3$ kg/m^3, was used, and the ratio of Sylgard 184 base to Sylgard 184 curing agent to 200 Fluid 20 cSt was 1 : 0.1 : 1. The resulting blend was considerably less viscous than normal and suitable for the airbrush. However, the cross-link density is lower than conventional Sylgard 184 and the consequent hardness of the polymer is expected to drop (see e.g. [2.24]).

An alternative diluent, hexane, used in the same ratio as the previous blend, was also investigated. The key benefit is that hexane has a high vapour pressure, and therefore tends to evaporate in flight. Therefore, the viscosity of the fluid reaching the target can be assumed to

be higher than the viscosity before spraying. Moreover, after curing, the deposited material can be considered to consist only of crosslinked PDMS, since all the solvent will have evaporated. When Fluid 20 cSt is used, the resulting coating contains low molecular weight silicone polymer chains trapped inside a matrix of Sylgard 184. The additional material can be a source of contamination in applications such as μCP and μTAS. As will be shown in Section 2.5.4, similar coating uniformity could be obtained with both diluents, although the hexane-diluted blend results in more conformal coatings (see Section 2.5.5).

Spray coating equipment

A commercial airbrush with a medium nozzle (Badger 350, Badger Airbrush Co., Illinois, USA) was used, as shown in Figure 2-7a. Such brushes are normally used in model painting, and can coat an area of ≈ 1 cm^2. The brush is driven by compressed N_2, which flows through a Venturi nozzle. The flow causes a local reduction in pressure, so that paint can be driven from a small jar by atmospheric pressure. On exit from the nozzle, the flow is broken into droplets by atomization much as in Figure 2-6. To increase the area that could be coated uniformly, the airbrush was held on a frame above a motor-driven rotating chuck on which small samples could be mounted for coating as shown in Figure 2-7b. Apertures were used to limit the extent of the spray, and the chuck could be heated to accelerate curing. Even in the atomisation regime, there can be an intact core of unbroken liquid within the spray near the nozzle. The exact length of this core depends on the internal nozzle design. Since the internal dimensions of the airbrush nozzle used here were unknown, a separation between the nozzle and the sample sufficient to avoid this core was determined empirically.

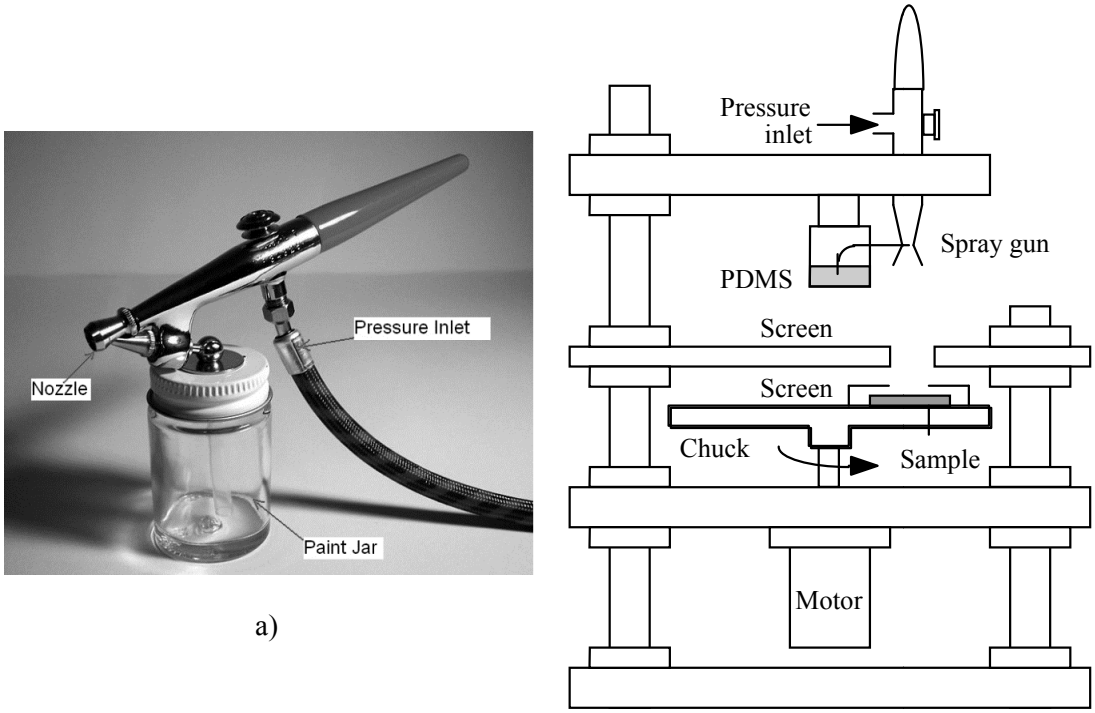


Figure 2-7 a) Modeller's airbrush used for spray coating. b) Rotating spray deposition system showing rotating chuck, screens, and spray gun.

The actual variation of the droplet size obtained at different pressures is difficult to measure, because the droplets distort and coalesce on contact with the surface. However, an estimate can be obtained from surface roughness measurements, as shown in the following Section. The use of a Venturi implies that high gas pressure, while reducing roughness, will also increase the flow rate of polymer. In initial experiments, the airbrush was placed normally above a stationary sample, and triggered manually for a controlled period. It was found that the film thickness rose to ≈ 10 μm in times as short as 1 second, and that the process was not reproducible for thinner films. All other experiments were therefore conducted with the stage rotating.

The rotating stage system coats samples within a radial band with r lying in the range $r_1 < r < r_2$. Assuming that all of the material contained in a cylindrical jet of radius a, with a volume flow rate $Q_L = \pi a^2 U$ m^3/sec, is deposited in that radial band, the film thickness d obtained in a time t is $d = Q_L t/\{\pi(r_2^2 - r_1^2)\}$. This expression is an overestimate if any apertures are used, but it is clear that the thickness should vary linearly with time and be independent of the angular rotation rate ω of the stage. However, it is possible that surface roughness could depend on ω and also that the roughness in the tangential and radial directions might differ due to centripetal effects.

Characterisation of deposited films

PDMS films, covering a 5 mm × 5mm area, were deposited on small (≈ 10 mm × 10 mm) pieces of silicon wafer and cured for 20 mins at 100 C. Film characteristics were then measured using a Dektak STIII mechanical surface profiler (Veeco Instruments Inc, Plainview, NY, USA), with the stylus force set to 10 μN to avoid deforming the film, and a Zygo NewView 200 white light interferometric microscope (Zygo Corp., Middlefield, CT, USA). Prior to optical measurements, the films were coated with a layer of Au to increase reflectivity. A low pass cut off wavelength of 600 μm was used for all measurements and the measurement length was at least 3 mm for stylus measurements or an area of 3 mm × 3 mm for interferometric measurements. Roughness was quantified separately along the radial and tangential directions by calculating the arithmetic mean roughness (Ra), found from the average height variation y(x) with distance x over a length L as $Ra = (1/L) \int_0^L y(x)\, dx$ [2.62]. A further parameter, the uniformity (the standard deviation of thickness divided by mean thickness, which can also be interpreted as the normalised roughness [2.42]) was also used to quantify film quality. The value of this parameter reduces as film quality improves.

2.5.4 PDMS Spray deposition: Results

Figure 2-8a shows the variation of thickness with deposition time, for an injection pressure of 40 psi, a separation between the airbrush and sample of 30 mm and different stage rotation rates. As expected, the deposition rate is effectively independent of rotation rate. Figure 2-8b shows the corresponding variation in radial roughness with thickness, for different rotation rates. Here, the roughness seems to depend on the rotation rate, although no clear trend can be deduced due to high data variability. However the roughness at 135 rpm is significantly higher than the roughness at 350 rpm and 600 rpm. The effect is attributed to centripetal force, which causes an outward smoothing movement of material. Figure 2-9a shows the variation in tangential roughness with injection pressure, for a rotation rate of 135 rpm and a separation of 30 mm. Higher pressures give slightly thicker films but no clear effect on roughness can be deduced due to high data variability. The effect is similar for radial and tangential roughness at a given rotation rate and is not presented here.

Based on further characterisation, an optimised set of coating parameters was determined. The separation was increased to 50 mm, since this separation was found to give uniform coverage over an annular band with $r_2 - r_1 = 5$ mm. The pressure was increased to 60 psi, since this gave low surface roughness, and the rotation speed was increased to 600 rpm for similar reasons. Figure 2-9b shows the variation of deposited thickness with time obtained using these parameters. The deposition rate is approximately constant, at 0.3 μm/sec. Uniformity clearly improves with thickness (see Figure 2-9c) and this is attributed to body forces overcoming surface tension forces that tend to form discrete droplets. Figure 2-10a and Figure 2-10b show corresponding variations of thickness and uniformity for hexane-diluted PDMS. Similar trends are observed. However, uniformity clearly improves much more

slowly with thickness in this case, presumably because the in-flight evaporation of diluent leads to more viscous droplets reaching the surface. This change in rheological properties results in a trade-off between roughness and conformality, as shown later.

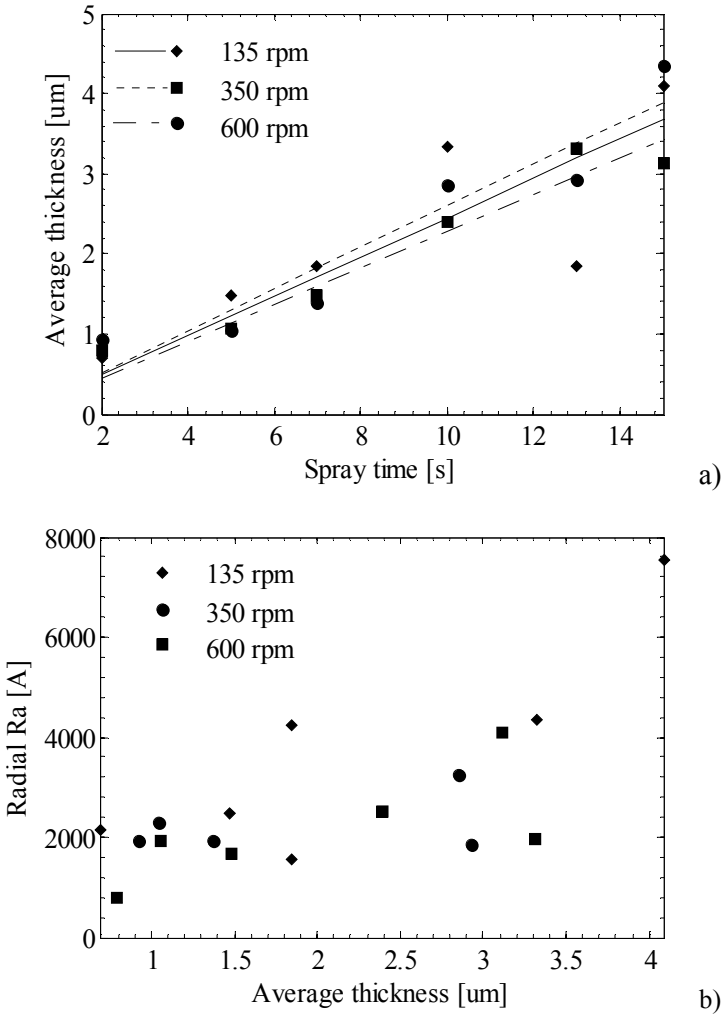
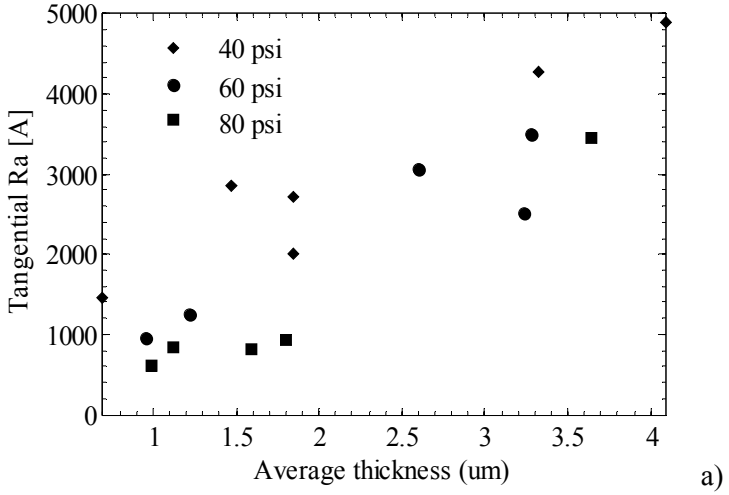
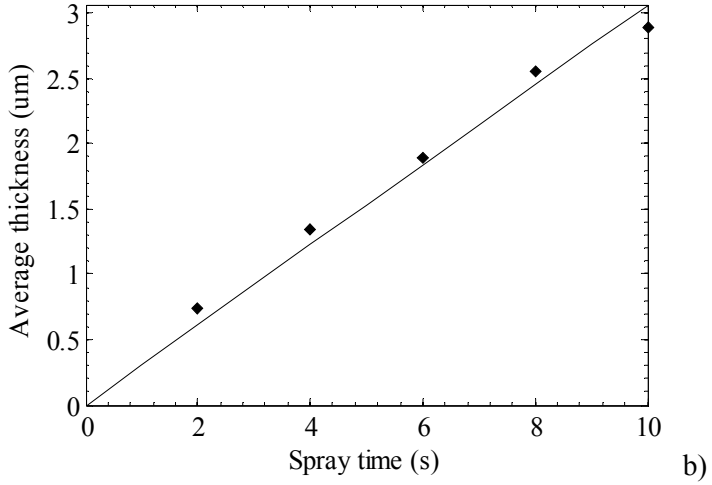


Figure 2-8 a) Variation of fluid 20cSt diluted, spray coated PDMS fim thickness with time, for different rotation rates. Points are data, straight lines are best fits. b) Variation of radial roughness with thickness, for different rotation rates. Injection pressure: 40psi; separation 30mm.





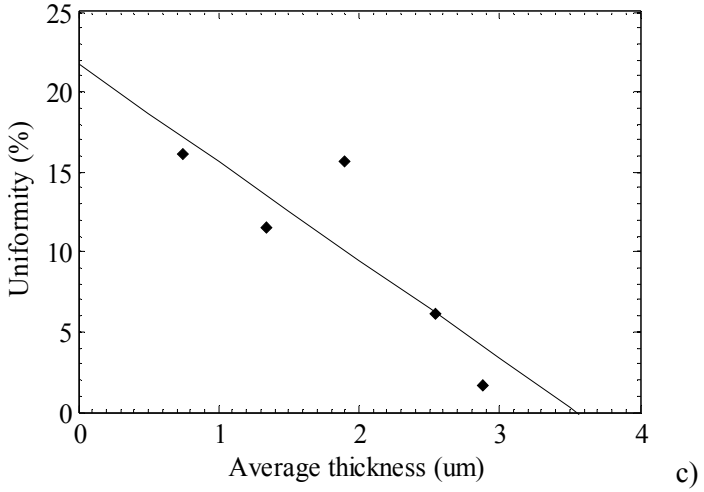


Figure 2-9 a) Variation of fluid 20cSt diluted, spray coated PDMS tangential roughness with thickness, for different injection pressures. Rotation rate: 135 rpm; separation 30 mm. b) Variation of film thickness with time for optimised parameters. c) Variation of uniformity with film thickness. Points are data, straight lines are best fits.

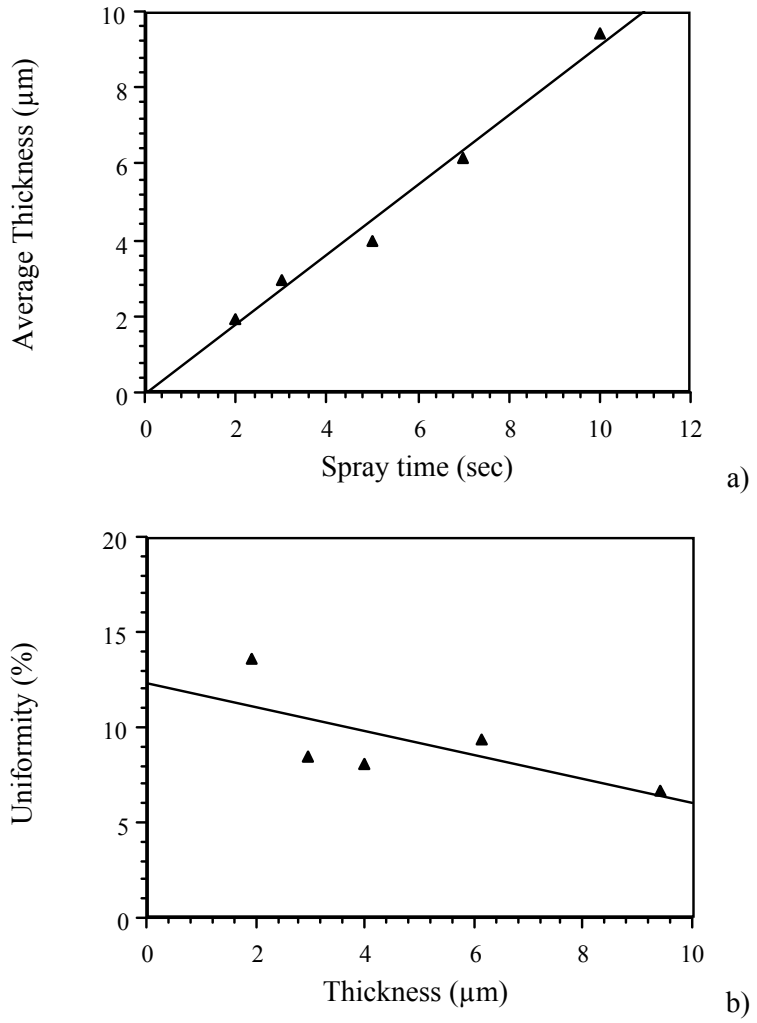
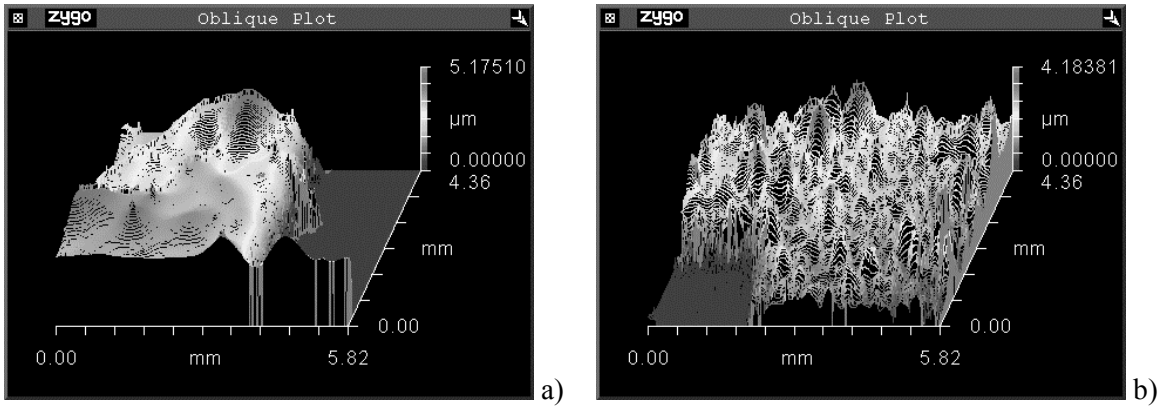


Figure 2-10 a) Variation of hexane-diluted spray PDMS film thickness with time, for optimised parameters. b) Variation of uniformity with thickness. Points are data, straight lines are best fits.

A 3D model of the surface profile of a 3.5 µm thick film sprayed under optimised conditions, obtained by white light interferometric microscopy, is shown in Figure 2-11a. The optical (Ra = 1760 Å) and mechanical (Ra = 1470 Å) roughness values were found to correspond. The film is smooth and of good quality and with a normalised roughness of 11%. In contrast, Figure 2-11b shows the surface profile of a film deposited using low driving pressure. Here, the discrete nature of sprayed droplets may clearly be seen, and the poor quality of the film is reflected in a normalised roughness of 23%.



a) b)

Figure 2-11 3D Maps of coated surfaces. a) Optimised conditions. b) Low Pressure Conditions

Wafer scale coating

Our existing spray-coating equipment is limited to small 5 mm ×5 mm areas. However, wafer scale spray coating of photoresist has been extensively investigated by Pham *et al.* [2.43] and a similar approach may clearly be used for PDMS. The process was developed on the EVG 101 system, which uses an ultrasonic spray nozzle mounted at an angle on a swivel arm to allow whole wafer coverage. The wafer is rotated at slow speed (50 rpm) to minimise centripetal effects, and the nozzle is swept across the wafer with a carefully programmed tangential velocity to ensure equal coating thickness at the centre and edge of the wafer. The requirement for a slow rotation rate may lead to higher roughness but is necessary for a constant film thickness over the whole wafer. Thickness variations of < 15% have been obtained on 100 mm diameter wafers after optimisation of the velocity profile [2.43], independent of the coating thickness [2.45].

2.5.5 PDMS spray deposition on microstructured surfaces

In this sub-section, the spray coating process is extended to microfabricated surfaces. The aim is to achieve conformal coating and applications include, but are not restricted to, rigid

thin stamps for μCP. Two types of test structures were used: shallow 6 μm tall parallel bars with varying mark-to-space ratios, and deep (≈ 100 μm) V-grooved structures. The former were formed by conventional lithography and DRIE, whilst the latter by anisotropic KOH etching of (100) Si.

Si mesas were coated using the optimised parameters described in Section 2.5.4 and empirically determined spray times. Scanning electron microscope images of PDMS-coated microstructures with different line widths and periods are shown in Figure 2-12. Figure 2-12a shows a structure with 5 μm wide bars and a 40 μm period, while Figure 2-12b shows 5 μm wide bars and a 10 μm period. In each case, little material is deposited on the tops of the mesas.

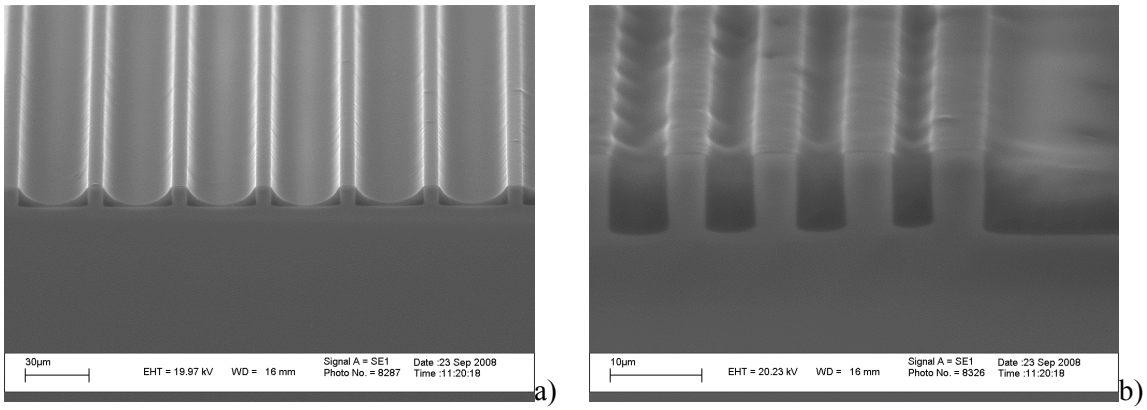


Figure 2-12 SEM views of Fluid 20cSt diluted PDMS. a) 5 μm wide bars and 40 μm period. b) 5 μm wide bars and 10 μm period.

In addition, the PDMS film only conforms to the underlying structure for low mark-to-space ratios (Figure 2-12a), and definition is lost due to bridging between adjacent bars for larger ratios (Figure 2-12b). Build-up of material at the base of high aspect ratio structures also occurs in spray coating of photoresist and is attributed to flow of the low viscosity polymer

required for atomisation [2.43-45]. The conventional solution is to reduce the viscosity of the resist after it reaches the target by using a solvent of appropriate volatility, or by heating the target to induce rapid evaporation. We have investigated the first approach using the hexane-diluted blend described in Section 2.5.2. The result is shown in Figure 2-13, for a structure with 5 μm wide bars and 10 μm period. Here, there is clearly more material on top of the mesas, compared with Figure 2-12b, without loss of definition.

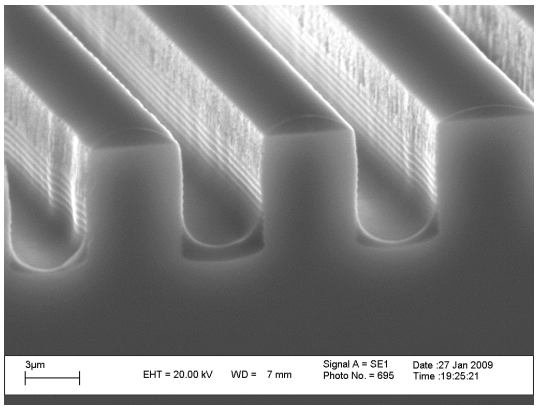
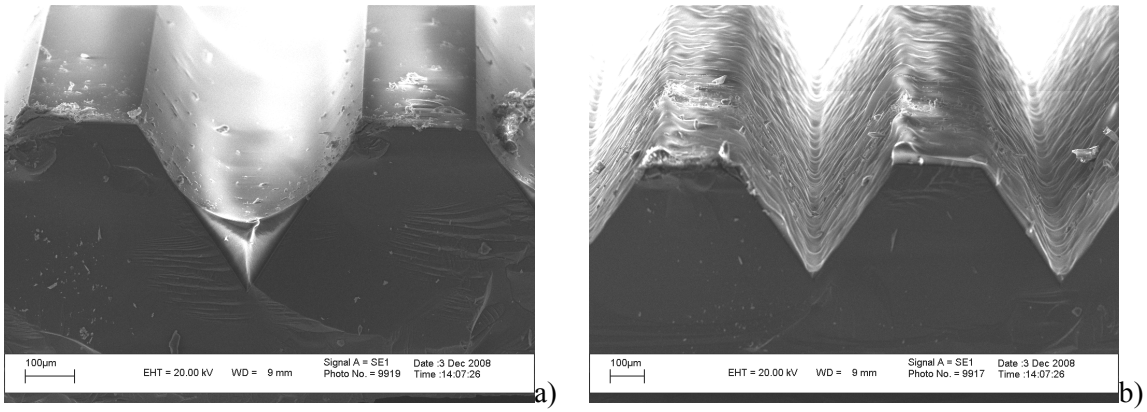


Figure 2-13 Hexane-diluted PDMS spray coated silicon microstructure with 5 μm width and 10 μm period.

For the Fluid 20 cSt diluted blend, the only mechanism to increase viscosity is thermally accelerated crosslinking of the siloxane polymer chains. Sylgard 184 cures relatively quickly, and becomes hard enough to handle after only 15 mins at 150 ^{o}C [2.63]. Further experiments were therefore conducted with the chuck heated to 150 ^{o}C. Over the short spraying time (≈ 10 sec), the polymer blend is not expected to harden fully. However, runoff might be expected to reduce, leading to a more conformal coating. 300 μm deep V-grooves, formed in (100) Si by KOH wet etching, were used to investigate the effect of target temperature on conformality and roughness. These structures were preferred over shallow parallel bar mesas as they required thicker (> 10 μm) PDMS coatings, whose deposition could be controlled accurately by spray coating stationary specimens heated on a hot plate. Typical coated V-grooves are

shown in Figure 2-14a and b. Here, the following coating parameters were used: separation of 50 mm, pressure of 60 psi, and stationary stage at various temperatures.



a) b)

Figure 2-14 SEM view of Fluid 20 cSt diluted PDMS spray coated silicon V-groove structure a) with chuck temperature = 20 C; b) with chuck temperature = 150 C

To quantify the results, we have used the ratio of PDMS thickness $t_{Plateau}$ on the plateau (Figure 2-15a) to the thickness in the valley t_{Valley} as a ratio of conformality. The use of V-groove structures also allowed the surface roughness to be measured on the plateau and on the sloping sidewalls using optical interferometry. To image the sidewalls, the specimen was first tilted by the V-groove angle $\cos^{-1}(1/\sqrt{3}) = 54.74^{o}$. Figure 2-15b shows the variation of conformality with roughness, and Figure 2-15c shows the variation of roughness with temperature. These results show that heating to accelerate cross-linking can improve conformality, but only at the expense of increased roughness.

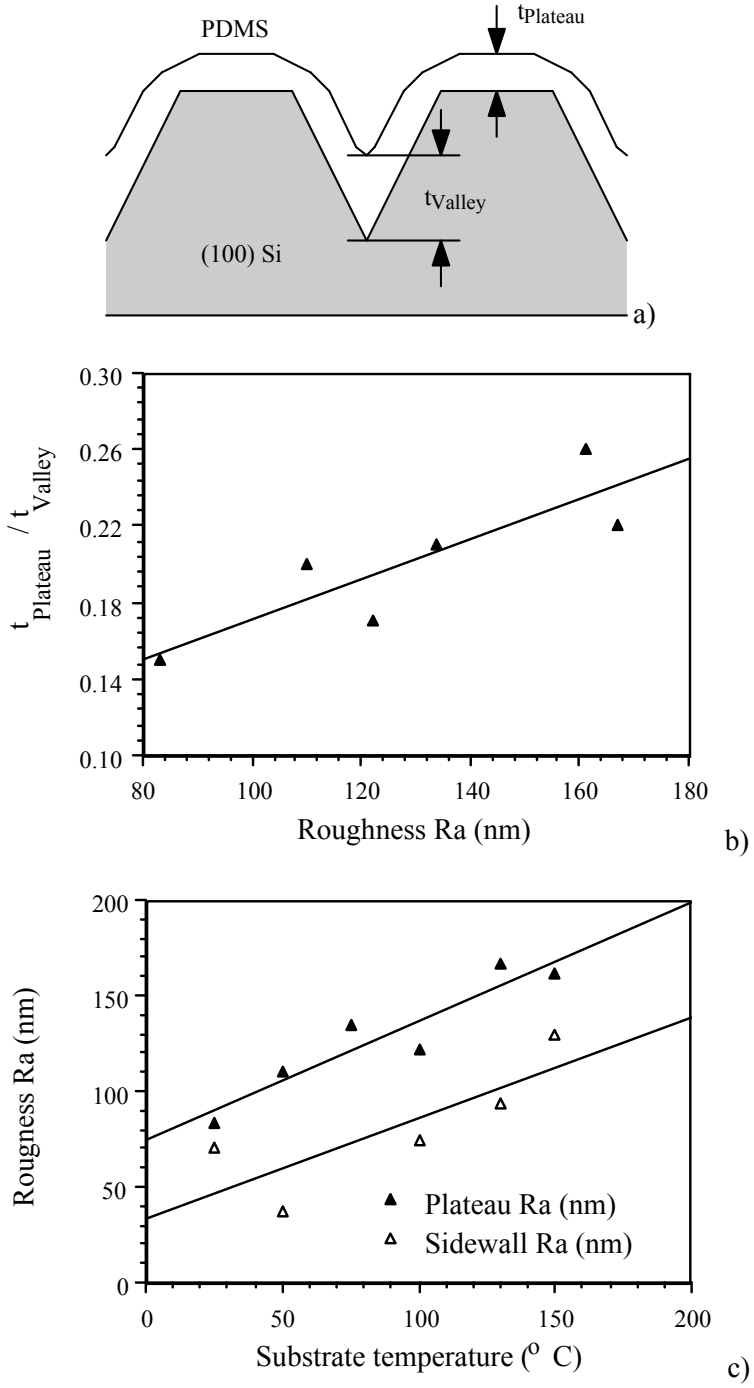


Figure 2-15 a) Key dimensions used in definition of conformality. b) Variation of conformality with temperature. c) Variation of surface roughness (Ra) with temperature. Material used is Fluid 20 cSt diluted PDMS.

2.5.6 Applications of PDMS spray coating

Although the drive behind the development of a deposition process was μCP, the technique is versatile and can have many applications, as described at the beginning of this chapter. Some of them are demonstrated below and these highlight the functionality of spray coated PDMS.

Plasma Activated Bonding

PDMS is heavily used in the microfluidics community because of its low cost, ease of processing, and the fact that it enables rapid prototyping of μTAS. An important technique in fabrication and packaging is that irreversible seals can easily be obtained by oxygen plasma activation. On exposure to the plasma, the methyl ($-CH_3$) groups of the polymer chain, $-O-Si-(CH_3)_2-$, are replaced by hydroxyl (-OH). When these silanol groups (-Si-OH), are brought into conformal contact at room temperature, they condense with those on another surface, such as on another oxidised PDMS or glass, yielding strong Si-O-Si bonds. The covalent bonds form the basis of tight irreversible seal that can easily resist pressures of 50-60 psi [2.64, 65].

Various combinations of samples were used to demonstrate plasma activated bonding, including 80 μm thick spin coated PDMS (Sylgard 184) on silicon, a few μm thick spray coated PDMS on Si, and glass. Samples were soaked in ethanol for ~10 minutes to extract uncured low molecular weight siloxane residues, and then cleaned in diluted hydrochloric acid (10%) for 15 minutes. The dilute acid cleaning step was included since some of the samples were over 1 week old [2.6]. A Plasmalab 80^+ parallel plate RIE was again used to provide a low power, high pressure, short oxygen plasma surface activation. A low power is required to avoid damaging the (-Si-O-) backbone and a short exposure minimises cracking

of the PDMS [2.65, 66]. The parameters used were 70 W RF power, 100 mTorr chamber pressure, 60 sccm O_2 flow rate, and 20 s exposure time. Activated samples were placed in contact a few minutes after plasma treatment and slight pressure was applied to ensure conformal contact. The specimens were then left in contact for ~1 hour before further testing or imaging.

The relative strengths of the different combination of materials are presented, rather than a quantitative analysis, which is beyond the scope of this thesis. In decreasing order of strength, the combination of bonded surfaces is as follows. The strongest bonds were obtained between 80 μm spin coated PDMS and glass (1), followed by 80 μm spin coated PDMS and 80 μm spin coated PDMS (2), and 80 μm spin coated PDMS and 5 μm spray coated PDMS (3). The weakest bonds were obtained between 20 μm spray coated PDMS and 20 μm spray coated PDMS (4). Thin (5 μm) spray coated PDMS layers hardly adhered to each other or to glass. It is believed that lack of conformal contact rather than the material itself is the cause of this behaviour. In contrast, the combinations (1) – (4), where at least one of the samples was flexible enough to mate with the other, bonded well. Applications for this technique would be in the fabrication of microchannels or for packaging of MEMS. In the former case, the use of masking to localise the coating to the bonding area could reduce latency in separation devices. Figure 2-16a and b show SEMs of microchannels formed by bonding a spray-coated, reactive ion etched Si groove to a planar surface. Figure 2-16c and d show encapsulation voids formed using much larger spray-coated KOH-etched V-grooves. In all four cases, the Si structures (upper) were spray coated, cured, plasma activated and contacted to a flexible 80 μm thick spin coated PDMS on Si substrate. Further work is required to quantify the bond strength, but these preliminary results show that spray coated PDMS has essentially the same functionality as cast or spin coated PDMS.

µCP with spray coated stamps

Spray coated structures such as those of Figure 2-12 and Figure 2-13 were used as stamps for µCP. Stamps were inked and brought into contact with a 30 nm thick Au substrate. Contact time was around 1 minute. The Au was then etched to reveal the printed pattern. Inking and etching are described in detail in Appendix A. Prints covering the full stamp area were obtained. Typical prints are illustrated in Figure 2-17a and b. However, defects such as pits, broken lines, and ill-defined edges become significant as line widths are reduced (Figure 2-17b). This is expected due to the random nature of the spray coating process.

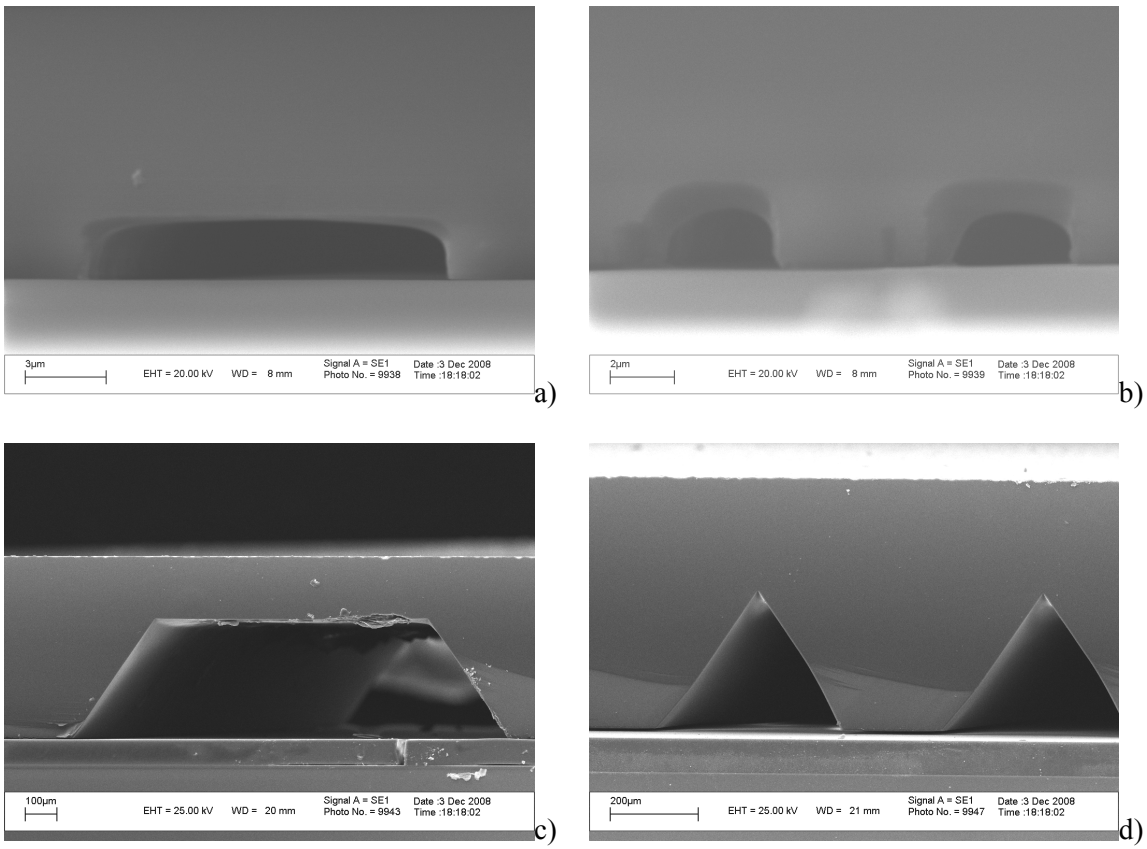
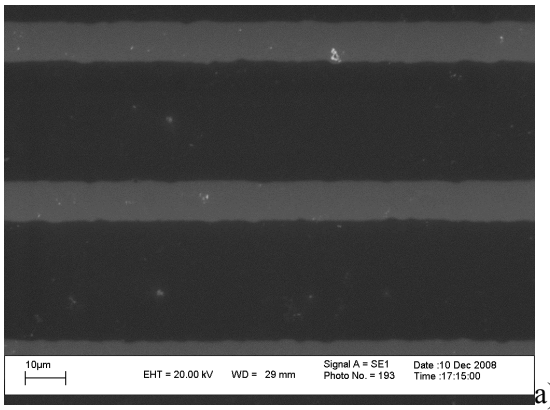
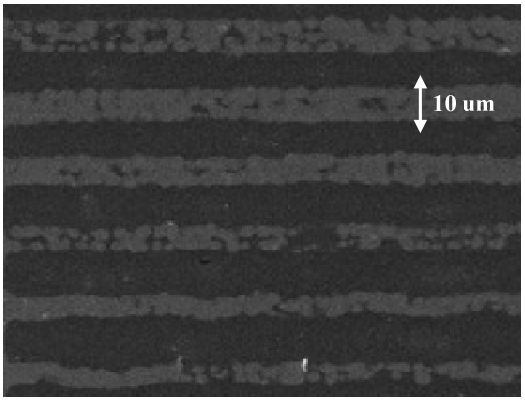


Figure 2-16. SEMs of plasma activated bonding of Fluid 20 cSt PDMS covered structures: a) and b) 2µm deep rectangular channels formed by DRIE. For high channel width to height ratios such as in b) the run off significantly alters the shape of the channel. c) and d) 300 µm deep channels formed by KOH etching of Si (100).



a)



b)

Figure 2-17 SEM views of Au patterns (bright) on Si (dark) made by µCP using a spray coated stamp: a) 10 µm bars, b) varying bar widths showing defects.

2.5.7 Summary: Spray deposition of PDMS

A method of spray-coating thin films of PDMS has been developed and characterised. The method is particularly appropriate for post processing of flexible MEMS that are too fragile to coat by other methods, or surfaces carrying deep features where spin-coating or casting cannot be used to obtain a conformal coating. The process avoids mechanical damage to microstructures and thermal damage to the PDMS, and might therefore provide a useful method of combining silicon MEMS and polymer microfluidics. For example, it might be used to provide layers with controlled or localised hydrophobicity, adhesion layers or gaskets on silicon. The method should also be appropriate for depositing other functional polymer layers onto completed devices, for example sensitised layers onto surface acoustic wave gas sensors or chemical preconcentrators.

Conditions for obtaining low surface roughness (low PDMS precursor viscosity, high gas pressure and sample motion) have been established. Coatings have been localised using simple apertures, but more generally precision stencils may be used. It has been shown that either an evaporating diluent or accelerated curing is required to reduce coating run-off on

structured surfaces. The functionality of the coated PDMS film has been confirmed by successful demonstration of plasma activated bonding and micro contact. Further improvements to the technique are required to increase the coated area, reduce surface roughness and improve film thickness uniformity on closely spaced high aspect ratio microstructures.

2.6 Conclusion

In this chapter, methods of machining PDMS have been reviewed. Tests have been made with embossing and replica moulding and some results have been presented. Spray deposition has been identified as particularly advantageous and a home-made jig for spray coating of PDMS has been built. The deposition process has been characterised and its applications demonstrated.

2.7 References

[2.1] Y. Xia and G. M. Whitesides, "Soft Lithography," *Angew. Chem. Int. Ed.,* vol. 37, pp. 550-575, 1998.

[2.2] H. Becker and L. E. Locascio, "Polymer microfluidic devices," *Talanta,* vol. 56, pp. 267-287, 2002.

[2.3] D. C. Duffy, J. C. McDonald, O. J. A. Schueller, and G. M. Whitesides, "Rapid Prototyping of Microfluidic Systems in Poly(dimethylsiloxane)," *Anal. Chem.,* vol. 70, pp. 4974-4984, 1998.

[2.4] R. Mukhopadhyay, "When PDMS isn't the best," *Anal. Chem.,* vol. 79, pp. 3248-3253, 2007.

[2.5] G. M. Whitesides, E. Ostuni, S. Takayama, X. Jiang, and D. E. Ingber, "Soft Lithography In Biology And Biochemistry," *Ann. Biomed. Eng.,* vol. 3, pp. 335-373, 2001.

[2.6] B. H. Jo, L. M. Van Lerberghe, K. M. Motsegood, and D. J. Beebe, "Three-dimensional micro-channel fabrication in polydimethylsiloxane (PDMS) elastomer," *J. Microelectromech. Syst.,* vol. 9, pp. 76-81, 2000.

[2.7] M. De Volder, F. Ceyssens, D. Reynaerts, and R. Puers, "A PDMS lipseal for hydraulic and pneumatic microactuators," *J. Micromech. Microeng.,* p. 1232, 2007.

[2.8] J. S. Go and S. Shoji, "A disposable, dead volume-free and leak-free in-plane PDMS microvalve," *Sensor Actuator Phys.,* vol. 114, pp. 438-444, 2004.

[2.9] N. L. Jeon, D. T. Chiu, C. J. Wargo, H. Wu, I. S. Choi, J. R. Anderson, and G. M. Whitesides, "Design and Fabrication of Integrated Passive Valves and Pumps for Flexible Polymer 3-Dimensional Microfluidic Systems," *Biomed. Microdevices,* vol. 4, pp. 117-121, 2002.

[2.10] H. Sato, S. Ito, K. Tajima, N. Orimoto, and S. Shoji, "PDMS microchannels with slanted grooves embedded in three walls to realize efficient spiral flow," *Sensor Actuator Phys.,* vol. 119, pp. 365-371, 2005.

[2.11] Y. S. Shin, K. Cho, S. H. Lim, S. Chung, S. J. Park, C. Chung, D. C. Han, and J. K. Chang, "PDMS-based micro PCR chip with Parylene coating," *J. Micromech. Microeng.,* vol. 13, pp. 768-774, 2003.

[2.12] B. A. Fogarty, K. E. Heppert, T. J. Cory, K. R. Hulbutta, R. S. Martin, and S. M. Lunte, "Rapid fabrication of poly(dimethylsiloxane)-based microchip capillary electrophoresis devices using CO2 laser ablation," *The Analyst,* vol. 130, pp. 924-930, 2005.

[2.13] C. S. Effenhauser, G. J. M. Bruin, A. Paulus, and M. Ehrat, "Integrated Capillary Electrophoresis on Flexible Silicone Microdevices: Analysis of DNA Restriction Fragments and Detection of Single DNA Molecules on Microchips," *Anal. Chem.,* vol. 69, pp. 3451-3457, 1997.

[2.14] J.-S. Kim and D. Knapp, R. , "Miniaturized multichannel electrospray ionization emitters on poly(dimethylsiloxane) microfluidic devices," *Electrophoresis,* vol. 22, pp. 3993-3999, 2001.

[2.15] S. Y. Chou, P. R. Krauss, and P. J. Renstrom, "Imprint of sub-25 nm vias and trenches in polymers," *Appl. Phys. Lett.,* vol. 67, pp. 3114-3116, 1995.

[2.16] M. Bender, U. Plachetka, J. Ran, A. Fuchs, B. Vratzov, H. Kurz, T. Glinsner, and F. Lindner, "High resolution lithography with PDMS molds," *J. Vac. Sci. Technol. B,* vol. 22, pp. 3229-3232, 2004.

[2.17] L. Malaquin, F. Carcenac, C. Vieu, and M. Mauzac, "Using polydimethylsiloxane as a thermocurable resist for a soft imprint lithography process," *Microelectron. Eng.,* vol. 61-62, pp. 379-384, 2002.
[2.18] S. Camou, "PDMS 2D optical lens integrated with microfluidic channels: principle and characterization," *LOC,* vol. 3, p. 40, 2003.
[2.19] K. Hosokawa, K. Hanada, and R. Maeda, "A polydimethylsiloxane (PDMS) deformable diffraction grating for monitoring of local pressure in microfluidic devices," *J. Micromech. Microeng.,* vol. 12, pp. 1-6, 2002.
[2.20] H. C. Ko, M. P. Stoykovich, J. Song, V. Malyarchuk, W. M. Choi, C.-J. Yu, J. B. Geddes Iii, J. Xiao, S. Wang, Y. Huang, and J. A. Rogers, "A hemispherical electronic eye camera based on compressible silicon optoelectronics," *Nature,* vol. 454, pp. 748-753, 2008.
[2.21] M. Paranjape, J. Garra, S. Brida, T. Schneider, R. White, and J. Currie, "A PDMS dermal patch for non-intrusive transdermal glucose sensing," *Sensor Actuator Phys.,* vol. 104, pp. 195-204, 2003.
[2.22] Z. Gao, J. S. Nahrup, J. Mark, E. , and A. Sakr, "Poly(dimethylsiloxane) coatings for controlled drug release. I. Preparation and characterization of pharmaceutically acceptable materials," *J. Appl. Polym. Sci.,* vol. 90, pp. 658-666, 2003.
[2.23] J. Mark, *Polymer Data Handbook*: Oxford University Press, Inc, 1999.
[2.24] Gelest Inc., "Gelest Reactive Silicones: Forging New polymer Links."
[2.25] DowCorningCorporation, "Product Information: Sylgard 184 Silicone elastomer." vol. Form 10-898F-01.
[2.26] H. Schmid and B. Michel, "Siloxane Polymers for High-Resolution, High-Accuracy Soft Lithography," *Macromolecules,* vol. 33, pp. 3042-3049, 2000.
[2.27] H. Lorenz and et al., "SU-8: a low-cost negative resist for MEMS," *J. Micromech. Microeng.,* vol. 7, p. 121, 1997.
[2.28] A. Folch, A. Ayon, O. Hurtado, M. A. Schmidt, and M. Toner, "Molding of Deep Polydimethylsiloxane Microstructures for Microfluidics and Biological Applications," *J. Biomech. Eng.,* vol. 121, pp. 28-34, 1999.
[2.29] W. Wang and S. A. Soper, *Bio-MEMS: Technologies and Applications*: CRC Press, 2007.
[2.30] Y. Xia, J. Tien, D. Qin, and G. M. Whitesides, "Non-Photolithographic Methods for Fabrication of Elastomeric Stamps for Use in Microcontact Printing," *Langmuir,* vol. 12, pp. 4033-4038, 1996.
[2.31] E. Delamarche, H. Schmid, B. Michel, and H. Biebuyck, "Stability of molded polydimethylsiloxane microstructures," *Adv. Mater.,* vol. 9, pp. 741-746, 1997.
[2.32] D. Haefliger, M. Nordstrom, P. A. Rasmussen, and A. Boisen, "Dry release of all-polymer structures," *Microelectron. Eng.,* vol. 78-79, pp. 88-92, 2005.
[2.33] T. N. Kim, K. Campbell, A. Groisman, D. Kleinfeld, and C. B. Schaffer, "Femtosecond laser-drilled capillary integrated into a microfluidic device," *Appl. Phys. Lett.,* vol. 86, pp. 201106-3, 2005.
[2.34] J. Garra, T. Long, J. Currie, T. Schneider, R. White, and M. Paranjape, "Dry etching of polydimethylsiloxane for microfluidic systems," *J. Vac. Sci. Technol. A,* vol. 20, pp. 975-982, 2002.
[2.35] H. Becker and U. Heim, "Hot embossing as a method for the fabrication of polymer high aspect ratio structures," *Sensor Actuator Phys.,* vol. 83, pp. 130-135, 2000.
[2.36] T. Bailey, B. J. Choi, M. Colburn, M. Meissl, S. Shaya, J. G. Ekerdt, S. V. Sreenivasan, and C. G. Willson, "Step and flash imprint lithography: Template surface treatment and defect analysis," *J. Vac. Sci. Technol. B,* vol. 18, pp. 3572-3577, 2000.

[2.37] R. H. Pedersen, O. Hansen, and A. Kristensen, "A compact system for large-area thermal nanoimprint lithography using smart stamps," *J. Micromech. Microeng.,* p. 055018, 2008.
[2.38] N. Jagannathan and P. Ian, "Polymer embossing tools for rapid prototyping of plastic microfluidic devices," *J. Micromech. Microeng.,* vol. 14, p. 96, 2004.
[2.39] M. Tormen, T. Borzenko, G. Schmidt, J. Liu, and L. W. Molenkamp, "Thermocurable polymers as resists for imprint lithography," *Electron Lett.,* vol. 36, pp. 983-984, 2000.
[2.40] M. Hoh, J. L. Werbin, J. K. Dumas, W. F. Heinz, and J. H. Hoh, "Nanometer-Scale Embossing of Polydimethylsiloxane," *Langmuir,* vol. 26, pp. 2187-2190, 2010.
[2.41] J. Stagg and R. R. A. Syms, "Low Temperature NIL and Bonding," *Unpublished,* 2006.
[2.42] T. Luxbacher and A. Mirza, "Spray Coating for MEMS, interconnects, and advanced packaging applications," in *Sensors*. vol. 16, 1999, pp. 61-64.
[2.43] N. P. Pham, E. Boellaard, J. N. Burghartz, and P. M. Sarro, "Photoresist coating methods for the integration of novel 3-D RF microstructures," *J. Microelectromech. Syst.,* vol. 13, pp. 491-499, 2004.
[2.44] V. K. Singh, M. Sasaki, K. Hane, Y. Watanabe, H. Takamatsu, M. Kawakita, and H. Hayashi, "Deposition of thin and uniform photoresist on three-dimensional structures using fast flow in spray coating," *J. Micromech. Microeng.,* vol. 15, pp. 2339-2345, 2005.
[2.45] N. P. Pham, J. N. Burghartz, and P. M. Sarro, "Spray coating of photoresist for pattern transfer on high topography surfaces," *Journal of Micromechanics and Microengineering,* vol. 15, pp. 691-697, 2005.
[2.46] EV Group, www.EVGroup.com.
[2.47] A. N. Watkins and F. S. Ligler, "Patterned Deposition of Sol-Gel Thin Films Using an Airbrush," *Anal. Lett.,* vol. 33, pp. 1899 - 1912, 2000.
[2.48] F. Bender, L. Wachter, A. Voigt, and M. Rapp, "Deposition of high quality coatings on SAW sensors using electrospray," in *Sensors, 2003. Proceedings of IEEE*, 2003, pp. 115-119 Vol.1.
[2.49] Z. Gao, J. S. Nahrup, J. E. Mark, and A. Sakr, "Poly(dimethylsiloxane) coatings for controlled drug release. I. Preparation and characterization of pharmaceutically acceptable materials," *J. Appl. Polymer. Sci.,* vol. 90, pp. 658-666, 2003.
[2.50] S. Kopetz, D. Cai, E. Rabe, and A. Neyer, "PDMS-based optical waveguide layer for integration in electrical-optical circuit boards," *AEU - International Journal of Electronics and Communications,* vol. 61, pp. 163-167, 2007.
[2.51] W. O. H. Mayer, "Coaxial atomization of a round liquid jet in a high speed gas stream: A phenomenological study," *Exp. Fluid.,* vol. 16, pp. 401-410, 1994.
[2.52] J. C. Lasheras and E. J. Hopfinger, "Liquid Jet Instability and Atomization in a Coaxial Gas Stream," *Annu. Rev. Fluid. Mech.,* vol. 32, pp. 275-308, 2000.
[2.53] S. P. Lin and R. D. Reitz, "DROP AND SPRAY FORMATION FROM A LIQUID JET," *Annu. Rev. Fluid. Mech.,* vol. 30, pp. 85-105, 1998.
[2.54] C. M. Varga, J. C. Lasheras, and E. J. Hopfinger, "Initial breakup of a small-diameter liquid jet by a high-speed gas stream," *J. Fluid Mech.,* vol. 497, pp. 405-434, 2003.
[2.55] A. Aliseda, E. J. Hopfinger, J. C. Lasheras, D. M. Kremer, A. Berchielli, and E. K. Connolly, "Atomization of viscous and non-newtonian liquids by a coaxial, high-speed gas jet. Experiments and droplet size modeling," *Int. J. Multiphas. Flow.,* vol. 34, pp. 161-175, 2008.

[2.56] X. Gamisans, M. Sarrà, F. J. Lafuente, and B. J. Azzopardi, "The hydrodynamics of ejector-Venturi scrubbers and their modelling by an annular flow/boundary layer model," *Chem. Eng. Sci.,* vol. 57, pp. 2707-2718, 2002.
[2.57] J. A. S. Gonçalves, M. A. M. Costa, P. R. Henrique, and J. R. Coury, "Atomization of liquids in a Pease-Anthony Venturi scrubber: Part I. Jet dynamics," *J. Hazard. Mater.,* vol. 97, pp. 267-279, 2003.
[2.58] S. Nukiyama and Y. Tanasawa, "An experiment on the atomization of liquid by means of an air stream," *Trans. Soc. Mech. Engrs. (Japan),* 1938.
[2.59] S. Calvert, "Venturi and other atomizing scrubbers efficiency and pressure drop," *AIChE journal,* vol. 16, p. 392, 1970.
[2.60] M. A. M. Costa, P. R. Henrique, J. A. S. Gonçalves, and J. R. Coury, "Droplet size in a rectangular Venturi scrubber," *Braz. J. Chem. Eng.,* vol. 21, pp. 335-343, 2004.
[2.61] Dow Corning Corporation, "Product Information: Low Viscosity Silicone fluids, 200 Fluid 20cs." vol. Form 25-941-97.
[2.62] Veeco Instruments_Inc., "Surface Texture analysis using Dektak Stylus Profilers." vol. Form AN525-1-1004, 2004.
[2.63] Dow Corning Corporation, "Product Information: Sylgard 184 Silicone elastomer," in *Form 10-898F-01*. vol. Form 10-898F-01.
[2.64] J. C. McDonald, D. C. Duffy, J. R. Anderson, D. T. Chiu, H. Wu, O. J. A. Schueller, and G. M. Whitesides, "Fabrication of microfluidic systems in poly(dimethylsiloxane)," *Electrophoresis,* vol. 21, pp. 27-40, 2000.
[2.65] S. Bhattacharya, A. Datta, J. M. Berg, and S. Gangopadhyay, "Studies on surface wettability of poly(dimethyl) siloxane (PDMS) and glass under oxygen-plasma treatment and correlation with bond strength," *J. Microelectromech. Syst.,* vol. 14, pp. 590-597, 2005.
[2.66] M. J. Owen and P. J. Smith, "Plasma treatment of polydimethylsiloxane," *J. Adhes. Sci. Tech.,* vol. 8, pp. 1063-1075, 1994.

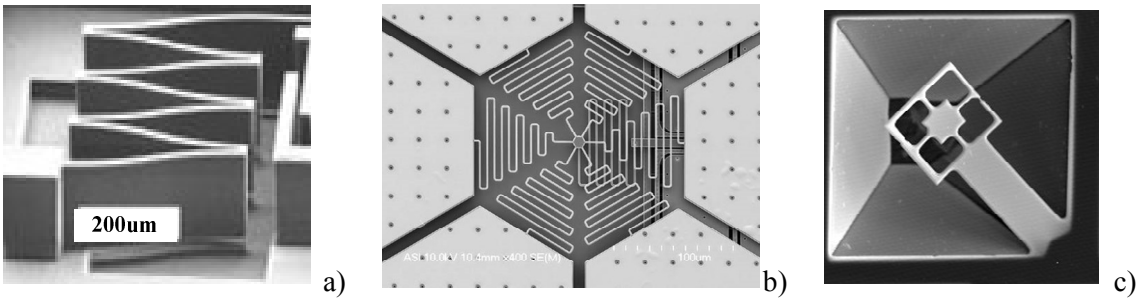
3 Silicon μCP engine

3.1 Introduction - MEMS

As reviewed in Section 1.4.3, alignment tools for μCP include a flexure suspension, an actuation mechanism, and alignment features. MEMS technology has the potential of integrating all these into silicon. A thorough review of microfabrication technology is presented by Madou in [3.1]. Important bulk machining techniques include anisotropic etching of crystalline silicon [3.2], and DRIE which is not restricted by crystal orientation, while the development of the mechanically stable photoresist SU8 [3.3] further enabled the fabrication of high-aspect ratio structures by an additive process. A wide range of micro-actuators has also been developed [3.4] and these typically combine an elastic suspension with an electrostatic, electrothermal, electromagnetic or piezoelectric drive.

3.1.1 Silicon springs

Springs can be formed in silicon by etching and releasing the movable parts and some examples are shown in Figure 3-1. Through-wafer etching and bonding can be used to form in-plane and out-of-plane springs as in Figure 3-1a and b. In BSOI wafers, springs can be fabricated by DRIE of Si followed by isotropic etching of the buried oxide layer to release moving parts [3.5]. Undercutting can also be used with single crystal Si to form thinner springs designed for out-of-plane motion (Figure 3-1c). The size, especially the thickness, of the spring is critical as the spring constant, k, scales as the product of the width , w, and the cube of the thickness, t, divided by the cube of the length, L [3.6].



a) b) c)

Figure 3-1 a) Leaf spring formed by through-wafer DRIE and bonding onto a substrate with pre-etched pits to enable movement [3.7]. The springs joins the proof mass of an accelerometer to its frame. b) Through wafer etched suspended springs [3.8]. c) Thin cantilever spring formed by undercutting [3.9].

3.1.2 Actuation

Silicon MEMS actuators can be classified as electrostatic, piezoelectric, thermal and magnetic [3.10]. Electrostatic actuators are most easily implemented in MEMS since all that is required is a well defined gap, and dielectric and conducting layers. These are easily implemented with microelectronic fabrication technology. An example of an electrostatic comb actuator is shown in Figure 3-2a. Here, the application of a voltage causes the interlocking fingers to attract each other and thus achieve linear in-plane motion. Piezoelectric actuators are well known for their large forces and high-frequency response [3.6, 11]. Deposition of the piezoelectric material, however, is not straightforward. Recent progress in the area is reviewed in [3.12]. Thermally driven MEMS are as simple to implement as electrostatic devices and an example is a 'hot'-arm polysilicon microactuator as described in [3.13] and illustrated in Figure 3-2b. Here, differential expansion of the asymmetric arms due to Joule heating of the different resistive arms drives the device. Other variants of thermal actuators use bi-morph involving materials of different coefficients of thermal expansion [3.6]. Magnetic MEMS are powerful devices capable of holding higher energy densities than electrostatic MEMS [3.6, 14], as well as being able to operate in

conductive fluids. However, integration of the soft magnetic materials (e.g. NiFe) remains problematic.

Driven by development in the area of μTAS, methods of machining non-silicon material have been developed [3.15, 16]. Flexible elastomers like PDMS have proven popular as their microfabrication by moulding is straightforward (see Chapter 2). The elastomeric properties and ability to provide good seals have led to the development of a number of hydraulic and pneumatic devices for microfluidics. However, this actuation mode remains rare in MEMS [3.17].

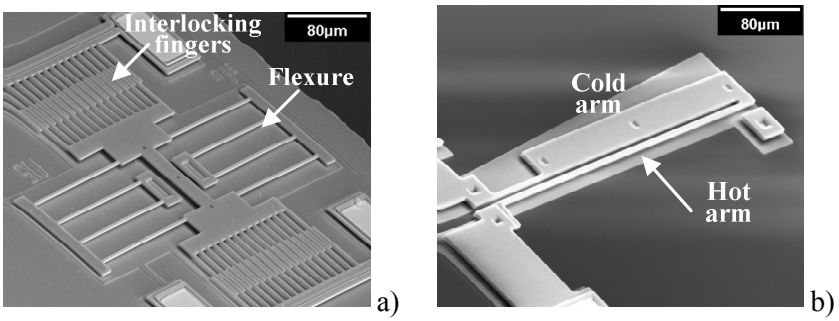
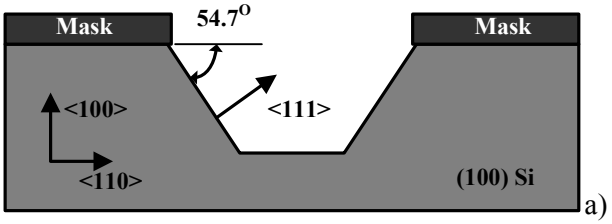


Figure 3-2 MEMS actuators (from [3.18]); a) electrostatic comb drive, b) thermal 'hot'-arm actuator.

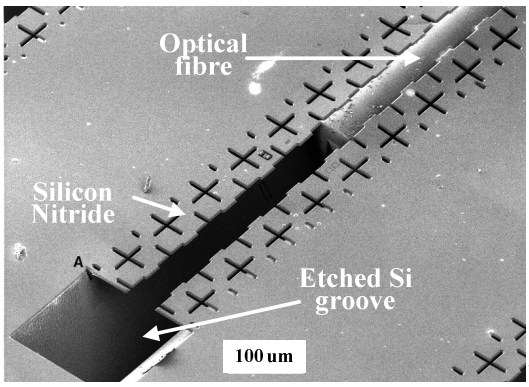
3.1.3 Alignment

Passive mechanical alignment methods for holding optical fibres have been developed using wet-etched V-grooves in combination with boron doped Si [3.19] or Si_3N_4 [3.20] springs. Using complementary pits and raised structures, wafers have been stacked onto each other with sub-micron accuracy [3.21]. This technique has been used to form spacer chips (see e.g. [3.22]) and alignment benches for cylindrical glass capillaries [3.23]. These structures are possible because strong bases like KOH exhibit orientation-dependent etch characteristics in silicon [3.1, 24]. {111} planes etch much less quickly than {100} or {110} planes and this

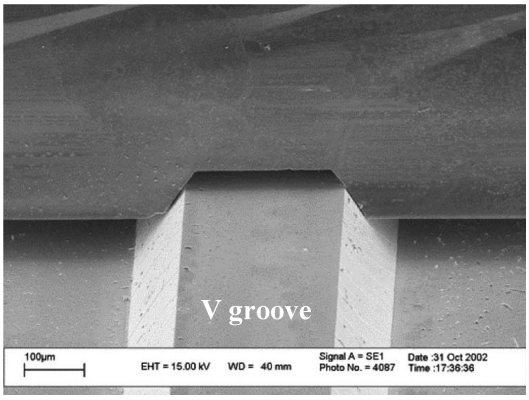
allows the creation of slanted features. Masking material for a KOH etch include thermally grown SiO_2, which etches slowly, or Si_3N_4, which is virtually untouched. For a (100) oriented Si wafer, which is often used in MEMS, the {111} planes make an angle θ with the wafer plane, where $\tan(\theta) = \sqrt{2}$, that is $\theta = 54.74°$. Therefore, when a square opening aligned to the primary flat of the (100) wafer is etched with KOH, an inverse pyramidal structure (a V-groove) is revealed, with the {111} planes forming the slanting angle. This is illustrated in Figure 3-3a. Figure 3-3b and c show SEMS highlighting applications of these structures as passive alignment mechanisms. The former shows a groove with overhanging silicon nitride springs that are used to guide and fix an optical fibre while the latter shows complementary groove and rail used to align two silicon parts.



a)



b)



c)

Figure 3-3 a) Illustration of crystal-plane orientation. b) Etched Si V-grooves combined with silicon nitride mechanical springs for aligning and fixing optical fibres [3.20]. c) Spacer chip formed by a matching teeth and grooves in single crystal silicon[3.22].

3.1.4 Outline of this chapter

In this chapter, the different elements above are integrated into a miniature silicon μCP engine. The device layout and fabrication is described and prototypes are characterised. Although the design is initially intended to be electrostatically driven, μCP has only reliably been achieved by manually deflecting the print head. In this chapter, for clarity, the emphasis is on the mechanical design and characterisation, whilst the electrostatic operation is analysed in detail in Chapter 4. The prototype devices are formed in both BSOI and single crystal (100) Si with an overall device size of c.a. 10 mm × 10 mm and a print area of c.a. 5 mm × 5 mm. Manually actuated μCP of hexadecanethiol (HDT) is carried out and the results, including multi level printing, are presented.

3.2 Concept and Design

3.2.1 Concept

Features that are required for μCP, such as flexure suspension, an actuation mechanism, and alignment features, as well as a hard backed soft stamp, are all combined into a silicon chip measuring c.a. 10 mm × 10 mm with an overall print area is c.a. 5 mm × 5 mm. The device could be made in BSOI or single crystal Si. The printing chip consists of a print head (carrying a PDMS stamp) attached to a rigid supporting frame via a suitable elastic flexure (which could be "thin" Si). The rigid frame would provide mechanical stability and contain the alignment features that would mate with corresponding features on a substrate. The elastic suspension would allow controlled out of plane deflection of the print head towards the substrate (Au typically). The PDMS pattern on the chip would be inked the usual way (see e.g. [3.25]), registered to the substrate using the alignment marks, deflected downwards to

make contact, and then retracted. Thus, all the µCP features are self contained within the chip and the substrate.

3.2.2 Self-alignment

Passive alignment features, such as U-grooves formed by DRIE and optical fibres (a), or V-grooves and rails formed by anisotropic wet chemical etching (b), have been used previously for electrical [3.22] or optical [3.26]connectors.

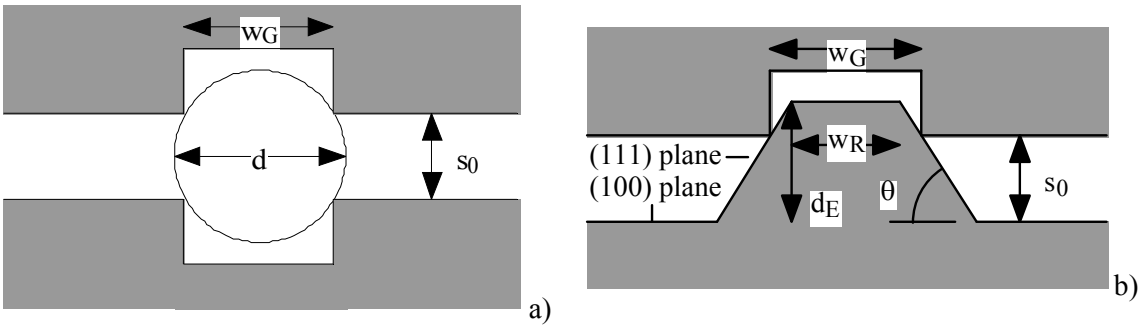


Figure 3-4 Self Alignment: a) U-grooves and fibre. b) V-grooves and rail

In the case of U-grooves and fibres, the grooves on both the engine and the substrate can be fabricated by DRIE. The optical fibre of diameter, d, (which also provides electrical insulation) and the groove width, w_G, determine the flying height, s_O as:

$$s_o = d\sqrt{1 - \left(\frac{w_G}{d}\right)^2} \tag{3.1}$$

For example, with w_G = 120µm, and single-mode fibres with d = 125µm, s_O = 35µm. Smaller separations are harder to achieve due to the limited availability of fibre diameters and due to high sensitivity to the groove width ($\partial s_O/\partial w_G \to \infty$ as $s_o \to 0$).

Rails formed by crystal plane etching (b) provide a slanting surface with constant slope, θ, and may be more appropriate for small separations, although they restrict the substrate to crystalline Si. Additional insulation layers can be grown if required. The flying height is determined from the etch depth d_E as:

$$s_0 = d_E - \left(\frac{1}{2}(w_G - w_R)\ \tan\theta\right) \tag{3.2}$$

Here θ is the angle between the (100) and (111) planes, and $\tan(\theta) = \sqrt{2}$. In this case, small separations may be achieved provided d_E may be suitably controlled.

3.2.3 Flexure – Elastic Suspension

Fixed-guided springs (see e.g. [3.27]) are used to enable out of plane translation. Each spring is fixed at one end (the end connected to the frame of the engine) while the other "guided" end is attached to the movable print head. With a symmetric design as in a, other displacement modes such as lateral in plane translation, is minimized.

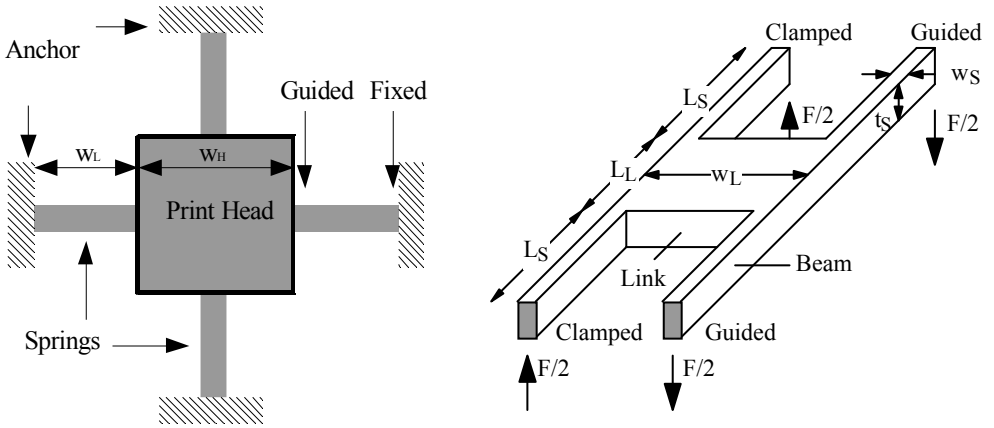


Figure 3-5 Elastic Suspension: a) Overall chip. b) Individual Springs

Each spring is implemented by the structure shown in b. It consists of four beams of length L_S, width w_S and thickness t_S on each side of a square print head of dimension w_H. Within each set, the bars are arranged in two pairs, connected by a rigid link bar of length w_L. The stiffness of this arrangement is simple to estimate. Deflection will arise from a combination of bending and torsion. Provided the material is linear, and the effects of bending and torsion do not interact, the deflections may be found separately and summed [3.27, 28]. For example, through bending alone, each bar will deflect as a clamped-guided beam with stiffness [3.29]:

$$k_{L1a} = \frac{12EI_S}{L_S^3} \tag{3.3}$$

Here E is the Young's modulus of the beam material, and I_S is the second moment of area of the cross-section, given by $I_S = w_S t_S^3/12$. Each set of four bars is arranged as a series-parallel combination, so their total stiffness is again k_{L1a}. For all four springs together, the combined stiffness is $k_{La} = 4k_{L1a}$.

The contribution of torsion to deflection may be found in a similar way. For a rectangular section measuring $w_S = 2a$ by $t_S = 2b$, and for $a \geq b$, the torsion constant is [3.29]:

$$k_T = ab^3 \left\{ \frac{16}{3} - 3.36 \left(\frac{b}{a}\right) \left[1 - \frac{b^4}{12a^4}\right] \right\} \tag{3.4}$$

The torque T required to twist one bar through an angle α is $T = Gk_T \alpha/L_S$, where G is the shear modulus of the beam material. If the torque is generated by a force F at a distance w_L,

we may write $F = T/w_L$, and if the twist due to F results in a linear displacement Δs we may put $\alpha = \Delta s/w_L$. The effective linear stiffness arising from the twist is then:

$$k_{L1b} = \frac{F}{\Delta s} = \frac{Gk_T}{L_S w_L^2} \tag{3.5}$$

In torsion, all bars act in parallel, so the total stiffness is $k_{Lb} = 16k_{L1b}$. If bending and torsion are considered together, the overall stiffness k_L can be found from:

$$\frac{1}{k_L} = \frac{1}{k_{La}} + \frac{1}{k_{Lb}} \tag{3.6}$$

Because of the dependence on k_{Lb} on the link bar length w_L, the relative contributions of bending and torsion to deflection can vary, and if w_L is sufficiently large, torsion dominates.

For Si(100), Young's modulus $E = 130\times10^9$ N/m^2 and a shear modulus of $G = 79\times10^9$N/m^2 are assumed [3.30]. Using design values of w_S=100 μm, L_S = 1.6 mm, and a link bar length w_L = 1.0 mm, and a typical suspension thickness of t_S = 80 μm, an overall spring constant of $k_L \approx 3.4$ mN/μm is obtained using equations (3.3-3.6). FEA of the spring structure of Figure 3-5b was carried out using Abaqus 6.8-1 to verify these basic conclusions, and it was found that the estimated stiffness was higher than the simulated value by around 40%, presumably due to neglect of link bar deformation. In addition, for deflections of up to the 100 μm, the value of k_L remained unchanged within 10 %, as illustrated in Figure 3-6.

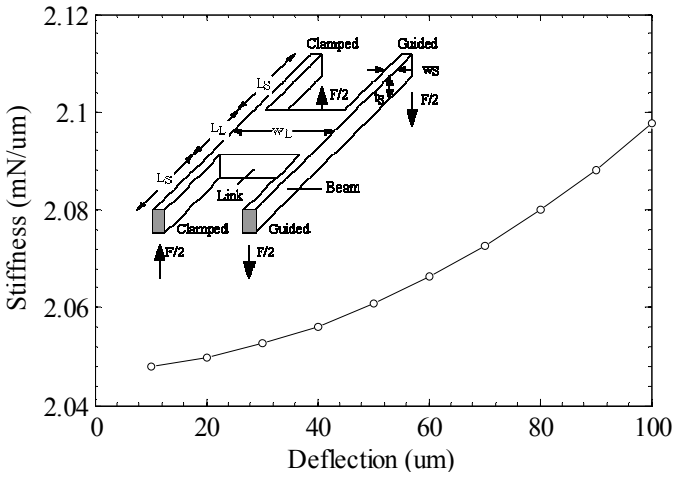


Figure 3-6 Variation of system stiffness with displacement

.

3.2.4 Print head

The print head influences mainly three aspects of operation: static sag (i.e. the deflection of the head when no load is applied due to its weight), stiction to the substrate after contact, and dynamic oscillations. For a block of thickness t_{SUB} (which is ≈500μm) and area A, and formed in a material of density ρ, the static sag, Δs_0, is given by $\Delta s_0 = At_{SUB}\rho g/k_L$, where g = 9.81 ms^{-2}. The variation of Δs_0 for different values of k_L is verified by plotting Δs_0 against w_S for different values of t_S. This is illustrated in Figure 3-7a, and clearly, for w_S > 50 μm, the static sag is sub-micron and negligible.

The print head, which essentially a proof mass is held by a spring may oscillate during actuation or retraction. The resonant frequency for the primary linear mode is given by $f_0 = 1/2\pi(k_L/\rho t_{SUB}A)^{1/2}$. The variation of f_0 with spring dimensions is illustrated in b, and lies in the kHz range, and should not interfere with the device when it is driven at dc.

.

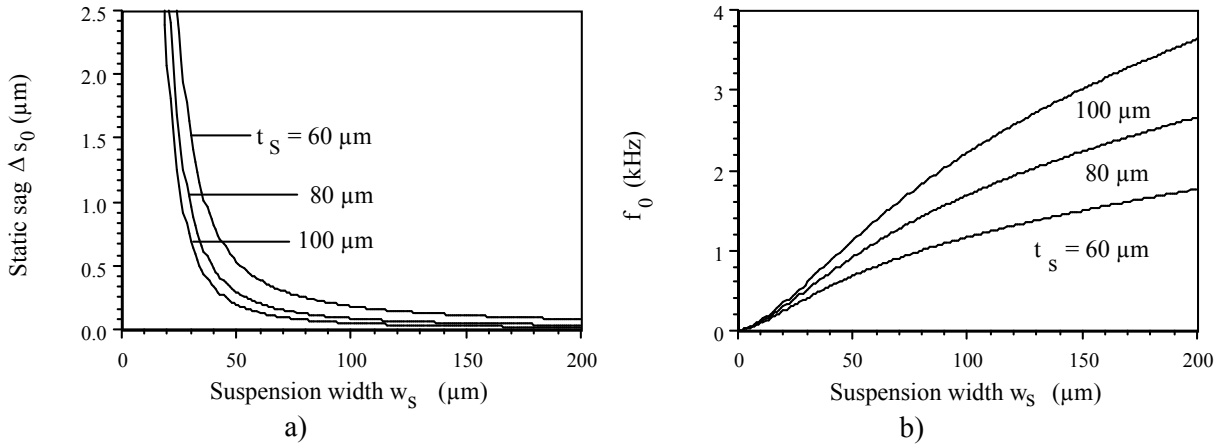


Figure 3-7 Variation of a) static sag, b) resonant frequency, with spring dimensions.

After contacting the substrate, the print head may not retract if the spring is not stiff enough to overcome the adhesion at the surface. This stiction problem is common in micromachining and has led to methods for determination of the work of adhesion in microstructures [3.31, 32]. Assuming that the fraction of the stamp (of area A) that is patterned is f, the work required to detach the stamp is $f \times A \times W$, where W is the work of adhesion. Hence, for stamp retraction, the elastic energy stored in the suspension needs to be greater, that is: $k_L s_0^2/2 > f \times A \times W$.

For a print head carrying a PDMS stamp, the relevant value of W to use is that of PDMS on gold (which is the typical substrate) which is equal to 0.5 J/m^2 [3.33]. Assuming f=1, and using A = 5 mm × 5 mm, and s_0 = 60 μm, the lower limit on the spring stiffness is: k_L > 6.94 mN/μm. This is easily achieved since, in practice, f will be much less than unity.

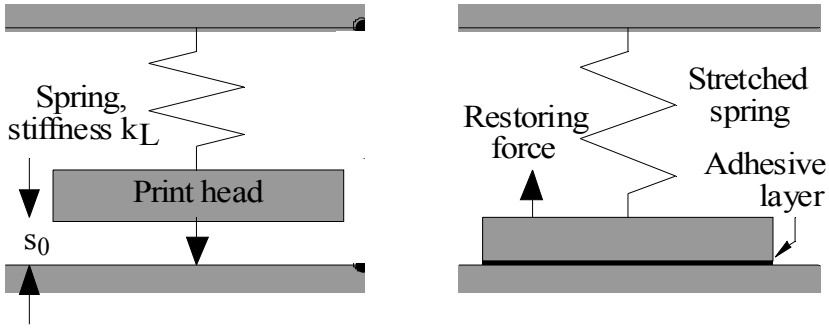


Figure 3-8 Print head deflection and retraction

3.2.5 PDMS Stamp

PDMS, under the commercial brand of Sylgard 184, is the elastomer usually used in μCP printing. It is, however, quite porous and tends to swell when exposed to a number of solvents, and can sustain temperatures of up to 200°C only [3.34], making it incompatible with a number of MEMS fabrication steps.

To circumvent this, the approach adopted here is to deposit the PDMS layer at the end of the MEMS fabrication using the method developed in Chapter 2. The silicon print head will carry raised features (≈10μm), which are formed by conventional lithography followed by DRIE. These are then conformally spray coated. Apart from successful process integration, this approach provides a relatively thin elastomer layer on a rigid substrate, which has been shown to reduce stamp distortion in μCP [3.35].

3.2.6 Actuation

A number of actuation mechanisms (e.g. manual, pneumatic, electrostatic or piezoelectric) can be used in combination with the above described prototype. The easiest and simplest method is manual, which does not restrict the choice of substrate but may result in

uncontrolled printing. Pneumatic systems, although substrate independent, would require a reliable seal to a plenum chamber above the stamper. Piezoelectric would require specialized materials and would over-complicate the device fabrication. Electrostatic actuation does require conducting electrodes, but this inherent in the alkanethiol–gold system anyway.

The prototype devices were designed with both manual and electrostatic drives in mind. However, the latter approach is problematic and is discussed in the next chapter. A parameter worth noting, however, is the pull-in voltage (V_{PI}) given by $V_{PI} = (8k_L s_0^3/27\varepsilon_0 A)^{1/2}$. For a varactor separated by an air gap, V_{PI} represents the drive voltage at which the stamp would contact the substrate, and should be kept as low as possible. The pull-in voltage varies as $\sqrt{k_L}$, and as $\sqrt{s_0^3}$ and these relationships impose upper bounds on the stiffness of the device and the flying height.

3.2.7 Prototype layout and operation

The layout of the prototype printing engine is illustrated in Figure 3-9a. Each device contains a print head carrying a raised pattern and supported on an elastic suspension allowing out-of-plane deflection. The engine's surround is grooved to mate with a rail pattern arranged on a grid. The device may easily be constructed in single crystal silicon or BSOI. Parts requiring mechanical strength (the print head and surround) are formed in the substrate and flexible parts (the suspension) in a thinner layer. The stamp pattern itself is ideally formed in or coated with PDMS. Figure 3-9b shows the operation. After coating the stamp with alkanethiol, the engine is placed over a substrate containing compatible alignment features that define its position, parallelism and height s_0. The head is deflected down to print, and finally retracted.

.

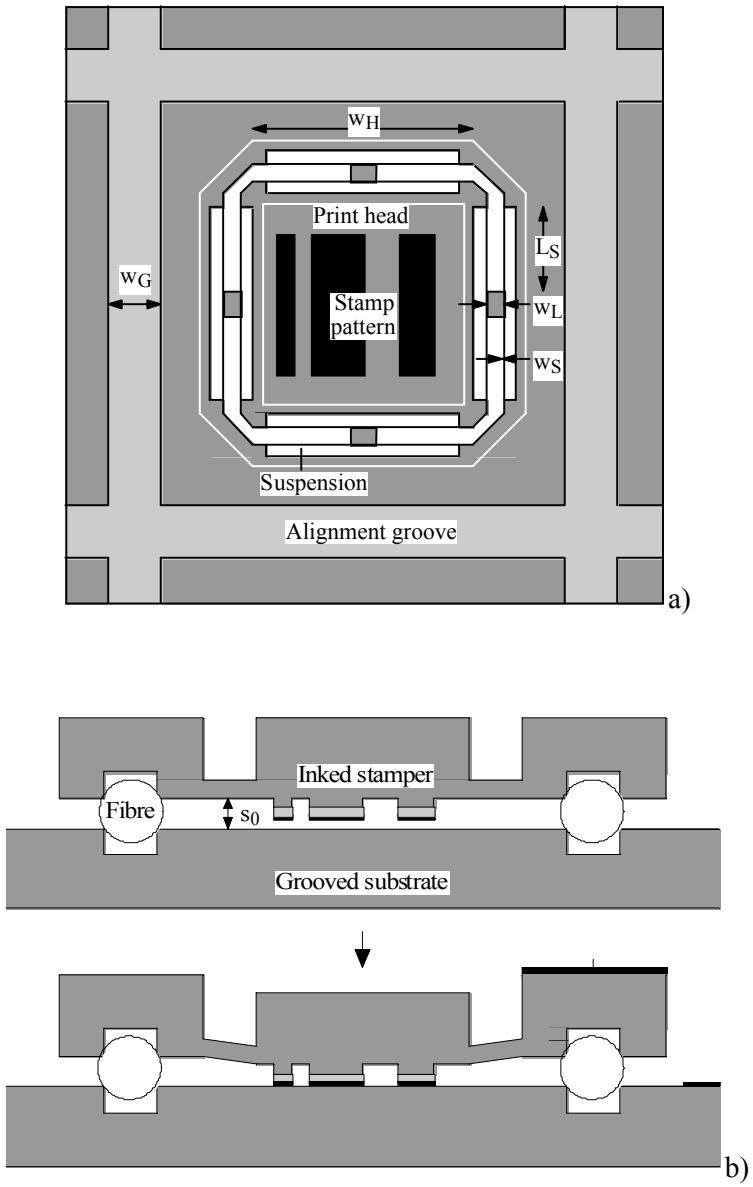


Figure 3-9 a) Plan and b) section view of a silicon µCP engine, showing alignment and deflection.

3.3 Fabrication

The materials and processes used for wafer scale fabrication of the prototype μCP engine are described in this Section. The process has been developed for both single-crystal silicon and BSOI. Bare silicon is obviously preferable on the grounds of cost. However, BSOI allows accurate definition of the thickness t_S of the elastic layer (here, 80 μm) and hence more controllable operation. In each case, 100 mm diameter (100) orientated wafers were used. BSOI wafers were obtained from Icemos, Belfast, UK with a bonded layer thickness of 80 μm and a buried oxide thickness of 2 μm. Prototypes were constructed with the layout of Figure 3-9a, an overall die size of 10 mm × 10 mm and the dimensional parameters described in Section 3.2. Two different device stiffnesses per wafer were obtained by setting w_S to 100 μm and 200 μm on different dies. Each wafer contained 36 devices.

3.3.1 Process Flow

Figure 3-10 shows the process flow for single crystal silicon and detailed process parameters are given in Table 3-1. The rear side of the substrate was first patterned with positive resist to define the elastic suspension and snap out groove, and this pattern was transferred to a set depth (400 μm etch depth for t_S = 150 μm) by deep reactive ion etching (step 1). Etching is carried out using a Surface Technology Systems inductively coupled plasma etcher, using a cyclic etching process based on SF_6 and C_4F_8 [3.36]. The resist was then stripped and the rear side was coated with 10 μm thick electroplated Ni (not shown). This metal layer strengthens the wafer, acts as etch stop, and maintains a hermetic seal during the subsequent through-etch from the front side. This is not required in BSOI wafers as the oxide layer plays this role. The front side was then patterned to define the stamp pattern, using a through-wafer mask-aligner (Quintel IR 4000). However, front-to-back alignment is not critical. The stamp pattern is

formed by optical exposure of 2 μm thickness of SU-8 2002 epoxy photoresist (Microchem) [3.37], followed by further 10 μm deep reactive ion etching (step 2). The front side was then patterned to define the elastic suspension and alignment grooves. Registration of the two front-side patterns is important, since it defines the relative position of the stamp and the alignment grooves (step 3). This final pattern is transferred down by DRIE to meet the original back-etch. Remaining resist and the etch stop layer (Ni for single crystal or oxide for BSOI) are then removed and 300 Å Cr and 1000 Å of Au is sputtered over the rear of the wafer for electrical contact (step 4). Individual engines are removed for use by breaking small silicon tabs (step 5). To allow the adsorption of alkanethiols, the stamp is spray coated with PDMS through a stencil (step 6), as described in Chapter 2.

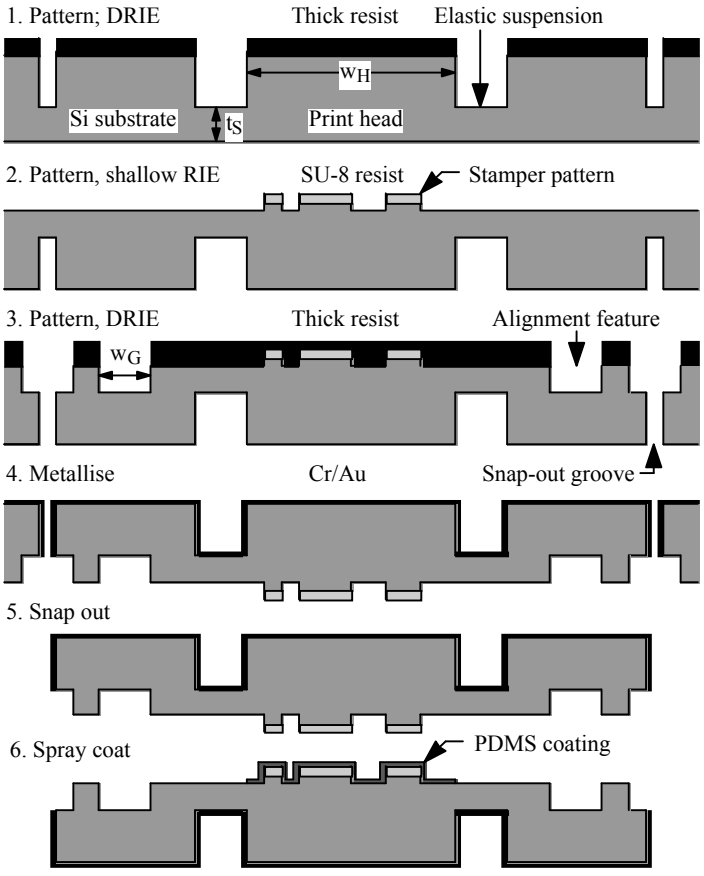


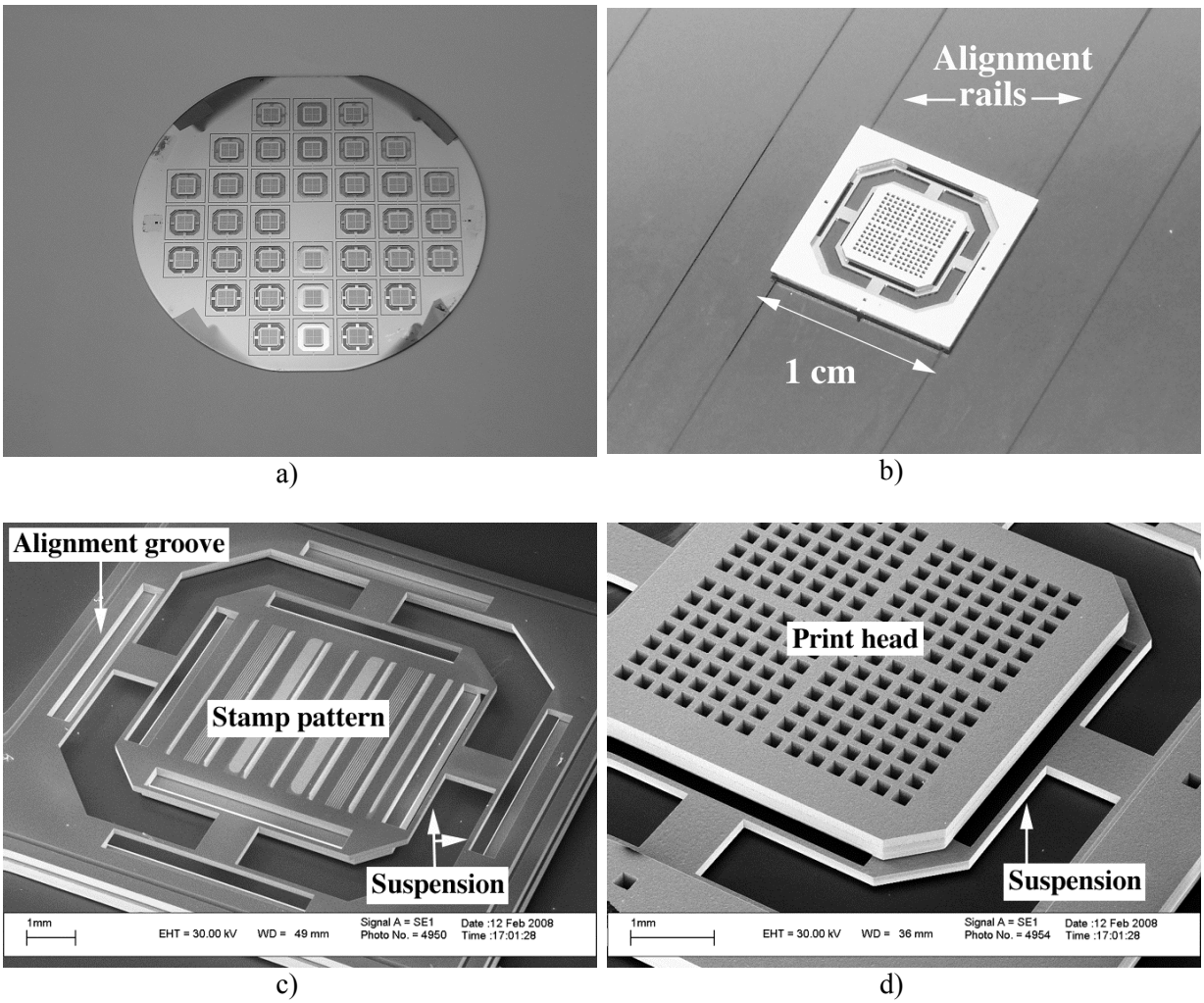
Figure 3-10 Process flow for μCP engine. Main steps are: elastic suspension patterning, stamper features formation, alignment groove and snap out tab etching, die release, and PDMS coating.

Si µCP engine		
Fabrication step	**Sub-steps**	**Parameters**
1. Rear side Patterning	Lithography 8 µm	- AZ9260, 8 µm thick, Spin1 : 500rpm, 5000rpm/s, 10 s, Spin2: 2000rpm, 5000rpm/s, 40 s - Softbake: 100 C (HP) - 2 min - Exposure 600 mJ/cm^2 - Develop :AZ400K:DI 1:4 (5 min) - Postbake: 120 ^{o}C (HP) – 2 min
	DRIE 400 µm (STS ICP)	- Recipe: LCD1 (stored on STS system) - Duration: 170 min
	Resist Strip	1165 @ 70 C immersion (30 min). DI rinse O_2 plasma clean:
	Nickel plating: 10 µm (skip for BSOI version)	- Sputter seed layer: 30 nm Cr/ 200 nm Cu - Solution: Nickel Sulphamate (Ni(SO3NH2)2.nH2O), 65%, 3.45L; Nickel Chloride,50g; Boric Acid, 350g; DI water, 10L - Bath temperature: 50 C, Plating current: 300 mA - Plating time: 90 min
2. Front side Stamper Patterns	Lithography 1.8 µm	- SU8 2002, 1.8 µm, Spin1: 500rpm/ 100rpms^{-1}/5s. spin 2: 1000rpm/ 200rpms^{-1}/60s - Softbake: 65 C (HP) - 1 min, 90 C (HP) – 2 min - Exposure 500 mJ/cm^2 . Post exposure bake: 50 ^{o}C (HP) – 1min, 75C (HP) – 5min, allow to cool down to <40 ^{o}C (HP). - Develop :EC Solvent (5 min), then IPA rinse
	DRIE 10 µm	- Recipe: LCD1 (stored on STS system) - Duration: 7 min
3. Front side Elastic Suspension	Lithography 8 µm	Same as lithography of step 1.
	DRIE	- Etch through to metal layer 200 µm (For BSOI etch to oxide layer) - Recipe: LCD1, Duration: 80 min
	Resist strip	1165 @ 70 C immersion (30 min). DI rinse O_2 plasma clean:
	Nickel layer strip (Rear side)	- Ni etchant, immersion (10 min) - Cr etchant immersion (2 min)
4.Metallise Rear side	Sputter coating (Nordiko)	- 30 nm Cr (adhesion) - 100 nm Au
5. Snap out		- Manually break tabs to release dies ~ 100% yield
6. PDMS Spray coating	3 µm thick PDMS	Fluid 20Cs diluted PDMS. Driving pressure: 60 psi. Chuck rotation: 600 rpm. Chuck temperature: 25 C. Separation : 50 mm. Spray duration: 10 s

Table 3-1 Process parameters for Si µCP engine

3.3.2 Prototype Devices

Prototype devices are shown here. Figure 3-11a shows the rear side of a completed 100mm wafer. The wafer is strong enough to handle provided the print heads are not subjected to excessive shock. Figure 3-11b shows a detached device mounted on an etched rail system (described in Figure 3-4b). Figure 3-11c shows a SEM view of the front side of the device. The parallel lines are ≈12µm tall with widths as small as 2µm. Figure 3-11d shows the rear of the device. The waffle pattern is to reduce mass and hence shock sensitivity.



a) b)

c) d)

Figure 3-11 Optical image of finished device (single crystal Si)) a) in a whole wafer, b) after detaching and aligning on machined target substrate. SEM images of c) bottom view, d) top of device.

3.4 Mechanical characterisation

3.4.1 Measurement of stiffness

Mechanical characterisation was performed by placing calibrated weights on the print head and measuring the relative vertical deflection. This was done by using an optical microscope equipped with a Mitutoyo height gauge. The stiff single crystal devices (t_S = 160 μm) required heavy loads to obtain any detectable deflection and could not be characterised using this method as heavy weights would not fit in the gap between the objective and the device. The deflection-load characteristics of the BSOI device (t_S = 80 μm) for different w_S, 100 μm and 200 μm, are shown in Figure 3-12 and the stiffnesses (k_L) are obtained from the inverse slopes as 1.6 mN/μm and 2.6 mN/μm. The simplified model of Section 3.2.3, i.e. equations (3.3-3.6), overestimate these values by 52% and 68% respectively. This is consistent with the FEA of Section 3.2.3 which predicts a lower stiffness due to bending of the link bar.

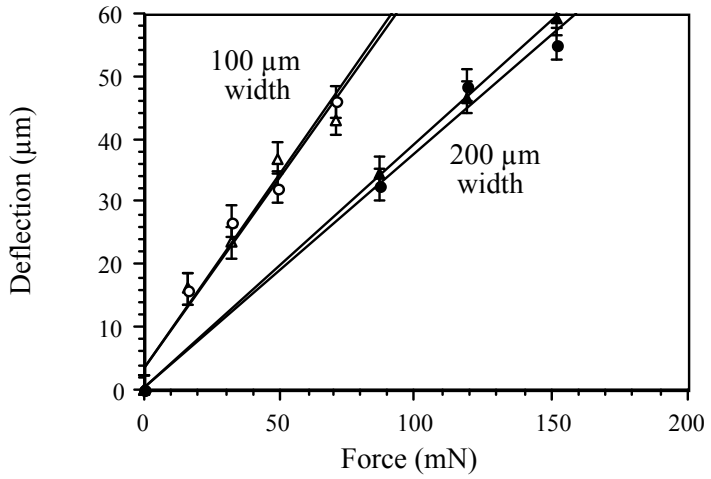


Figure 3-12 Load deflection characteristic for BSOI devices

3.4.2 Manually actuated µCP

Micro-contact printing was carried out using 0.5 mM HDT solution (see Appendix A for detailed procedure). Stamps were coated with ink using a brush and then blown dry in N_2. Pattern transfer was achieved by contacting the inked stamp to Si surfaces coated with 30 nm Au for around 1 minute, and stamps were cleaned of ink residues between prints using ethanol. Patterns were transferred into the gold, by etching exposed Au. The print quality is not currently uniform over the full area of the stamp. Pits as well as broken lines have been observed. This can be attributed to the PDMS spray coating process which involves jet break-up into discrete droplets. An SEM of a spray coated stamp pattern is shown in Figure 3-13 and distinct droplets are clearly visible.

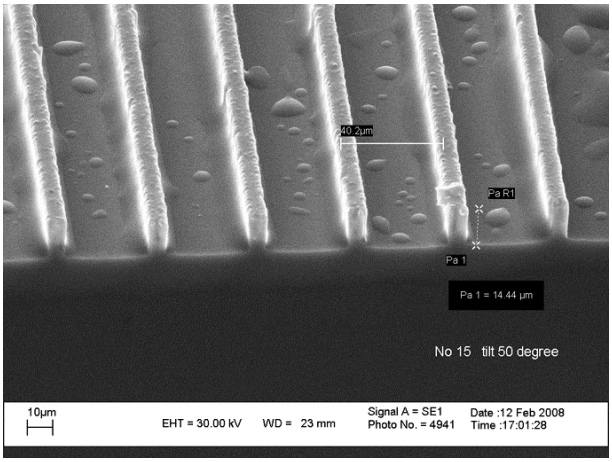


Figure 3-13 Stamp pattern with SU-8 photoresist and Si after PDMS spray coating.

Manually actuated printing was performed using bare silicon devices, since their suspensions were more robust. Inked print engines were placed on a gold-coated substrate carrying a pair of etched alignment rails, as shown in Figure 3-4b and Figure 3-11b, and a pair of tweezers was used to deflect the print head down to the substrate. The printed pattern was revealed by etching away the uncovered Au using the protocol described in Appendix A. Single-layer

printing was demonstrated first. SEM imaging was used to verify pattern transfer. 5μm and 10μm lines were reliably and uniformly imaged, as illustrated in Figure 3-14.

Multilayer printing was then demonstrated. Figure 3-15 shows patterns formed by printing once, rotating the print engine through 90°, replacing it on the rail and printing a second time. Here, lines of width down to 2 μm have been transferred, although there is some fragmentation of narrow lines attributed to poor stamp quality. The increased pattern width at line intersections is evidence of ink diffusion. Large area patterning, >3mm×3mm, is illustrated in Figure 3-15d. To demonstrate aligned printing, which really requires two stamps with complementary patterns, a single stamp was used. A first imprint was made, the stamp was then shifted laterally by ≈ 1 mm, and a second imprint was made. The combined pattern was then transferred into the gold by etching away the uncontacted metal using a cyanide based etchant (see Appendix A). Figure 3-16 shows the result. The boundary between the two imprints lies in the centre of the figure. The quality of the second print is unfortunately low, but the overlay error is extremely small.

3.5 Discussion

MEMS technology has been used to construct a µCP engine combining a print head, a pattern, a mechanical alignment system and a flexure suspension. Although work remains to be done to improve pattern quality, it is clear that µCP using a MEMS printing engine is a viable solution. In manual operation, once the device (and corresponding substrate) is fabricated, no additional equipment is required for multilevel patterning.

As for high resolution, it definitely possible to reduce the line width of the underlying Si structure using techniques such as electron beam lithography (see e.g. [3.1]), but an interesting question is the minimum size definable using the spray coating process. Furthermore, statistical analysis of the overlay accuracy would quantify the capability for multilevel printing, and this requires suitable complementary patterns.

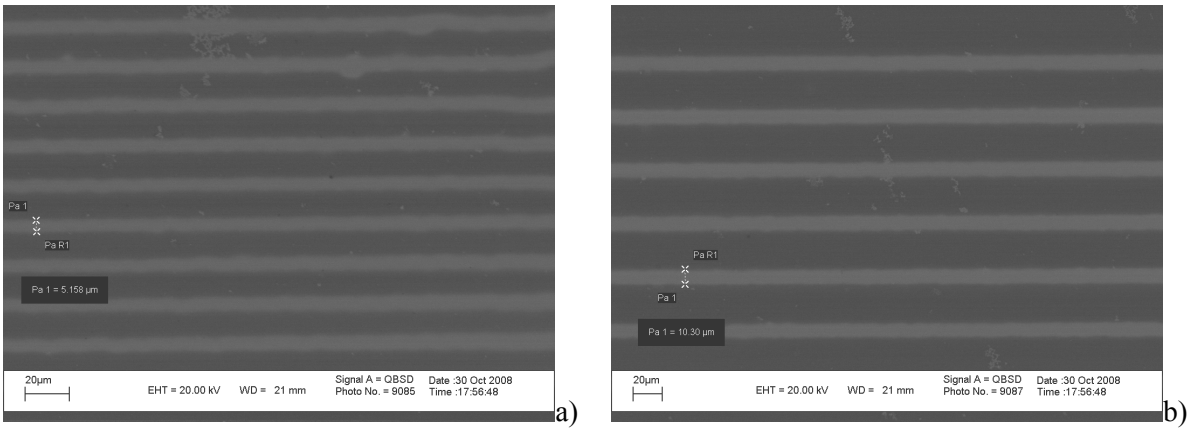


Figure 3-14 SEM of patterned 5µm and 10µm Au lines on Si (dark: Si, pale: Au)

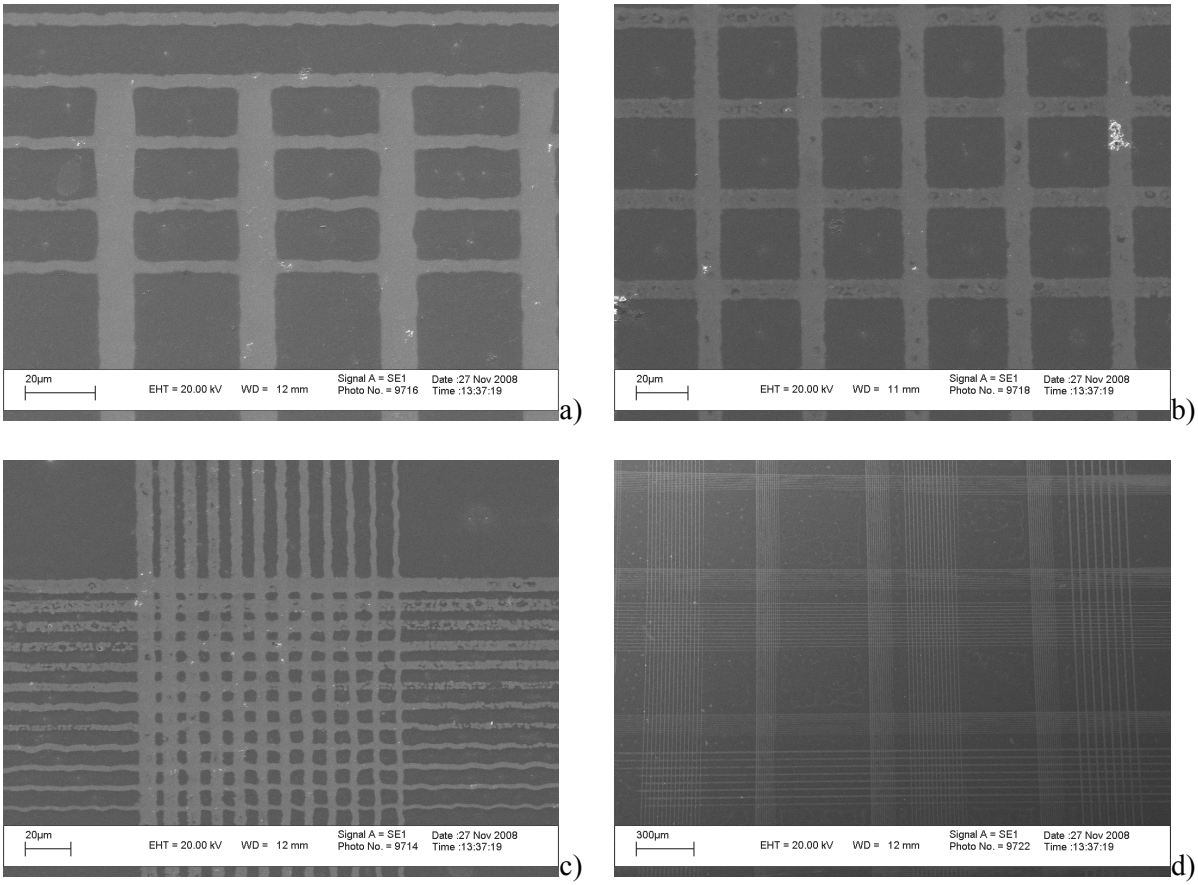


Figure 3-15 SEM images of Au (bright) patterns on Si (dark) formed aligned µCP and etching showing a) intersections of 10µm and 2µm lines b) intersections of 10µm and 10µm lines c) intersecting decreasing line widths from 10µm to 2µm. d) large area > 3mm ×3mm patterning.

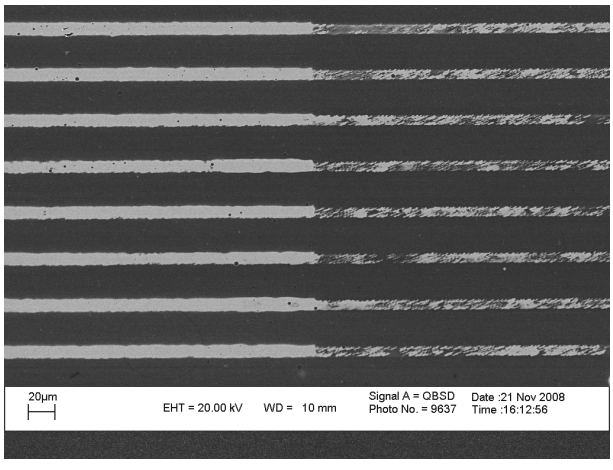


Figure 3-16 Alignment accuracy of overlaid patterns (dark: Si, pale: Au). A first print is made, the stamp shifted laterally by a few mm, and a second print made. The combined print is revealed by etching away the uncovered Au. The left side of the image shows the region printed twice whilst the right side shows the region printed only once.

3.6 References

[3.1] M. Madou, *Fundamentals of Microfabrication*: CRC Press, 1997.

[3.2] K. E. Bean, "Anisotropic etching of silicon," *IEEE Trans. Electron Devices,* vol. 25, pp. 1185-1193, 1978.

[3.3] H. Lorenz and et al., "SU-8: a low-cost negative resist for MEMS," *J. Micromech. Microeng.,* vol. 7, p. 121, 1997.

[3.4] H. Fujita, "Microactuators and micromachines," *Proc. IEEE,* vol. 86, pp. 1721-1732, 1998.

[3.5] J. Mark Noworolski, E. H. Klaassen, J. R. Logan, K. E. Petersen, and N. I. Maluf, "Process for in-plane and out-of-plane single-crystal-silicon thermal microactuators," *Sensors and Actuators A,* vol. 55, pp. 65-69, 1996.

[3.6] W. J. Jack, "Microelectromechanical systems (MEMS): fabrication, design and applications," *Smart Mater. Struct.,* vol. 10, p. 1115, 2001.

[3.7] E. H. Klaassen, K. Petersen, J. M. Noworolski, J. Logan, N. I. Maluf, J. Brown, C. Storment, W. McCulley, and G. T. A. Kovacs, "Silicon fusion bonding and deep reactive ion etching: a new technology for microstructures," *Sensors and Actuators A,* vol. 52, pp. 132-139, 1996.

[3.8] Microscopic positionable mirror, MEMS micro-mirror springs, http://www.bacteria-world.com/mems-mirror.htm.

[3.9] Portfolio of SEM microphotographs, Tunnel tips (Cantilever type), http://www.ee.iitb.ac.in/~apte/PFOLIO.htm.

[3.10] D. J. Bell and et al., "MEMS actuators and sensors: observations on their performance and selection for purpose," *J. Micromech. Microeng.,* vol. 15, p. S153, 2005.

[3.11] E. M. Yeatman, M. M. Ahmad, and R. R. A. Syms, "Piezoelectric films in silicon-based microactuation structures," in *Active Drives for Microengineering Applications, IEE Colloquium on*, 1995, pp. 2/1-2/3.

[3.12] P. Muralt, "Ferroelectric thin films for micro-sensors and actuators: a review," *J. Micromech. Microeng.,* vol. 10, p. 136, 2000.

[3.13] E. S. Kolesar, M. D. Ruff, W. E. Odom, J. A. Jayachadran, J. B. McAllister, S. Y. Ko, J. T. Howard, P. B. Allen, J. M. Wilken, N. C. Boydston, J. E. Bosch, and R. J. Wilks, "Single- and double-hot arm asymmetrical polysilicon surface micromachined electrothermal microactuators applied to realize a microengine," *Thin Solid Films,* vol. 420-421, pp. 530-538, 2002.

[3.14] O. Cugat, J. Delamare, and G. Reyne, "Magnetic micro-actuators and systems (MAGMAS)," *Magnetics, IEEE Transactions on,* vol. 39, pp. 3607-3612, 2003.

[3.15] P. Gravesen and et al., "Microfluidics-a review," *J. Micromech. Microeng.,* vol. 3, p. 168, 1993.

[3.16] T. Fujii, "PDMS-based microfluidic devices for biomedical applications," *Microelectron. Eng.,* vol. 61-62, pp. 907-914, 2002.

[3.17] M. De Volder and D. Reynaerts, "Pneumatic and hydraulic microactuators: a review," *J. Micromech. Microeng.,* vol. 20, p. 043001.

[3.18] IMMR, Simon Fraser University, MEMS Actuators, http://www.sfu.ca/immr/.

[3.19] C. Strandman and Y. Bäcklund, "Passive and fixed alignment of devices using flexible silicon elements formed by selective etching," *J. Micromech. Microeng.,* vol. 8, p. 39, 1998.

[3.20] R. M. Bostock and et al., "Silicon nitride microclips for the kinematic location of optic fibres in silicon V-shaped grooves," *J. Micromech. Microeng.,* vol. 8, p. 343, 1998.

[3.21] A. H. Slocum and A. C. Weber, "Precision passive mechanical alignment of wafers," *J. Microelectromech. Syst.,* vol. 12, pp. 826-834, 2003.
[3.22] M. P. Larsson and R. R. A. Syms, "Self-Aligning MEMS In-Line Separable Electrical Connector," *J. Microelectromech. Syst.,* vol. 13, p. 365, 2004.
[3.23] R. R. A. Syms and et al., "A microengineered alignment bench for a nanospray ionization source," *J. Micromech. Microeng.,* vol. 17, p. 1567, 2007.
[3.24] S. D. Senturia, *Microsystem design*: Kluwer Academic, 2001.
[3.25] A. Kumar and G. M. Whitesides, "Features of gold having micrometer to centimeter dimensions can be formed through a combination of stamping with an elastomeric stamp and an alkanethiol ``ink" followed by chemical etching," *Appl. Phys. Lett.,* vol. 63, pp. 2002-2004, 1993.
[3.26] C. M. Schroeder, "Accurate silicon spacer chips for an optical fiber cable connector (A)," *J. Opt. Soc. Am. B,* vol. 67, p. 708, 1977.
[3.27] C. Liu, "Foundation of MEMS," Pearson Education, 2006.
[3.28] J. M. Gere and S. P. Timoshenko, *Mechanics of Materials*, 4th ed.: Stanley Thornes, 1999.
[3.29] W. C. Young, *Roark's formulas for stress and strain*, 6th ed. New York: McGraw Hill Book Co., 1989.
[3.30] J. C. Greenwood, "Silicon in mechanical sensors," *J. Phys. E: Sci. Instrum.,* p. 1114, 1988.
[3.31] N. Tas, T. Sonnenberg, H. Jansen, R. Legtenberg, and M. Elwenspoek, "Stiction in surface micromachining," *J. Micromech. Microeng.,* p. 385, 1996.
[3.32] C. H. Mastrangelo and C. H. Hsu, "A simple experimental technique for the measurement of the work of adhesion of microstructures," in *Solid-State Sensor and Actuator Workshop, 1992. 5th Technical Digest., IEEE*, 1992, pp. 208-212.
[3.33] A. Bietsch and B. Michel, "Conformal contact and pattern stability of stamps used for soft lithography," *J. Appl. Phys.,* vol. 88, pp. 4310-4318, 2000.
[3.34] DowCorningCorporation, "Product Information: Low Viscosity Silicone fluids, 200 Fluid 20cs." vol. Form 25-941-97.
[3.35] M. Tormen, T. Borzenko, B. Steffen, G. Schmidt, and L. W. Molenkamp, "Using ultrathin elastomeric stamps to reduce pattern distortion in microcontact printing," *Appl. Phys. Lett.,* vol. 81, pp. 2094-2096, 2002.
[3.36] A. M. Hynes, H. Ashraf, J. K. Bhardwaj, J. Hopkins, I. Johnston, and J. N. Shepherd, "Recent advances in silicon etching for MEMS using the ASE(TM) process," *Sensors and Actuators A,* vol. 74, pp. 13-17, 1999.
[3.37] Microchem Corp, "SU-8 200 permanent epoxy negative photoresist," Product Description.

4 Electrostatically driven μCP

In this Chapter, electrostatic actuation of the silicon μCP engines designed in Chapter 3 is investigated. Electrostatic actuation is conceptually simple to implement in this case as the system already includes a pair of parallel electrodes (the Si print head and the Au substrate). In practice, the voltages required are so high that electric discharge occurs. Electrostatically actuated μCP has been demonstrated but remains very problematic.

This chapter is organised as follows: 1) the electromechanical model of the Si engine is presented and analysed; 2) experimental characterisation is carried out and evidence of electrostatic discharge is presented; 3) discharge mechanisms are briefly discussed and further experimental data is presented; 4) a method of circumventing discharge is presented; 5) a simple experiment using a low stiffness membrane is used to show that electrostatic actuation can be used for μCP, i.e. the electric fields do not interfere with the SAM formation; 6) finally, a guideline for using the method in 4) is formulated. Concluding remarks and summary are presented at the end.

4.1 Silicon μCP engine as a parallel plate electrostatic actuator

4.1.1 Model

The arrangement of Figure 4-1a is electrically equivalent to a parallel plate capacitor with one fixed and one mobile plate. In steady state operation, the mechanical behaviour of the mobile plate can be modelled by a spring (Figure 4-1b).

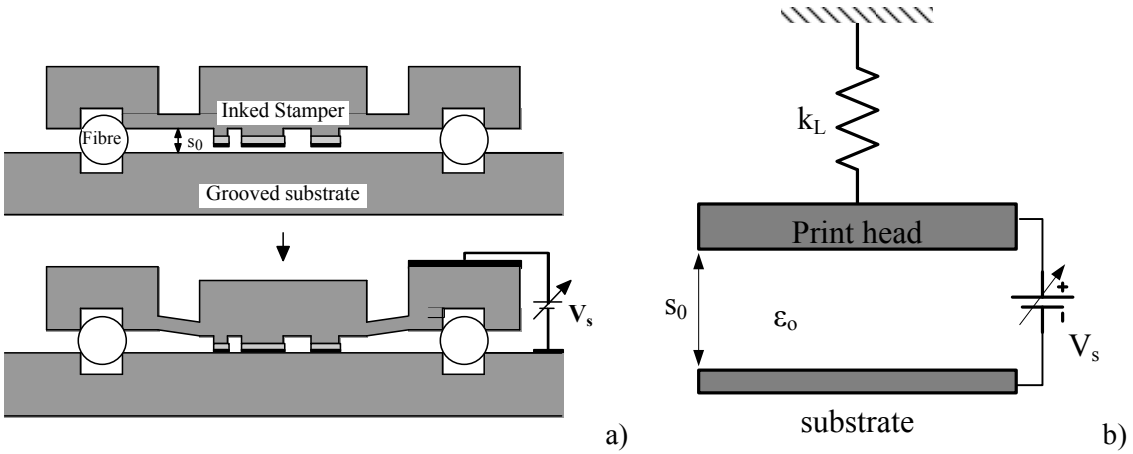


Figure 4-1 a) Electrostatic operation of Si µCP engine, b) Equivalent electro-mechanical model.

The initial separation between the plates is approximated to the flying height, s_0, and neglects the raised features and the PDMS coating. This assumption may be inaccurate as s_0 is reduced, but simplifies the analysis. The analysis of such structures is well documented (see e.g. [4.1]) and an important aspect is the pull-in voltage, V_{PI}, which denotes the voltage at which the electrostatic force overcomes the elastic force resulting in the upper plate snapping down.

4.1.2 Pull-in in a simple parallel plate actuator

When the upper plate is displaced from the initial position s_0 such that the new gap is s, the elastic restoring force, $F_{elastic}$, exerted by the spring of stiffness k_L is: (taking upwards displacement/forces to be positive)

$$F_{elastic} = k_L(s_0 - s) \tag{4.1}$$

In the electrical domain, the energy stored in the capacitor is

$$U = \frac{1}{2}CV_s^2, \text{ where } C = \frac{\varepsilon_0 A}{s}$$

And hence the electrostatic force is given by:

$$F_{electrostatic} = \frac{\partial(U)}{\partial s}$$

$$F_{electrostatic} = -\frac{1}{2}V_s^2\frac{\varepsilon_0 A}{s^2} \tag{4.2}$$

At equilibrium, the net force is equal to zero so:

$$F_{electrostatic} + F_{elastic} = 0$$

$$\frac{\varepsilon_0 A V_s^2}{2s^2} = k_L(s_0 - s) \tag{4.3}$$

Introducing the normalised force variable $\eta = \frac{\varepsilon_0 A V_s^2}{2k_L s_0^3}$, and normalised displacement $\sigma = \frac{s}{s_0}$, and rearranging yields:

$$\eta = \sigma^2 - \sigma^3 \tag{4.4}$$

For low η Equation (4.4) has three solutions, of which only the largest is physically realisable and the variation of σ with η for the two positive solutions is shown in Figure 4-2. At a critical value, η_C, these two roots are repeated and equation (4.4) reduces to $(\sigma - \alpha)^2(\sigma - \beta) = 0$. By equating and expanding coefficients, $\alpha = 2/3$, $\beta = -1/3$, and $\eta_c = \alpha^2\beta = 4/27$.

Denormalising, pull-in therefore occurs when:

$$s_C = \frac{2s_0}{3} \tag{4.5}$$

and

$$V_{PI} = \sqrt{\frac{8k_L s_0^3}{27\varepsilon_0 A}} \tag{4.6}$$

For μCP, a low V_{PI} is required so that contact can be easily achieved, and hence, k_L and s_0 must be kept as small as possible.

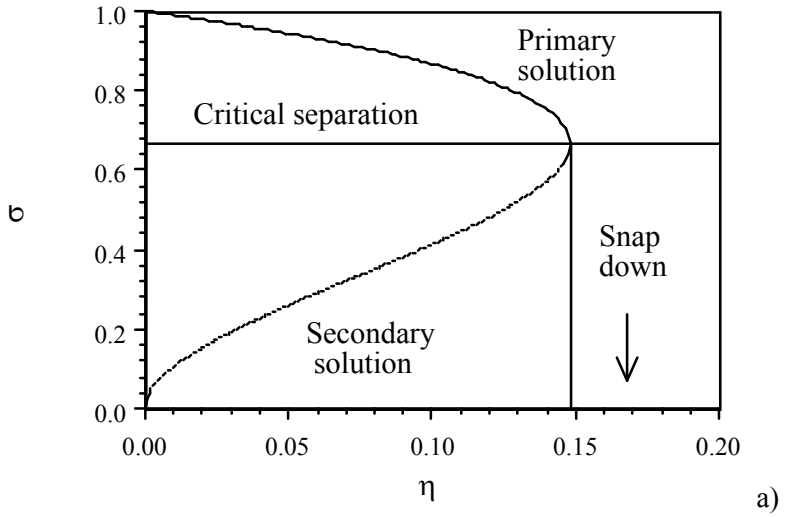


Figure 4-2 Variation or normalised separation σ with normalised electrostatic force η

4.2 Electrostatic actuation

4.2.1 Characterisation

Electrostatic operation was quantified by placing a print engine at a calibrated height above a gold coated substrate and applying a voltage between the two as illustrated in Figure 4-1a. Vertical deflections were measured using an optical microscope fitted with a Mitutoyo height gauge. The initial flying height was set using 125 μm thick single mode optical fibres and machined substrate (as shown in Figure 4-1a), or by using thin (25 - 50 μm) insulating Mylar and Kapton PI films with a flat Au coated substrate. Electrical contact to the frame of the print engine was achieved by using a micromanipulator. The arrangement with PI spacers is

shown in Figure 4-3. Both floppy devices (BSOI) with $k_L \approx 1.6$mN/µm, and rugged devices (single crystal Si) with $k_L \approx 30$mN/µm, were characterised.

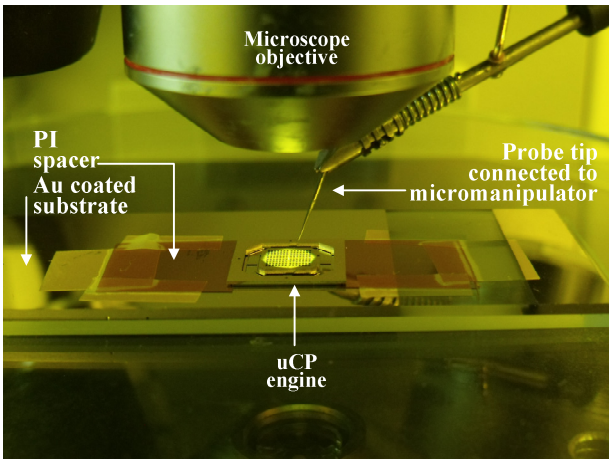


Figure 4-3 Electrical characterisation of µCP engine using PI spacers

The variation of separation, s, with applied voltage, V_S, was measured and the results are illustrated in Figure 4-4. Qualitatively, the results agree with Figure 4-2. However, for the BSOI devices, pull-in occurs at $V_{PI} = 370$ V, instead of $V_{PI} = 690$ V as predicted by Equation 4.6, suggesting that the print head may have tilted as it deflected. For stiff devices, the initial separation was reduced to 25 µm to minimise the operating voltages. Even then, $V_{PI} = 800$ V and dc discharge occurred during actuation. Apart from observing sparks across the gap, examination of the Au substrate after the experiment revealed that the Au seemed to have been eroded (Figure 4-5), and the damaged substrate to roughly correspond to the proud features on the stamp, which act as field concentrators.

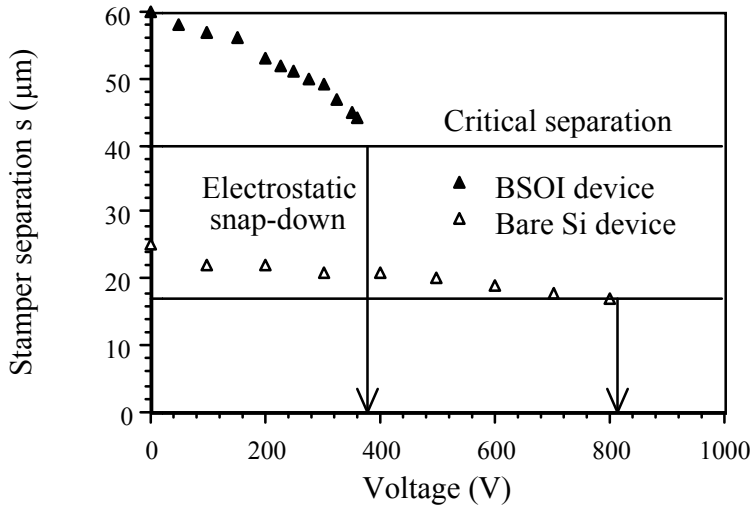


Figure 4-4 Experimental voltage-deflection characteristics of different devices

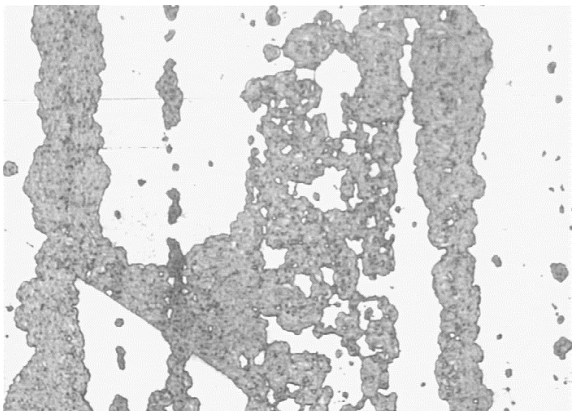


Figure 4-5 Optical image showing damage to substrate due to discharge.

4.2.2 Electrostatically driven μCP

To enable μCP, the discharge problem needs to be mitigated. Interesting effects were observed when the operating voltages were too high. After imposing the voltage, the print head was observed to deflect towards the substrate until a discharge initiated. At this point, the print head retracted, and this cycle was repeated with a period of a few seconds, which was presumably determined by the electrical RC time constant rather than a mechanical time constant.

Some successful µCP was achieved by using low k_L devices and small gaps s_0. Low spacing were achieved by using 25 µm PI spacer, and by gently placing a small weight (5 g -8 g) on top of the print head to reduce the flying height even further to ≈ 10 µm.

In one attempt, a device with k_L ≈ 30 mN/µm and ≈ 8 µm tall relief features was inked with HDT using the usual procedure (Appendix A) and dried and set up as above. The driving circuit containing a 200 MΩ current limiting resistor was used to apply a step input of 600 V. Current flow in the circuit indicated that capacitor was conducting some current, and therefore, contact had been made. Visual examination of the substrate revealed that some discharge had occurred, but after etching, some faint patterns were also observed, indicating that some monolayer formation had occurred (see Figure 4-6).

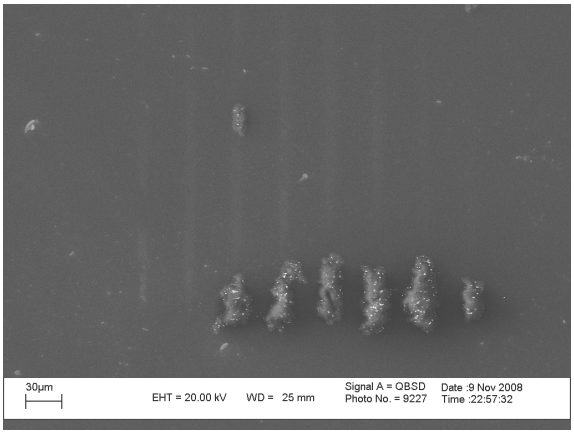
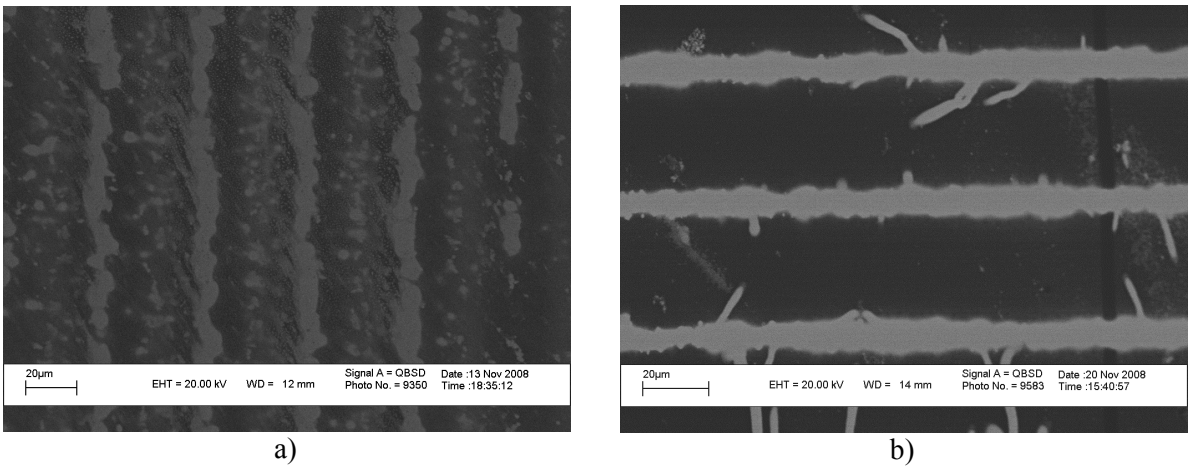


Figure 4-6 Electrostatically actuated contact, showing discharge damage and faint pattern transfer

In another experiment, floppy BSOI devices (k_L ≈ 1.6 mN/µm) with relatively shallow (4 µm) relief structures were used. A series 200 MΩ current limiting resistor and a 5 nF dc blocking capacitor were included. The series capacitor increases the pull-in voltage slightly, as will be explained in Section 4.3.2. After few electrostatic tests with this device, the PDMS layer was

found not to absorb ink and print uniformly. This is attributed to possible damage caused to the polymer by electric discharge combined with the non-uniform spray coating process. Hence, exceptionally, rather than thoroughly drying the stamp after inking (as described in Appendix A), it was left slightly wet. The print engine was then placed on spacers, and weights (≈ 6g) were added to reduce the gap. A step input of 600 V was applied, then V_S was dropped to 200 V and maintained for 1 min. No discharge damage was observed in that case, and after etching, Au patterns were observed (see Figure 4-7). The pattern quality over the printed area varied significantly, presumably because of the non homogeneous ink distribution. In Figure 4-7a, ink is clearly transferred in the non-relief regions, line width resolution is poor, and comet-like marks emanate from the lines. Figure 4-7b shows a different part of the same print. Here, ink transfer is confined to the relief features, but dentritic features now emanate from the sides of the lines. These artefacts could be due to ink ejection during snap-down or to field-driven ink migration. The former is more likely given the macroscopic amounts of ink present on the stamp.



a) b)

Figure 4-7 SEM images of electrostatically actuated μCP showing a) ink transfer in non relief regions, b) dentritic features emanating from each side of the lines (image rotated compared to (a)).

4.2.3 Discussion: Electrostatic μCP

The high operating voltages are problematic and prevent the successful μCP with an electrostatic drive. Although voltages have been minimised by using the smallest possible values of k_L and s_0, discharge and other field induced effects still prevent successful μCP. Whilst the results obtained indicate that electrostatically driven μCP is possible, there are concerns regarding the experimental technique and the repeatability.

A key problem is the addition of weights to reduce initial gap. The increase in mass increases the sensitivity to mechanical noise and it is possible that the induced vibration interfered with the electrostatic operation, especially at such small gaps.

Another problem is co-planarity of the two electrodes; achieving a gap of ≈ 10 μm over lengths of > 5 mm is challenging, if not impossible, given the manual assembly, and strong variations in the electric field are expected. This field inhomogeneity is made worse with the presence of raised features, which are no longer negligible compared to the flying height.

Lastly, once contact is made, the applied voltage, V_S, appears across a thin (a few μm thick) insulating polymer material, and there is a possibility that this material may break down as well.

In summary these experimental findings show that V_{PI} needs to be kept small by adjusting the parameters that appear in equation 4.6. A key question, however, is the maximum voltage that an air gap can support, and this is addressed in the next section.

4.3 Overcoming electrical discharge

In this section, a brief discussion of electrical discharge is presented and an empirical breakdown voltage-gap spacing characteristic curve is presented. The use of a series capacitor to avoid breakdown in an electromechanical system like Figure 4-1b is then analysed, and, finally, upper limits to the stiffness are calculated.

4.3.1 Electrical discharge

Dielectric breakdown can be initiated by *avalanche ionisation* or *vapour arc* [4.2]. The former was initially described by Paschen and Townsend and typically occurs in a gaseous environment, whilst the latter occurs in vacuum gaps. According to the Paschen model, at small gap distances, there is only a small number of mean free paths for electrons, and hence the voltage required for breakdown increases rapidly. However, at small gaps, vapour arc, rather than avalanche ionisation, becomes the dominant breakdown mechanism. Vapour arc breakdown arises from a high localised field emission current density heating a small surface feature until it explosively vaporises and creates a conductive path between the electrodes and initiates a breakdown. In [4.2], Strong *et al.* review published experimental work on the subject and present graphs of breakdown voltage against separation from various articles, and in a previous work [4.3], the same authors propose a modified Paschen curve that combines both vapour arcing and avalanche ionisation. This is illustrated in Figure 4-8. Another publication [4.4] presents data for plane-to-plane and comb drive devices and their results confirm that silicon-to-metal, but not silicon-to-silicon, electrodes agree with Figure 4-8. In addition, they report that similar damage to the metal electrode where the metal appears to have evaporated, leaving behind 2-4 μm wide craters. This is consistent with our results except that discharge in case appears to occur at higher gaps and voltages, and the size of the

craters are bigger. These differences are attributed to the proud features of the stamp, which act as field concentrators.

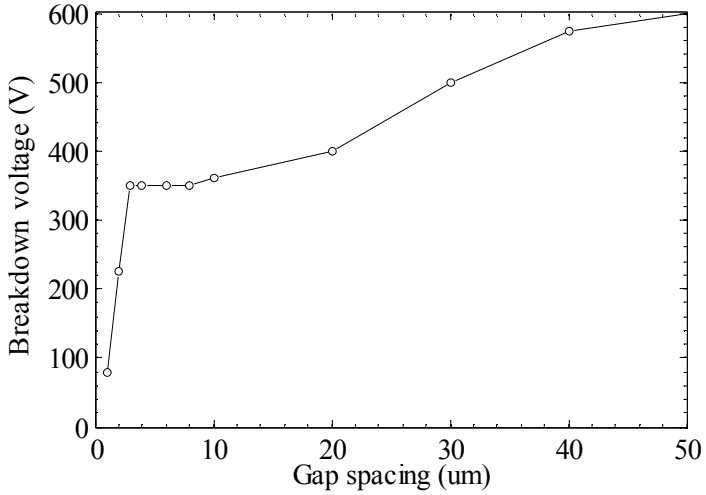


Figure 4-8 Modified Paschen curve combining avalanche ionisation with vapour arc [4.3] at atmospheric pressure

4.3.2 Reducing voltages across the air gap

For μCP, it is desirable that the movable electrode contacts the fixed electrode at a small voltage. Hence, the pull-in voltage needs to be small and this can be set by minimising the values of the geometrical parameters in equation 4.6. An alternative method is to include a series capacitor to distribute the applied voltage across two components rather than across a single air gap.

External series capacitor

Most MEMS electrostatic devices, except for those in [4.5], are designed to operate in their stable regions and methods have been devised to increase the stable range (see e.g. [4.6, 7]). These methods include the addition of an external capacitor, C_1, in series with the MEMS

varactor. As will be shown in the analysis, the downside of this method is an increase in pull-in voltage, and this issue is exacerbated by parasitic capacitances.

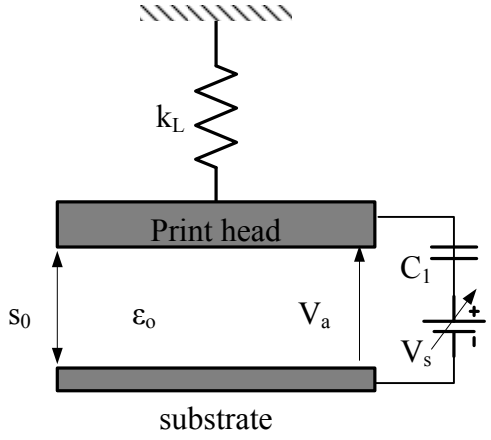


Figure 4-9 Electro-mechanical model with series C1

The electro-mechanical model is illustrated in Figure 4-9 and the analysis is similar to Section 4.1.2 except that the voltage across the air gap, V_a, is now a fraction of V_S by potential division. The capacitance at the initial gap is given by $C_0 = \varepsilon_0 A/s_0$ and the capacitance at a gap, s, can be expressed as $C = C_0 s_0/s$. following Chan *et al.* [4.7], C_1 is defined as C_0/n, where n is a unitless. The electrostatic force therefore becomes $F_{electrostatic} = -V_a^2 \varepsilon_0 A/2s^2$. Replacing this expression into equation 4.3, introducing the normalised force variable $\eta = \frac{\varepsilon_0 A V_S^2}{2k_L s_0^3}$, and normalised displacement $\sigma = \frac{s}{s_0}$, and rearranging yields:

$$\begin{aligned} \eta &= (\sigma + n)^2 - \sigma(\sigma + n)^2 \\ &= (1 - \sigma)(\sigma + n)^2 \end{aligned} \tag{4.7}$$

As before, equation (4.7) has three solutions, of which only the largest is physically realisable, and at the pull-in point, it reduces to $(\sigma - \alpha)^2(\sigma - \beta) = 0$. By expanding and matching

coefficients, $\alpha = (2\text{-}n)/3$, $\beta = -(1+4n)/3$, and $\eta_c = 4(1+n)^3/27$, and. Denormalising, pull-in occurs when:

$$s_C = \frac{(2-n)s_0}{3} \tag{4.8}$$

and

$$V_{PI} = \sqrt{\frac{8k_L s_0^3 (1+n)^3}{27\varepsilon_0 A}} \tag{4.9}$$

V_{PI}, the value of the source voltage at pull-in, unfavourably scales as $(1+n)^{3/2}$, but the stable travel range can now be extended; e.g., when $n = 2$, $s_C = 0$, implying that the movable electrode can travel across the entire gap without snapping down. Also, the voltage across the air gap is now a fraction of the total applied voltage and is equal to $V_a = V_s/(1+s_0/s)$, although V_S itself is higher. Capacitive stabilisation increases the voltage required to make contact but also distributes energy across two capacitors rather than across a single air gap. Moreover, as the gap decreases, $s \rightarrow 0$, $V_a \rightarrow 0$, and there may therefore be benefits to this approach.

However, there are additional parasitic capacitances, C_2, that appear between the actuator and the substrate due to the frame, as illustrated in Figure 4-10. C_2 appears in parallel with the actuator capacitance, C, and reduces the actuator voltage even further.

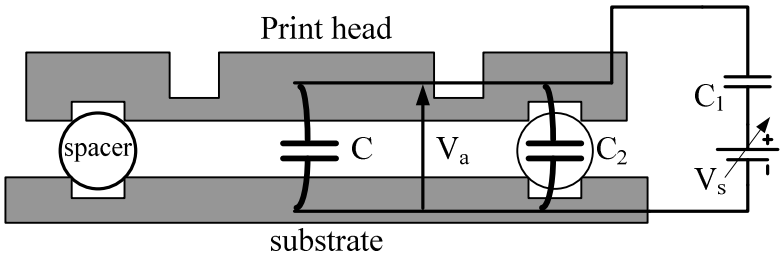


Figure 4-10 Introduction of C_1 implies that parasitic capacitance, C_2, between the frame of the actuator and the substrate, starts to influence the operation.

Following Chan *et al.* [4.7] the capacitor values are defined in terms of C_0 as $C = C_0 s_0/s$, $C_1 = C_0/n$, and $C_2 = C_0/m$ where n and m are unitless. By potential division, $V_a/V_s =$ C1/(C_1+C_2+C), and the electrostatic force acting on the electrode can be expressed as $F_{electrostatic} = -V_s^2 (\varepsilon_0 A/2s^2)(s/((1+n/m)s+ns_0))^2$. Replacing this expression into equation 4.3, introducing the normalised force variable $\eta = \frac{\varepsilon_0 A V_s^2}{2k_L s_0^3}$ and normalised displacement $\sigma = \frac{s}{s_0}$, letting $\gamma = 1+n/m$, and rearranging yields:

$$\eta = (1-\sigma)(\sigma\gamma + n)^2 \tag{4.10}$$

Substituting $n' = n/\gamma$, and $\eta' = \eta/\gamma^2$ into Equation 4.10 yields:

$$\eta' = (1-\sigma)(\sigma + n')^2 \tag{4.11}$$

Comparing Equation 4.11 to 4.7, the roots are found as $\alpha = (2-n/\gamma)/3$, $\beta = -(1+4n/\gamma)/3$, and $\eta_c = 4\gamma^2 (1+n/\gamma)^2/27$. Denormalising, pull-in occurs when:

$$s_C = \frac{s_0\left(2 - \frac{n}{\gamma}\right)}{3} \tag{4.12}$$

and

$$V_{PI} = \sqrt{\frac{8ks_0^3\gamma(\gamma+n)^3}{27\varepsilon_0 A}} \tag{4.13}$$

For large values of m, i.e. $C_2 \gg C_0$, $\gamma \rightarrow 1$ the parasitics hardly have any effect. On the actual prototypes, the value of m is estimated to be $m \approx 0.15$ by comparing the area of the frame to the area of the print head. At this value of m, $\gamma = 1+n/m$ is amplified, and V_{PI} increases even faster, and the distribution of energy across the various capacitors no longer offsets the additional applied voltage.

Internal series capacitor

A more suitable method of applying a series capacitor to distribute the electrostatic energy is to include a thick dielectric between the electrodes. In μCP, this is inherent to the system as PDMS layer is included. This is illustrated in Figure 4-11a. A key advantage compared to an external series capacitor is that the parasitic capacitance C_2 appears in parallel to both C_{air} and C_{PDMS}. The C_{air} and C_{PDMS} combination is still driven by V_S and hence steady state operation is not affected by C_2.

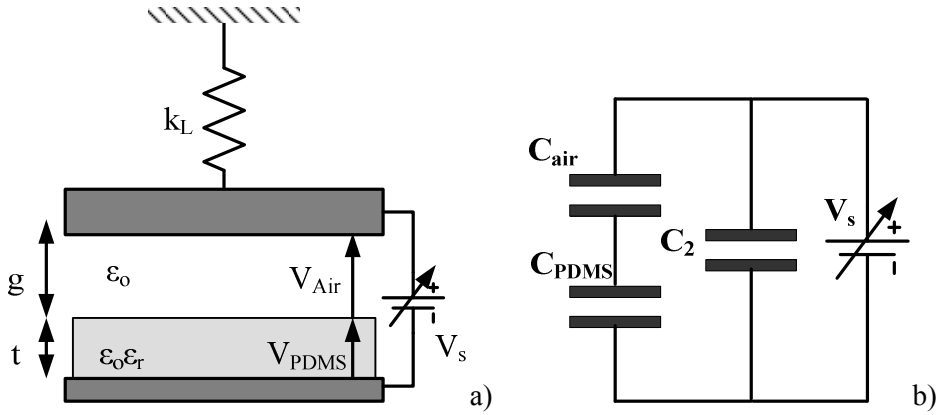


Figure 4-11 a) Parallel plate capacitor with built-in series capacitor, b) electrical equivalent circuit

The analysis is very similar to that of Figure 4-9. The electrostatic force is now given by $F_{electrostatic} = -V_S^2\varepsilon_0 A/2(t/\varepsilon_r+g)^2$. Equating the electrostatic force to the elastic force, $F_{elastic} = k_L(g_0-g)$, introducing normalised variables as before and letting $n = t/\varepsilon_r g_0$ yields Equation 4.7 again. This equation, as well as the pull-in parameters, is repeated here.

$$\eta = (1-\sigma)(\sigma+n)^2$$

$$V_{PI} = \sqrt{\frac{8k_L g_0^3(1+n)^3}{27\varepsilon_0 A}} \tag{4.14}$$

$$g_c = \frac{g_0(2-n)}{3}$$

The voltage across the air gap is now $V_{air} = V_S/(1+ng_0/g)$. Using $\varepsilon_r = 2.6$, $g_0 = t = 50$ μm, $A = 25$ mm^2, and $k_L = 1600$ N/m, the voltage distribution across the air and PDMS dielectrics are evaluated and plotted in Figure 4-12. The applied voltage is reaches ≈ 840 V at pull-in, but the maximum voltage across the air gap only reaches ≈ 500V. The difference appears across the PDMS dielectric and the latter is robust enough to sustain 540V across 25 μm [4.8].

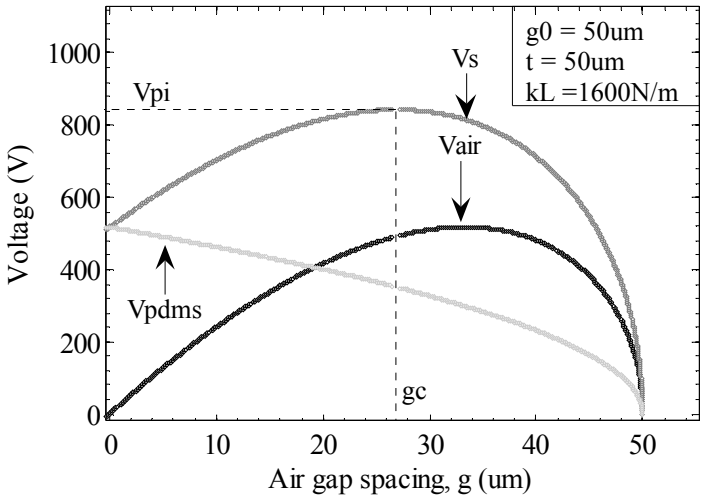


Figure 4-12 Voltage across dielectrics in varactor

4.3.3 Design rules to avoid dielectric breakdown

In the previous section, the benefit of including series capacitor in the form of a dielectric within the gap is demonstrated. Referring to the electrical model of Figure 4-11b, $V_{air} = V_S/(1+ng_0/g)$, and as $g \rightarrow 0$, $V_{air} \rightarrow 0$, and this trend is illustrated graphically in Figure 4-12.

From Section 4.3.1, it is known that the breakdown voltage of air at atmospheric pressure drops very quickly below gaps of 10 μm. When a system like Figure 4-11a is used to carry out μCP, a key question concerns the upper limits on the stiffness and/or flying height as these strongly influence the operating voltages. To address this, values of g_0 and t are arbitrarily chosen, A is kept at the value of the Si engine (25 mm^2), and Equation 4.14 is solved for different values of k_L using the built-in "*solve*" function in *Matlab*. Using this solution, voltage-deflection characteristics across the air gap are extracted and the results are plotted on the same axes as the Paschen curve to illustrate graphically whether the chosen stiffness lies below or above the breakdown curve.

With the self-alignment concept of the silicon μCP engine, a flying height of a few tens of μm is reasonable and hence a value of g_0 = 50 μm is assumed. The thickness of the dielectric, t, is also set to 50 μm. Using these values and k_L ranging from 100 N/m to 2000 N/m, voltage-displacement characteristics are plotted (see Figure 4-13). For $k_L \approx$ 1600N/m, the air gap voltages just go above the modified Paschen curve and discharge is likely to occur. A stiffness of 1000 N/m appears to be a safe upper limit for the chosen dielectric thicknesses.

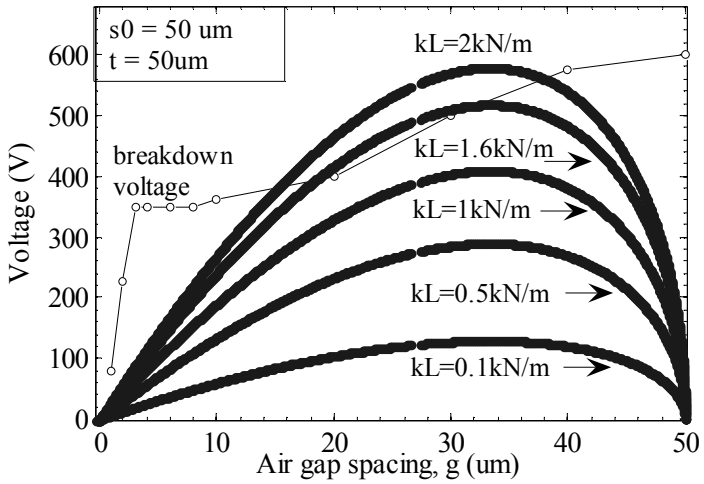


Figure 4-13 Voltage-gap characteristic for the air gap at different spring stiffness's. Breakdown voltage is overlaid for comparison.

4.4 Experimental verification of electrostatic µCP with built in dielectric

In this section, a simple experiment is devised to verify electrostatic operation using a built-in dielectric.

4.4.1 Experimental setup

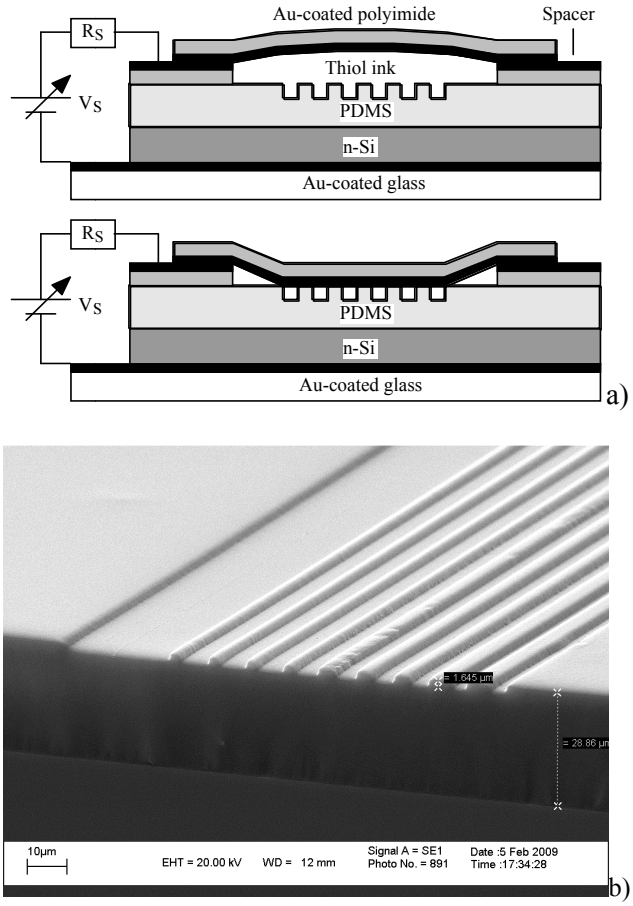


Figure 4-14 a) Experimental arrangement used to test electrostatic µCP. Conductive surfaces are painted black. b) SEM of thick PDMS stamp.

A low-stiffness movable electrode was implemented using a thin sheet (12 µm) of Kapton film covered in Au. The Young's modulus of Kapton and the cube of the membrane thickness are respectively two and three orders of magnitude less than the floppy Si engine used and the

equivalent stiffness is therefore five orders of magnitude lower. Although, the behaviour of the membrane differs from that of the linear spring model developed in Section 4.3.2, this comparison is enough to demonstrate that the stiffness is significantly lower.

Figure 4-14a shows the arrangement for membrane-based electrostatic μCP. The stamp is ≈ 30 μm thick PDMS formed on a doped piece of n-Si wafer by embossing (see Chapter 2). The patterned stamp area measures ≈ 5 mm x 3 mm and consists of recessed parallel lines with widths ranging from 5 μm to 20 μm. A further gold layer is included at the base of the n-Si wafer for electrical contact. The flying height of the membrane is set by the thickness of the spacer, which is a 25 μm polyimide film sputter coated with ~80 nm of Au for electrical contact to the membrane electrode. The membrane itself is ~12 μm thick polyimide with a ~30 nm Au layer on the bottom side, and a ~80 nm Au layer on the top (not shown). The upper layer Au coating was included to increase the reflectivity of the surface during interferometric measurement (see below). The membrane is effectively 6 mm long and 3 mm wide, and is simply supported on three sides and free on the fourth.

The behaviour of a rectangular membrane is governed by the differential equation [4.9]: $\partial^4 w/\partial x^4 + 2\partial^2 w/\partial x^2 \partial y^2 + \partial^4 w/\partial y^4 = q/D$. Here w represents the deflection at a point (x, y) in the plane of the plate, q is the applied pressure, and D is the flexural rigidity. Approximate solutions for different boundary conditions have been tabulated [4.10] but these are usually valid for small deflections (relative to the plate thickness). In this case, a 12 μm film is displaced by ~25 μm and the strains in the middle plane of the plate due to bending are appreciable. This so called diaphragm stress cannot be neglected [4.9, 10]. Furthermore, the membrane is Au-coated by sputter coating, and this induces further stress and pre-distortion

in the film. These constraints make the arrangement hard to model and beyond the scope of this work. Experimental results are therefore presented instead.

The deflection profile of the membrane was monitored using a scanning white light interferometer (Wyko NT9100, Veeco Inc.). As the applied voltage was increased, the membrane was observed to bend slightly about the edge of the spacer before suddenly buckling and contacting the PDMS stamp as shown in Figure 4-15. After initial contact was made, the total contact area was observed to increase with increasing voltage. Cross sections of the membrane at different applied voltages are shown in Figure 4-16. At a voltage of ~700V, practically all the patterned stamp area is contacted.

Note that the gaps in the data correspond to the inclined regions of the membrane. For these regions, the reflected light is not captured in the imaging lens of the interferometer due to its limited numerical aperture.

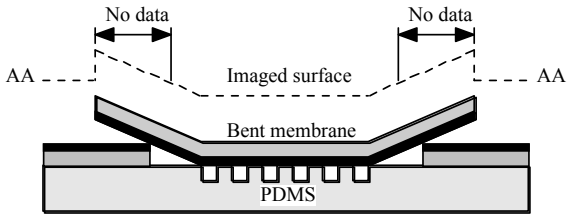


Figure 4-15 Membrane cross-section during imaging. The inclined segments are not reliably captured. Surfaces AA represent the flat spacer surface which is the reference plane

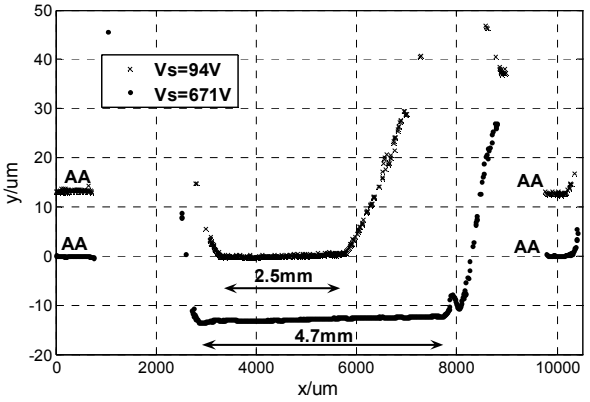
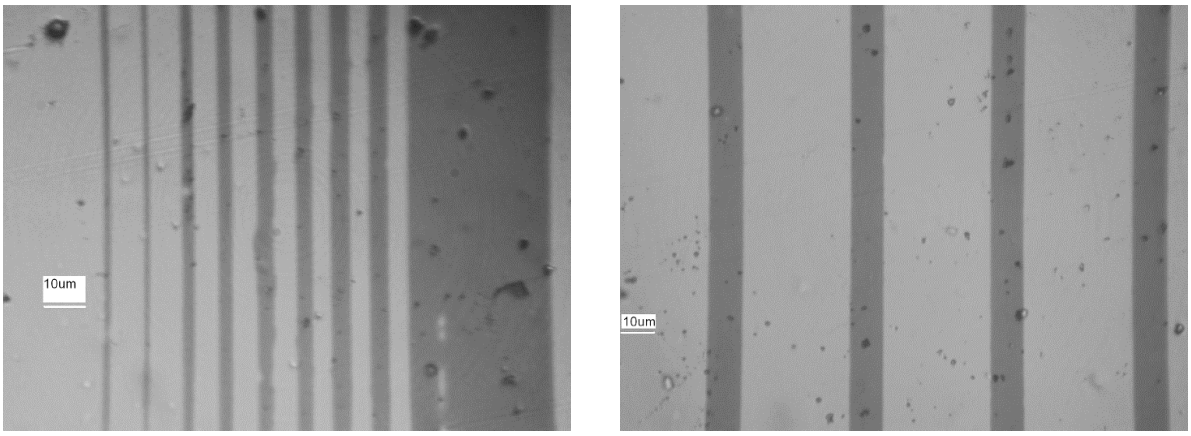


Figure 4-16 Deflection profile of membrane at different applied voltages. The two datasets are displaced with respect to each other for clarity.

4.4.2 µCP Results

For this µCP experiment, the stamp was first inked (as described in Appendix A) and then combined with spacers and an Au coated PI substrate to form the arrangement in Figure 4-14a. A voltage of ~700 V was applied and maintained for 1 minute. The substrate was then pulled away from the stamp and etched (see Appendix A) to reveal the printed pattern. The results are shown in Figure 4-17 and highlight successful printing. Figure 4-17a shows Au patterns of varying line widths ranging from ~2µm to ~30µm while Figure 4-17b highlights the pattern fidelity for 10µm wide lines spaced by 25µm.



a) b)

Figure 4-17 Optical microscope images of a) varying line widths. and (b) 10µm wide lines. The darker regions are polyimide and the bright regions are Au.

No electrical discharge is observed during these experiments, confirming that the voltages across the gap remain under the modified Paschen curve. In addition, this experiment also indicates that the 30 μm PDMS dielectric is robust enough to sustain a voltage of ≈ 700V for 1 min, and that the high electric field involved does not interfere with SAM formation.

4.5 Conclusion

In this chapter, electrostatic operation of the silicon μCP engine is analysed and experimental results are presented. Electrical discharge is observed due to the high operating voltages and using the same Si engine, the experimental conditions (flying height, and external resistor or capacitor) are tweaked to enable actuation without breakdown. μCP remained problematic although the results indicate that electrostatically driven μCP is possible.

Published data concerning electrical discharge in microscale gaps (Paschen curve) was then reviewed and an upper bound for the electric potential allowed in an air gap was determined. The use of a series capacitor as a method of dividing the voltages across the air gap is also investigated, and parametric curves showing the effect of stiffness are drawn. These showed that with a low enough stiffness, μCP with electrostatically actuated electrodes is possible. This hypothesis was successfully verified using a low stiffness membrane as electrode for μCP.

The findings of this chapter confirm that electrostatically driven μCP is possible in principle, but is in practice limited to low-stiffness devices. Low-stiffness devices make retraction after printing problematic as well as resulting in flimsy devices. Considering the adhesion energy

of a 5 mm × 5 mm Au substrate against a PDMS stamp (with a fill factor of 1), the minimum stiffness required for retraction is 6.94 kN/m (based on the analysis of Section 3.2.4). The parametric study of Section 4.3.3 indicates that for this geometry with a flying height of 50 μm, the upper bound on the stiffness is 1.6 kN/m.

Whilst these numbers are specific to this configuration, they already point out the difficulty of balancing these conflicting needs. Due to these design tradeoffs, other actuation modes need to be investigated.

4.6 References

[4.1] S. D. Senturia, *Microsystem design*: Kluwer Academic, 2001.
[4.2] F. W. Strong, J. L. Skinner, and N. C. Tien, "Electrical discharge across micrometer-scale gaps for planar MEMS structures in air at atmospheric pressure," *J. Micromech. Microeng.,* p. 075025, 2008.
[4.3] F. W. Strong, J. L. Skinner, P. M. Dentinger, and N. C. Tien, "Electrical breakdown across micron scale gaps in MEMS structures," in *Reliability, Packaging, Testing, and Characterization of MEMS/MOEMS V*, San Jose, CA, USA, 2006, pp. 611103-9.
[4.4] O. Takahito and et al., "Micro-discharge and electric breakdown in a micro-gap," *J. Micromech. Microeng.,* vol. 10, p. 445, 2000.
[4.5] P. M. Osterberg and S. D. Senturia, "M-TEST: A test chip for MEMS material property measurement using electrostatically actuated test structures," *J. Microelectromech. Syst.,* vol. 6, pp. 107-118, 1997.
[4.6] J. I. Seeger and S. B. Crary, "Stabilization of electrostatically actuated mechanical devices," *Proc. Transducers '97, Chicago, IL,* vol. 2, pp. 1133-1136, June 16-19 1997.
[4.7] E. K. Chan and R. W. Dutton, "Electrostatic micromechanical actuator with extended range of travel," *J. Microelectromech. Syst.,* vol. 9, pp. 321-328, 2000.
[4.8] Dow Corning Corporation, "Product Information: Sylgard 184 Silicone elastomer," in *Form 10-898F-01*. vol. Form 10-898F-01.
[4.9] S. P. Timoshenko and S. Woinowsky-Krieger, *Theory of Plates and Shells*, 2 ed.: McGraw Hill Book Co., 1959.
[4.10] W. C. Young, *Roark's formulas for stress and strain*, 6th ed. New York: McGraw Hill Book Co., 1989.

5 Replica moulded μCP engine

In this chapter, a multi-level μCP system that allows patterning of up to 6 different levels without using alignment optics is reported. This μCP system is based on the layout of the Si engine presented in Chapter 3, but is this time made of PDMS. Cost and complexity are driven down by wafer scale replica moulding against a microfabricated Si master. Flexible 50 μm thick photo-etched stainless sheets are bonded onto the polymer prior to demoulding to improve mechanical stability. Self-alignment is achieved by using the V-groove and rail mechanism demonstrated in Chapter 3. Actuation is currently manual and further investigation into more controlled drives is required. Complete ca. 10 mm × 10 mm prototypes are fabricated and six-level μCP is demonstrated with an average layer-to-layer misalignment of 5-10 μm.

5.1 Concept and design

In this section the PDMS μCP system is described. Replica moulding is used to cast membrane-like PDMS devices on microfabricated Si <100> 100 mm wafers. Each die is ca. 10 mm×10 mm and carries alignment features, the pattern to be printed, and a suspension in the form a membrane. The geometry of the alignment features and the pattern are determined by the bi-level etched silicon whilst the thickness of the membrane is determined by the thickness of the PDMS.

In this section, the self-alignment mechanism is reviewed, followed by a description of the elastic steel backing. Roof collapse is avoided by including a supporting frame into the

pattern and the performance of the latter is verified via FEA. Lastly, the use of different patterns on the wafer to enable characterization of multilevel accuracy is explained.

5.1.1 Self-alignment

Self-alignment is achieved by micromachining a Si <100> target substrate to form complementary V-grooves that mate with V-shaped rails on the PDMS stamp. This is illustrated in Figure 5-1.

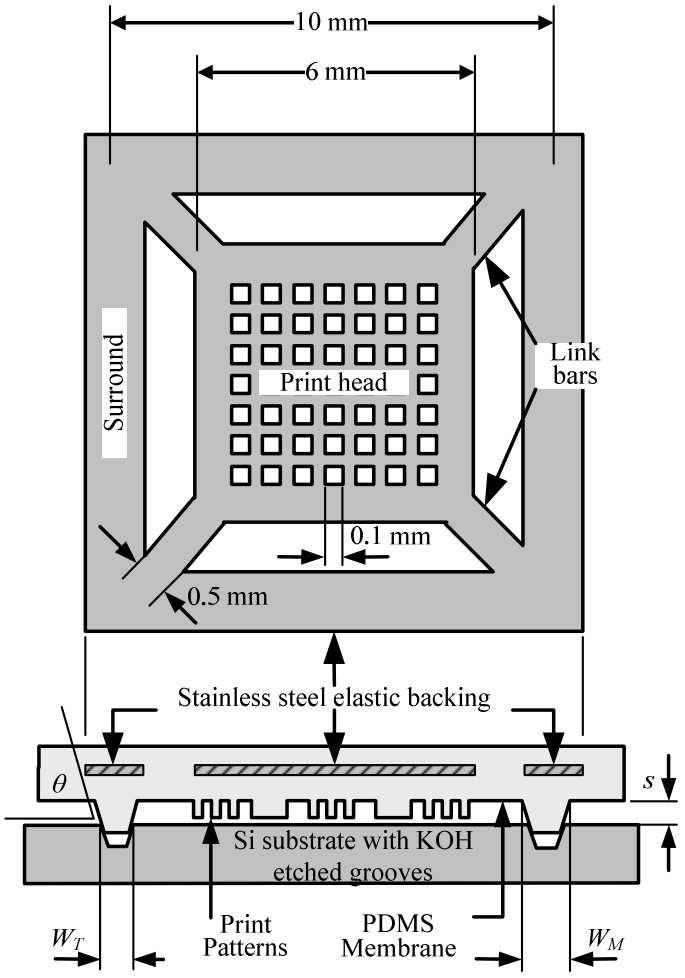


Figure 5-1 Self-aligned μCP system. The upper image shows the plan view of the steel elastic backing while the lower image shows the cross-sectional view of the device showing self-alignment.

With crystalline <100> Si, θ is the angle between the (100) and (111) planes and tan (θ) = √2. The flying height, s, then depends on the groove widths on the substrate, W_T, and on the stamp, W_M, as $s = (W_M - W_T)/\sqrt{2}$. Here, W_M = 1000 μm and W_T = 930 μm, giving s = 50 μm. When the rail and groove are tall/deep enough (200 μm in this case) the male and female parts can easily be aligned and registered by hand. Due to the elastomeric nature of the male part, some misalignment is expected.

5.1.2 Elastic backing

The softness of PDMS, typically 1-2 MPa, is critical as it enables conformal contact but it also makes stamp handling and registration very difficult. The stress induced by the thermal curing process adds further complications especially since the PDMS stamp needs to be aligned to Si substrates. Therefore, an elastic backing to strengthen the stamp is included.

A stamp cured at ~100 ^{o}C shrinks by 1.5% (in a linear dimension) [5.1] when it is released from a hard master like Si and a solution is to bond a flexible but stiff backing layer [5.2] prior to demoulding. We have experimentally verified this by using layers such as 50 μm stainless steel sheets, 25-100 μm Kapton polyimide sheets and overhead transparencies, and have found that the shrinkage is reduced to 0.1%.

Furthermore, as the stamp is deflected to make contact, it is expected to stretch and distort. By locally stiffening the print head area and the alignment rail, and allowing the membrane region to stretch instead, pattern distortion is minimized. This is done by bonding a 50 μm thick photo-etched stainless steel sheet (Photofab Ltd, Cambridgeshire, UK) to the PDMS after casting. The layout of the patterned elastic backing and its position in the PDMS stamp are illustrated in Figure 5-1. The surround overlays the PDMS alignment rail and ensures

dimensional stability whilst the steel print head strengthens the print pattern region and keeps it flat. The link bars hold all of it together and ensure that the stamp retracts after contact, while the 100 μm square holes on the steel print head allow trapped bubbles to escape during the fabrication process.

5.1.3 Pattern Stability

Due to its low Young's modulus, PDMS patterns are prone to collapse during printing [5.3-5]. With a feature height (10 μm) to width (10 μm) ratio of unity, pattern buckling or pairing up is avoided, but roof collapse, which occurs when features are widely spaced from each other, could be a problem. One solution, apart from avoiding sparse areas, is to use flexible backing layers [5.6]. Here, both measures are implemented by including 500 μm supporting bars that surround the patterns, and by using a flexible stainless steel backing. The effectiveness of the supporting bars is elaborated further in Section 5.1.4 and the layout is illustrated in Figure 5-2.

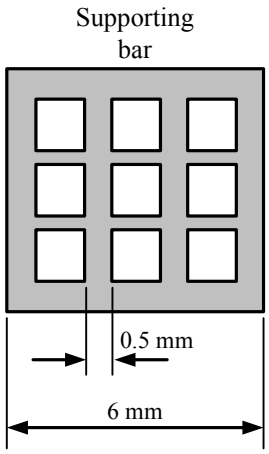
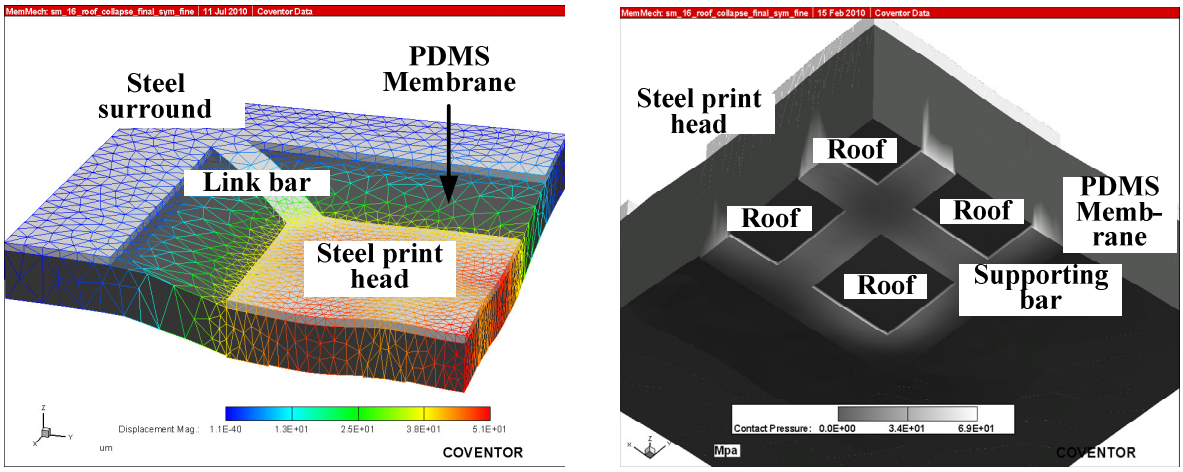


Figure 5-2 Layout of supporting bar. The 3 × 3 array can now carry any features without any risk of roof collapse between the cells.

In addition, sub-micron features can be patterned by using composite stamps as described in earlier reports [5.7, 8]. To test these, a different master carrying 500 nm wide gaps with a pitch of 5 μm in 7 μm tall posts is used. The layouts of these masters are described in Section 5.1.5 whilst fabrication is explained in Section 5.2.

5.1.4 Simulation

The mechanical response of the stamp and the interaction with the substrate is investigated via FEA in the CoventorWare software. Exploiting the symmetrical geometry, only ¼ of the device is simulated, with the symmetry planes constrained in the X or Y plane as required. A uniform pressure is applied to the top of the metal plate and the outer edges of the stamp and the metal surround are fixed.



a) b)

Figure 5-3 Images of the model used for FEA of the membrane stamp. a) Deflection profile of the stamp under load of 20 MPa. b) Contact pressure (pale) on the underside of the stamp for the same load.

The simulated model under a load of 20 MPa is illustrated in Figure 5-3a and excludes the print patterns, the 100 μm square holes in the steel plate, and the PDMS alignment ridge. Contact is modelled by including a contact surface 50 μm below the roof of the stamp. The membrane areas bend more, with the metal-bound region staying mostly flat. Contact is illustrated in Figure 5-3b which shows that the full length of the supporting bar can be in contact with the substrate without any contact of the roof. This implies that the patterns, which are of the same height, would also make contact. The variation of normalized contact area of the supporting bars and of the roof with applied load is plotted in Figure 5-4a, showing that essentially full contact of the print patterns can be achieved without roof collapse.

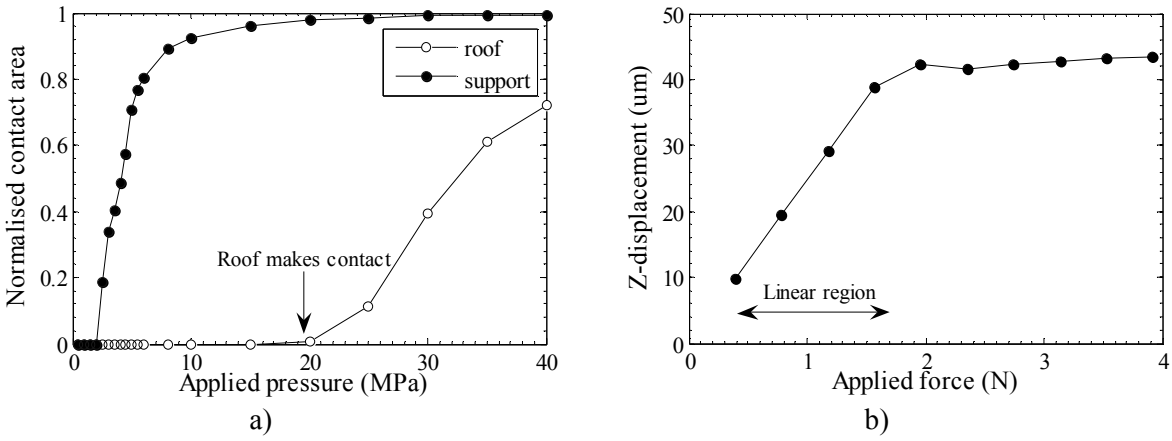


Figure 5-4 a) Normalised contact area variation with applied load. b) Displacement of the print head with applied force.

Although not simulated *per se*, the retraction of the stamp after contact can be predicted. Considering the deflection of the print head with varying loads (Figure 5-4b), for deflections of up to 40 μm (i.e. prior to contact being made), the relationship is linear. From the inverse gradient of the linear part, a stiffness term can be estimated (k = 50 kN/m). The maximum displacement that this node can undergo is s_0 = 40 μm. Hence, the elastic energy stored (=

$ks_0^2/2$) is at least 40 μJ (since even more energy is stored as the stamp deforms during contact). On the other hand, the work required to release the stamp is given by the product of the area in contact and the work of adhesion, W. Here, the relevant value of W to use is that of Sylgard 184 on gold [5.9], which is 0.5 J/m^2 , and the total area in contact is approximated by the area of the bottom surface of the supporting bars which is 4.6×10^{-6} m^2. The adhesion energy is thus 2.3 μJ. Since the stored elastic energy is much greater than the adhesion energy, stiction is not expected to be a problem.

5.1.5 Stamps and patterns for multilevel characterisation

To test for overlay accuracy, 7 stamps carrying different patterns are made from the same silicon wafer. Variants are labelled #1, #2…#6 and "all" and their layout on the wafer is illustrated in Figure 5-5a. Each variant contains the same mechanical features (alignment, supports and suspension) but different patterns. The variants consist of a 3×3 array of identical cells of size 1.2 mm×1.2 mm, with each cell containing an identical periodic pattern of ten 10 μm wide vertical bars with a pitch of 20 μm, and 10 μm wide horizontal bars for identification, as illustrated in Figure 5-5b. The 3×3 array of cells carrying the patterns are surrounded by 500 μm wide supports and, together, they form the 5.6 mm×5.6 mm printed area. The print head itself lies in a membrane-like structure framed by 10 mm×10 mm alignment rails. The variants differ only in the position of the periodic bar pattern within each cell, as illustrated in Figure 5-5c, which shows that the pattern carried by each variant is laterally shifted by an amount depending on the variant number. Sequentially printing with variants #1 to #6 and comparing the measured separation with the designed value allows multilevel accuracy to be measured.

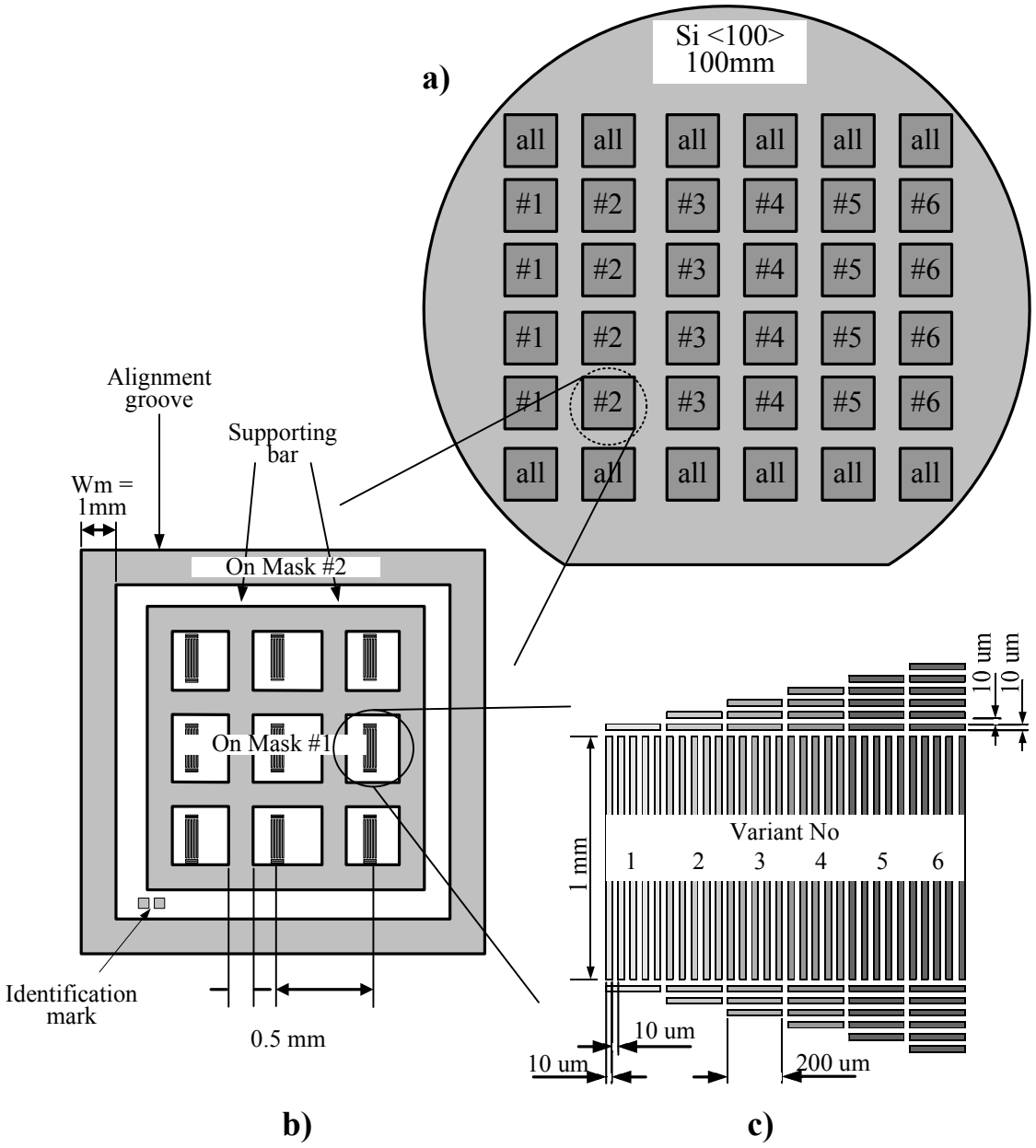


Figure 5-5 a) multiple stamps on a single silicon wafer. b) schematic of a single die showing 3×3 cells containing print pattern and supporting bar (Mask #1) and alignment groove (Mask #2). c) Close up of the pattern. Variants carry the same periodic bar pattern but shifted laterally, e.g. variant #1 carries the leftmost group, variant #2 the second group from the left, and so on. Variant "all" carries all six groups.

In addition, a different silicon master, termed high resolution master, carrying the same mechanical features but different print patterns was fabricated for testing sub-micrometer patterning. The print patterns in this case consist of 7 μm tall periodic bar patterns of different

sizes, namely; 10 μm bars with 20 μm pitch, 5 μm bars with 10 μm pitch, and 2.5 μm bars with 5 μm pitch. During processing, the 2.5 μm bars are narrowed to 500 nm by oxidation and the subsequent oxide removal. This results in a PDMS stamp having 4.5 μm bars separated by 500 nm gaps. The layout of the patterns on these high resolution masters are illustrated in Figure 5-6.

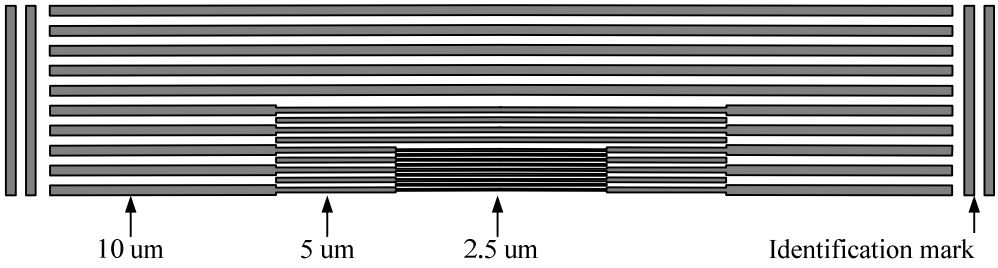


Figure 5-6 High resolution pattern carrying 10μm, 5μm and 2.5μm wide bars with mark to space ratios of unity. The pattern is rotated compared to Figure 5-5c.

5.2 Fabrication

In this section, the wafer scale process for the fabrication of the master and target is presented. Wafer scale PDMS casting and bonding is discussed and limitations of the process are outlined.

5.2.1 Master and Target

The master and target substrate are fabricated by conventional MEMS fabrication techniques using two-level lithography on the master and single level lithography for the target. The process flows are illustrated in Figure 5-7a and Figure 5-7b. Both master and target carry 36 dies. In the case of the target, the dies are identical, while for the master, the dies correspond

to different variants. The masters carrying the fine 2.5 μm patterns are made with the same process flow. Detailed process parameters are provided in Table 5-1 for the master and Table 5-2 for the target substrate.

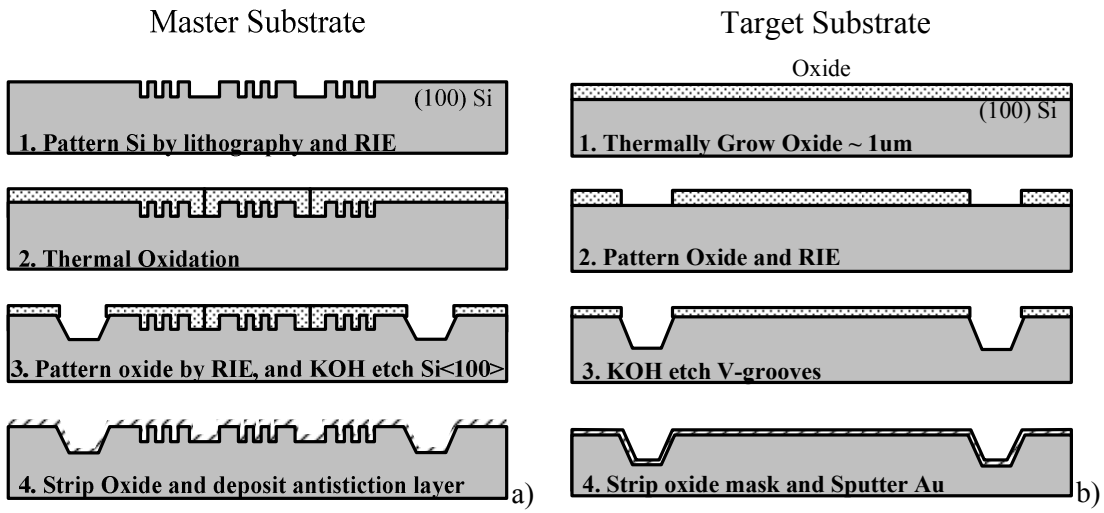
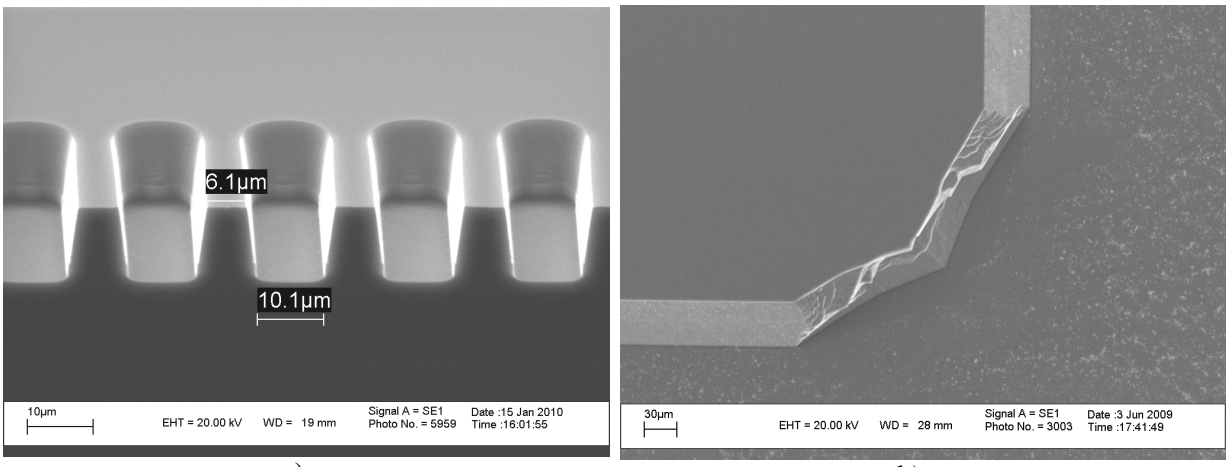


Figure 5-7 Process flow for a) Master and b) target wafers.

For the master, the print patterns and the supporting posts are defined in a single mask (Mask #1) and transferred to the Si substrate by a RIE using a recipe that yields a slightly tapered sidewall (≈10^o to the normal) that facilitates demoulding. A cross-section view of the etched pattern is shown in Figure 5-8a. A 1.2 μm thick oxide layer is then grown by dry oxidation at 1100 ^{o}C on both the microstructured master and the target. A thick 17 μm resist layer (AZ9260, MicroChem) is then spun on the master to cover the shallow structures, whilst a thinner resist layer is used for the flat target. The master is patterned with Mask #2 to define the 1000 μm wide rail (W_M), whilst the target is patterned with Mask #3 to define the 930 μm wide mating grooves (W_T). The patterns are transferred to the oxide mask by RIE. Using the oxide layer as mask, the Si master and target are then etched in a 40% KOH solution at 80 ^{o}C up to a depth of 200 μm. The oxide mask is then stripped and, for the master, an antistiction layer, such as the passivation layer of a DRIE (STS, Newport, UK), is deposited, whilst the

target is sputter coated with a 30 nm Au layer. The passivated master could be used for ~10 PDMS mouldings/castings before the release layer deteriorated and needed to be redeposited.



a) b)

Figure 5-8 SEMs of a) the cross-section of the 10 μm periodic bar patterns formed by RIE, b) the V-grooves at the convex corners formed by KOH etching.

Note that at the convex corners, additional (211) planes are revealed so the grooves are not precisely V-shaped there (see Figure 5-8b). To ensure a good fit between the stamps and the targets, both the target and master substrates are etched together and to the same depth.

Stamp master substrate		
Fabrication step	**Sub-steps**	**Parameters**
1. Print patterns	Lithography Mask #1	- S1828, 500nm thick, Spin: 3000rpm, 1000rpm/s, 40 s - Softbake: 65 C (HP)- 2 min, 85 C (HP)– 2min, 90 C (Oven) – 2 min - Exposure 460 mJ/cm^2, - Developer MIF319 (1 min)
	Silicon RIE – 10 μm	SF_6 (30 sccm), O_2 (10 sccm), Base pressure 120 mTorr, RF power 100 W.
	Resist Strip	Acetone immersion (3min), Then IPA and DI, then O_2 plasma clean.
2. Thermal Oxidation	Dry oxidation: 1.2 μm	Carbolite furnace, 1100 C, 72 hours.
3a.Pattern Oxide	Lithography	- AZ9260, 17 μm thick, Spin1 : 500rpm, 100rpm/s, 10 s,

	Mask #2	Spin2: 1000rpm, 500rpm/s, 40 s - Softbake: 60 C (HP)- 3 min, 80 C (HP)– 3min, 100 C (HP) – 1min, 90 C (Oven) – 2 min - Exposure 1110 mJ/cm^2, - Developer :AZ400K:DI 1:4 2.5 (min)
	RIE SiO_2	CHF_3 (25 sccm), Ar (25 sccm), O_2 (2 sccm), Base pressure 30 mTorr, RF power 200 W. Duration: 60min
	Resist strip	1165 @ 65 C immersion (15 min). DI rinse, then O_2 plasma clean.
3b. V-groove etch	KOH etch – 200 μm	40 % KOH solution in DI, with 1% IPA @ 80 C (~200 minutes)
	SiO_2 strip	CHF_3 (25 sccm), Ar (25 sccm), O_2 (2 sccm), Base pressure 30 mTorr, RF power 200 W. Duration: 60min
4. Antistiction	Passivation phase of DRIE (CF_x)	C_4F_8 (120 sccm), Base pressure 12 mTorr, Coil RF power 300W, frequency: HF, Platen power 20 W. Duration 120 s. Hardbake: 150 C (HP) – 5min.

Table 5-1 Process parameters for master substrate

Target substrate

Fabrication step	Sub-steps	Parameters
1. Thermal Oxidation	Dry oxidation: 1.2 μm	Carbolite furnace, 1100 C, 72 hours.
2.Pattern Oxide	Lithography Mask #3	- AZ9260, 8 μm thick, Spin1 : 500rpm, 5000rpm/s, 10 s, Spin2: 2000rpm, 5000rpm/s, 40 s - Softbake: 100 C (HP) - 2 min - Exposure 600 mJ/cm^2 - Develop :AZ400K:DI 1:4 (5 min) (HP) – 1min, 90 C (Oven) – 2 min - Developer :AZ400K:DI 1:4 (2.5 min)
	RIE SiO_2	CHF_3 (25 sccm), Ar (25 sccm), O_2 (2 sccm), Base pressure 30 mTorr, RF power 200 W. Duration: 60min
	Resist strip	1165 @ 65 C immersion (15 min). DI rinse, then O_2 plasma clean.
3. V-groove etch	KOH etch – 200 μm	40 % KOH solution in DI, with 1% IPA @ 80 C (~200 minutes)
	SiO_2 strip	CHF_3 (25 sccm), Ar (25 sccm), O_2 (2 sccm), Base pressure 30 mTorr, RF power 200 W. Duration: 60min
4. Gold deposition	Sputter coating (Nordiko)	- 10 nm Cr or 10 nm Ti(adhesion) - 30 nm Au

Table 5-2 Process parameters for target substrate

5.2.2 PDMS Stamp Casting

The stamp replication process is illustrated in Figure 5-9. A standard PDMS composition, Sylgard 184 (Dow Corning Corp), is prepared and spun coated onto the master to form a ~200 μm thick PDMS layer. After spinning, the master is degassed in a desiccator to remove air bubbles (Step 1 and 2). The PDMS is then partially cured so that it is set and does not flow, but is still sticky.

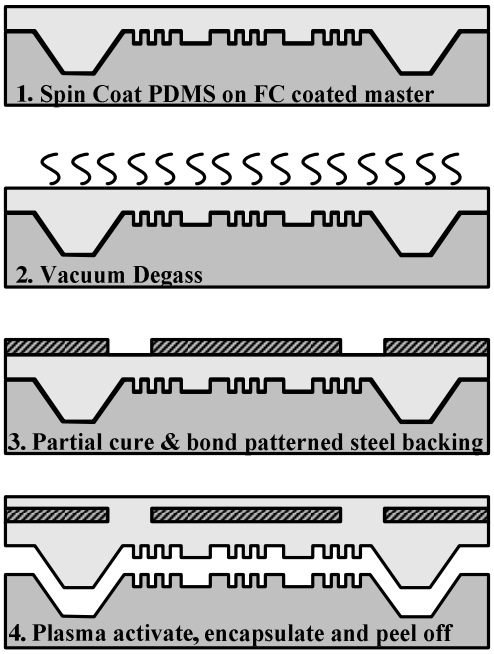


Figure 5-9 Stamp replication process. PDMS is first cast, then the steel elastic backing attached, followed by a encapsulating PDMS layer. The completed stamp is cured and then peeled off from the master.

For submicron features cast on the high resolution master, composite PDMS stamps with a 30 μm hard layer of Sylgard 184 mixed with its modulator in the ratio 1:5, followed by a 200 μm thick layer in a 1:10 formulation were made. The remainder of the stamp casting process is identical. This "hard" 1:5 layer is reported [5.10] to have an ultimate tensile strength 50% that of conventional 1:10 Sylgard 184 and this initial test indicates that the stamp replication process is suitable for brittle PDMS. The successful casting is illustrated in Figure 5-10,

which shows an SEM of a stamp which has been spun cast as above, peeled off, and coated with a thin film of Au for reliable imaging.

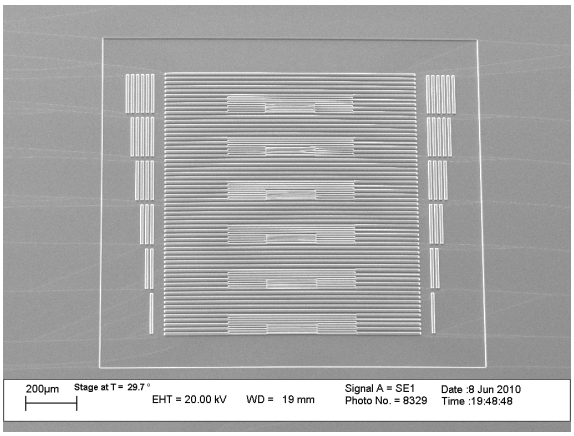


Figure 5-10 SEM of one of the patterns of PDMS stamp cast on high resolution master. For reliable imaging, the polymer was coated with a ~ 10 nm layer of Au prior to SEM.

The patterned steel layer is then bonded onto the PDMS (Step 3). Alignment is carried out by using the alignment optics of a mask aligner (Quintel Q4000IR) with the PDMS coated substrate held on the wafer stage and the steel sheet (which is first mounted on a glass plate) held on the mask chuck. To avoid stiction during the pre-contact phase, the PDMS curing time had to be increased and consequently the PDMS-steel bond weakened significantly and the yield was quite poor. This aspect can be improved on with a contact aligner system where the pre-contact phase can be overridden. Alternatively, the steel sheet is cut into strips covering 2×6 or 1×6 dies and coarsely aligned by hand using the alignment grooves as guide. Much fewer dies are obtained per wafer with this method but the dies are of better quality.

After bonding, a release layer in the form of a flexible polycarbonate sheet (such as an overhead transparency) is placed on top of the steel sheet, followed by a blank silicon wafer

and a 1.2 kg weight. The whole assembly is cured on a hot plate for at least 1 hr at 90 ^{o}C. After cooling, the top Si wafer and the polycarbonate sheet are removed, and the stainless steel surface is plasma activated in a System 80 RIE (RF power:70W, base pressure: 100 mTorr, O_2 flow rate: 60 sccm, duration: 20 s) and a second (~200 μm) PDMS layer is spun cast on top and then cured to encapsulate the device.

Finally, the entire PDMS device is peeled off from the master and cut with sharp scissors into either individual dies or arrays carrying a few stamps. Figure 5-11a shows an optical image of a fully assembled stamp while Figure 5-11b shows a SEM of the polymer part. Figure 5-12 shows an array of stamps aligned and locked onto a target substrate.

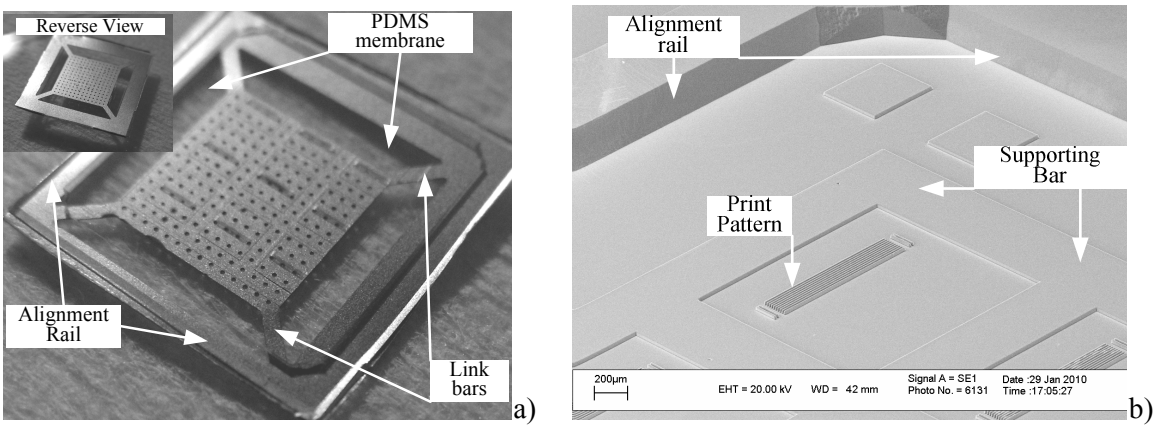


Figure 5-11 a) Optical image of a completed stamp. b) SEM of finished die highlighting successful moulding.

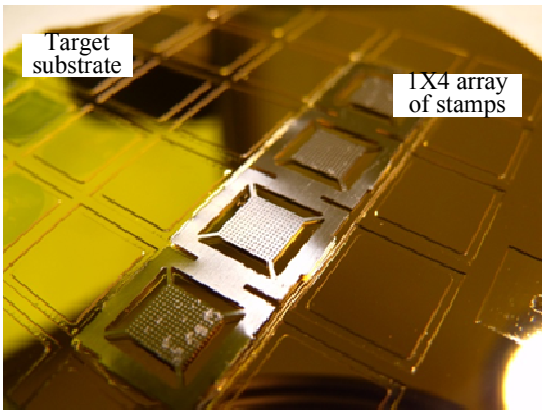


Figure 5-12 Optical image showing an array of 4 stamps aligned onto a target substrate

5.3 Experimental methods

In this section, the methods used to achieve multi-level μCP, and to measure the alignment accuracy are described.

5.3.1 μCP protocol

μCP for was carried out using HDT, as described in Appendix A. The stamps were inked, dried and then aligned by hand onto a site on the target substrate. To ensure uniform loading, a ≈ 6 mm×6 mm piece of Si was placed over the print head. Contact was made by pressing the print head with tweezers and was maintained for ~30 s. For multi-level printing, this was repeated with a different stamp as required. The SAM pattern was then transferred to the Au by etching off the unprotected regions (see Appendix A). SEM was carried out on the etched Au/Si samples to reveal the pattern.

For demonstration of multi-ink patterning, HDT ($HS(CH_2)_{15}CH_3$) and 11-mercaptoundecanoic acid ($HS(CH_2)_{10}C0_2H$) were used. Even stamp variants were inked with 0.5 mM HDT in ethanol, as above, whilst odd variants were inked with 1mM mercaptoundecanoic acid in ethanol. The inking and drying step is the same for the both inks. All six stamps were sequentially aligned and printed onto a single target die as described above. For the odd variants carrying the carboxylic acid terminated thiol, contact time was increased to ~60 seconds.

5.3.2 Absolute distortion and layer-to-layer alignment

The performance of the printing system was quantified using 1) the absolute distortion and 2) the layer-to-layer alignment accuracy. The patterns were printed as described in Section 5.3.1

and the uncovered Au etched away (as per Appendix A) to reveal the image. The printed patterns were characterised using an optical microscope (Wyko NT9100, Veeco Inc.) with a calibrated *x*-*y* stage (±5 μm) when large areas were concerned, and by SEM for higher resolutions over smaller areas.

The absolute distortion refers to the difference between the printed image and the original master once relative rotation and translation have been removed and can be visualised by a distortion map. Considering a point *A* on the master with origin *O*, and the corresponding points *A'* and *O'* on the image, the distortion at that point *A*, is a vector equal to $O'A' - OA$. Using this approach, a distortion map can be constructed for several points on the printed image. The landmarks used in this case are the corners of the supporting bar (see Figure 5-2) and the positions on the printed images were characterised using the optical microscope.

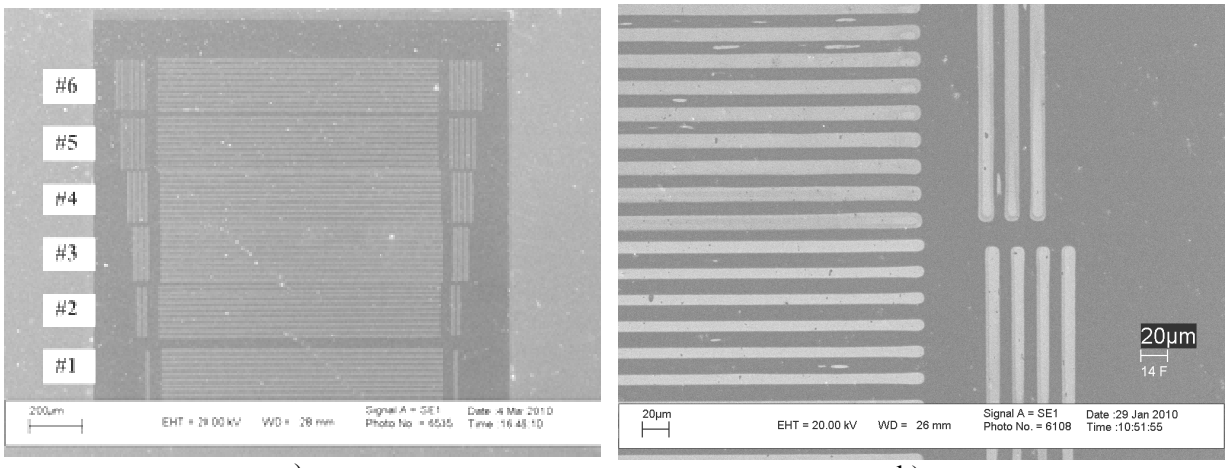
Layer-to-layer accuracy refers to how accurately the different stamps can be placed with respect to each other. It is obtained by measuring the centre line to centre line spacing of the periodic bar images formed by images from adjacent stamps and subtracting the nominal design value (20 μm). Using high magnification SEM images, this can be evaluated to the nearest μm. An example is shown in the next section in Figure 5-13b, where patterns from stamp #3 and #4 are printed and the misalignment between them quantified.

5.4 Results and Discussion

In this section, the fabricated stamps are used for μCP. 6-level patterning is demonstrated and the resulting layer-to-layer accuracy is presented and discussed. Printing with different inks is also verified.

5.4.1 6-level μCP

6-level μCP using correlated stamps, that is, those made on a single wafer and bound with the same strip of steel, was carried out as described in Section 5.3.1 onto a single target die. Typical results are illustrated in Figure 5-13a and Figure 5-13b. Sub-micrometer patterning was carried out in the same way and the results are illustrated in Figure 5-14.



a) b)

Figure 5-13 Experimental results of μCP showing a) 6-level μCP, b) close up of adjacent prints showing small misalignment. The SEM images show Au patterns (bright) on Si formed by contact printing (6 times) and etching (see Section5.3.1)

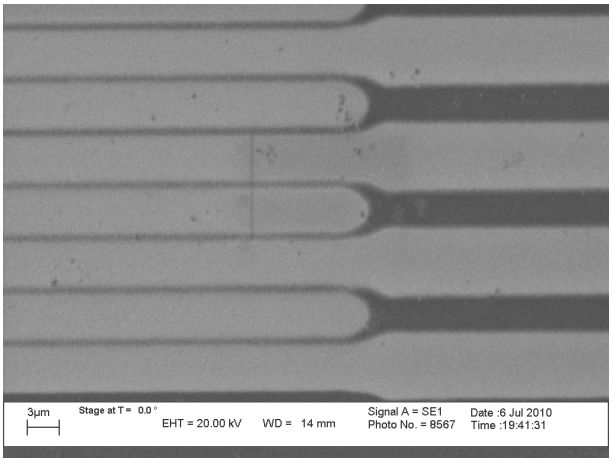


Figure 5-14 SEM of Au (pale) on Si (dark) showing 500nm features

5.4.2 Absolute distortion

The pattern reproducibility of the stamps carrying 10 μm features was characterised by measuring the *absolute* distortion as described in Section 5.3.2. For each stamp variant, a print was made and the vector distortions calculated using the inner corners of the supporting bar as landmarks. The average distortion of the six stamp variants at each landmark is then calculated and presented as a vector map in Figure 5-15. The maximum offset noted was 23 μm whilst the mean was 11 μm. The offsets appear to be randomly distributed with no clear trend.

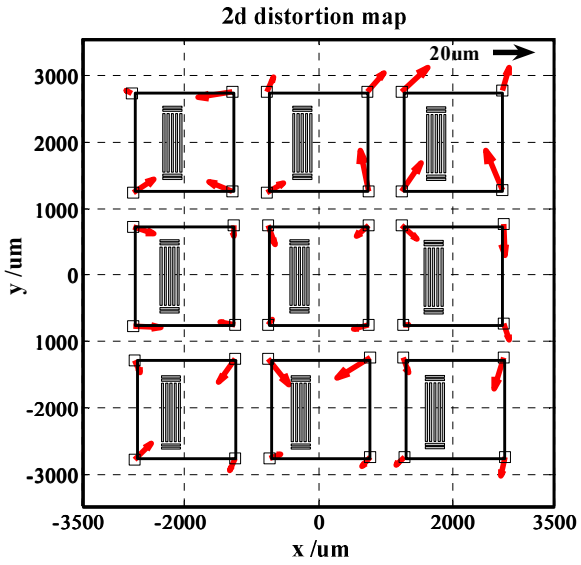


Figure 5-15 Absolute distortion between the printed images and the silicon master. The schematic shows a typical print head with the inner corners of the supporting bar marked by squares. The arrows, which are on a different scale, illustrate the magnitude and difference of the printed image with respect to the master. The distortion data shown is the average of all six stamps.

5.4.3 Layer-to-layer accuracy

Layer-to-layer accuracy of the different stamps is obtained as described in Section 5.3.2. Distribution of the misalignment data is presented in Figure 5-16, based on 50 prints in the central cell of the 3×3 array. Average misalignments of 9.1 μm (standard deviation 8.2 μm) are obtained, whilst the median value is 5.5 μm, suggesting that the misalignments lie mostly in the 0-10 μm range. These values are also consistent with the measured absolute distortion.

For those prints that lie within the 0-5 μm band (Figure 5-16), there is hardly any deviation (<2 μm) in the misalignment within different cells of the array of patterns. For those prints with large misalignment >15 μm, the deviation between cells could be as much as 15 μm. Moreover, those stamps that gave inaccuracies of >15 μm tended to consistently do so and this points towards defects within those stamps due to processing, rather than towards the

inherent limit of the self alignment system. In fact, these stamps had curled slightly due to shearing of the steel backing when they were cut with scissors.

The use of a more controlled actuation is verified by using a linear motion manipulator (PVX 500, Wentworth Laboratories, Ltd., Bedfordshire, England) with the probe tip removed to cause deflection. The average layer-to-layer misalignment then drops to 3.4 μm (with a standard deviation of 3.3 μm) and the median to 2.1 μm. The distribution is shown in Figure 5-16 while the experimental setup is illustrated in Figure 5-17. These preliminary results indicate that a controlled actuation can significantly improve accuracy.

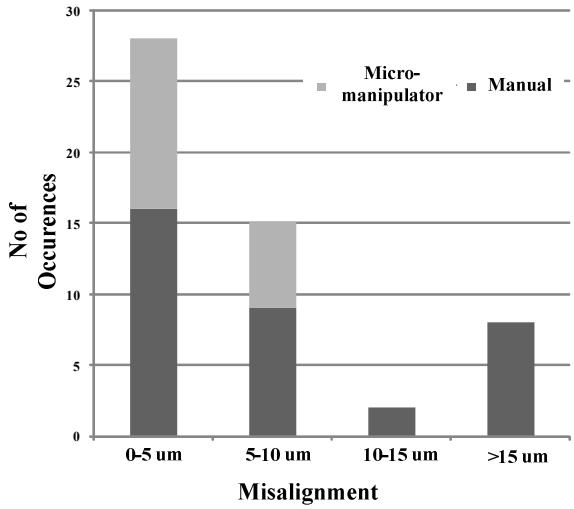


Figure 5-16 Distribution of layer-to-layer misalignment based on 50 prints

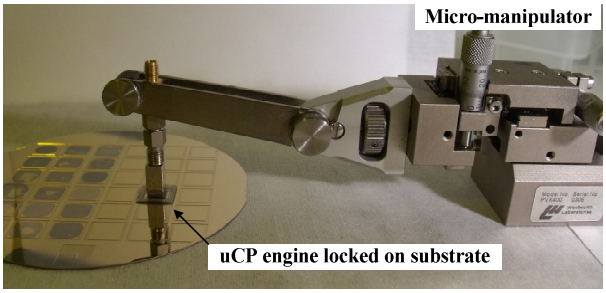


Figure 5-17 Controlled Actuation using a micro-manipulator: the stamp is aligned on the target as before but the deflection is now controlled with a micro-manipulator

5.4.4 Comparison with previous work

Despite the large body of work tackling pattern fidelity in μCP, few present data regarding multilevel accuracy. Most focus on the difference between the printed image and the original master/stamp, termed *absolute* distortion. James *et al*.[5.11] and Lauer *et al*.[5.12] report 3-axis stages with alignment optics capable of ±1 μm print to print accuracy (for stamp sizes ~10×10 mm). A commercial solution, the μCP2.1[5.13] (Gesim), consists of alignment stages with optics and a pneumatic actuation that enables 5 μm positioning accuracy. Others such as Decré *et al*.[5.14] or Burgin *et al*.[5.15] present high fidelity contact printers (absolute distortions of 0.69 μm over 100 mm and 1 μm over 75 mm respectively) with alignment optics that presumably allow ±1 μm accuracy from run to run. Rogers *et al*.[5.16] present relative alignment data by printing an image on a reference grid, displacing and rotating the stamp, and printing again. After subtracting translational and rotational errors, the maximum difference between the two prints with respect to the reference grid is reported as 4μm over a length of 4.5 mm (0.09%). This reflects the errors that would have occurred even if the prints were perfectly aligned. An approach similar to ours in spirit has been presented by Tien *et al.*[5.17]. Here, a single stamp with patterns distributed over 4 levels is designed and by varying the applied pressure, different areas of the stamp make contact thereby making

complementary inherently self-aligned patterns. Feature sizes are of the order of 100 μm and no alignment data is presented but values of 10s of μm can be inferred from the images. This approach is very simple and easy to implement but requires careful loading and cross contamination can be an issue, especially as sizes are scaled down.

The approach presented here, with a layer-to-layer accuracy of 10 μm over a length of 5 mm (0.2 %) is relatively inaccurate, but still allows multi-level patterning with no overhead such as alignment optics. The complexity of the silicon masters may be of concern, but once these are available, hundreds of stamps can be made by simple replica moulding. As for bonding of the steel backing to the polymer, it is low yield as it requires hand-eye manipulation, and ways of improving this aspect need to be investigated.

The main drawback of the proposed system is that a matching micro-fabricated substrate is still required. These can be reused by stripping the Au layer and coating a fresh one for new experiments. Another avenue to be investigated would be injection/replica moulding these substrates and then coating with Au.

5.4.5 μCP with different inks

Patterning of different monolayers is demonstrated using 1-hexadecanethiol ($HS(CH_2)_{15}CH_3$) and 11-mercaptoundecanoic acid ($HS(CH_2)_{10}C0_2H$) as described in Section 5.3.1.To facilitate imaging, the underivatized Au was etched to reveal the SAM covered regions. Condensation figures were used to differentiate between the hydrophilic and hydrophobic SAM [5.18]. The target substrate was cooled down after patterning and then exposed to ambient conditions where water vapour would condense. The droplet size distributions differ significantly

between regions covered by the two SAMs as shown Figure 5-18. Two different inks were used here as demonstration but it is clear that up to 6 different compatible monolayers with different terminations could be patterned by μCP and a further 7th monolayer could be deposited from solution on the empty areas.

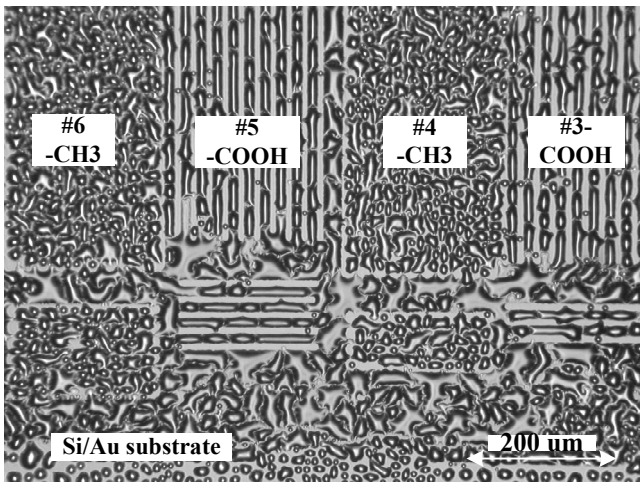


Figure 5-18 Condensation figure revealing the patterns of SAMs with different monolayers. The different droplet distributions on the hydrophilic (-COOH) and hydrophobic (-CH3) provide sufficient contrast for imaging by optical microscopy.

5.5 Conclusion

A 6-level μCP tool with self-alignment features has been designed and its operation demonstrated. Multi-level accuracy has been shown to lie within the 5-10μm range with a manual operating mode, and without the need for optical alignment. Areas requiring further investigation are the passive alignment mechanism and its limits and scaling to larger die sizes. The fabrication process also needs to be optimized to enable true wafer scale processing. In addition, more consistent print actuation mechanisms, such as pneumatic, which would not overly complicate the current set up, warrant further study.

Potential applications lie in the area of biochemistry where multi level μCP for sensitizing surfaces (e.g. in a biosensor array or multi-analyte bio-chips) is required. Six-level patterning to impart different biochemical and/or tribological properties to a substrate has been demonstrated and more levels could be implemented. The polymer moulding approach significantly drives down cost and opens new possibilities for patterning in geometrically challenging microstructures such as micro-channels.

Most importantly perhaps is that reliable aligned multilevel patterning can be carried out without any additional equipment, except for a compatible substrate. A batch fabrication process for structured substrates, e.g. by injection moulding and then coating with an appropriate layer, could be envisaged.

5.6 References

[5.1] A. Govindaraju, A. Chakraborty, and C. Luo, "Reinforcement of PDMS masters using SU-8 truss structures," *J. Micromech. Microeng.,* vol. 15, pp. 1303-1309, 2005.

[5.2] C. Moraes, Y. Sun, and C. A. Simmons, "Solving the shrinkage-induced PDMS alignment registration issue in multilayer soft lithography," *J. Micromech. Microeng.,* vol. 19, p. 065015, 2009.

[5.3] C. Y. Hui, A. Jagota, Y. Y. Lin, and E. J. Kramer, "Constraints on Microcontact Printing Imposed by Stamp Deformation," *Langmuir,* vol. 18, pp. 1394-1407, 2002.

[5.4] E. Delamarche, H. Schmid, B. Michel, and H. Biebuyck, "Stability of molded polydimethylsiloxane microstructures," *Adv. Mater.,* vol. 9, pp. 741-746, 1997.

[5.5] M. M. J. Decre, P. H. M. Timmermans, O. van der Sluis, and R. Schroeders, "Numerical and Experimental Study of Critical Roof Collapse Conditions in Soft Lithography," *Langmuir,* vol. 21, pp. 7971-7978, 2005.

[5.6] E. Menard, L. Bilhaut, J. Zaumseil, and J. A. Rogers, "Improved Surface Chemistries, Thin Film Deposition Techniques, and Stamp Designs for Nanotransfer Printing," *Langmuir,* vol. 20, pp. 6871-6878, 2004.

[5.7] H. Schmid and B. Michel, "Siloxane Polymers for High-Resolution, High-Accuracy Soft Lithography," *Macromolecules,* vol. 33, pp. 3042-3049, 2000.

[5.8] T. W. Odom, J. C. Love, D. B. Wolfe, K. E. Paul, and G. M. Whitesides, "Improved Pattern Transfer in Soft Lithography Using Composite Stamps," *Langmuir,* vol. 18, pp. 5314-5320, 2002.

[5.9] A. Bietsch and B. Michel, "Conformal contact and pattern stability of stamps used for soft lithography," *J. Appl. Phys.,* vol. 88, pp. 4310-4318, 2000.

[5.10] A. Mata, A. Fleischman, and S. Roy, "Characterization of Polydimethylsiloxane (PDMS) Properties for Biomedical Micro/Nanosystems," *Biomed. Microdevices,* vol. 7, pp. 281-293, 2005.

[5.11] C. D. James, R. Davis, M. Meyer, A. Turner, S. Turner, G. Withers, L. Kam, G. Banker, H. Craighead, M. Issacson, J. Turner, and W. Shain, "Aligned microcontact printing of micrometer-scale poly-L-Lysine structures for controlled growth of cultured neurons on planar microelectrode arrays," *IEEE Trans. Biomed. Eng.,* vol. 47, pp. 17-21, 2000.

[5.12] L. Lauer, S. Ingebrandt, K. Scholl, and A. Offenhauer, "Aligned microcontact printing of biomolecules on microelectronic device surfaces," *IEEE Trans. Biomed. Eng.,* vol. 48, pp. 838-842, 2001.

[5.13] GeSIM, Micro-Contact Printing Instruments, http://www.gesim.de.

[5.14] M. M. J. Decre, R. M. Schneider, D. Burdinski, J. Schellekens, M. Saalmink, and R. Dona, "Wave Printing (I) : Towards Large-Area, Multilayer Microcontact Printing," *Mater. Res. Soc. Symp. Proc. Vol. EXS-2,* vol. M4, p. 9, 2004.

[5.15] T. Burgin, V. E. Choong, and G. Maracas, "Large Area Submicrometer Contact Printing Using a Contact Aligner," *Langmuir,* vol. 16, pp. 5371-5375, 2000.

[5.16] J. A. Rogers, K. E. Paul, and G. M. Whitesides, "Quantifying distortions in soft lithography," *J. Vac. Sci. Technol. B,* vol. 16, pp. 88-97, 1998.

[5.17] J. Tien, C. M. Nelson, and C. S. Chen, "Fabrication of aligned microstructures with a single elastomeric stamp," *Proc. Natl. Acad. Sci.,* vol. 99, pp. 1758-1762, February 19, 2002 2002.

[5.18] G. P. Lopez, H. A. Biebuyck, C. D. Frisbie, and G. M. Whitesides, "Imaging of features on surfaces by condensation figures," *Science,* vol. 260, pp. 647-649, April 30, 1993 1993.

6 Hydraulically actuated μCP engine

In this chapter, controlled actuation of μCP engines using hydraulics is investigated. Prototypes combining the replica moulded stamps described in Chapter 5 with a precision machined Perspex chuck are constructed and characterised. The difficulties of interconnecting macroscopic hydraulic parts with MEMS are highlighted and some solutions are provided. Lastly, single-level μCP with a hydraulic drive is demonstrated.

6.1 Hydraulic and pneumatic actuation in microsystems

Hydraulic and pneumatic micro-actuators can deliver high force and power densities at the microscale in comparison to electrostatic, thermal or piezo-electric actuators [6.1]. Despite this property, this class of actuators is often overlooked in MEMS, although applications are more common in microfluidics and μTAS. For example, numerous pneumatically operated valves and pumps have been developed and some examples are reviewed by Oh *et al.* [6.2] and Laser *et al*. [6.3] respectively.

In MEMS, the most common forms of hydraulic/pneumatic actuators are membrane type actuators [6.1] due partly to their ease of fabrication. Silicone rubber is popular in such applications because of its low stiffness, which implies large deflections under small loads, and ease of fabrication. Examples of such actuators include a refreshable Braille cell array actuated with compressed air [6.4], a tunable elastomeric mould whose shape is adjusted pneumatically [6.5], and various other components for microfluidic systems as summarised in [6.6]. In the field of μCP, fluidic actuators driven by compressed air have been proposed by Gesim [6.7] and Philips [6.8].

Hydraulic actuation, on the other hand, appears less popular despite the fact that the use of an incompressible fluid allows larger pressures to be exerted. In fact, interconnecting microsystems with hydraulics in the macro world is non- trivial and is often a hurdle in microfluidics especially when a large number of connections are involved, as discussed in [6.9] and [6.10]. Commercial solutions exist and are described in [6.11]. The operating pressure in this case is limited to 600 kPa. Bhagat *et al*. [6.12] provide an adhesive free solution which can sustain operating pressures of up to 1.7 MPa.

In this chapter, the use of water as a hydraulic fluid to actuate stamps for uCP is investigated. Water is appropriate given the hydrophobic nature of the PDMS stamp, while a hydraulic drive implies that actuation can easily be controlled using a benchtop syringe driver.

6.2 Design and Concept

In this section, the hydraulically actuated μCP engine is described. The replica moulded stamp described in Chapter 5 is modified and the operation of the modified design is verified through FEA and analytical models.

6.2.1 Hydraulic actuation

The main features of the proposed hydraulic system are illustrated in Figure 6-1. It consists of a machined chuck with inlet and outlet pipes, a square cavity of length l_o = 8800 μm which is equal to the movable area of the μCP engine. Controlled volumes of hydraulic fluid (water in this case) are injected with the syringe driver. Since water is practically incompressible (see e.g. [6.13]), the volume enclosed by the deformed stamp is equal to the injected volume, ΔV.

The outlet is closed off by a tap which can be opened for flushing the system or deflating the deformed membrane after actuation. By Pascal's principle, neglecting the height differences, the pressure throughout the closed system is constant and equal to P.

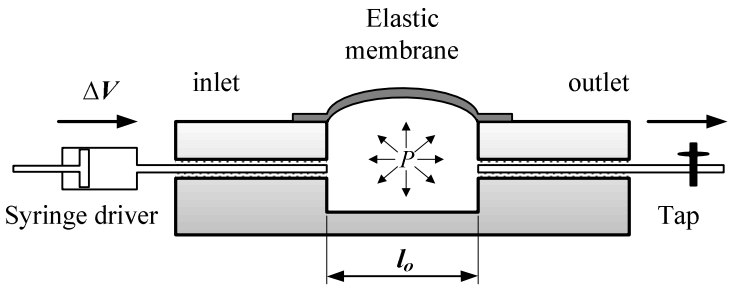


Figure 6-1 Outline of hydraulic system consisting of inlet/outlet, hydraulic cavity, and a deformable membrane

6.2.2 Replica moulded μCP stamp

The stamps in this case are similar to those described in Chapter 5 except that the patterned steel backing is replaced by a plain 50 μm thick Kapton polyimide (PI) sheet. The print head area is stiffened relative to the membrane area by adding a third layer made out of structured PDMS. The stamps are illustrated in Figure 6-2. Detailed fabrication steps are presented later, but briefly, Part A and part B are first spin cast and cured on their respective masters. Part A is identical to the PDMS layer of the device in Chapter 5. The PI film is bonded to part B whilst it is on the master. The PI-part B stack is peeled off, aligned to the print head of part A, and bonded together. The main advantages of plain PI film over photo-etched steel are low cost, simplicity, and inherent material compatibility as PI-PDMS stacks are less likely to delaminate. However, a possible concern is that the elastic modulus of the PI is two orders of magnitude lower than that of steel and the relative softness of the structure may be prone to roof collapse. This is countered by lower operating pressures and a thick 250 μm layer of

backing PDMS over the print head (c.f. ≈ 50 μm thick only over the membrane regions). The low pressures and avoidance of roof collapse are verified by FEA in Section 6.2.4.

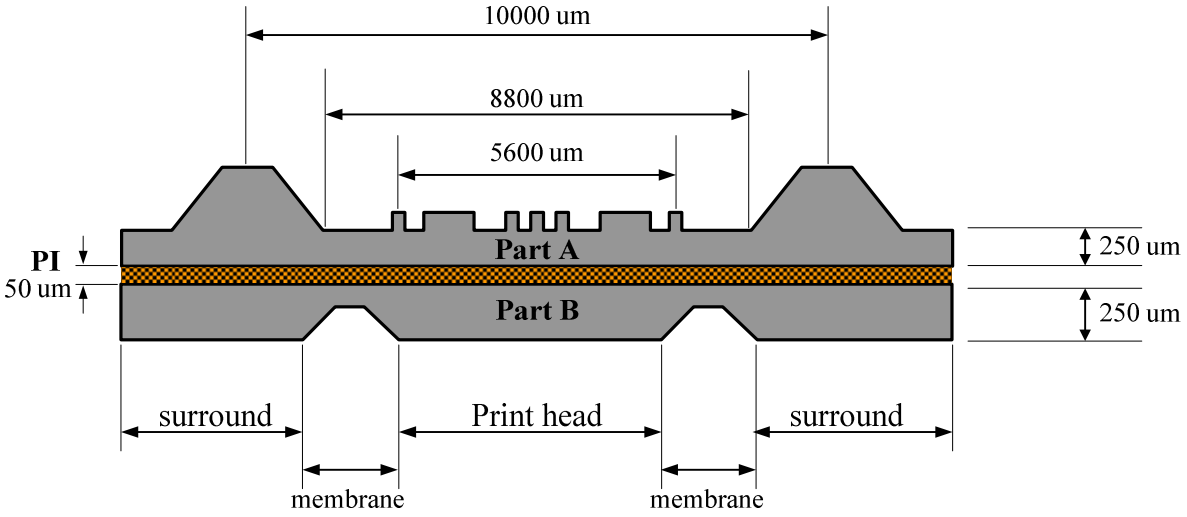


Figure 6-2 Cross-section view of μCP engine with PI elastic backing

6.2.3 Modelling of Membrane

In this Section, the simple models that describe the mechanical deformation of the μCP engine are presented. Two aspects are discussed: 1) the deflection under an applied load and the relationship to strain energy; 2) the deformation volume required to cause a certain area to be in contact.

Strain energy stored in bending

The multi-layered replica moulded stamp is simplified and modelled as a single-layered homogeneous elastic membrane of Young's modulus, E_m, and Poisson's ratio v_m. Using thickness-weighted average values, the Young's modulus and Poisson's ratio can be expressed as $E_m = (E_1h_1 + E_2h_2)/(h_1+h_2)$, and $v_m = (v_1h_1 + v_2h_2)/ (h_1+h_2)$. The elastic constants for both material and the average value for the multilayer structure are tabulated in Table 6-1

	PDMS	PI	Thickness weighted average
Thickness /μm	500	50	550
Young's Modulus / MPa	1	2500	218
Poisson's Ratio	0.5	0.35	0.49

Table 6-1 Thickness weighted average values of elastic constants for multilayer structure

Following Timoshenko [6.14], Chapter 13, and Section 101, an approximate solution to the large deflection of thin plates (i.e. deflections many times larger than their thickness) can be obtained from the energy method. For such thin plates, the resistance to bending can be neglected and the flexural rigidity $D = Eh^3/(12(1-\nu))$ can be taken to be zero. The strain energy is then due only to the stretching of the middle plane and can then be expressed solely in terms of tensile and shear strains in the x-y plane (i.e. in the plane of the membrane). See equation (248) of [6.14].

Assuming suitable expressions for the displacements on the membrane, and $\nu = 0.25$, the strain energy of the membrane due to the stretching of its middle surface when a hydrostatic pressure is applied is can be expressed as:

$$V = \frac{Eh}{7.5}\left[\frac{5\pi^4}{64}\frac{w_o^4}{a^2} - \frac{17\pi^2}{6}\frac{cw_o^2}{a} + c^2\left(\frac{35\pi^2}{4} + \frac{80}{9}\right)\right] \tag{6.1}$$

Here, $2a$ is the length of the square membrane, $c = 0.147w_o^2/a$, w_o is the maximum deflection at the centre, and h is the thickness of the membrane. Using Equation (6.1) with $h = 550$ μm and $E = E_m = 218$ MPa, the maximum displacements measured can be related to the strain energy in the membrane. Note that this expression assumes $\nu = 0.25$, whilst, $\nu_m = 0.49$. In the case of large deflection of a membrane, the energy is weakly dependent on the Poisson ratio (see e.g. [6.14, 15]) and hence equation (6.1) provides a reasonable approximation.

Volume enclosed by deformed membrane under contact

The membrane after deformation and contact with a flat surface at a flying height s is illustrated in Figure 6-3. The membrane is assumed to deform to a trapezoidal shape, although the sloping edges are likely to be curved in reality. However, given the small value of s (190 μm) compared to the base (8800 μm), the volume under the slopes is negligible compared to the total volume enclosed.

The volume enclosed is thus approximated by the difference between two square-based pyramids, one with a base of length l_o = 8800 μm, and height d, and the other of base length l, and height (d - s). For $0 < l < 5600$ μm, $d = sl_o/(l_o - l)$, and the volume enclosed is given by

$$\Delta V = \frac{1}{3}\left(l_o^2 d - l^2(d - s)\right) \tag{6.2}$$

The normalised contact area is given by $(l/5600)^2$, where l is in μm.

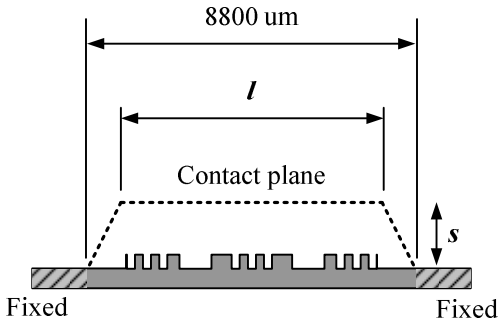


Figure 6-3 Schematic of the cross-section of the stamp fixed at the edges. In contact, the deformed stamp can be approximated by a pyramidal shape (marked by dotted lines) and the volume enclosed by deformed membrane is given in Equation 6.2.

6.2.4 Simulation

The mechanical response of the stamp and the interaction with the substrate is investigated by FEA in the CoventorWare package. The steady-state operation is characterised using a mechanical solver by applying a uniform load to the surfaces of part B that are exposed to the hydraulic fluid and computing the deformation. Exploiting symmetry, only a quarter of the structure is simulated with appropriate boundary conditions applied to the symmetry planes. The surround on part B is fixed to emulate the stamp when it is glued to the chuck. The simulated model is illustrated in Figure 6-4 highlighting the relevant surfaces. In the figure, the stamp is subjected to a load of 20 MPa and is in contact with a surface (not shown) 190 μm above the initial position.

Both deformation without contact and deformation with contact to surface at a flying height s are simulated. Cross sectional views of the membrane under different loads are illustrated in Figure 6-5. The upper row illustrates free deformation whereas the lower row illustrates contact with a surface separated by 190 μm. Under free deformation, the print head does deform although much less than the membrane area, indicating that the stiffening of the print head is successful. In contact, the local stiffening appears to be enough to avoid roof collapse. This is quantified in Figure 6-6 which shows the variation of contact area with applied load. Over the range simulated, no roof collapse occurred. When s = 50 μm, full contact is achieved very quickly (≈ 2 MPa), whereas a load of ≈ 10MPa is required for s = 190 μm.

Clearly, low operating pressures are desired to facilitate contact printing and minimise the risk of pattern deformation. Another reason is to avoid leaks at the interface between the membrane and the hydraulic or pneumatic chuck onto which the stamp is bonded. For

example, the ultimate bond strength of plasma-bonded PDMS, which is a convenient method of assembling the hydraulic stamp, is of the order of 0.5 MPa [6.16, 17]. As shown in Figure 6-6, one method of reducing the operating pressures in to use small flying height, but even with s = 50 µm, the pressure required are higher than the ultimate bond strength of plasma-activated PDMS. Other methods of dropping the operating pressures would be to reduce the stiffness of the membrane by e.g. increasing the length of the membrane relative to the length of the print head, or reducing the thickness of the membrane. These aspects are beyond the scope of this thesis but warrant further exploration.

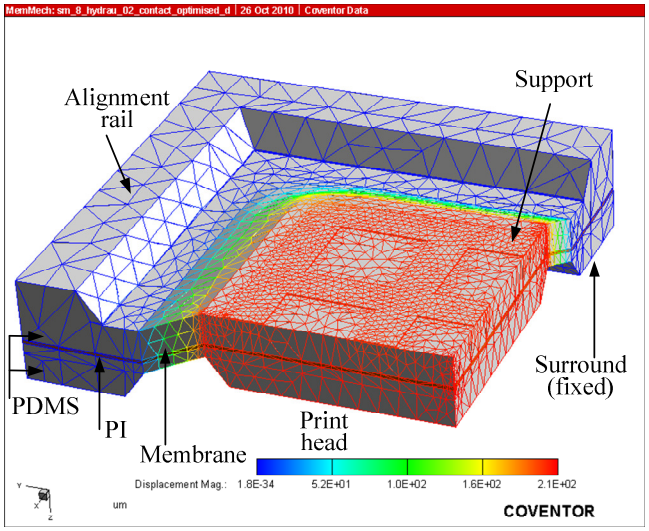
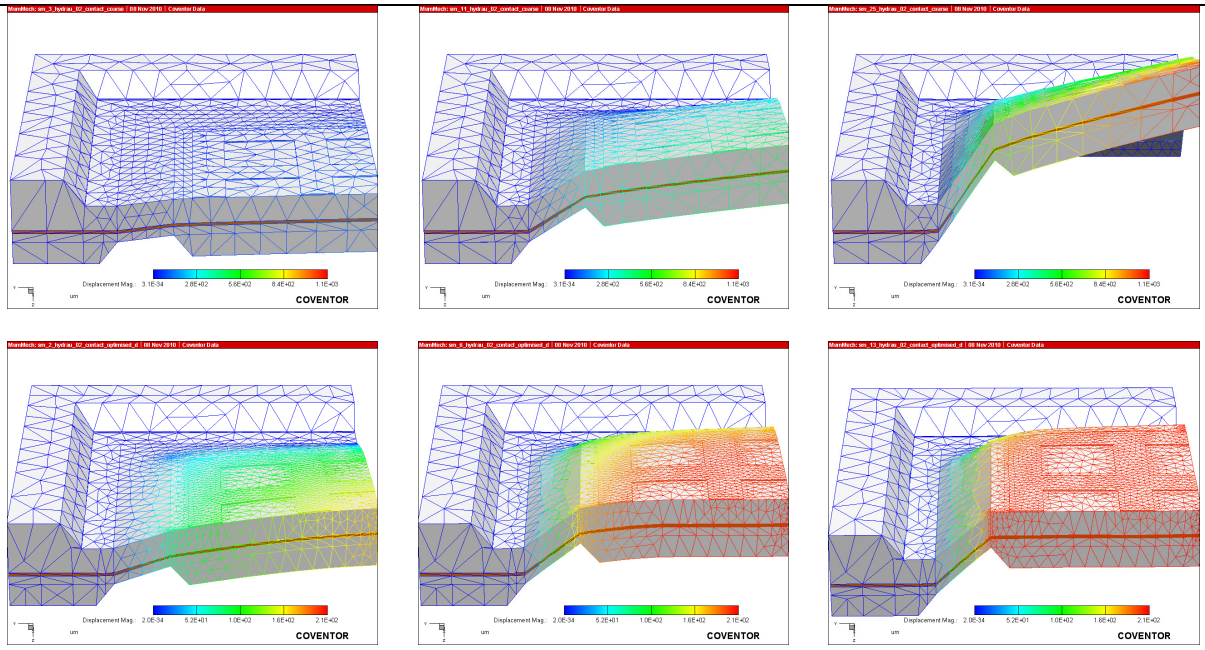


Figure 6-4 Model used for simulation. Relevant surfaces/parts are labelled.



1 MPa **5 MPa** **12 MPa**

Figure 6-5 Upper row: deformation of membrane without any contact surface. Lower row: deformation of membrane with a contact surface 190 µm from the initial surface. Deformation in bottom row is exaggerated for clarity. Z-scale is different in each row.

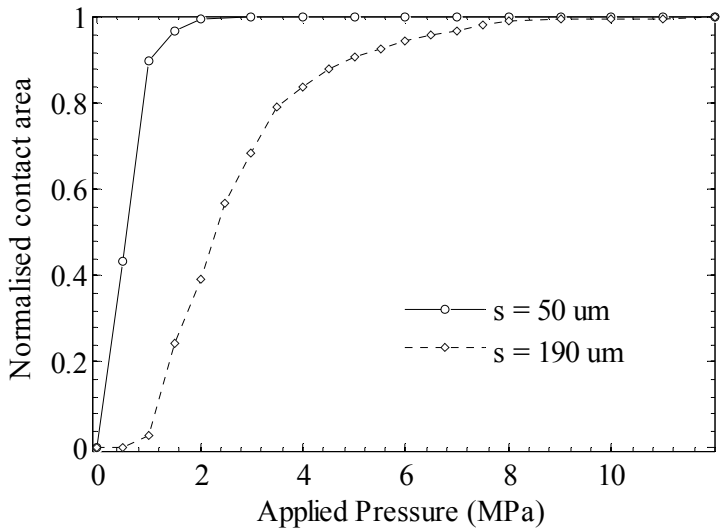


Figure 6-6 Simulation results showing variation of support contact area as the load is applied. For the range of loads displayed, the roof does not make contact at all.

6.3 Fabrication

In this section, replica moulding of the PDMS parts and stacking of the different layers are described. The fabrication of the silicon masters is first described, followed by the stamp casting process. Bonding of the different layers by using partially cured PDMS and assembly of the membrane to the hydraulic chuck are presented next. Difficulties faced in assembling the PDMS part to the Perspex chuck are highlighted and a modified assembly process is finally proposed.

6.3.1 Si master fabrication

The masters used for moulding the PDMS parts are fabricated by conventional MEMS fabrication techniques. The part A master is identical to the master of chapter 5 and is formed using 2-level lithography and etching, while the part B master is formed by single level lithography and etching. The main steps are illustrated in Figure 6-7a and b whilst SEMs of the completed masters are shown in Figure 6-8a and b.

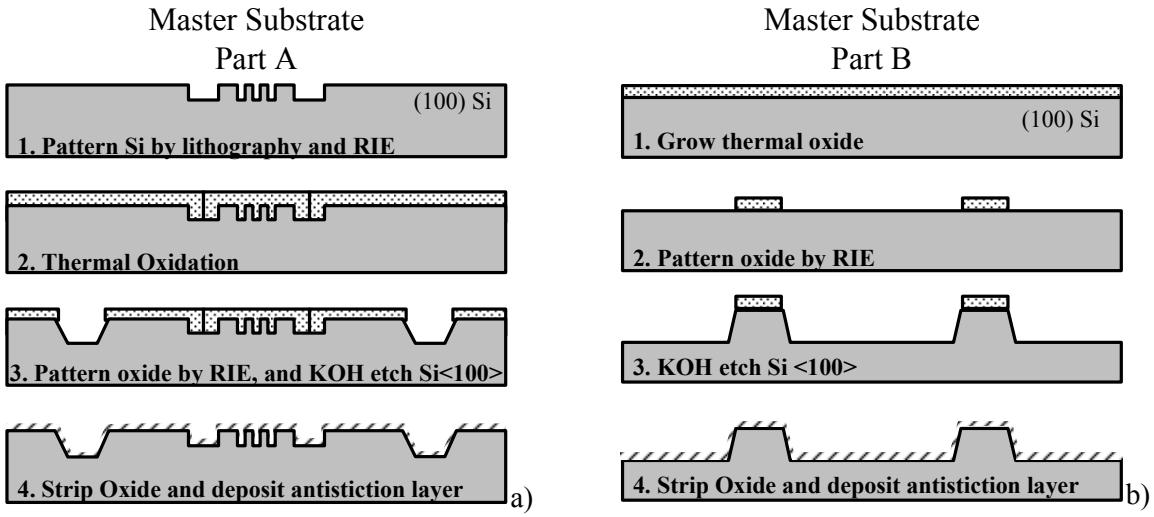
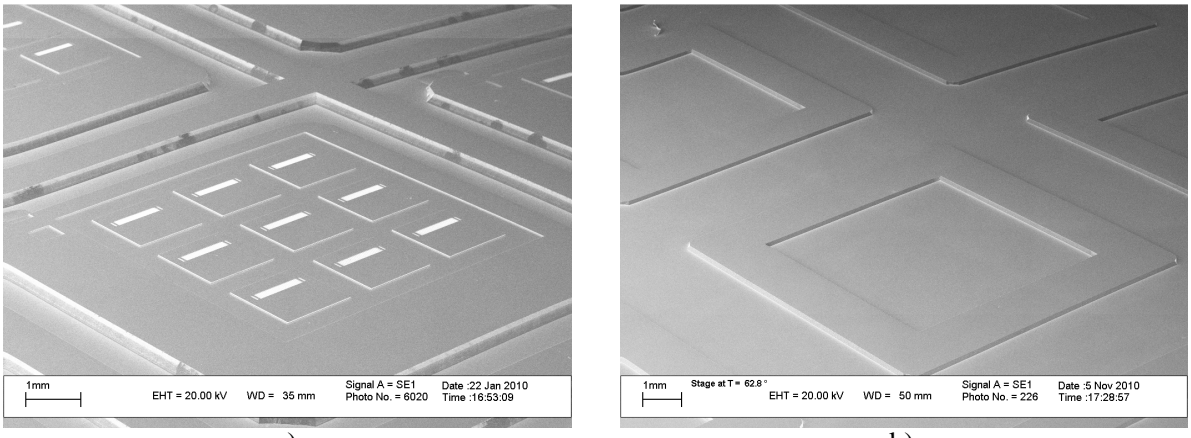


Figure 6-7 Process flow for Si master for a) Part A, b) Part B

For the part A master, the fine features are formed by lithography and RIE of the underlying substrate to a depth of ≈10 μm. The patterned substrate is then oxidised and subjected to a second lithography step to pattern the oxide. The oxide layer is then used as mask for an anisotropic etch of the Si(100) to a depth of 200 μm using a KOH solution. The completed structure, after removal of the masking layers, is shown in Figure 6-8a showing good resolution of the bi-level etch, whilst the process parameters are shown in Table 6-2.

The part B master is formed by oxidising an Si(100) wafer and patterning the oxide layer by lithography and RIE. The latter is then used as mask for an anisotropic etch, as with the part A master. The machined master is shown in Figure 6-8b and illustrates the thick print head backing relative to the membrane region. The process parameters are tabulated in Table 6-3. Both masters are coated with a Teflon-like layer to facilitate demoulding.



a) b)

Figure 6-8 SEMS of completed a) Part A master, b) part B master

Part A Master		
Fabrication step	**Sub-steps**	**Parameters**
1. Print patterns	Lithography	- S1828, 500nm thick, Spin: 3000rpm, 1000rpm/s, 40 s - Softbake: 65 C (HP)- 2 min, 85 C (HP)– 2min, 90 C (Oven) – 2 min

		- Exposure 460 mJ/cm^2, - Developer MIF319 (1 min)
	Silicon RIE – 10 μm	SF_6 (30 sccm), O_2 (10 sccm), Base pressure 120 mTorr, RF power 100 W.
	Resist Strip	Acetone immersion (3min), Then IPA and DI, then O_2 plasma clean.
2. Thermal Oxidation	Dry oxidation: 1.2 μm	Carbolite furnace, 1100 C, 72 hours.
3a.Pattern Oxide	Lithography	- AZ9260, 17 μm thick, Spin1 : 500rpm, 100rpm/s, 10 s, Spin2: 1000rpm, 500rpm/s, 40 s - Softbake: 60 C (HP)- 3 min, 80 C (HP)– 3min, 100 C (HP) – 1min, 90 C (Oven) – 2 min - Exposure 1110 mJ/cm^2, - Developer :AZ400K:DI 1:4 (2.5 min)
	RIE SiO_2	CHF_3 (25 sccm), Ar (25 sccm), O_2 (2 sccm), Base pressure 30 mTorr, RF power 200 W. Duration: 60 min
	Resist strip	1165 @ 65 C immersion (15 min). DI rinse, then O_2 plasma clean.
3b. V-groove etch	KOH etch – 200 μm	40 % KOH solution in DI, with 1% IPA @ 80 C (~200 minutes)
	SiO_2 strip	CHF_3 (25 sccm), Ar (25 sccm), O_2 (2 sccm), Base pressure 30 mTorr, RF power 200 W. Duration: 60 min
4. Antistiction	Passivation phase of DRIE (CF_x)	C_4F_8 (120 sccm), Base pressure 12 mTorr, Coil RF power 300W, frequency: HF, Platen power 20 W. Duration 120 s. Hardbake: 150 C (HP) – 5min.

Table 6-2 Process parameters for Part A master

Part B Master

Fabrication step	Sub-steps	Parameters
1. Thermal Oxidation	Dry oxidation: 1.2 μm	Carbolite furnace, 1100 C, 72 hours.
2.Pattern Oxide	Lithography	- AZ9260, 17 μm thick, Spin1 : 500rpm, 100rpm/s, 10 s, Spin2: 1000rpm, 500rpm/s, 40 s - Softbake: 60 C (HP)- 3 min, 80 C (HP)– 3min, 100 C (HP) – 1min, 90 C (Oven) – 2 min - Exposure 1110 mJ/cm^2, - Developer :AZ400K:DI 1:4 (2.5 min)
	RIE SiO_2	CHF_3 (25 sccm), Ar (25 sccm), O_2 (2 sccm), Base pressure 30 mTorr, RF power 200 W. Duration: 60 min
	Resist strip	1165 @ 65 C immersion (15 min). DI rinse, then O_2 plasma clean.
3. V-groove etch	KOH etch – 200 μm	40 % KOH solution in DI, with 1% IPA @ 80 C (~200 minutes)
	SiO_2 strip	CHF_3 (25 sccm), Ar (25 sccm), O_2 (2 sccm), Base pressure 30 mTorr, RF power 200 W. Duration: 60 min

4. Antistiction	Passivation phase of DRIE (CF_x)	C_4F_8 (120 sccm), Base pressure 12 mTorr, Coil RF power 300W, frequency: HF, Platen power 20 W. Duration 120 s. Hardbake: 150 C (HP) – 5min.

Table 6-3 Process parameters for Part B master

6.3.2 PDMS stamp casting and assembly

This Section describes the casting of the PDMS parts and their assembly. The PDMS parts are made of a 1:10 formulation of Sylgard 184 and the two parts are moulded separately on their respective masters and then bonded, as illustrated in Figure 6-9. Layers are glued together using a thin 30 μm thick partially cured PDMS layer. As shown in [6.17], partially cured PDMS exhibit higher bond strengths compared to plasma activated PDMS surfaces. In addition, for this device, alignment is required and the partially cured adhesive allows adjustment even after initial contact has been made. Furthermore, air bubbles are bound to be trapped given the manual alignment process and this method is more resilient since the trapped air pockets are confined to the thin adhesive layer and do not significantly affect the mechanical properties of the bonded structure.

The casting and bonding process is shown in Figure 6-9 while the process parameters are given in Table 6-4. Part B is spun cast and the PI film is attached using a partially cured adhesive layer. Part A is replica moulded in a similar manner to form a ~200 μm thick layer. After crosslinking, a further ~30 μm partially cured layer of PDMS is deposited as adhesive. The PI-part B assembly is peeled off from its master, turned upside down, aligned to part A and contacted. Alignment and bonding can be carried out using the alignment optics of a mask aligner (Quintel Q4000IR), but in this case, for prototyping, the PI-part B bi-layer is cut into arrays of 4 × 2 dies and then aligned by hand to the part A wafer. After bonding, a transparency is placed on top of the stack as a release film, followed by a flat surface (blank Si wafer) and a 700g weight and the stack is cured on a hot plate. After cross-linking, the

finished stamp is finally peeled off from the master and cut with scissors into individual dies. Since the soft PDMS is always in bound by a rigid surface (either the Si master or the PI backing) no shrinkage is induced. Moreover, because of the quasi-symmetric structure, curling of the multilayer structure after release is minimised.

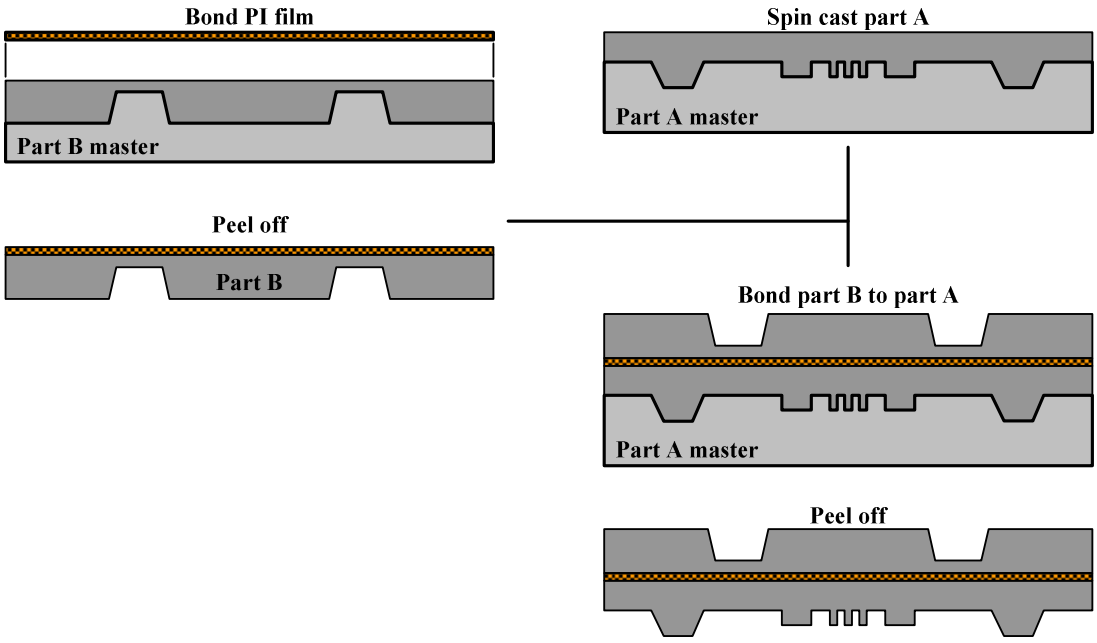


Figure 6-9 Moulding and stacking of PDMS parts with PI elastic backing. At all times, the PDMS parts are held by a rigid surface (either the Si master or the PI film).

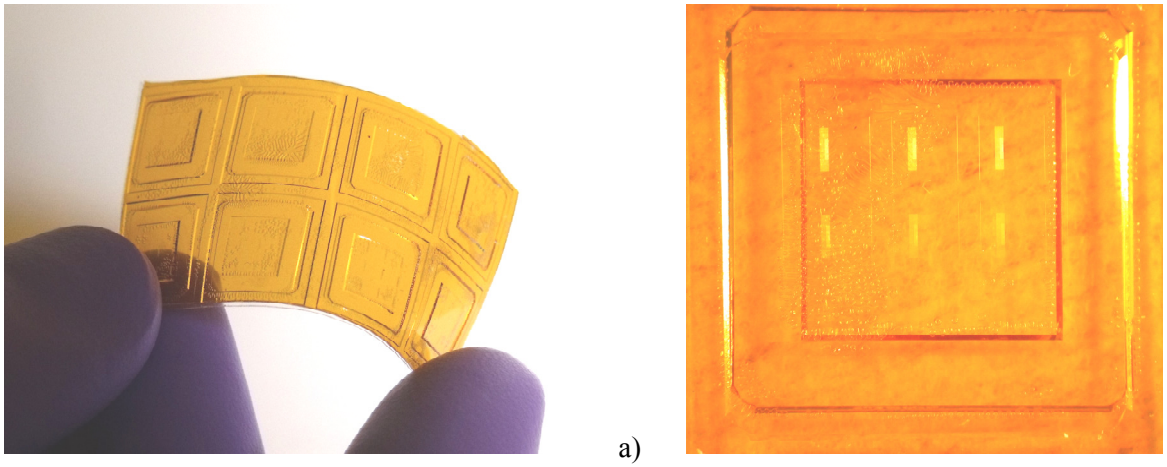
Replica moulding part A and B and bonding

Fabrication step	Sub-steps	Parameters
1. Part B casting	Spin Casting	- Sylgard 184 (1:10), 200 μm thick, Spin1 : 300rpm, 300rpm/s, 10 s, Spin2: 600rpm, 500rpm/s, 40 s - Desiccator ~ 15 minutes
	Crosslinking	90 C (HP) – 3.5 min
2. PI Bonding	Spin adhesive layer	Sylgard 184 (1:10), 30 μm thick, Spin1 : 600rpm, 1000rpm/s, 10 s, Spin2: 2500rpm, 1000rpm/s, 40 s
	Partial curing	90 C (HP) – 1.5 min
	Bond PI	Place PI onto adhesive, minimising bubbles and applying gentle pressure. Place a release film, e.g. acetate sheet, a flat Si wafer and a 700g weight and cure at 90 C (HP) for 1 hour.
3. Part A casting	Spin Casting	- Sylgard 184 (1:10), 200 μm thick, Spin1 : 300rpm,

		300rpm/s, 10 s, Spin2: 600rpm, 500rpm/s, 40 s - Desiccator ~ 15 minutes
	Crosslinking	90 C (HP) – 3.5 min
4. Part B bonding	Spin adhesive layer	Sylgard 184 (1:10), 30 μm thick, Spin1 : 600rpm, 1000rpm/s, 10 s, Spin2: 2500rpm, 1000rpm/s, 40 s
	Partial curing	90 C (HP) – 1.5 min
	Bonding	Align part B dies by hand and apply gentle pressure. Place a release film, e.g. acetate sheet, a flat Si wafer and a 700g weight and cure at 90 C (HP) for 1 hour.
5. Stamp release		Gently peel off multilayer structure from Si master

Table 6-4 Process parameters for moulding and bonding parts A and B

Completed stamps are illustrated in Figure 6-10a and b. Figure 6-10a shows a 4 × 2 array as photographed from the part B side of the device. The tri-layer structure is mechanically stable and strong although it retains its flexibility. Although not quantified, the stamp appears to maintain its flatness due to its symmetric structure. During the bonding process, some bubbles are inevitably trapped, and these can be observed in Figure 6-10b. However, these bubbles are restricted to the 30 μm adhesive layer and hence do not significantly affect the mechanical behaviour of the stamp. In addition, some misalignment between part A and part B is expected due to the manual aligning process. The latter issue can become problematic when the hydraulic stamp is eventually used for multilevel printing and requires further investigation.



a) b)

Figure 6-10 Optical images of finished stamp showing a) 4× 2 array peeled off from master, b) single die

6.3.3 Bonding onto hydraulic chuck

The hydraulic chuck onto which the stamp is mounted is made out of 10 mm thick Perspex by precision machining and is shown in Figure 6-11a. The square hydraulic cavity is formed using a computer controlled milling tool and the length of each side is 9mm and corresponds to the size of the movable part of the stamp. Inlet and outlet ports connecting to the hydraulic chamber are drilled in from the sides and accommodate clear PTFE tubes (RS, rswww.com, #399-811) with bore diameter 1.01 mm and wall thickness 0.3 mm (not shown in the image).

The PDMS part and the PTFE tubing were bonded to the hydraulic chamber using a 2-part epoxy glue (Araldite Precision). The tubing was fitted in and the epoxy polymer pasted into the gaps around the ports and allowed to set. The Perspex surface in contact with the stamp was roughened, cleaned and a thin layer of epoxy was applied to both the Perspex and the surround of part B on the stamp. The PDMS-PI assembly was aligned to the chuck, and gently pressed to make contact. An even weight was applied and the assembly was clamped together and allowed to cure for 48 hours before any handling. A schematic showing how the different parts fit together is shown in Figure 6-11b.

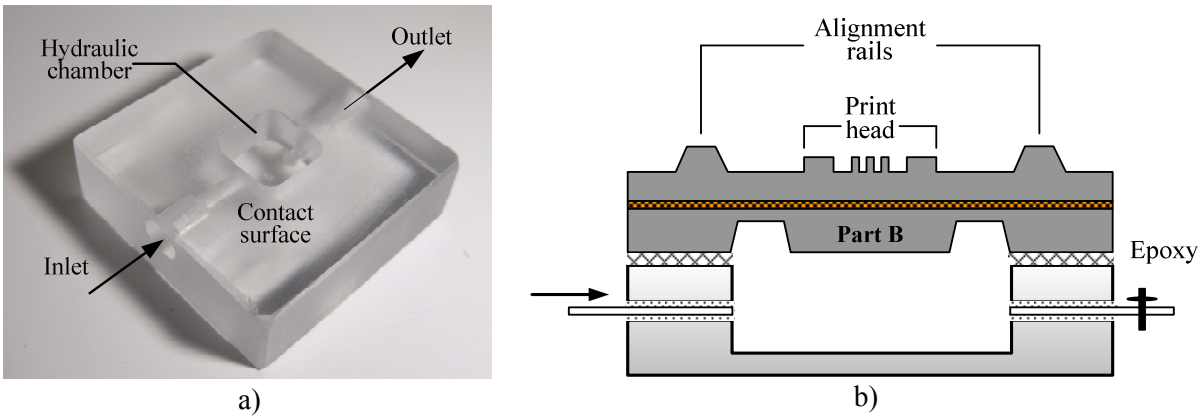


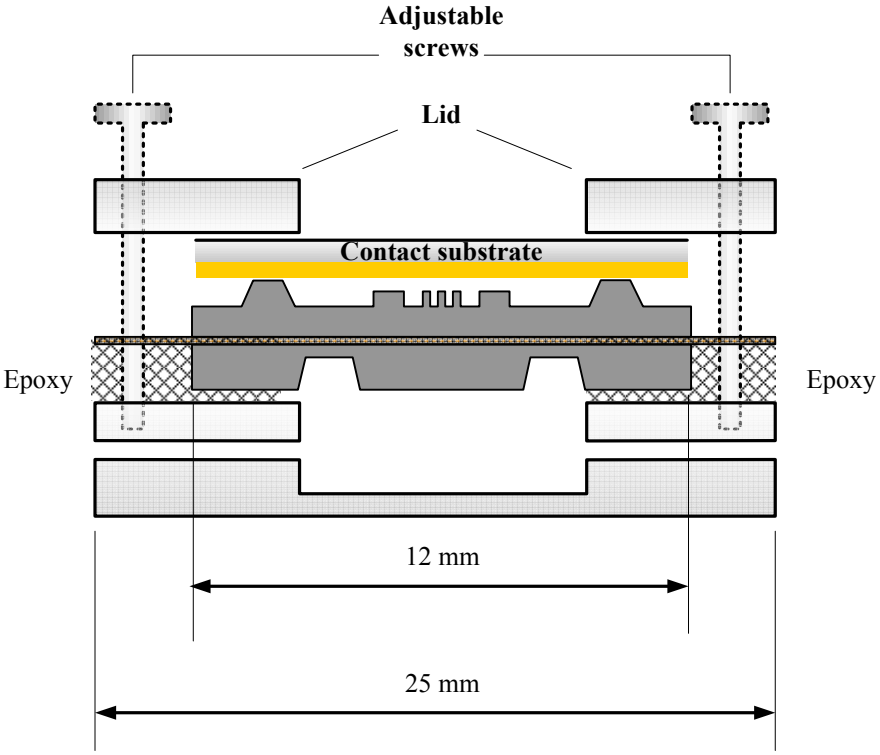
Figure 6-11 a) Optical micrograph of Perspex hydraulic chuck, b) schematic of PDMS membrane bonded onto chuck

6.3.4 Modified assembly process

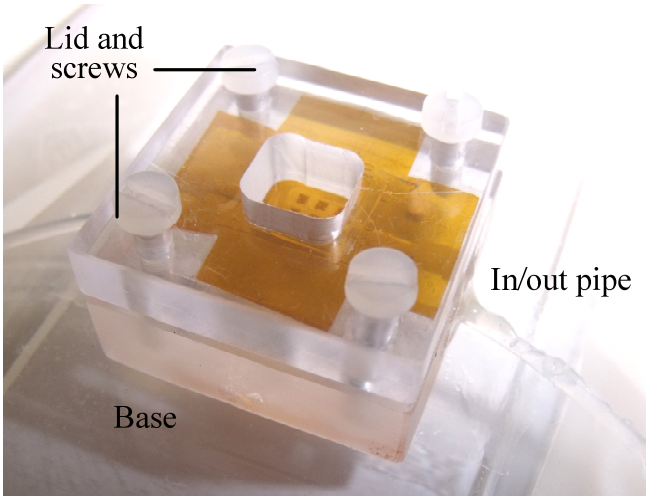
In practice, the arrangement of Figure 6-11b was found to be prone to leakage at the interface between the PDMS and the epoxy, presumably due to the small contact area of the PDMS surround. This is circumvented by increasing the contact area, as illustrated in Figure 6-12a, which shows how the PI backing is extended to a size of $\approx 25 \times 25$ mm . Another problem is that the high pressures exerted onto the membrane imply that the stamp exerts large pressures onto the contact substrate. To ensure that the latter is held stationary, a 5 mm thick Perspex lid with an opening over the movable region of the stamp is fabricated and bolted to the chuck by means of adjustable screws. This is illustrated in the diagram of Figure 6-12a. Figure 6-12b shows an optical image of the hydraulic chuck after the stamp has been bonded using the large PI film. The contact substrate is not included for clarity, but it would be placed between the stamp and the lid and held down firmly by tightening the screws.

To allow a large gluing area larger than the stamp surround, the fabrication process was modified from that described in Figure 6-9. Part B was moulded, peeled off, and then bonded to a 25 mm × 25 mm PI film. The chuck-facing surface of part B and the surrounding PI were

then activated using mild oxygen plasma, and a thin layer epoxy was applied to the PI surface. The part B-PI structure was then aligned and glued to the Perspex chuck as before. Part A was spun cast, peeled off, and then aligned and placed onto the glued part B-PI layer.



a)



b)

Figure 6-12 Modified assembly of PDMS onto hydraulic chuck: a) schematic, b) photograph with the contact surface removed

6.4 Experimental results and discussion

In this Section, experiments are carried out on the hydraulic chuck and the results are presented. The pipes and the hydraulic chamber are first flushed by opening the tap on the outlet side and driving liquid through to ensure no air bubbles are trapped. The outlet tap is then closed and a known volume, ΔV, is injected using a syringe driver (KDS 100, KD Scientific Inc.) at a flow rate of 2 mL/hour. With a 5 mL or a 1 mL syringe, the resolution of the driver is 0.01 mL.

6.4.1 Free deformation

In this Section, the contact substrate (and the supporting lid) is removed and the unrestrained deformation of the square membrane is characterised. A known volume is injected, and the maximum vertical displacement, w_o, at the centre of the stamp is measured using a microscope fitted with a Mitutoyo gauge. The membrane under a deformation volume of 0.1 mL, as well as with no injected liquid, is illustrated in Figure 6-13 showing a clear vertical displacement in the centre and an increase in curvature.

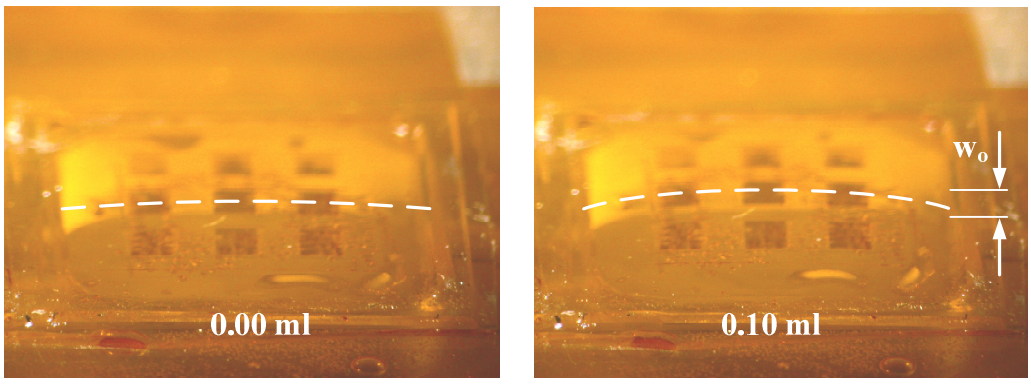


Figure 6-13 Optical micrographs showing the stamp with no injected liquid (left) and 0.1 mL injected volume (right)

In addition, 2d areal metrology of the membrane under deformation was attempted using a white light interferometer (Wyko NT9100, Veeco Instruments Inc.). To enable reliable imaging, the part A PDMS stamp was sputter coated with a 50 nm thick layer of Au to increase the reflectivity of the surface. The PDMS part was then placed on the hydraulic chuck as described in Section 6.3.4. The stamp after Au coating is illustrated in Figure 6-14 whilst the inset zooms on a single cell withing the stamp. A large number of cracks now appear on the stamp, presumably due to ion bombardment during the sputter coating process. Another issue is the limited numerical aperture of the objective of the microscope, which limits the ability to capture data on sloping or curved edges. Contour maps of the membrane with no injected water and with 0.10 mL deformation are illustrated in Figure 6-15. Note that a low pass filter was applied to the displayed image to remove the cracks visible in Figure 6-14 and highlight the stamp features.

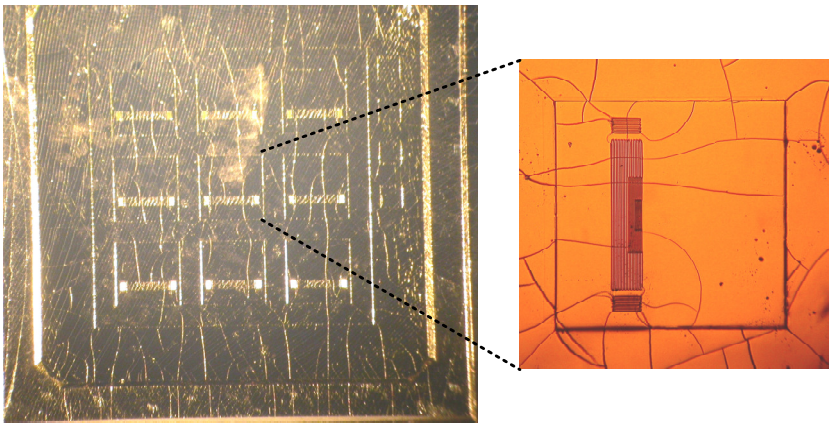


Figure 6-14 Optical micrograph of Au-coated stamps used for imaging. The cracks are due to the metal coating process.

In Figure 6-15a the entire movable area of the stamp is reliably imaged whilst the lack of data points in the membrane region of Figure 6-15b is due to the large slope. With 0.00 mL

injection, the maximum height difference across the print head is ≈ 10 µm, whilst with an injection of 0.10 mL, the maximum height difference is ≈ 140 µm. As for curvature, with no deformation, the membrane has an estimated radius of curvature of ~120mm, whilst with a deformation volume of 0.10 mL, the radius is ~40mm.

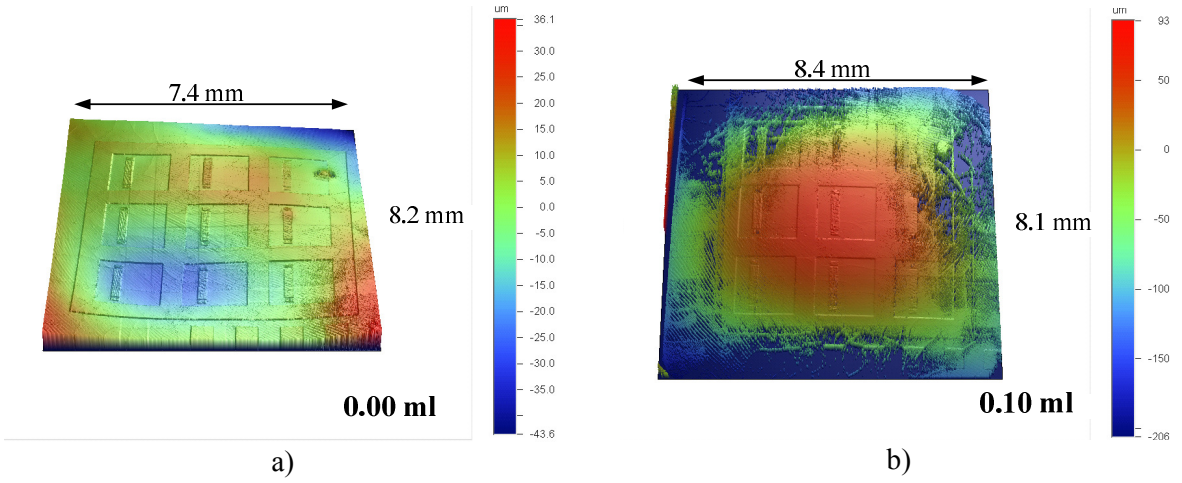


Figure 6-15 White light interferometer contour plots of membrane with a) 0.0 mL, b) 0.10 mL deformation

The variation of w_o with injected volume is illustrated in Figure 6-16 and is measured using the conventional microscope fitted with a height gauge. The maximum deflection initially rises very quickly with injected volume and the rate of increase decreases as volume increases. In the case of 0.01 mL injections, the deformation volume was increased in small increments of 0.01 mL and the corresponding value of w_o measured in each case. In the large injection data set, a certain volume was injected, w_o measured, and the membrane was "deflated" by opening the tap on the outlet. This is repeated for different deformation volumes. As illustrated in Figure 6-16, both sets of measurements show good agreement, indicating there is no hysterisis due to inflation and deflation at the injection rate tested.

The measured results were compared to the simulated model by relating the experimental data to the strain energy stored by the deformed membrane using Equation (6.1). Strain energy, rather than injected volume was used as the former was more easily extracted from the CoventorWare software. Both plots are shown in Figure 6-17 revealing good agreement between experiments and simulation.

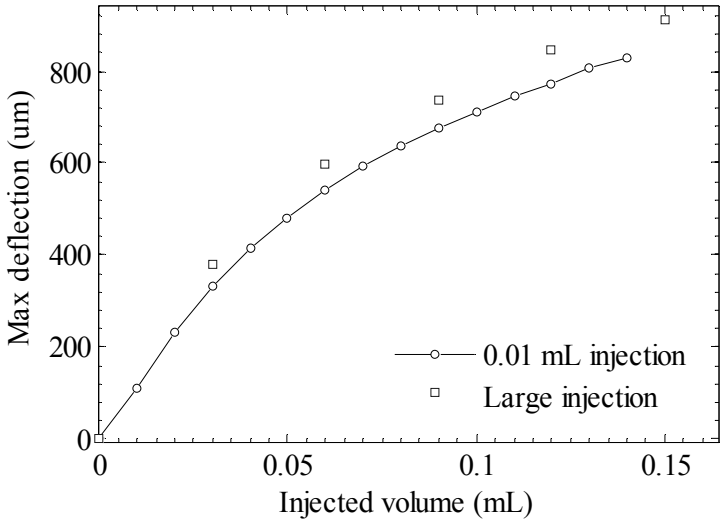


Figure 6-16 Maximum deflection at the centre of membrane as a function of injected volume

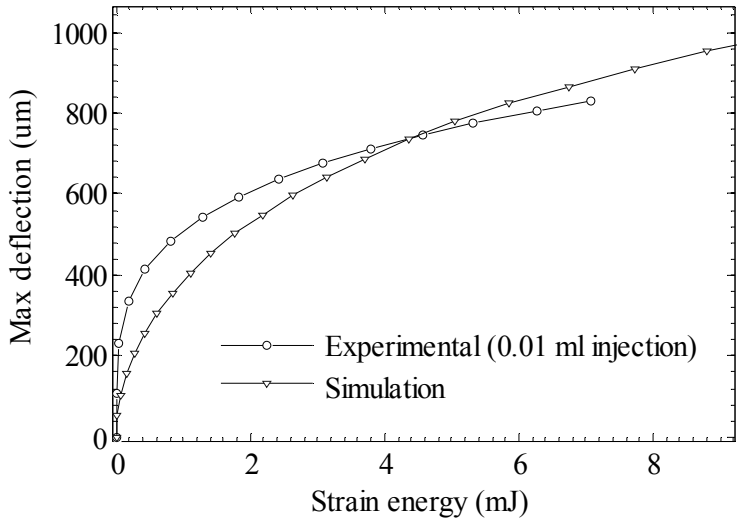


Figure 6-17 Comparison of free deformation results from experimental set up with FEA

6.4.2 Contact and µCP with a hydraulic drive

For µCP experiments, the stamp and substrates were arranged as per Figure 6-12. Part A of the stamp was inked (as described in Appendix A) prior to being placed on the hydraulic membrane, whilst the contact substrate was placed with the Au side facing the stamp. The lid was evenly tightened to hold the substrate flat and still against the alignment rail of the stamp. In this configuration, the flying height, *s*, is 190 µm.

A known volume is injected and contact is maintained for 1 minute. The outlet tap is then opened to retract the stamp and the substrate is replaced for another printing experiment. The images formed after printing and etching are illustrated in Figure 6-18. For the range of volumes tested, up to 70% of the total target area was contacted, and neither roof collapse nor pattern deformation was observed.

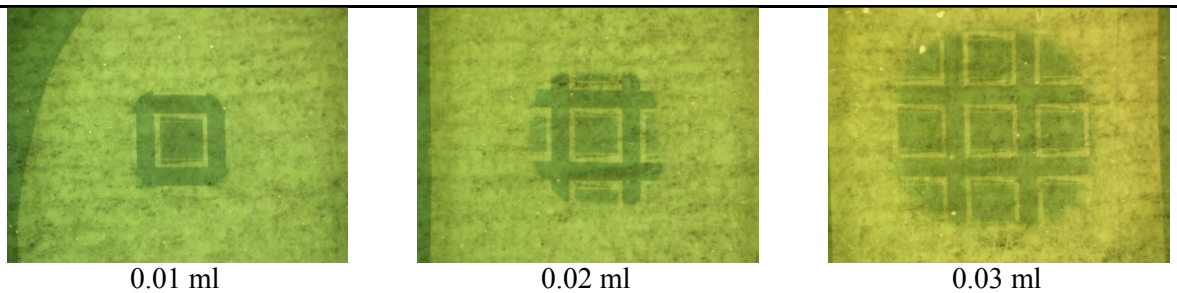


Figure 6-18 Optical micrographs showing Au patterns (dark) on glass (pale/transparent). The Au patterns are formed by µCP with different volumes and etching (as per Appendix A).

As expected, the contact area increases with deformation volume. This trend is illustrated in Figure 6-19 where both experimental values and the trend predicted by the simplified model (equation 6.2) are displayed. The volumes that are required to cause contact are significantly larger than those estimated. One explanation could be the difficulty in consistently setting the

same flying height due to the soft alignment rail. Hence, there may still be some movement of the substrate itself as the stamp is actuated. Another possibility is the presence of trapped air bubbles in the hydraulic cavity or pipes that are compressed as the pressure is increased. However, the latter effect is unlikely to cause such a large difference since the system is thoroughly flushed before actuation.

Finally, the experiment suffers from poor resolution in that the volume injected can be controlled only to the nearest 10 μL. This can be addressed by using finer pipes and a smaller hydraulic cavity which would enable the use of a smaller capacity syringe, thus allowing smaller volumes to be injected. Despite these shortcomings, the proposed system provides proof of concept for hydraulically driven μCP.

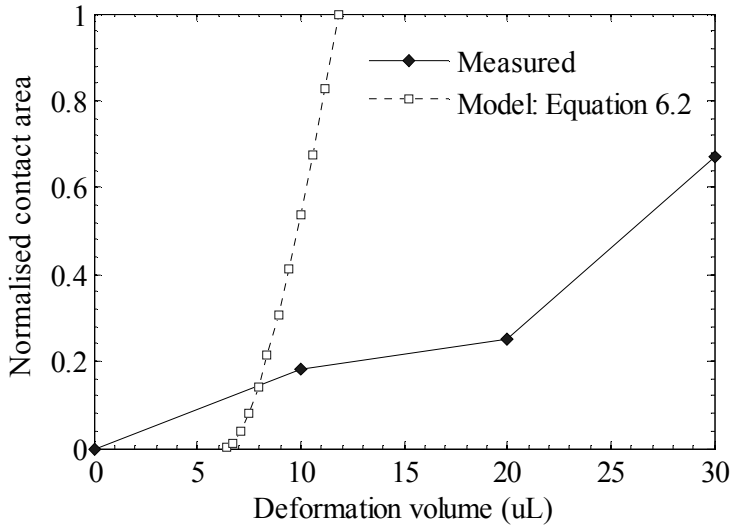


Figure 6-19 Normalised contact area as a function of injected volume

6.5 Conclusions

In this chapter, hydraulically driven μCP has been proposed and demonstrated. A tri-layered PDMS stamp was made by replica moulding and bonded to a precision machined Perspex chuck. Difficulties related to bonding the two parts together were identified and the stamp design was modified to solve the problem. The modifications made implied that multi-level operation with matching machined substrates could not be verified and hence only flat substrates were tested. Nevertheless, single level μCP with hydraulic actuation has been demonstrated and the proposed system serves as a springboard for further development of this class of actuator.

6.6 References

[6.1] M. De Volder and D. Reynaerts, "Pneumatic and hydraulic microactuators: a review," *J. Micromech. Microeng.,* vol. 20, p. 043001, 2010.

[6.2] K. W. Oh and C. H. Ahn, "A review of microvalves," *J. Micromech. Microeng.,* vol. 16, p. R13, 2006.

[6.3] D. J. Laser and J. G. Santiago, "A review of micropumps," *J. Micromech. Microeng.,* vol. 14, p. R35, 2004.

[6.4] C. Moraes, Y. Sun, and C. A. Simmons, "Solving the shrinkage-induced PDMS alignment registration issue in multilayer soft lithography," *J. Micromech. Microeng.,* vol. 19, p. 065015, 2009.

[6.5] J. M. Hoffman, J. Shao, C. H. Hsu, and A. Folch, "Elastomeric Molds with Tunable Microtopography," *Adv. Mater.,* vol. 16, pp. 2201-2206, 2004.

[6.6] M. A. Unger, H.-P. Chou, T. Thorsen, A. Scherer, and S. R. Quake, "Monolithic Microfabricated Valves and Pumps by Multilayer Soft Lithography," *Science,* vol. 288, pp. 113-116, April 7, 2000 2000.

[6.7] GeSIM, Micro-Contact Printing Instruments, http://www.gesim.de.

[6.8] M. M. J. Decre, R. M. Schneider, D. Burdinski, J. Schellekens, M. Saalmink, and R. Dona, "Wave Printing (I) : Towards Large-Area, Multilayer Microcontact Printing," *Mater. Res. Soc. Symp. Proc. Vol. EXS-2,* vol. M4, p. 9, 2004.

[6.9] C. K. Fredrickson, "Macro-to-micro interfaces for microfluidic devices," *LOC,* vol. 4, p. 526, 2004.

[6.10] Z. Yang, "A world-to-chip socket for microfluidic prototype development," *Electrophoresis,* vol. 23, p. 3474, 2002.

[6.11] Upchurch, NanoPorts, http://www.upchurch.com.

[6.12] A. A. S. Bhagat and et al., "Re-usable quick-release interconnect for characterization of microfluidic systems," *J. Micromech. Microeng.,* vol. 17, p. 42, 2007.

[6.13] R. A. Fine and F. J. Millero, "Compressibility of water as a function of temperature and pressure," *J. Chem. Phys,* vol. 59, pp. 5529-5536, 1973.

[6.14] S. P. Timoshenko and S. Woinowsky-Krieger, *Theory of Plates and Shells*, 2 ed.: McGraw Hill Book Co., 1959.

[6.15] S. D. Senturia, *Microsystem design*: Kluwer Academic, 2001.

[6.16] S. Bhattacharya, A. Datta, J. M. Berg, and S. Gangopadhyay, "Studies on surface wettability of poly(dimethyl) siloxane (PDMS) and glass under oxygen-plasma treatment and correlation with bond strength," *J. Microelectromech. Syst.,* vol. 14, pp. 590-597, 2005.

[6.17] M. A. Eddings and et al., "Determining the optimal PDMS-PDMS bonding technique for microfluidic devices," *J. Micromech. Microeng.,* vol. 18, p. 067001, 2008.

7 Conclusions

7.1 Summary

MEMS μCP printing engines are reported in this thesis. Two main versions are presented; the first is made of Si, whilst the second is made of PDMS and is formed by replica moulding on a microfabricated Si master. Both versions successfully harness MEMS concepts to meet the design objectives set in Chapter 1 and provide low-cost and accessible solutions to the problem of alignment and registration in multilevel μCP. An overview of the findings and achievements of this thesis is presented next.

Chapter 2 presents a novel method of depositing PDMS by spray coating. This technique allows the integration of the soft PDMS polymer with MEMS processing by adding the polymer after all the MEMS steps have been done. Suitable diluents are reported and optimised coating parameters are determined. Post-processing of micro-structures is investigated and methods of improving conformality have been explored. Functionality of the spray coated material is shown to be similar to conventionally cast PDMS. This deposition method contributes to the field of bio-MEMS, where PDMS and other polymers are often used, by enabling the fabrication of novel structures such as the deposition of polymer layers on fragile Si devices.

In Chapter 3, a c.a. 10 mm × 10 mm silicon μCP engine is designed, fabricated and characterised. The engine is self-contained and includes the stamp, an elastic suspension and passive alignment features that allow accurate registration to a complementary substrate. The engine is designed to operate with both an electrostatic and a mechanical drive, but only

mechanical operation is considered in this chapter. Single-level and two-level μCP over the entire stamp area (5 mm × 5 mm) is successfully demonstrated. This printing engine is the first reported μCP scheme that employs MEMS technology for self-alignment.

In Chapter 4 electrostatic actuation of the Si μCP engine is investigated. Electrostatic operation is analysed and verified experimentally but electrostatic discharge across the air gap is observed and μCP cannot be reliably carried out. The use of a series stabilising capacitor combined with a low stiffness structure is shown to keep voltages below the Paschen limit and μCP is successfully demonstrated with this approach. This work confirms the feasibility of electrostatically driven μCP but highlights the difficulty of this method.

In Chapter 5, a polymer μCP engine based on Si version is designed and fabricated by wafer-scale replica moulding PDMS onto a bi-level Si master. A photo-etched stainless steel sheet is bonded to the polymer prior to demoulding to improve mechanical stability and self-alignment is achieved with complementary groove and rail structures. Cost and complexity are driven down thanks to the batch moulding process and therefore cross contamination can be avoided since different stamps can be used for different inks. For the first time, six-level μCP is demonstrated with an average layer-to-layer misalignment of 10 μm over a 5 mm × 5 mm area. This contribution is especially noteworthy as such resolutions are achieved without external alignment optics or precision manipulation equipment and is therefore a truly low cost and accessible solution.

In Chapter 6, the replica moulding approach is preserved and the use of hydraulics for controlled actuation is investigated. The replica moulded μCP engine from Chapter 5 is modified by replacing the photo-etched stainless steel layer with a plain PI film and a

structured PDMS backing. This leads to lower operating pressures and FEA confirms pattern fidelity. Completed engines are glued to a precision machined Perspex chuck and actuated by injecting a controlled volume of water with a syringe driver. Reliable sealing of the engine to the chuck, however, requires further investigation. Single level μCP using a hydraulic drive is finally demonstrated and confirms the suitability of this novel approach.

7.2 Conclusions and Future work

μCP engines have been designed fabricated and tested, showing successful patterning of SAM. Passive alignment has been demonstrated and the pinnacle of this work is six-level patterning with different inks (Chapter 5) without the use of external aligning equipment. This dissertation contributes to the fields of bio-MEMS and μCP by enabling multi-level surface functionalization and opens up new possibilities.

Pattern fidelity (Absolute distortion / length of stamp)	11 μm / 5 mm → 0.2 %
Layer-to-layer accuracy (normalised to length of stamp)	10 μm / 5 mm → 0.2 %
Resolution	500 nm
Patterned area	5 mm × 5 mm

Table 7-1 Performance of replica-moulded multi-level μCP engines

The performance achieved by the replica-moulded multi-level μCP system is summarised in Table 7-1. Pattern fidelity of 0.2% is obtained and although this value is poorer than what is presented by others (see Section 5.3.3 for a detailed comparison), this method is cheaper and much more accessible to non-silicon end-users. Similarly, the six-level layer-to-layer accuracy is unique and noteworthy given that it is achieved without the need for alignment optics. A resolution of 500 nm has been achieved but this can be reduced further with the

availability of suitable masters. As for patterned area, further investigation is required to determine the upper limit of the current method. The main weakness of the μCP system is the actuation mechanism. Initial experiments (see Section 5.3.2) indicate that layer-to-layer accuracy would improve with a better regulated deflection mechanism.

Controlled actuation has been problematic throughout, although a manual drive performs well enough especially given the lack of other comparable solutions. Hydraulic actuation appears to be a viable solution although improvements are required. The limiting factor for successful hydraulic drive in the current attempt is the high operating pressure, which makes integration of the μCP engine with the hydraulic cavity difficult. The geometry of the engine used, i.e. a c.a. 10 mm × 10 mm stamp with a 5 mm × 5 mm print head, has been inherited from previous iterations of the μCP engine, and if the frame was made larger with respect to the print head, lower operating pressures could be obtained. With lower pressures, integration of the μCP stamp to the hydraulic chuck would be facilitated and one could even envisage bonding the PDMS engine to a hydraulic cavity made out of PDMS if pressures could be reduced to < 0.5 MPa. Such a proposed system would be very similar to the stamps of Chapter 6 and is illustrated in Figure 7-1a. The structure would be monolithic after bonding and the volume of the hydraulic cavity could be minimised. Fine capillaries can be drilled in and sealed using adhesive. In fact, just increasing the size of the stamp to 20 mm × 20 mm, whilst keeping a 5 mm × 5 mm print head, would drop operating pressures enough (i.e. < 0.5MPa when s = 50 μm). As shown in Figure 7-1b, with these dimensions, full contact is achieved at lower pressures for both 50 μm and 190 μm separations compared to the small device at a separation of 50 μm. This simulation uses the model of Chapter 6 with larger device dimensions. As the device gets flimsier, other factors such as static sag and stiction to the substrate need to be taken into account. Hence, the simulation model needs to be modified to

include these parameters and the operation of the engine verified further. Furthermore, to enable multilevel printing, a number of engines such as the one in Figure 7-1a will be required, and to ensure the stamps are correlated with respect to each other, a method of bonding an array (say 2 × 2) of stamps to a 2 × 2 array of hydraulic chucks could be explored.

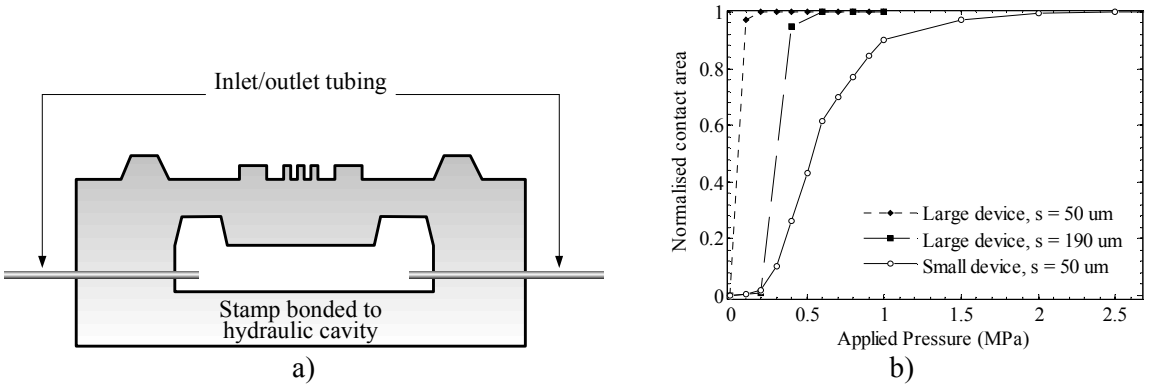


Figure 7-1 a) Illustration of monolithic PDMS stamp, b) Simulation data showing operating pressure required to induce contact with different device size

7.3 List of Publications

The following conference and journal papers are due in part to the work in this dissertation:

- R.R.A. Syms, H. Zou, K. Choonee, "Micro contact printing engines" Int. Conf. on MEMS (ICMEMS 2009), Madras, India, 3-5 Jan (2009)
- R. R. A. Syms, H. Zou, K. Choonee, and R. A. Lawes, "Silicon microcontact printing engines," *J. Micromech. Microeng.,* vol. 19, p. 025027, 2009.
- K. Choonee, R. R. A. Syms, M. M. Ahmad, and H. Zou, "Post processing of microstructures by PDMS spray deposition," *Sensors and Actuators A,* vol. 155, pp. 253-262, 2009.
- K. Choonee, R. R. A. Syms, and H. Zou, “Self-aligned micro contact printing using MEMS” Transducers 2009, Denver, Colorado, USA, 21-25 June (2009).
- K. Choonee, R. R. A. Syms, “Multi-level self-aligned micro-contact printing system,” *Langmuir*, vol. 26, pp. 16163-16170, 2010.

Appendix A: Inks and Etchants for μCP

This appendix provides detailed information concerning inks, suitable substrates, etching solutions, and practical tips regarding μCP of SAMs.

A1 Inks

For metallic substrates such as Au, alkanethiols are typically used. They have the general formula $CH_3(CH_2)_nSH$ and a list of suitable thiol is listed in Table A-1. As reported in[A.1], n>9 for the formation of sufficiently ordered SAMs. In the literature, hexadecanethiol (HDT, n=15) is most often used. However, lower weight thiols diffuse more and limit the resolution of μCP as reported in [A.2] whilst larger molecules do not protect as well [A.3].

Alkyl chain length, *n*	Thiol Name	Molecular weight/g	Comments
10	Dodecanethiol (DDT),	202	Shortest chain thiol that forms well ordered SAM, but too much diffusion
15	Hexadecanethiol (HDT)	258.5	Most commonly used thiol, but diffuses. (HDT is the longest range thiol that is liquid at room temp- melting point = 18 degrees)
17	Octadecanethiol (OCT)	286.6	Good compromise between HDT and ECT [A.3]
19	Eicosanethiol (ECT)	314	Does not protect as well as HDT[A.3]

Table A-1 Alkanethiols for μCP on Au

Typically, these thiols are diluted in ethanol to a concentration of ~ 0.1-10mM. No clear guideline or procedure has been found in the literature, but higher concentrations tend to crytallise and need to be warmed/ sonicated before use. In this work, unless specified otherwise, 0.5mM HDT is used without the need for agitation. The HDT is obtained from Sigma Aldrich U.K (Product #674516-500MG).

A2 Substrates

Au-coated Si or glass slides are used as substrates. The metal is deposited in a d.c magnetron sputter coater (Nordiko) and consists of a ~10 nm Ti adhesion layer followed by 30 nm thick Au. When possible, substrates are used for μCP soon after deposition of the metal. Otherwise, substrates are rinsed in acetone/isopropanol/ethanol and thoroughly blow-dried with filtered dehumidified clean dry air (CDA).

A3 Stamps and inking

PDMS stamps are thoroughly rinsed (and where possible sonicated) in ethanol prior to inking. Inking is carried out by placing a drop of the ink solution on the stamp using a pipette. The solution is allowed to penetrate the stamp for at least 1 minute and then blown dry with CDA until no bulk liquid could be observed. The same stamp could be used for multiple prints, although, for consistency, the cleaning and inking procedure is repeated in between prints.

A4 Printing

μCP is carried out by placing the inked and dried stamp onto the substrate, and maintaining contact for 30s. Light pressure is required to make contact, especially when the PDMS stamp is affixed to a rigid layer.

A5 Etchants

Suitable etchants that attack Au but not the thiol-covered regions is summaried in [A.4]

A potassium ferrycianide based etchant is used primarily for safety and convenience reasons. Also, [A.5] suggests that this etchant is more selective. The composition of the solution is: Potassium thiosulphate, $K_2S_2O_3$ (0.1M), Potassium hydroxide, KOH (1M), Potassium Ferricyanide, $K_3Fe(CN)_6$ (0.01M), and DI water is used as diluent. A typical recipe: 50ml DI, 2.8g KOH, 0.1645g $K_3Fe(CN)_6$, 0.9515g $K_2S_2O_3$.

The etch rate for a freshly prepared solution is ~5nm/min, and a 7 minute long etch provides good contrast with 30nm thick Au. The solution oxidises very quickly and the etch rates drop.

A method of improving the resilience to defects is to add a small amount of Potassium Ferrocyanide, $K_4Fe(CN)_6$ (0.001M) to the mixture. For a 50 ml DI solution, this amounts to 0.0211g of $K_4Fe(CN)_6$.Etch rate is not noticeably affected.

A6 References

[A.1] M. D. Porter, T. B. Bright, D. L. Allara, and C. E. D. Chidsey, "Spontaneously organized molecular assemblies. 4. Structural characterization of n-alkyl thiol monolayers on gold by optical ellipsometry, infrared spectroscopy, and electrochemistry," *J. Am. Chem. Soc.,* vol. 109, pp. 3559-3568, 1987.

[A.2] E. Delamarche, H. Schmid, A. Bietsch, N. B. Larsen, H. Rothuizen, B. Michel, and H. Biebuyck, "Transport Mechanisms of Alkanethiols during Microcontact Printing on Gold," *J. Phys. Chem. B,* vol. 102, pp. 3324-3334, 1998.

[A.3] R. B. Bass and A. W. Lichtenberger, "Microcontact printing with octadecanethiol," *Appl. Surf. Sci.,* vol. 226, pp. 335-340, 2004.

[A.4] A. Kumar, H. A. Biebuyck, and G. M. Whitesides, "Patterning Self-Assembled Monolayers: Applications in Materials Science," *Langmuir,* vol. 10, pp. 1498-1511, 1994.

[A.5] Y. Xia, X.-M. Zhao, E. Kim, and G. M. Whitesides, "A Selective Etching Solution for Use with Patterned Self-Assembled Monolayers of Alkanethiolates on Gold," *Chem. Mat.,* vol. 7, pp. 2332-2337, 1995.